Small Ag Clusters Supported on an LTA Zeolite Investigated by CW and Pulse EPR spectroscopy, XAS, and SQUID Magnetometery

Von der Fakultät Chemie der Universität Stuttgart zur Erlangung der Würde eines Doktors der Naturwissenschaften (Dr. rer. nat.) genehmigte Abhandlung
Vorgelegt von

M.Sc. Amgalanbaatar Baldansuren
aus Ulan Bator, Mongolei

Hauptberichter: Prof. Dr. Emil Roduner
Mitberichter: Prof. Dr. Micheal Hunger
Mitberichter: Prof. Dr. Wolfgang Kaim

Tag der mündlichen Prüfung: 06 April 2009

Institut für Physikalische Chemie der Universität Stuttgart

Dezember 2008

Diss. OPUS... WS 2008/2009

Dissertation for the degree of
Doctor of Natural Sciences
submitted to the
University of Stuttgart

Small Ag Clusters Supported on an LTA Zeolite Investigated by CW and Pulse EPR Spectroscopy, XAS and SQUID Magnetometry

presented by
M.Sc. Amgalanbaatar Baldansuren
from Ulan Bator, Mongolia

Institute of Physical Chemistry

December 2008

accepted on the recommendation of
Prof. Dr. Emil Roduner, examiner
Prof. Dr. Micheal Hunger, co-examiner
Prof. Dr. Wolfgang Kaim, co-examiner

This study is an experimental result of the work carried out from October 2004 to December 2008 at the Institut für Physikalische Chemie, Universität Stuttgart, under the supervision of Prof. Dr. Emil Roduner.

The text was created using LaTeX 2ε system with the combination of document class scrbook and KOMA-Script by the author. Typeset is in 11pt Palatino. Figures were produced by the combination of Matlab, Origin and CorelDraw.

This thesis is printed at the Rechenzentrum Universität Stuttgart (RUS).

To my mother, my wife and my sweet daughter

Synopsis

Due to the increasing use of their unique properties, metal nano-clusters are very promising candidates for developments in new age nano-electronic and nano-magnetic devices. In many respects, metal clusters no longer follow classical physical laws as most bulk materials do, but are correctly to be considered by means of quantum mechanics.

The paramagnetic silver cluster containing catalysts were prepared in the pores of LTA zeolite support by chemical methods including aqueous ion-exchange, oxidation and hydrogen reduction. Depending upon the silver loading different paramagnetic species and clusters, i.e. Ag^0, Ag_3^{n+}, Ag_4^{n+} and Ag_6^+, have been observed in the hydrogen reduced 6 - 12% (wt.) Ag/NaA. A single, well-defined cluster consisting of 6 equivalent Ag nuclei is of major interest and focus of this thesis.

Solid-state continuous wave and pulse X-band electron paramagnetic resonance (EPR)[1] are proved as principle tools for the investigation of the dynamics of unpaired electron spins and of the nuclear spins coupled to the unpaired electrons of well-defined Ag clusters. A hyperfine spectrum, i.e. a direct measurement of hyperfine splittings validates the existence of well-defined Ag clusters as individual species and resolves various structural fingerprints. In the first instance, the reduced Ag_6^+ cluster is well isolated, and all silver atoms are close to equivalent. Pulse EPR experiments reveal no direct spin density on the protons in the vicinity of the reduced Ag_6^+ cluster, while the presence of the ^{27}Al "*matrix peak*" confirms the close proximity of the lattice to the reduced silver cluster. Reduced Ag_3^{n+} and Ag_4^{n+} clusters practically exhibit the isotropic hyperfine interactions of nearly equivalent silver nuclei with the unpaired electrons, whereas the Ag^0 clusters demonstrate hyperfine anisotropy. To interpret the experimental spectra reliably numerical spectrum simulations were performed. They provide full information on the electronic and symmetry state of the measured paramagnetic Ag clusters.

Since electron spin echo detected pulse methods have many advantages over continuous wave methods, the cylindrical TE_{011}-mode microwave resonator has been constructed and implemented in the home-built pulse Q-band spectrometer for field-sweep ESE and ESE-detected ENDOR operating at a low temperature of 1.5 K.

For a better understanding of inextricable relations between the electronic state and static magnetism of reduced Ag clusters, the experiments on the temperature and magnetic field dependence of the electron magnetic susceptibility and magnetization have been performed using a SQUID magnetometer. The effective electron spin of ensembles of supported small Ag clusters mainly depends on the fundamental symmetry of the electron Hamiltonian. The EPR active odd-electron Ag clusters, which are comprised of very small fractions of all exchanged silver ions, dominate the EPR-silent even-electron Ag clusters and suggest that magnetic states consists of diamagnetic, low spin ($S = 1/2$) paramagnetic states, and high spin states. Magnetization measurements reveal the total magnetization of the reduced Ag cluster system, whereas EPR probes selectively paramagnetic Ag_6^+ clusters in the field domain. Applying the double integration of the first-derivative EPR signals, the temperature dependent electron susceptibility of the

[1] also termed as Electron Spin Resonance - ESR

paramagnetic Ag_6^+ cluster exhibits a Curie type dependence and odd-electron susceptibility dominates even-electron susceptibility.

X-ray absorption spectroscopy (XAS) measurements at the Ag *K*-edge (25.514 keV) were performed at the Swiss-Norwegian Beamline (SNBL) BM01B of the Storage Ring of the European Synchrotron Radiation Facility (ESRF) in Grenoble, France. The experimental findings showed that the structure of silver nano-clusters differs significantly from that of the bulk metal. EXAFS experiments using direct *in-situ* hydrogen reduction yield precise and important information on a local structure which supports an estimate of the mean size of reduced silver clusters on average. A quite mono-disperse structure of ca. six-atomic clusters exhibiting $N = 4.00 \pm 0.05$ revealed significant bond length contraction in comparison with a regular atomic spacing in the bulk Ag (2.889 Å). Hydrogen reduction just leads to a partial reduction of oxidized silver clusters, indicating that the agglomeration of the cluster is either incomplete, or the cluster shape is less spherical.

To understand the role of silver clusters during the adsorption of adsorbate molecules, several test experiments had been carried out under various conditions, and conversions were monitored directly by means of conventional and pulse EPR spectroscopies. In the $^2\Pi_{1/2}$ state, the spin and orbital angular momentum are anti-parallel in the free NO molecule, thus the spin magnetism is compensated. As NO is adsorbed on the reduced Ag_6^+ cluster, the orbital degeneracy is lifted by the cluster crystal field or electrostatic field, and an EPR signal becomes observable. The hyperfine splitting of the reduced Ag_6^+ cluster disappears immediately, and there is no significant spin density on the cluster. We consider that we are observing either the NO adduct to a previously diamagnetic and therefore EPR silent Ag cluster, or that a red-ox reaction precedes NO adsorption. In addition, the adsorbed NO_2 exhibits a kind of Brownian molecular slow-motion which is responsible for a large amplitude tilting or flipping of the molecule about its molecular *y* axis. By analyzing the EPR lineshapes, the $\tau_\perp$ components of the correlation time are derived to provide the kinetic parameters, and an Arrhenius representation gives access to the activation energy $E_a = 550$ J mol^{-1} for the overall rotational motion. The higher tumbling rate of NO_2 on the silver-free zeolite proves that adsorption on the silver clusters is slightly stronger than on sodium ions. The interaction of $^{17}O_2$ with the cluster surface revealed some anisotropy of the hyperfine structure at 3.0 K. The energy separation between the first two rotational levels of the $^{17}O_2$ molecule is on the order of $\Delta E = 96$ J mol^{-1} which can be simply calculated from a relation between the total angular momentum *J* and the moment of inertia *I*. The very weak hyperfine couplings of the remote protons were resolved by applying pulse X-band Mims ^{1}H-ENDOR and HYSCORE after the adsorption of C_2H_4 on the reduced Ag_6^+ clusters.

In-situ EXAFS spectroscopy is also a very suitable and powerful tool to investigate the nature of the cluster-adsorbate interactions, and the changes in electronic or structural state of Ag clusters were demonstrated based upon the analyses of the absorption fine structure spectra. A reduced silver cluster undergoes a slight structural change, and a red-ox reaction precedes adsorption of NO. As noted before, the adsorbed NO is bound on diamagnetic and EPR-silent Ag clusters but the cluster still exhibits the same structure as determined by EXAFS. This averaging technique detects an ensemble of different clusters on average, i.e. no matter whether silver clusters are diamagnetic or paramagnetic.

Zusammenfassung

Dank der steigenden Anzahl an Anwendungen ihrer einzigartigen Eigenschaften, sind metallische Nano-Cluster vielversprechende Kandidaten für die Entwicklung zukunftsweisender nano-elektronischer und nano-magnetischer Bauteile. In vielerlei Hinsicht können Metallcluster im Gegensatz zu grösseren Festkörpern nicht mehr mit klassischer Physik beschrieben werden, sondern müssen korrekterweise quantenmechanisch betrachtet werden.

Die Katalysatoren, die paramagnetische Silbercluster enthalten, werden in die Poren des LTA-Zeolithgerüsts durch chemische Methoden wie wässrigem Ionenaustausch, Oxydation und Wasserstoffreduktion, eingebracht. Abhängig von der Ladung der Silberionen wurden verschiedene paramagnetische Typen von Clustern wie z. B. Ag^0, Ag_3^{n+}, Ag_4^{n+} und Ag_6^+ in dem mit Wasserstoff reduzierten 6 - 12% (gew.) Ag/NaA beobachtet. In dieser Dissertation geht es hauptsächlich um einen einzelnen, wohl-definierten Cluster, der aus sechs äquivalenten Silberkernen besteht.

ESR-Spektroskopie in Festkörpern ist sowohl im continous wave als auch im gepulsten Verfahren eine bewährte Methode zur Untersuchung sowohl der Dynamik ungepaarter Elektronenspins als auch der Kopplung der Kernspins mit ungepaarten Elektronen in den wohldefinierten Silberclustern. Das Hyperfeinspektrum, welches direkt durch die Hyperfeinstruktur-Aufspaltung gemessen werden kann, bestätigt die Existenz einer einzigen wohldefinierten Art von Silberclustern und löst die verschiedenen strukturellen fingerprints in dem Zeolithgerüst. Zunächst ist der Ag_6^+ Cluster gut isoliert und alle Silberatome können als nahezu äquivalent angesehen werden. Die experimentell erhaltetenen Spektren wurden numerisch simuliert, um die gesamte Information über den Elektronen- und Symmetriezustand der gemessenen paramagnetischen Silbercluster zu erhalten. Da die Puls-Elektronenspin-Echo Spektroskopiemethode viele Vorteile gegenüber continuous wave Methode hat, wurde ein zylindrischer TE_{011}-mode Mikrowellenresonator gebaut und in das selbstgebaute Puls-Q-band Spektrometer für Fieldsweep ESE und ESE-detektiertes ENDOR eingebaut und bei einer niedrigen Temperatur von 1,5 K betrieben.

Um ein besseres Verständnis der Beziehungen zwischen dem Elektronenzustand und dem statischen Magnetfeld zu erhalten, wurde unter Verwendung eines SQUID die Temperatur- und Magnetfeldabhängigkeit der elektromagnetischen Suszeptibilität experimentell bestimmt. Der effektive Elektronenspin von einem Ensemble kleiner Ag-Cluster hängt von der fundamentalen Symmetrie des Hamiltonians des Elektrons ab. Die EPR aktiven Ag-Cluster mit ungerader Anzahl an Elektronen, die aus einem sehr kleinen Bruchteil von allen ausgetauschten Silberionen bestehen, dominieren die EPR-inaktiven Ag-Cluster mit gerader Anzahl an Elektronen und bedeuten, dass der magnetische Zustand aus diamagnetischen, paramagnetischen low spin ($S = 1/2$), und high spin Zuständen besteht. Messungen der Magnetisierung zeigen die gesamte Magnetisierung des redzuierten Silbercluster-Systems, EPR Messungen zeigen hingegen selektive nur die paramagnetischen low spin Ag_6^+ Cluster. Wird das EPR-Signal doppel integriert, erhält man die temperaturabhängige Elekronen-Suszeptibilität der paramagnetischen Ag_6^+ Cluster, welche Curie-type Abhängigkeit zeigt, und dabei die ungerade

Elektronen-Suszeptibilität die gerade dominiert.

Röntgenstrahlungsabsorptionsspektroskopie (XAS) an der Ag *K*-Kante (25,514 keV) wurden an der schweizerisch-norwegischen Beamline (SNBL) des Speicherrings der Europäischen Synchrotron-Strahlungs-Einrichtung (ESFR) in Grenoble in Frankreich durchgeführt. *In situ* EXFAS unter Verwendung direkter Wasserstoff-Reduktion, liefert präzise und wichtige Informationen über die lokale Struktur, welche eine Schätzung der durschnittlichen Silbercluster-Grösse unterstützt. Eine ziemlich mono-disperse Struktur, ca. sechs atomige Cluster, mit einer mittleren Koordinationsanzahl von $N = 4.00 \pm 0.05$ hat offenbar eine bedeutsame Reduktion der Bindungslänge im Vergleich mit einer regelmässigen atomaren Bindungselänge im Bulksilber (2,889 Å). Wasserstoffreduktion führt nur zu einer teilweisen Reduktion von oxidierten Silberclustern, was darauf hindeutet, dass die Agglomeration zu Silberclustern entweder unvollständig oder die Clusterform weniger kugelförmig ist.

Um die Rolle von Ag-Clustern während der Adsorptionsreaktionen gegen Adsorbatmoleküle zu verstehen, waren mehrere Versuche unter verschiedenen Bedingungen durchgeführt worden, und Reaktionen wurden direkt mittels konventionellen und Puls-EPR-Spektroskopien überwacht. Im $^2\Pi_{1/2}$ Zustand stehen der Spin und das Bahnmoment im freien NO-Molekül anti-parallel, und daher ist der Spinmagnetismus kompensiert. Wenn NO auf die reduzierten Ag_6^+ Cluster adsorbiert, wird die Orbital-Entartung durch das Kristallfeld des Clusters oder das elektrostatische Feld aufgehoben, und ein EPR-Signal wird beobachtbar. Die Hyperfeinaufspaltung der reduzierten Ag_6^+ Clusters verschwindet instantan, und es gibt keine nennenswerte Spindichte mehr auf dem Cluster. Wir denken, dass wir entweder das NO-Addukt an einer vorher diamagnetischen und daher EPR-inaktiven Ag-Cluster beobachten, oder dass eine Redoxreaktion der NO-Adsorption vorausgeht. Adsorbiertes NO_2 zeigt eine Dynamik. Verantwortlich dafür ist möglicherweise eine Art Kippbewegung des Moleküls um seine *y*-Achse. Über eine Analyse der EPR-Linienformen können die $\tau_\perp$ Komponenten der Korrelationszeiten bestimmt und daraus die kinetischen Parameter abgeleitet werden. Eine Arrhenius Darstellung ermöglicht den Zugang zu der Aktivierungsenergie von $E_a = 550$ J mol^{-1} für die gesamte Rotationsbewegung. Das schnellere Taumeln von auf silberfreien Zeolithen adsorbiertem NO_2 belegt, dass die Adsorption auf die Ag-Cluster geringfügig stärker ist als diejenige auf Na^+. Die Wechselwirkung von $^{17}O_2$ mit der Clusteroberfläche lässt eine Anisotropie der Hyperfeinstruktur bei 3.0 K erkennen. Die Energielücke zwischen den ersten beiden Rotationsniveaus des $^{17}O_2$-Moleküls liegt im Bereich von etwa $\Delta E = 96$ J mol^{-1}, was leicht aus der Beziehung zwischen dem Bahnmomen *J* und dem Trägheitsmoment *I* berechnet werden kann. Nach der Adsorption von C_2H_4 wurden sehr schwache Hyperfeinkopplungen entfernter Protonen mittels gepulsten X-band Mims ^{1}H-ENDOR und HYSCORE aufgelöst.

In situ EXAFS-Spektroskopie ist auch ein sehr passendes und aussagekräftiges Werkzeug, um die Natur der Cluster-Adsorbat-Wechselwirkungen und die Änderungen in elektronischem oder strukturellem Zustand von Ag-Clustern zu untersuchen. Ein reduzierter Ag-Cluster vollführt eine kleine Strukturänderung, und eine Redoxreaktion geht der Adsorption von NO voraus. Wie bereits früher bemerkt, adsorbiert das NO auf diamagnetische und EPR inaktive Silbercluster, aber der Cluster zeigt immer noch diesselbe Struktur wie durch EXAFS bestimmt. Diese Mittelungsmethode detektiert im Mittel ein Ensemble von verschiedenen Clustern, d.h. unabhängig davon, ob die Silbercluster dia- oder paramagnetisch sind.

Preface

It is proposed that this thesis be a treatise predicting and highlighting some particular aspects of supported silver clusters. It basically puts the crucial emphasis on understanding the unpaired electron effect of paramagnetic clusters on the electronic and structural state. The valuable insights into the most basic but very important properties of such clusters have been gained based upon the careful examinations and interpretations of the experimental facts. By including experimental materials, it collects all the new results to provide a consistent framework for further research and investigations. It also helps readers to figure out the experimental results which are published and to be reported in scientific journals.

This thesis is not entirely written in a formal language. A large fraction of the text might be written in proper standards[2] along with scientific publishing, and a sloppy speech is always avoided as much as possible. If most complicated formulations are found, I refer readers to the cited publications and books. When writing this thesis, it was trying to relieve a dry formalism of science.

Not only the form, but also the content of this thesis are proposed explaining the scientific emphasis simply and clearly. A beginner or rookie PhD student with little or without prior knowledge of the cluster science would be able to read this thesis and to learn all that is needed for successfully synthesizing silver clusters using chemical methods in the support pores and characterizing them by means of spectroscopic techniques operating at the particular frequency range of electromagnetic radiations and waves. The interpretations of the powder magnetic resonance spectra and their numerical simulations are also to be reported in the scientific journals so that further overviews will collectively come in very handy. The theoretical fit to the spectra of X-ray absorption spectroscopy is normally the province of a few specialists, it is addressed here to a larger audience.

This thesis is concerned with just some particular aspects of the vast field of cluster science, i.e. physics and chemistry in general, and reports a series of experimental studies of supported Ag clusters using magnetic resonance spectroscopy, X-ray absorption (XAS) spectroscopy and SQUID magnetometry. The work mostly focuses on the validation of theoretical and quantitative approaches to the features of supported Ag clusters inferred from conventional and pulse electron paramagnetic resonance (EPR), on the interpretation of EPR parameters in terms of symmetry of the electron Hamiltonian, and on the understanding of the electron spin state and electronic configuration underlying the contributions to static magnetism and magnetic states.

This thesis consists of seven chapters basically. **Chapter 1** will give a brief overview of the scientific importance and a comprehensive survey of small Ag clusters supported on an LTA zeolite. As a brief introduction of the bulk silver, the synthetic zeolites[3], the novel properties of small metal clusters, and physical principles of experimental spectroscopic techniques applied for characterizations of supported Ag clusters will

[2] not strict standards

[3] known as micro-porous polycrystalline materials

appear in **Chapter 2**. The systematic of chemical methods for preparations of small silver clusters in the support pores, various cluster species exhibiting paramagnetic properties, the basic concepts and fundamental aspects of spin paramagnetism, a static magnetic property and a local structure property measurements will be briefly given in **Chapter 3**. Some of the theoretical and technological concepts for designing a microwave resonator are summarized. The cylindrical TE_{011} mode resonator implemented in the home-built pulse Q-band spectrometry have been tested by collecting several hyperfine spectra at low temperatures. It is described briefly in **Chapter 3**. The high resolution transmission electron microscopy (HR-TEM) applying transmission of electrons will be added in this chapter as additional tools for determining the size of supported silver species.

Chapters from **4** to **6** are entirely devoted to explain all experimental achievements and approaches of this thesis. **Chapter 4** will be concerned with all the experimental results of spin paramagnetism of the reduced Ag clusters due to the unpaired electron spin leading to the delocalized spin-density distribution in the cluster molecular orbital. By the presence of the diamagnetic and high spin state, static magnetic properties underlying the low spin paramagnetic state will focus on the effect of the temperature and the external applied magnetic field on the electron magnetic susceptibility in **Chapter 5**. The mean size and local structure of the nominal Ag_6^+ cluster will be discussed based upon the interpretations of the structural parameters derived from the absorption fine structure spectra in terms of surface and geometrical effects on magnetism. In **Chapter 6**, the particular subjects concerning chemical interactions will be reviewed covering the characteristic chemical and stoichiometric or fertile catalytic properties of the reduced Ag_6^+ cluster against the number of adsorbate molecules. Some kinetic information deduced from the analyses of a kind of molecular slow motion of conversion products will be also given. A few words will be added in **Chapter 7** for **Conclusions** touching on the importance of the gained insights into the specific properties along which supported small Ag cluster physics and chemistry may trace their development trends towards various technical applications.

The results obtained using different experimental approaches on a supported Ag cluster system will contribute one step forward to the complete understanding the unique characteristics. Indeed, when starting this work, novel properties of the system were almost incompletely explored from viewpoints of physics, chemistry, and heterogeneous catalysis.

Acknowledgments

I would like to thank many people who contributed in a diversity of ways to a successful accomplishment of this work.

My very special thanks go to Prof. Dr. **Emil Roduner** for giving me such a nice opportunity to conduct a highly motivated project in his research group and for his scientific supervisory role in the accomplishment of my PhD project. I am also highly grateful for his invaluable guidance, counsel, teaching of many different subjects of small metal clusters and physical chemistry. I am happy to emphasize his encouragement to perform X-ray absorption spectroscopy measurements and the push for learning this kind of modern technique at the ESRF in Grenoble, France. I am very grateful for him who let me to introduce recent progress of our research into numerous conferences, workshops, and seminars. I would like to quote from Confucius[4]: ... *One day's teacher is all life's father* ... for him.

I gratefully acknowledge Prof. Dr. **Micheal Hunger** for writing the second advisory opinion. Prof. Dr. **Wolfgang Kaim** is kindly acknowledged for taking the chairmanship of the examination board.

It is great pleasure to thank PD Dr. **Rüdiger-Albert Eichel** for his enormous help for performing state-of-the-art pulse EPR experiments on the reduced Ag clusters in the support system and for invaluable advice on interpretations of HYSCORE and ENDOR spectroscopy results, and for convincing me to learn the EasySpin simulation package.

I would like to thank Dr. **Herbert Dilger** for his very admirable help with lots of programming and for solutions of many technical problems in particular. Thank you Herbert for being with me for several creative and instructive weeks for XAS measurements in Grenoble.

I specially thank Dr. **Igor Tkach** for his very valuable discussions on advanced pulse EPR techniques, and appealing guidances and advice on the construction of the pulse Q-band resonator.

I thank Prof. Dr. **Jeroen A. van Bokhoven** from the Institute for Chemical and Bioengineering at the Department of Chemistry and Applied Biosciences at the Swiss Federal Institute of Technology Zürich in Switzerland for instructions in the ways of EXAFS analyses using XDAP software and guidances for accomplishing XAS experiments in Grenoble. His group members are also kindly acknowledged for being generally helpful during the my several visits.

I thank PD Dr. **Joris van Slageren** from the 1. Physikalisches Institut, Universität Stuttgart, for helping me to do experiments on static magnetic properties of the supported Ag cluster system using a SQUID magnetometer.

Dr. **Olga Safonova** is also acknowledged to introduce me an amazing ability of contemporary synchrotron radiation facility in Grenoble during my stays for XAS experiments on the supported silver cluster system.

Dr. **Lin Gu** is also acknowledged for performing HR-TEM measurements of the supported clusters at the Stuttgart Center for Electron Microscopy in the Max-Planck Insti-

[4]551 BC - 479 BC - social philosopher

tute for Metals Research.

A special thank goes to Mrs. **Inge Blankenship**, who is always very helpful for me in handling all sorts of administration documents and problems during these four years. Mrs. **Susan Luginsland** is also acknowledged for her nice discussions about Mongolia and the Mongolian.

I thank all the **members** of our research group in the present and the past for providing me with a pleasant working atmosphere.

I would like to express my special thank to Mr. **Werner Hoff** for his superb craftsmanship of glass blowing. Without his help all kind of EPR measurements and the sample preparations would be unthinkable. Mrs. **Gabriele Bräuning** is also acknowledged for her numerous helps in getting the chemical reactants and other laboratory items. Prof. Dr. **Klaus Müller** is acknowledged for providing us with isotopically enriched $^{17}O_2$ gas for experiments.

The Graduate College **"Advanced Magnetic Resonance Type Methods in Materials Science"** is gratefully acknowledged for funding supported by the German Research Foundation - DFG. Mrs. **Otgontuul Tsetsgee** is also acknowledged for being a Mongolian colleague of mine in the Graduate College and the Institute of Physical Chemistry.

I thank my mother **Namjilmaa**, my brothers and sister, **Amgalanbayar, Amgalantugs and Amgalantuul** - for moral supports, even though they are at a distant place in Mongolia.

Most of all, I want to thank **Ugtakhbayar**, my lovely wife and wonderful mother of my sweet daughter **Saruul-Oyu** who more than anyone has provided inspiration, encouragement, friendship and love for me. This work is dedicated to three wonderful women in my life: my mother, my wife and my sweet daughter.

Amgalanbaatar Baldansuren Stuttgart, December 2008

Contents

1 Introduction and motivation

Catalysts, i.e. heterogeneous, homogeneous and enzymes, are often nano-clusters or nano-particles. These are vital for the functioning of the human body, for photosynthesis, and for producing fuels and chemicals in the petroleum and chemical industries [1]. The ultimate aim of the modern cluster science is the development of cluster systems in the nano-size range exhibiting well-controlled properties suitable for particular applications [2]. To achieve the particular task successfully, it requires the development of physical and chemical procedures to synthesize the cluster systems with great stability and homogeneity of size and shape distributions. The use of the micro-porous zeolite supports meets the requirements for obtaining such clusters at the nano-scale. The size of zeolite-supported clusters is constrained along one or more dimensions. Such constraints usually render substantial changes in the structural, physical, electronic and magnetic properties of the clusters. Furthermore, the zeolite cages provide a practical means of preventing the cluster cohesion, because small metal clusters have a strong tendency to form larger particles ($d > 10$ nm) driven by surface energy minimization. In addition, the chemical methods are totally sufficient and are even not very complicated to prepare small metal clusters in the pores of the zeolite supports. Zeolite supported transition metal clusters feature prominently as catalysts in different branches of chemistry [3].

An inherent advantage, particularly of small metal clusters, is due to the fact that the unpaired electrons are assumed to occupy molecular orbitals delocalized throughout the overall cluster atoms, which can be expressed surprisingly well by a simple *tight-binding approximation* leading to a simple Fermi level which is being used extensively for electronic states confined in a low dimension [4]. A few electronic levels near the highest occupied electronic state of energy are of great interest, and their interactions/repulsions with the lowest unoccupied electronic state result in different energy level distributions depending upon the symmetry of the electron Hamiltonian. The energy difference between HOMO and LUMO is the energy gap δ (or Kubo gap) which will be comparable to other energies such as the thermal energy $k_B T$, the electron Zeeman energy $\mu_B H$ and the nuclear Zeeman energy $\mu_N H$ at low temperatures. The Fermi level lies in the energy gap, while the electron excitation/transfer through the energy gap is extensively studied by applying the external magnetic field [5]. Time-dependent DFT calculations revealed that a transfer/excitation of 5*s*-electrons from HOMO to LUMO is mainly responsible for the absorption spectra of very small Ag clusters [6].

For noble-metal clusters, the electronic structure is dominated by the number of valence electrons[1], and the ionic-core is of secondary importance [7]. Unfortunately, this is not always absolutely true, at least not for paramagnetic Ag clusters. From the theoretical point of view the corresponding orbitals are nevertheless affected by core electrons to ensure orthogonality to core orbitals [8]. Pseudopotentials and effective core potentials can represent the effect of the core electrons and are derived from relativistic calculations including *relativistic effects*. On the contrary, non-relativistic theory is basically

[1] distribution is modeled by *free-electron approximation*

applied to valence electrons. If it is the use of pseudopotentials to substitute for core electrons, the hyperfine couplings often arise mostly from spin polarisation of core orbitals of paramagnetic Ag clusters. This naturally makes things complicated and less convenient, it takes longer to run calculations when all the electrons must be included, rather than just the valence electrons.

The individual neutral Ag atom has one unpaired electron, thereby exhibiting paramagnetism, which is due to a strong spin-orbit coupling, whereas bulk metallic silver is diamagnetic. Interestingly, nano-size reduced Ag clusters are often paramagnetic [9, 10, 11, 12, 13, 14, 15, 16, 17, 18, 19] and appear to provide a bridge between the limits of the isolated atom and the bulk. With a few exceptions, this magnetism is assumed due to the number of unpaired electrons which lead to the electronic size effects. Furthermore, the hyperfine splitting of individual silver clusters was usually complicated to interpret reliably due to coexistence of many different structures. It was mostly dependent on the reduction procedures of Ag^{+} into silver clusters, i.e. chemical reduction, X-ray and γ-ray irradiation, in the support pores. The irradiation method specially renders a coexistence of different hyperfine structures by creating many defect centers in the support lattice. This led to difficulties in characterizing the reduced Ag clusters in the support pores as a single small species. Furthermore, the reduced Ag clusters had a lifespan of only a few hours under isolated conditions from initial preparation conditions [15, 16, 17, 18, 19]. These particular disadvantages therefore imposed the restrictions on a better understanding of the physical, electronic and chemical properties to date. These *motivations* are still fundamental and the main driving forces to study the formation and particular properties of reduced Ag clusters in the pores of NaA.

Electron paramagnetic resonance (EPR) is a spectroscopic method for determining the structure, dynamics, and the spatial distribution of paramagnetic species. Such species possessing at least one unpaired electron are often **chemically reactive**. With a few exceptions, unpaired electrons lead to a non-vanishing spin of a particle which can be used as a spectroscopic probe. The transitions between electron spin states can be induced by on-resonant electromagnetic radiation, which is chemically nondestructive, and the energies of the electron spin states depend on a number of structure-related parameters. Therefore, EPR is used to provide an unambiguous determination of the existence of mono-disperse Ag clusters supported on Ag/NaA.

Paramagnetic properties of reduced silver clusters can be described in terms of *electronic transitions* between the discrete energy levels of the angular momentum in a quantum well exposed to the external magnetic field as it gives rise to an observable experimental spectrum. However, the individual contributions of spin and orbital angular momenta to the total angular momentum are not experimentally observable. The spectrum observability is therefore related to changes in the *total* angular momentum and must be interpreted in terms of the corresponding *total* quantum numbers. The energy levels of the Hamiltonian can be obtained from the first-order perturbation theory taking the secular part of the electron Zeeman splitting as zero-order approximation of the Hamiltonian, and the nuclear Zeeman and hyperfine interactions as the first-order perturbations. In paramagnetic Ag clusters, the unpaired 5*s* electrons occupy molecular orbitals delocalized over all atoms equally. It implies that there are allowed transitions $\Delta m_S = \pm 1$ between m_S = - 1/2 and m_S = + 1/2 states of electron spin angular momentum, and energy quantization or energy level spacing appears as intrinsic sharp lines of the spectrum. It is well known that the energy quantization is relative to the modified physical properties of small metal particles [5, 20, 21]. In 12% (wt.) Ag/NaA, the

highest nuclearity of the reduced Ag_6^+ cluster generally leads to the lowest hyperfine interactions of the silver nuclei with the unpaired electron. Since the bulk Ag has the electronic configuration of Kr[$4d^{10}5s^1$], the paramagnetic property of reduced Ag clusters derives from the odd-number of 5*s* valence electrons in the open-shell configuration. It was however reported that, even in an assembly of mono-disperse small particles, the precise structure of electronic energy levels will vary from particle to particle by virtue of the extreme sensitivity to slight irregularities of the surface structure [21, 22].

The surface structural characteristic of metal nano-clusters is a matter of greatest importance to the more structure-sensitive properties such as magnetism [23]. Indeed, surface-induced effects strongly distinguish the nano-clusters from the bulk metal. This is because the surface effects arise from the boundary condition for the electronic wavefunction at the surface. The high proportion of atoms at the surface makes a crucial contribution to the cluster total energy. If all the atoms are at the surface, while no atoms are in the core, the effect of the cluster surface will be considerable. A simple geometrical consideration is a packing order driven by surface energy minimization. Most metals of face-centered-cubic (fcc) structure in the bulk exhibit five-fold symmetry, when they (e.g. Pd and Pt) form very stable and magnetic clusters of icosahedral structures [24]. For extremely fine clusters the coordination number of the first shell is continuously reduced, ca. $N \leq 12$ direct neighbors are to be detected on average [25]. The bond length contraction of a regular atomic spacing in the bulk is an essential concomitant of a low mean coordination. This is a typical *nano-size effect*. X-ray absorption spectroscopy (XAS) offers an excellent potential for estimating the mean size and local structure of the small metal clusters [25, 26]. The coordination in the nearest neighboring two shells is a main structural parameter reflecting the mean size of the supported Ag clusters.

The growing understanding of the connection between magnetism and chemical structure has shown that magnetism can be a valuable tool in the elucidation of the finer details of molecular electronic structure, and the use of magnetic materials in many technological devices has provided a strong applied-science stimulus to research into chemical magnetism. Bulk metallic Ag exhibits a diamagnetic ordering, because the incompletely filled $5s^1$ electronic state is inside the completely filled $4d^{10}$ electronic state. Principally, the $5s^1$ electrons can be considered free and are responsible for electric conduction. Thus, the total susceptibility receives a more important diamagnetic contribution from $4d^{10}$ electrons, whereas $5s^1$ electrons lead to a small paramagnetic contribution to susceptibility. EPR probes selectively the paramagnetic components in the field domain, whereas magnetization measurements reveal the overall magnetic properties of the whole system. In the case of small paramagnetic clusters, the odd-number of electrons in terms of the cluster size manifests a Curie type paramagnetic property by temperature increases [22]. Since the reduced Ag cluster is a supported system, it probably follows the Curie-Weiss paramagnetism on account of an inescapable cluster-support interaction. The magnetization is proportional to the magnetic moment per Ag atom of the reduced clusters at a low temperature of 1.8 K, and the unpaired electrons partly reduce the diamagnetic susceptibility and contributes to paramagnetic susceptibility. The overall magnetization reveals many more unpaired electrons than are observed by EPR, but is still less than a single unpaired electron per atom on average. This suggests that a mixture of diamagnetic, EPR active spin-1/2 and EPR silent high-spin species is present. It is emphasized that the subtraction/correction of a constant and temperature independent component for magnetization excludes the determination of any diamagnetic or Pauli paramagnetic susceptibility.

Understanding the activities of small metal clusters is a matter of the greatest importance to many research fields such as surface physics or chemistry, and heterogeneous catalysis. The low-energy chemistry of molecules and solids is governed by valence electrons. For the Ag atom, the ionization energy of the $5s^1$ electron is only 7.58 eV (731 kJ mol^{-1}), thus indicating that the $5s^1$ valence electron is much less tightly bound than $4d^{10}$ electrons to its atomic core. However, it is very often chemically inactive in the bulk form. Relatively large ($\approx$ 5 nm) Ag particles supported on a non-porous α-Al_2O_3 surfaces are tailored to catalyze a specific reaction, viz. a selective oxidation of ethylene to ethylene-oxide at an elevated temperature of 523.5 K [27]. This is the only well-known example of catalytic applications of the supported silver clusters. In fact, the chemical properties of the paramagnetic Ag clusters are incompletely explored from viewpoints of the heterogeneous catalytic activity and selectivity. It seems that the paramagnetic Ag clusters are not completely chemically reactive species, even though the unpaired 5*s* electrons are available or prevail in the cluster electronic structure. At this stage it probably means that the ionic core of $4d^{10}$ electrons have enormous influences on the activities of these cationic Ag clusters, and this is however a rather difficult task to prove experimentally. Some experimental results fortunately proved that the paramagnetic Ag_6^+ cluster is active enough against some nitrogen gases, and a red-ox reaction proceeds adsorption of NO. X-ray absorption spectroscopy has been proven as a suitable characterization tool to study the changes in the local environment of the supported silver clusters under various experimental and reaction conditions. The red-ox properties of Ag^+ and silver clusters in Ag/NaA and adsorption of NO can be monitored by EXAFS experiments.

The much larger magnetic moment of the electron than the magnetic moment of the nucleus requires higher frequencies/fields and faster timescales, it is needed feasible to implement many new methods and instrumentation developments in EPR. Particularly, the time-domain pulse EPR has enhanced capabilities and is successfully applied to study the type of interactions of many different paramagnetic systems [28]. This is because pulse EPR relies on transverse magnetization of the electron spin system, thereby leading to a more sensitive detection of the dynamics of the electron-nuclear spin system. The extensions of continuous wave and time-domain EPR to high fields/high frequencies require to harness the promising technologies in microwave and millimeter wave electronics [29, 30, 31]. The unique features of the high field time domain EPR spectroscopies have inspired us to build up our own pulse Q-band spectroscopy in our group. I was partly involved in the construction project of the pulse Q-band spectrometer and designed the cylindrical TE_{011}-mode microwave resonator.

2 Theoretical background and fundamentals

In this chapter, physical principles of absorption spectroscopy techniques operating at a particular range of frequency of the electromagnetic radiations/waves are briefly summarized. Electron Paramagnetic Resonance (EPR), Superconducting Quantum Interference Device (SQUID), and X-ray Absorption Spectroscopy (XAS) are principle tools for investigating paramagnetic properties, a static magnetism and a local structure of supported Ag clusters. Necessarily this is only a brief overview aimed at those readers who are unfamiliar with the topics.

Theoretical and practical aspects of EPR are treated extensively in the books on the subject by John A. Weil, James R. Bolton and John E. Wertz; and Charles P. Poole; and Arthur Schweiger and Gunnar Jeschke; and all these books are basically intended to explain the magnetic resonance phenomena concerned with transitions between electronic states [32, 33, 34].

A book written by Koningsberger and Prins is devoted to principles and applications of X-ray absorption spectroscopy including the theoretical background of EXAFS and XANES techniques [35].

Principles and applications of SQUID serve as a textbook by John Clarke and Alex I. Braginski providing both basic aspects and recent progress in SQUID technology [36].

In addition, short statements about the basic properties of bulk silver, i.e. physical, atomic and chemical properties, are introduced at the very beginning. The classification of the synthetic zeolites, and the spectroscopic characterization methods employed for zeolites are also briefly summarized. General classifications of clusters as well as physical and electronic novel properties of small metal clusters are also briefly introduced.

2.1 Silver

Silver is a chemical element represented by the symbol Ag (Latin: *argentum*) and has the atomic number 47 in the periodic table. Silver is one of the *noble* metals, but is usually considered a *transition* metal in the 11^{th} group. Ag has an atomic weight of 107.8682 g mol^{-1} and the electronic configuration is Kr[$4d^{10}5s^1$] for atomic silver.

2.1.1 Physical, atomic and chemical properties

Ag is a solid at 298 K, and is a very ductile and malleable (slightly harder than Au) coinage metal with a brilliant white metallic luster (soft white luster). The melting point of Ag is 1234.93 K (961.78 ^{0}C or 1763.2 ^{0}F). Ag has the highest electrical conductivity (the electrical resistivity is 1.59 μ-ohms cm^{-1}) of all metals even higher than Cu. Pure Ag has the highest thermal conductivity of 429 W m^{-1} K^{-1} at 300 K and the highest optical reflectivity, but is a very poor reflector of ultraviolet light. Ag also has the lowest contact resistance of any metal. A crystal structure of Ag is face centered cubic. The

magnetic ordering in the bulk is diamagnetic and its mass magnetic susceptibility is of -2.27×10^{-9} emu/g. However, atomic Ag is paramagnetic.

Bulk Ag is quite stable in air and water, but does tarnish when it is exposed to ozone (O_3), hydrogen sulphide (H_2S), or sulfur (S) containing air. The most common oxidation state of silver is +1 (e.g. in $AgNO_3$), a few +2 compounds (e.g. AgF_2), and rare +3 compounds (e.g. $Ag_2(SO_4)_3$) are also known. Silver incompatibilities are with following chemical compounds: acetylene, ammonia, hydrogen peroxide, bromoazide, chlorine tri-fluoride, ethyleneimine, oxalic acid, and tartaric acid.

2.1.2 Isotopes

Naturally occurring Ag is composed of the two stable isotopes ^{107}Ag and ^{109}Ag possessing almost the same percentage, viz. ^{107}Ag 51.839% and ^{109}Ag 48.161%, in natural abundance. Their nuclear magnetic moments are nearly equal, viz. -0.11 μ_N of ^{107}Ag and -0.13 μ_N of ^{109}Ag, and each has a nuclear half integer $I = 1/2$ spin. The radioactive palladium isotope ^{107}Pd decays by beta (β) emission to ^{107}Ag with a half-life of 6.5 million years. Iron meteorites are the only objects with a high enough Pd/Ag ratio to yield measurable variations in ^{107}Ag abundance.

2.1.3 Applications

Pure Ag is rather costly and tarnishes easily; these problems have prevented it from being widely used in place of Cu for electrical purposes. In 2001[1], photography required 24% of silver used in the form of silver nitrate and silver halides, while 33% was used for jewelery, 40% industrially processed to catalyze chemical reactions and only 3% for coins and medals. Silver ions and silver compounds exhibit a disinfection or toxic effect on some bacteria, viruses, algae and fungi, but without high toxicity to the human body. Silver germicidal effects kill many microbial organisms *in vitro*.

2.2 Synthetic zeolites

Zeolite structures are formed by combining a framework of tetrahedra that consist of central cations, e.g. Si, Al, P, Ga, Ge, and B, surrounded by four oxygen atoms and all oxygen atoms are at the apex of tetrahedra. The tetrahedra stack in well-defined and regular arrays of cages, cavities and channels. The possible ways for the stacking to form a structure is virtually limitless, and more than 130 zeolite types with unique structures have been synthesized to date [37]. The synthetic zeolites possess some key advantages to natural analogues. In the first instance, the synthetics can be manufactured in a uniform and phase-pure state. There is also a possibility to synthesize desirable structures which do not occur in nature and zeolite LTA is a well-known example. Disadvantages are, however, the inabilities to create crystals with dimensions of a comparable size to natural analogues.

Most of synthetic zeolites have been produced by a process of slow crystallization of a silica-alumina gel in the presence of alkalis and organic templates. The important process for sol-gel processing is a high pressure treatment, and the final product properties basically depend on a reaction mixture composition, pH of the system, processing temperature, pre-reaction "*seeding*" and reaction time, and the concentration or

[1] source: Wikipedia

stoichiometry of templates. In sol-gel process, other elements, e.g. metals and metal oxides, can easily be incorporated.

The chemical composition of the zeolites can fundamentally be represented by the formula

$$A_{y/n}^{n+}[(SiO_2)_x \cdot (AlO_2^-)_y] \cdot zH_2O \tag{2.1}$$

where A is a cation with the charge $n+$, $(x + y)$ is the number of tetrahedra per crystallographic unit cell, and x/y is the framework silicon-to-aluminium ratio n_{Si}/n_{Al} or simply Si/Al [38].

Loewenstein's rule precludes that only one of the two contiguous tetrahedral frameworks contains single aluminium on the central positions which means direct Al-O-Al linkages are totally forbidden [39]. An allowed linkage between tetrahedral framework atoms, i.e. Si-O-Al, results in a long-range order of the three-dimensional structure.

2.2.1 Properties

In zeolites, Si exists in a +4 oxidation state, and typical $(SiO_2)_x$ tetrahedra are electrically neutral. The oxidation state of Al is +3 and then $(AlO_2^-)_y$ tetrahedra form centers that are electrically deficient in an electron. Thus, zeolite frameworks are basically anionic, and negative charge compensating cations populate the pores to provide electrical neutrality. Charge compensating cations can participate partially in ion-exchange processes, and yield some important properties for zeolites. Thus zeolites are common ion exchangers. When negative charge compensating cations are the "*soft*" cations such as Na^+ and K^+, zeolites are excellent water softeners, because these cations can replace the "*hard*" cations Mg^{2+} and Ca^{2+} in water. If cations are protons (H^+), the zeolite becomes a solid acid. Such solid acids provide the zeolites with the properties of catalytic applications. Zeolites are often applied as "*shape-selective catalysts*" and this terminology is derived from the unique structures of the channels, cavities and cages with certain shape and dimensionality [40].

2.2.2 Characterization methods

A number of experimental techniques can be applied selectively for characterization depending upon the specific properties examined for zeolites [38].

Usually, atomic absorption spectroscopy (AAS) and inductively coupled plasma (ICP) spectroscopy are applied to determine the accurate chemical composition of zeolites with different Si/Al ratios. Thermal analysis, i.e. DTA or TGA, gives information on the water and the organic molecule content [38]. For characterizing the void volume, this technique is very powerful, because it yields the amount of adsorbed molecules.

In order to define the structure, various spectroscopic techniques have been applied, for instance, NMR is very powerful to acquire information about the silicon-aluminium ordering [41]. NMR [42] is also an alternative of IR spectroscopy to characterize the acidic sites [43].

The combination of EPR, DRS, and UV-Vis spectroscopies is useful to determine the environment of the exchanged transition metal ions and their complexes in the zeolite supports [44].

In-situ Raman spectroscopy can provide valuable information on zeolitic surface structures, especially when distinguishing between nearly similar structures [45].

The iron impurities are always present in the zeolites which substitute silicon and aluminium in the lattice, Mössbauer spectroscopy is therefore used to determine the coordination and oxidation state of iron ions [46].

As zeolites are polycrystalline materials, X-ray diffraction (XRD) spectroscopy is applied extensively to define the crystalline phase and inter-facial region of zeolite crystals [47].

2.2.3 Structure of LTA (NaA) and FAU (NaY) zeolites

Zeolite A exhibits an LTA (Linde Type A) structure. It has a 3-dimensional pore structure with pores running perpendicularly to each other in the x, y, and z planes and is made of the secondary building units 4, 6, 8, and 4-4. The pore diameter is defined by an eight member oxygen ring and is small at 4.2 Å. This leads to a larger cavity of minimum free diameter 11.4 Å. The cavity is surrounded by eight sodalite cages (truncated octahedra) connected by their square faces in a cubic structure. The unit cell is cubic (a = 24.61 Å) with Fm-3c symmetry [38, 48]. Zeolite A has a void volume fraction of 0.47, with a Si/Al ratio of 1.0. It thermally decomposes at 700^0C.

Zeolite Y exhibits a FAU (faujasite) structure. It has a 3-dimensional pore structure with pores running perpendicularly to each other in the x, y, and z planes similar to LTA and is made of the secondary building units 4, 6, and 6-6. The pore diameter is large at 7.4 Å since the aperture is defined by a 12 member oxygen ring and leads to a larger cavity of diameter of 12 Å. The cavity is surrounded by ten sodalite cages (truncated octahedra) connected on their hexagonal faces. The unit cell is cubic (a = 24.7 Å) with Fd-3m symmetry [38, 48]. Zeolite Y has a void volume fraction of 0.48, with a Si/Al ratio of 2.43. It thermally decomposes at 793^0C.

2.3 Clusters

Clusters are finite aggregates of atoms which are bound by bonds which may be metallic, covalent, ionic, van der Waals, and can contain between a few atoms to hundreds, with a radius of $\approx$ 2 nm. Depending on the type of bonding, we can classify them as simple metal clusters (e.g. Na_n), semiconductor clusters (e.g. Si_n, C_n including C_{60} or C_{70}) and so on. Moreover, molecular clusters are bound together by various interactions, e.g. hydrogen bonding for H_2O clusters, ionic bonding for NaCl clusters, van der Waals force for $(N_2)_n$ clusters and noble-gas (e.g. Xe, Ar) clusters. Small metal clusters are among others the most promising objects of extensive fundamental and applied research [49, 50].

2.3.1 Correlation between physical and electronic properties

Physical properties of metal nano-clusters are fundamentally different from those of the bulk [5, 51] and can be considered a bridge between bulky and molecular state. Depending on temperature and especially on the applied physical method used for investigations, the clusters might still behave as a piece of metal or as a molecule-like system that can probably be described by means of the rules of quantum mechanics. Therefore, physics of metal nano-clusters cannot be understood completely without a proper account regarding the electronic effects. In general, the physical principle for open shell clusters, which are electronically degenerate in their spherical conformation,

can be lowered in the total energy by distorting the cluster structure, thereby lifting the degeneracy. Quantum properties usually dominate in the size range of ≤ 2 nm of the clusters [2, 5]. In these size ranges, nano-clusters indeed exhibit the discrete nature of the electronic energy levels similar to atoms.

2.3.2 Size-dependent effects

Much interest has focused on the evolution of properties due to an alteration in the size of the clusters. There are basically two types of size-dependent effects [52].

When size (actual diameter) of the clusters is of the same order of magnitude as the Fermi wavelengths of the electrons, the discrete energy level can be modeled by quantum mechanical treatment of a *particle-in-a-box*. Here the electronic wavefunctions are confined in a spherical square well potential which causes a discreteness of the energy levels or the energy gap [53]. Properties which results from the energy gap are called *quantum size effects*. Finally, the shape of the cluster will be reflected in the electronic structure. This means that the electronic structure of small metal clusters is discrete compared with the (quasi) continuous bands of the bulk and the electronic energy spectrum of them is more like a molecule. If the electronic levels are assumed to be non-degenerate (except for spin degeneracies) and equally spaced (or separated), then the energy gap between adjacent levels is approximately equal to the Fermi energy divided by the total number of conduction electrons. The discreteness of the energy level spectrum will manifest itself in physical properties in particular when the temperature T is low enough, i.e. $k_B T < \Delta E$. Elementary quantum mechanical considerations were first formulated by Kubo [22]:

$$\delta = \frac{4E_F}{3N} \propto \frac{1}{V} \tag{2.2}$$

where δ (or ΔE) is the mean energy spacing of adjacent levels, E_F is the Fermi energy, N is the number of conduction electrons, and V is the volume of the particle. The quantity δ in Equation (2.2) is just the inverse of the average density of electronic states, i.e. $\delta = 1/n$, for a single spin at the Fermi energy which is the width of the conduction band which is the level near the highest occupied electronic state. More importantly, the average spacing of successive quantum levels, i.e. δ equals the energy gap or Kubo gap and can be controlled to make a system metallic or nonmetallic with regard to the tight-binding approximation, i.e. $\delta = 2\pi E_F/3N$.

A high fraction of atoms on the surface of clusters makes a crucial contribution to the cluster total energy, for example, all atoms of a fullerene cluster are at the surface [54]. The fraction of surface atoms in a spherical cluster with N atoms is approximately $3N^{-1/3}$. It implies that a simple geometrical consideration or packing order can be related to a minimal surface energy. With extremely small sizes, the equilibrium structure changes to a specific one with special symmetry, e.g. cuboctahedral, icosahedral [55, 56], and decahedral, depending upon the electronic state and its Hamiltonian. High symmetry of an icosahedral structure has five-fold symmetry axes that lead to a highly degenerate spin state of the electronic configuration and an enhanced magnetism of metal nano-clusters. The atomic rearrangements at the surface coincide with the lowest mean coordination number and this is a typical *surface effect*. The fraction of surface atoms (called *dispersion*, F) and the mean coordination number obey the same scaling law and are equivalent measures of surface effects. Furthermore, the inter-atomic bond length is basically contracted due to surface rearrangements. Thus the efforts towards

high accuracy structure determination is driven by the fact that even very tiny changes in inter-atomic bond length can have a marked effect on the properties of clusters. For instance, the key polaron distortion in giant magneto-resistive materials is of the order of 1/10 (one tenth) of an ångström [57].

It should finally be noted that quantum confinement effects and surface effects could not smoothly scale with each other by the same scaling law.

2.3.3 Impact on science fields

Small metal clusters have attracted great attention from many scientists in different fields of physics, chemistry, biological medicine and electronic engineering with regard to the practical application. Clusters can be used in different ways of technical applications, for instance, bimetallic Pd-Au clusters for relieving organic pollutants in groundwater [58], iron oxide nano-clusters used as a resolution enhancer in magnetic resonance imaging (MRI) [59, 60] and the next generation devices such as single-electron transistors (SET) with Au-SiO_2 core-shell nano-particles [61]. Plasmonic nano-particles demonstrate unique optical properties, i.e. nonlinear optical activity [62], chirality of plasmon modes [63], and quantum size effects in the two photon excited luminescence [64]. Since optical measurements are an important means for determining the existence of the surface and the size effects, which are from different sources than the general size-dependent effects, surface enhanced Raman scattering [65], photo-activated fluorescence [66] and luminescence [67] measurements have been performed for Ag nano-clusters.

Almost all of the complete modern chemical industry depends on the development, selection, and application of catalysts. The most valuable use of supported noble metal clusters therefore prevails in heterogeneous catalytic processes, and an ability to react with molecular species depending on the cluster size [68]. The nano-structures of Ag/NaY and Ag nano-clusters in Ag/NaA were reported to be the effective catalyst for the exclusive synthesis of sialosaccharides containing specific glycol linkage, oxidation of hydrocarbons, and dimerization of alkanes [69, 70, 71]. Nevertheless, in numerous application fields there are still certain difficulties in understanding the size effects that make it difficult to isolate effects which are dependent on the cluster size and cluster-support interactions.

2.4 Principles of EPR spectroscopy

At the beginning of the last century, scientists began to apply the principles of quantum mechanics to describe atoms or molecules and then it was discovered that an atom or molecule has discrete states. Spectroscopy is the measurement and interpretation of the energy differences between the atomic and molecular states. Through the energy differences, one gains insight into the identity, structure, and dynamics of the sample under study. The energy differences, ΔE, can be measured as there is an important relationship between ΔE and the absorption of electromagnetic radiation. According to Planck's law, electromagnetic radiation will be absorbed if:

$$\Delta E = h\nu \tag{2.3}$$

where h is Planck's constant and ν is the frequency of the radiation. The absorption of energy causes a transition from the lower energy state to the higher energy state.

Electron Paramagnetic Resonance (EPR) is a branch of Magnetic Resonance (MR) spectroscopy concerned with transitions between electronic states. This technique can be used to investigate very tiny energy differences between individual energy levels in magnetic systems. The measured energy difference depends linearly on the magnetic field and the frequency of the electromagnetic radiation. Without an applied magnetic field, there is no energy difference to measure. The transition term can be formulated via

$$\Delta E = h\nu = g_{\mathrm{e}}\beta_{\mathrm{e}}B_{\mathrm{r}}m_S \tag{2.4}$$

where B_{r} is the resonance field, m_S is the magnetic spin quantum number of the electron. It implies that if the photon energy matches the energy difference between the states of electron spin angular momentum (e.g. for a single electron of $m_S = \pm\frac{1}{2}$), the resonant transition will be induced by the application of an oscillating electromagnetic field of the appropriate frequency ν of electromagnetic radiation, having a magnetic component B_{r} perpendicular to B_0. Therefore, EPR measurements are a study of the transitions between electronic Zeeman levels with $\Delta m_S = \pm 1$ according to the *selection rule* (or angular momentum conservation) for EPR. The electromagnetic radiation in the gigahertz (GHz) range is used for conventional EPR spectroscopy [32]. The high-frequency EPR spectroscopies have become more popular nowadays, and the primary advantages in replacing gigahertz by subterahertz frequencies include increased signal-to-noise ratio and improved spectral resolution of g tensor anisotropy due to proportionality to the electron Zeeman splitting to the applied magnetic field B_0 [72, 73, 74]. EPR provides good spectral and spatial resolution with much higher sensitivity per spin.

2.4.1 Paramagnetic entities

Magnetism arises from the motion of charge on an atomic or sub-atomic (or nuclear) scale. Charge (e) is inevitably associated with mass (m_e), this implies an intimate relation between the angular momentum and the resultant magnetic moment of an atomic entity. The magnetic moment of the atom is then given by the ground state expectation value of the momentum operator

$$\hat{\mu} = -\beta_{\mathrm{e}}(\hat{L} + |g_{\mathrm{e}}|\hat{S}) \tag{2.5}$$

where g_{e} is called the electronic g factor, β_{e} is the Bohr magneton and equals $e\hbar/2m_ec = 9.274015 \times 10^{-24}$ J T^{-1}, $\hat{L}$ and $\hat{S}$ are the spin and orbital angular momentum operators [32]. A similar expression can be written for a nucleus with net angular momentum. Equation (2.5) implies that isolated atoms or ions will frequently have magnetic moments since outer-shell electrons will not all be paired (or exhibit non spin-pairing symmetry), except in the rare-gas configurations. The simplest case occurs for spherical symmetry (an isolated atom) when the orbital ($L = 0$) and spin ($S = 1/2$) angular momenta are inherent or intrinsic quantum numbers. To better understand the more precise quantum mechanical description of paramagnetic property, one has to focus on the Hamiltonian of the electrons which contains linear and quadratic terms in the magnetic field. The linear term is present when the total magnetic moment in Equation (2.5) is nonzero that tends to align magnetic moments with the field. This is the *paramagnetic* contribution.

Most bulk matters do not usually exhibit paramagnetic properties. The magnetism is suppressed because the chemical bonding mostly requires transfer (ionic bonds) or sharing (covalent bonds) of electrons in such a way that those atoms acquire a rare-gas configuration. When atoms form covalent bonds the freedom of movement of the

electrons, and hence their orbital angular momenta, can be much reduced and this also reduces the corresponding magnetic moments. However, this *quenching* of the orbital angular momentum which results from bonding is very difficult to calculate. The magnetic moments due to pairs of electrons occupying orbitals with equal and opposite values of m_l in $\mu_z = -g_l m_l \mu_B$ for z-component, e.g. for a filled shell of $4d^{10}$ electrons, cancel each other and such atoms can have no orbital magnetic moment [75]. The presence of magnetism due to orbital electronic motion is therefore a characteristic of atoms with incompletely filled electron sub-shells. Transition metals have incomplete or unfilled $3d$, $4d$, $5d$, $4f$ and $5f$ shells [76, 77]. Nuclei do not form chemical bonds and hence nuclear magnetism is quite common or of insignificant importance for paramagnetic matters.

Fortunately, there is a number of ways for condensed matter and solids to retain the net magnetic moment, the most important of which involve trapping the unpaired electrons in the radical species, and transition metal ion centers or particular point defects in solids. Certain defects such as guest or free transition ions, and ion vacancies in crystalline matrices may gain or lose an electron relative to the chemically bonded host, thereby producing a localized moment [78, 79].

2.4.2 Zeeman splitting and hyperfine interaction

The two spin states, α and β, of an unpaired electron are degenerate in the absence of a magnetic field. When a magnetic field is applied, the interaction of the field with the magnetic moment of the unpaired electron induces an energy difference proportional to the field strength. This is called *Zeeman* effect[2] or splitting for the electron, and parametrized by the electronic g tensor. Two states are labeled by the projection of the electron spin, m_S, in the direction of the magnetic field and illustrated in Figure 2.1. The electron is a spin $\frac{1}{2}$ particle, the parallel (α) state is designated as $m_S = -\frac{1}{2}$ and the antiparallel (β) state is $m_S = +\frac{1}{2}$. The electron g factor provides valuable information concerning the electronic structure of a system, the value of $g_e \approx 2.002322$ is for a free unpaired electron. However, the g factor can deviate from g_e due to an orbital angular momentum contribution of the electron or simply spin-orbit coupling (SOC) [80]. It means that the g factor of the electron in an atomic or molecular orbital is different and may also be anisotropic, i.e. dependent on the orientation of the magnetic field B_0 relative to the system. In this case, the electronic g tensor is calculated in a perturbation-theoretical manner. As the g tensor exhibits a 2nd-order tensor property of $\boldsymbol{g} = g_e\mathbf{1} + \boldsymbol{\Delta g}$ with magnetic field, the magnetic field and the spin-orbit coupling are considered as perturbations [32, 81, 82]. For paramagnetic systems of spin multiplicity greater than 2, i.e. with more than one unpaired electron, additionally marked important structure appears due to the non-degeneracy of different spin states ($S > 1/2$) even in the absence of the magnetic field. This is called *Zero-field splitting*. This thesis is concerned only with doublet states, and so ZFS will not be discussed further.

Furthermore, the hyperfine coupling tensor or $\boldsymbol{A}$ tensor is a measure of the interaction of the unpaired electron spin (e.g. $S = 1/2$) and the surrounding nuclear spin (e.g. $I = 1/2$) in the environment. The $\boldsymbol{A}$ tensor may be taken as the sum of the the isotropic and the anisotropic or dipolar coupling [32, 82]. This can be simply described via $\boldsymbol{A} = A_{iso}\mathbf{1} + \boldsymbol{A}_{dip}$ in the sum. The magnitude of the nuclear hyperfine coupling depends on the occupation of the unpaired electron in the particular orbital, i.e. s, p or d orbital, or simply the spin density distribution. In the non-relativistic limit, A_{iso} arises from

[2] EPR relates to the *anomalous Zeeman effect*

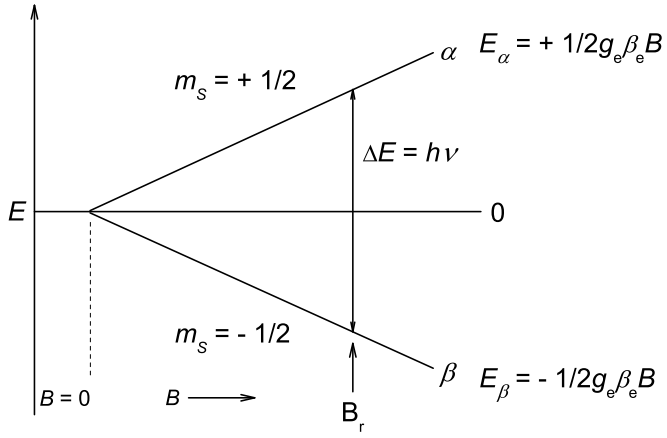

Figure 2.1: Energy-level scheme for the simplest system (e.g. free electron) as a function of the applied magnetic field B, representing EPR absorption. E_α and E_β represent the energies of the $m_S = +\frac{1}{2}$ and $m_S = -\frac{1}{2}$ states. m_S is for electron spin projections.

the Fermi contact term, which is directly proportional to the spin density $(\rho_\alpha - \rho_\beta)$ at the nucleus under investigation and hence easy to estimate. However, the result depends strongly on the quality of the wavefunction at the nucleus. It implies that the unpaired electron is in an s orbital, the electron density at the nucleus is enormous and the hyperfine coupling constant will be large. Because s orbitals have a spherical symmetry, A_{iso} is independent of orientation. The isotropic hyperfine coupling (A_{iso}) or Fermi contact interaction term can be described by the formula of

$$A_{\text{iso}} = \frac{2}{3}\frac{\mu_0}{\hbar} g_e \beta_e g_n \beta_n |\psi_0(0)|^2 \tag{2.6}$$

where g_n is the nuclear g factor, β_n is the nuclear magneton and $|\psi_0(0)|^2$ is the density probability for the electron per unit volume at the nucleus.

The most important coupling of the electron and nuclear spin is the dipolar coupling. In the non-relativistic limit, the anisotropic hyperfine tensor $\boldsymbol{A}_{\text{aniso}}$ describes through-space dipolar coupling between the electron and nuclear magnetic dipoles. It is remarkably less sensitive to the quality of the wavefunction than A_{iso}. When the unpaired electron occupies the p or d orbital, there is no direct electron spin density at the nucleus. This interaction experiences the dipolar interaction between the electron spin S and the nuclear spin I. This is because the magnetic moments of the unpaired electron and the nucleus can be regarded as interacting magnetic dipoles. However, the unpaired electron has density at the nucleus in the nodal plane of the SOMO. It is known that p and d orbitals have a nodal plane and never approach the nucleus, and the spin density is delocalised. The magnitude of the interaction is usually small and dependent on the

orientation of the orbital with respect to the applied magnetic field and the distance. The anisotropic hyperfine coupling (A_{aniso}) can be described by the formula of

$$A_{\text{aniso}} = \frac{\mu_0}{8\pi} g_e \beta_e g_n \beta_n \left\langle \frac{3\cos^2\theta - 1}{r^3} \right\rangle \tag{2.7}$$

where θ is the angle between the applied magnetic field B_0 and the vector line joining the magnetic dipoles, r is their distance. Generally, the hyperfine couplings give access to distances between nuclei and the unpaired electron up to ≈ 0.5 nm, while couplings between the electron spins provide geometric information on distances up to at least 5.0 nm [83].

2.4.3 Pulse EPR

Pulse EPR is based on detecting a spin-echo, wherein the inhomogeneous spectral line broadening cancels. Spin echo temporal evolution is governed by the weaker effects of the spin relaxation and not refocused electron-electron dipolar and exchange couplings, and electron-nuclear super-hyperfine and nuclear quadrupole couplings. The dipolar and exchange coupling are basically isolated from the rest by means of a suitable pulse sequence [34].

In the simple magnetic system, the unpaired electron spin $S = 1/2$ interacting with the nuclear spin I (e.g. the simple $I = 1/2$ spin), the spin Hamiltonian operator can be formulated by

$$\hat{\mathcal{H}} = \beta_e \mathbf{B_0} \cdot \mathbf{g} \cdot \mathbf{S} + h \sum_{i=1}^{N} \mathbf{S} \cdot \mathbf{A_i} \cdot \mathbf{I_i} - \beta_n \sum_{i=1}^{N} g_{n,i} \mathbf{B_0} \cdot \mathbf{I_i} \tag{2.8}$$

where β_n is the nuclear magneton. The third term in the Equation (2.8) describes the nuclear Zeeman interaction.

HYSCORE is 2D (two-dimensional) four-pulse ESEEM technique in which a microwave (mw) π-pulse is inserted between the second and the third $\pi/2$ pulse of the well-known three-pulse ESEEM [84]. In the pulse sequence of HYSCORE spectroscopy, as described in Figure 2.2, the mixing mw π-pulse creates correlations between the nuclear coherences of the two different electron spin (m_S) manifolds of the simple $S = 1/2$ and $I = 1/2$ spin system. Indeed, the mw π-pulse will transfer the nuclear coherence created by the first two $\pi/2$-pulses from one m_S manifold to another [84]. Independent variations of the two time intervals t_1 and t_2 and subsequent two-dimensional Fourier transform gives rise to *cross peaks* linking nuclear frequencies of the different (m_S) manifolds (see Figure 2.2). It can be simply said that the symmetric nuclear coherence transfer pathways ν_α and ν_β during the evolution period $t_1 - \pi - t_2$ lead to cross peaks (ν_α,ν_β)(ν_β,ν_α) in the 2D spectrum, where ν_α and ν_β are the nuclear transition frequencies in the two different m_S states. The nuclear transition resonance frequencies in the electron spin m_S manifolds are described by the formula [34, 85]

$$\nu_{\alpha,\beta} = \left[\left(\nu_L \pm \frac{A}{2} \right)^2 + \left(\frac{B}{2} \right)^2 \right]^{\frac{1}{2}} \tag{2.9}$$

where the nuclear Larmor frequency is $\nu_L = -g_n \beta_n B_0 / h$, and A and B represent the principle values of the hyperfine $\boldsymbol{A}$ tensor and the dipolar coupling constant T. In disordered systems, the A_{aniso} results in a spread of the ν_α and ν_β frequencies which leads, together with the correlations between ν_α and ν_β, to two different ridges for the two

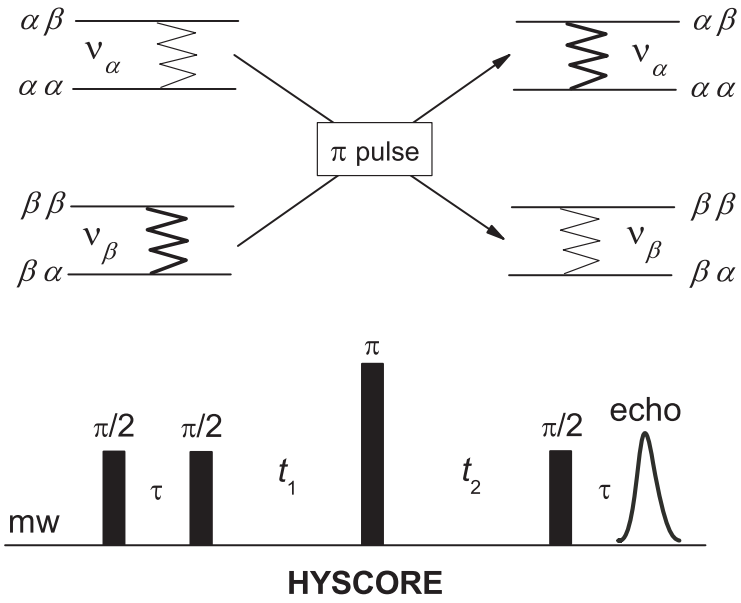

Figure 2.2: Upper part: in the case of $S = 1/2$ and $I = 1/2$, the cross peaks linking nuclear frequencies of the two different electron spin m_S manifolds. Lower part: typical pulse sequence of HYSCORE experiments in which the mw π pulse is inserted between the second and third $\pi/2$ pulse of the three-pulse ESEEM.

nuclear coherence transfer pathways in the 2D spectrum. These ridges are directed perpendicularly to the frequency diagonal $\nu_1 = \nu_2$ in the case of small hyperfine coupling constant, $2\pi T_\perp + \pi A_{\text{iso}} < \nu_L$ [34, 84, 85]. The shape of the ridges and their degree of separation depend on the dipolar hyperfine magnitude. In the point-dipole approximation, the dipolar coupling constant is formulated via

$$T_\perp = \frac{g_e \beta_e g_n \beta_n}{\mathbf{r}^3 h} \tag{2.10}$$

where the vector **r** connects the electron spin and nucleus lying in the plane perpendicular to the direction of the applied magnetic field.

In **E**lectron **N**uclear **DO**uble **R**eosnance (**ENDOR**), the NMR quanta are detected in the microwave, rather than radio frequency (rf) range (known as quantum transformation) resulting in a sensitivity enhancement of several orders of magnitude over conventional NMR spectroscopy. Therefore, ENDOR is regarded as NMR detected EPR spectroscopy. The stronger hyperfine couplings, in the range of 20 - 40 MHz, can be observed and are generally thought to be only accessible by pulse ENDOR techniques [86].

The pulse sequence of ENDOR introduced by Davies [87] is based upon selective mw pulses, as is illustrated in Figure 2.3. In polarization-transfer pulse ENDOR experiments, the effect of ENDOR is based on the polarization transfer between electron and nuclear transitions. Nuclear polarization is created by a single mw pulse or a sequence of mw pulses. Single or several selective rf pulses can change the nuclear polarization during the subsequent mixing period. During the detection period, the nuclear polarization is transferred to an electron coherence and indirectly observed via **FID** or an **echo** of

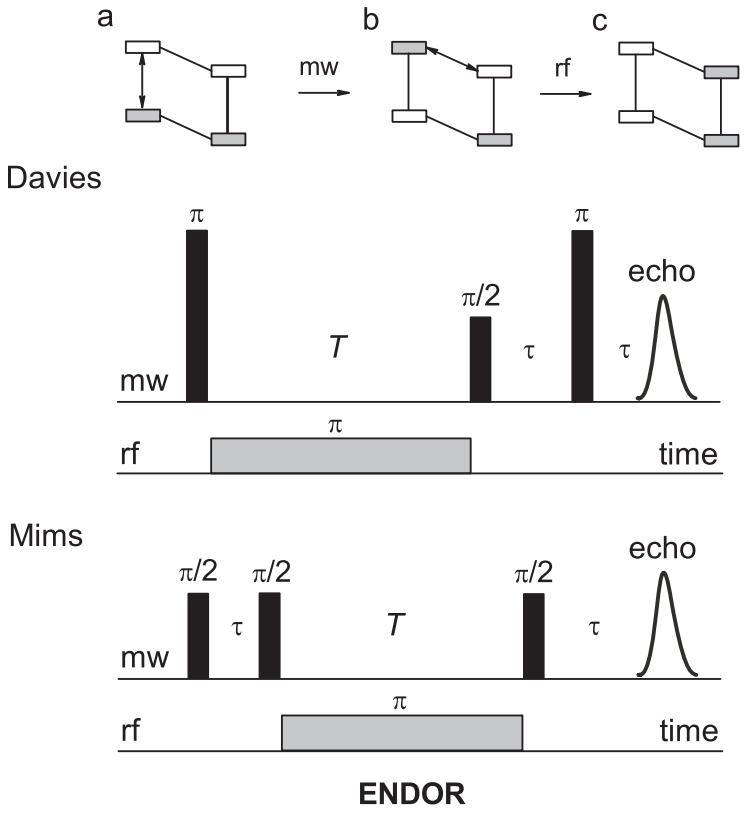

Figure 2.3: Schematic representations of Davies and Mims ENDOR pulse sequences. In the upper part: a) mw pulse b) off resonance c) on resonance conditions for Davies ENDOR experiments, respectively. All interpulse delays are fixed and only the radio frequency is varied for both kinds of ENDOR experiments.

the electron spins. It is also possible that the polarization is transferred via an electron coherence generated by a probe pulse. The mw resonant π pulse creates the transition with two-spin order $2S_zI_z$ that is described in the entry (b) of Figure 2.3. During the mixing period, the polarization of this transition is changed accordingly with the entry (c) by a selective rf pulse which is resonant with one of the nuclear frequencies. This change also alters the polarization of the electron spin observer transition and is then measured via a primary electron spin echo. Finally, a single spin packet comprising the two allowed EPR transitions ($S = 1/2$ and $I = 1/2$) is split by the isotropic hyperfine coupling constant A_{iso}. If the EPR linewidth is small compared to A_{iso}, the hyperfine splitting is resolved in the EPR spectrum.

The original sequence of pulse ENDOR was introduced by Mims [88] which is basically based on the stimulated echo sequence with three non-selective mw $\pi/2$ pulses. The polarization changes by a selective rf pulse are recorded as a function of ν_{rf} via a stimulated electron spin echo. In the Mims-ENDOR experiment the ENDOR efficiency

$$F_{\mathrm{ENDOR}} = \frac{1}{4}(1 - \cos(A_{\mathrm{iso}}\tau)) \tag{2.11}$$

depends on the isotropic hyperfine coupling constant A_{iso} and on time τ. It implies that if the hyperfine coupling approaches zero, the signal of Mims-ENDOR will disappear,

therefore, the signal intensity is a function of A_{iso}. In both Davies and Mims ENDOR, the electron coherence evolves during the fixed time intervals τ. Moreover, the ENDOR efficiency is close to 50% for the weakly coupled protons [34]. Since the pulse length t_{rf} is limited by the longitudinal relaxation time T_1 of the electron spin, an optimum ENDOR signal intensity has to be balanced with optimum resolution.

2.5 Fundamentals of SQUID and magnetism

There are numerous methods for measuring magnetic susceptibilities, e.g. **Gouy**, **Evans**, and **Faraday** methods. There is **SQUID** which is very suitable for investigating the "*electronic*" magnetism, i.e. the static and dynamic magnetization, and the electronic magnetic susceptibilities of materials. The growing understanding of the connection between magnetism and chemical structure has demonstrated that magnetism can be a valuable tool in the elucidation of the finer details of molecular electronic structure. This thesis is concerned only with a static magnetism and effective magnetic moments of supported Ag clusters, and so dynamics of magnetism will not be further discussed. With a few exceptions, SQUID measurements of magnetization and magnetic properties are not directly related to the existence of the quantum size effects.

2.5.1 SQUID

The **S**uperconducting **QU**antum **I**nterference **D**evice (**SQUID**) combines the physical phenomena of flux quantization and Josephson tunneling [36]. Flux quantization was

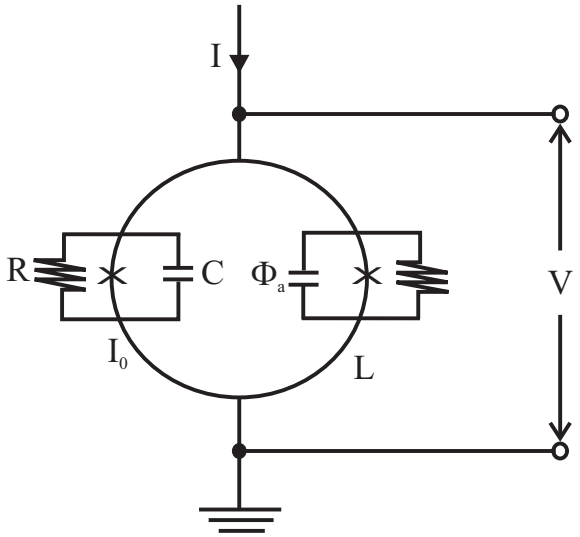

Figure 2.4: Schematic drawing of the dc SQUID in which two Josephson junctions are connected in parallel in a superconducting loop. Each junction has a resistive shunt to eliminate hysteresis on the I - V characteristics, thus being called the resistively- and capacitively-shunted junction (RCSJ).

observed, and it was proven experimentally that the flux contained in a closed superconducting loop is quantized in units of the flux quantum $\Phi_0 = h/2e \approx 2.07 \times 10^{-15}$ Wb [89, 90]. Here, $h = 2\pi\hbar$ is Planck's constant, and e is the electronic charge.

An external magnetic field $H = B/\mu_0$ is applied to the loop, and the increase of the bias current is monitored at fixed magnetic field until a nonzero dc voltage develops across the junctions. The static or "dc" (direct current) property of a Josephson junction is described via

$$I = I_0 \sin\delta \tag{2.12}$$

where I is the current flowing through a junction, $\delta = \varphi_1 - \varphi_2$ is the difference between the phases φ_1 and φ_2 of the capacitors in the two superconducting electrodes, and I_0 is the critical current [91, 92]. Figure 2.4 illustrates the typical dc SQUID where two Josephson junctions are connected in parallel in a superconducting loop. In most operating schemes each junction has a resistive shunt to eliminate hysteresis on its $I - V$ characteristics (see Figure 2.4). The dc SQUID is almost invariably operated in a flux-locked feedback loop. This is because the flux is modulated sinusoidally by the modulating flux frequency ranging from 100 kHz to 10 MHz [36]. Feedback basically linearizes the response of the SQUID to the applied flux and enables tracking the changes in flux corresponding to many flux quanta as well as detecting the changes in flux corresponding to a tiny fraction of a flux quantum. Simply, the quantized voltage (or state) of the superconducting coil, the nonlinearity of the Josephson junction, and tiny changes in the magnetic flux density through the loop are continuously detected.

As SQUID uses the properties of an electron-pair wave coherence for measuring the applied magnetic flux (or field), it provides information of a magnetic system inferred from principal experiments on magnetization as a function of the applied magnetic field $M(H)$ and susceptibility as a function of temperature $\chi(T)$ [93, 94].

2.5.2 Magnetization and susceptibility

Magnetism is inseparable from quantum mechanics, for a strictly classical system in thermal equilibrium can display no magnetic moment, even in a magnetic field. The study of magnetism dates back to the 19th century when the classical phenomena of *paramagnetism*, *diamagnetism* and *ferromagnetism* were identified and defined.

If a substance is placed in a *magnetic field* of strength H (units A m^{-1}) then a *magnetic moment* of magnitude of M (A m^{-1}) will be induced in that substance. The *magnetic flux density* within a substance, B (Tesla $\sim$ T = J C^{-1} s m^{-2}), is related to the strength of the applied field and the magnetization by:

$$B = \mu_0(H + M) = \mu_0(1 + \chi)H \tag{2.13}$$

where μ_0 is the *vacuum permeability* which is defined to have the value $4\pi \times 10^{-7}$ J C^{-2} s^2 m^{-1}.

DC magnetization is the magnetic moment (M) per unit volume of a sample. If the sample has no permanent magnetic moment, a field is applied to induce the moment. When the sample is stepped through a superconducting array and the SQUID's output voltage is processed and the magnetic moment of the sample is computed. Systems can be configured to measure the hysteresis loop, the relaxation time, the magnetic field and the temperature dependence of the magnetic moment.

The field dependence of magnetization of a classical paramagnet is described by the classical Langevin function [95],

$$M(H) = N\mu\Big[\coth\Big(\frac{\mu H}{k_B T}\Big) - \frac{k_B T}{\mu H}\Big] \tag{2.14}$$

where N is the total number of atoms per unit volume, T is the temperature, H is the magnetic field, μ is the magnetic moment per atom, and k_B is the Boltzmann's constant. However, this is a semi-classical treatment of paramagnetism and corresponds to a $J = \infty$ system. It is therefore important that the classical moment be replaced by a quantum spin J in a quantum mechanical system. Subsequently, a specific function can be derived and described via

$$\frac{M}{M_S} = \frac{\langle m_J \rangle}{J} = \tanh y \tag{2.15}$$

where $y = \mu_B H/k_B T = gJ\mu_B H/k_B T$ for a $J = 1/2$ and $g = 2$ system, and M_S is a saturation magnetization.

The magnetic moment of a free atom has three principal sources: **the spin** of the electron, **the orbital angular momentum** of the electron orbiting the nucleus, and **the change** in the orbital moment induced by an applied magnetic field. The first two effects exhibit paramagnetic contributions to the magnetization, and the third gives a diamagnetic contribution. The dimensionless scalar susceptibility is related to the magnetic permeability via

$$\mu = (1 + \chi)\mu_0 \tag{2.16}$$

where χ is the dimensionless *volume susceptibility* or *bulk susceptibility*. In CGS and SI systems of units χ is dimensionless. The magnetic susceptibility per unit volume is defined as

$$\chi = \frac{\mu_0 M}{H} \tag{2.17}$$

where H is the macroscopic magnetic field intensity. Substances exhibiting a negative susceptibility ($\chi < 0$) are called **diamagnetic**, whereas the positive susceptibility ($\chi > 0$) is for **paramagnetic** substances. Nuclear paramagnetism is due to nuclear magnetic moments, however, the magnetic moment of the nucleus is of the order of 10^{-3} times smaller than the magnetic moment of the electron. This is the great importance of a high sensitivity of EPR compared to NMR.

Diamagnetism is associated with the tendency of electrical charges partially to shield the interior of the quantum sphere from an applied magnetic field. The orbital motions of the electrons creates the magnetic field of the induced currents. When the external magnetic field is applied to the substances, the induced current loops align the associated magnetic moments oppositely to the magnetic field according to the *Lenz's law*. Diamagnetic susceptibility per unit volume is defined as

$$\chi = \frac{\mu_0 N\mu}{H} = -\frac{\mu_0 NZe^2}{6m}\langle r^2 \rangle \tag{2.18}$$

where N is the number of atoms per unit volume [96]. This is the classical Langevin result. The diamagnetic susceptibility is largely independent of temperature fluctuations. Thus, diamagnetism is almost inherent for most substances and arises from the motion of the electrons constituting the electric current. Experiments on the temperature dependence of the electronic susceptibility provide a possibility to separate a diamagnetic contribution to magnetism [95, 96].

Paramagnetism is a particular property exhibited by substances containing an odd number of the electrons. As the applied magnetic field induces the magnetization, the magnetic moment of the unpaired electron spin is more likely aligned with the magnetic

field (parallel) than against it (antiparallel). Thus, the magnetization usually increases linearly with the applied magnetic field. It implies that if $\chi > 0$ H and M add to increase B within the magnetized substance. Contrary to the tendency to align the magnetic moment of the unpaired electron with the applied field, the thermal motion is to force the opposite alignment of the magnetic moment with the field. Thus the susceptibility of paramagnetic substances varies inversely with temperature. This temperature dependence is called *Curie's law*, and the susceptibilities proportional to $1/T$ are in general known as *Curie susceptibilities*.

$$\chi_{\text{mol}} = \frac{M}{H} = \frac{C_{\text{m}}}{T} \tag{2.19}$$

Experimental data are often quoted as *molar susceptibility*, χ_{mol} in units of emu/mol (or cm^3/mol, or m^3/mol). Paramagnetism is not a collective phenomenon and can therefore have many different origins. Generally, the temperature dependence of paramagnetic susceptibility is much more complex in the quantitative measure of the response of a system to the applied magnetic field. The magnetic moment of the unpaired electron can interact with the magnetic moments of the other electrons in the environment. These interactions can induce an additional magnetic field of the magnetic moments which compete to align the magnetic moments of the neighboring electrons in the same directions or in the opposite directions. This paramagnetic contribution to χ_{mol} is frequently expressed using the *Curie-Weiss* law, and the formula is basically described via

$$\chi_{\text{mol}} = \frac{M}{H} = \chi_0 + \frac{C_{\text{m}}}{T - \theta} \tag{2.20}$$

where M is the magnetization in electromagnetic units (emu/mol), H is the applied magnetic field in Oersted (Oe), C_{m} is the molar Curie constant in emu·K/mol, θ is the Curie-Weiss temperature in Kelvin (K). All units are in CGS for Equation (2.20). This susceptibility can also vary inversely with temperature

$$\chi^{-1} = [\chi_{\text{mol}} - \chi_0]^{-1} = \frac{T - \theta}{C_{\text{m}}} \tag{2.21}$$

where χ_0 is a temperature independent contribution, normally the diamagnetic ($\chi < 0$) susceptibility or for many metals the Pauli-paramagnetic ($\chi > 0$) susceptibility. The Curie-Weiss temperature θ is related to the strength of the interactions of the magnetic moments. For $\theta > 0$, the magnetic moments are aligned in the same directions and contribute to the ferromagnetic susceptibility. For $\theta < 0$, all the moments are aligned in the opposite directions and a system is called antiferromagnetic. All the magnetic moments are completely independent of each other in a pure paramagnetic system indicated by $\theta = 0$.

The magnetic susceptibility of a system is usually converted into the effective magnetic moment, μ_{eff}, derived from C_{m} using the formula of

$$C_{\text{m}} = \frac{N_{\text{A}}\mu_{\text{eff}}^2}{3k_B} = \frac{N_{\text{A}}g^2J(J+1)\mu_{\text{B}}^2}{3k_B} \tag{2.22}$$

where N_{A} is Avogadro's number, k_B is Boltzmann's constant, J is the total angular momentum, and g is a spectroscopic splitting factor.

Pauli paramagnetism arises from the response of the magnetic moments of conductions electrons in a metal to the applied magnetic field. It is well known that the conduc-

tion of free electron gases is dominated by the Pauli principle, the Pauli susceptibility χ_{Pauli} to the density of states at the Fermi energy level. This is nearly independent of temperature and has a small positive value [95, 96, 97].

Van-Vleck paramagnetism occurs in a system having no magnetic moment in the ground state, and thus there is no paramagnetic susceptibility in a first-order perturbation limit. According to second-order perturbation theory, the excited state will mix with the ground state and contribute to susceptibility. Diamagnetism, Pauli paramagnetism, and Van-Vleck paramagnetism are all virtually independent of temperature [95, 96, 97].

An ordering of the magnetic moment can be **ferromagnetic**, **ferrimagnetic**, **antiferromagnetic**, **helical**, or more complex in form [97]. However, the magnetic ordering effect usually dominates in the long range order of crystallites, solids and in relatively larger metal particles, and so it will not be further discussed. Furthermore, the energy excitations are different for magnetically ordered systems that are called *magnons* [98].

2.5.3 Magnetism in reduced dimensions - Clusters

Magnetism is inextricably linked with the electronic state of the system which is enormously changed in the nano-size range. In reduced dimensions, e.g. clusters, the electronic state or configuration can be a strong function of the cluster size and develops unusual properties, especially magnetic behavior [22]. In general, the incompletely filled degenerate highest occupied molecular orbital (HOMO) leads to magnetism. As is stated elsewhere (page 9 of Chapter 2), for small enough clusters the energy gap δ near the Fermi level will be large compared to $k_B T$ even at $T > 100$ K. It fundamentally implies that electrons in the highest filled level require much more energy than the available thermal energy in order to change their states, and the clusters behave differently according to whether they contain the odd-numbered or even-numbered electrons. Furthermore, if the energy gap[3] is sufficiently small, electrons will occupy the levels with parallel spins obeying Hund's rule that leads to a high spin state accompanied by a high magnetic moment [24]. However, when the energy gap exceeds the spin pairing energy, the state switches to a low spin state. The picture is further complicated by symmetry, while a high symmetry is related to a high degeneracy. If the symmetry is broken, e.g. when further atoms are added to a completed shell, the degeneracy is lifted by interatomic electron interaction and the ground state is a low spin state. This means that the energy gap δ is closely connected with the change in the energy state by adding the electron to the clusters. It is therefore apparent that a lower symmetry of clusters leads to molecular orbitals of lower degeneracy. It is however an indirect relationship that the density of states (DOS) at the Fermi level scales inversely with the energy gap δ.

From the point of view of quantum mechanics, the magnetic moment is dependent on the contributions of spin and orbital angular momentum which sum up into the magnetic moment vector. In the presence of the magnetic field, the electron Zeeman splitting or spin-orbit coupling (SOC) can compete with level splittings at the Fermi level leading to an additional magnetic field and also temperature dependent spin state. When quenching the orbital contribution to the effective magnetic moment μ_{eff}, the spin-orbit coupling has no effect on magnetism. This is a low symmetry case and implies that the unpaired spin is in the highest occupied level, hence there is paramagnetic susceptibility for a system. A pure spin $S = 1/2$ magnetism results in a temperature-independent μ_{eff} = 1.73 μ_{B} (Bohr magneton) according to the spin-only model.

[3] also termed Kubo gap

X-ray magnetic circular dichroism (XMCD) is a very powerful tool for the separation of the contribution of the orbital angular momentum m_L to the magnetic moment of the clusters [99, 100]. An increasing ratio of m_L to m_S is expected by decreasing dimensionality or coordination of the cluster. Clusters may have to be regarded as pseudo-atoms, with the important difference that the cluster orbital momentum should be expected to be much larger than for atoms, because it scales with the square of the radius [101]. It is quite likely that the orbital momentum has important implications for the magnetic character of the cluster.

It is ultimately apparent that the electronic ground-state orbital is an important factor for diamagnetism of the system under investigation, which is fundamentally different from the temperature-independent paramagnetism, since the latter requires the use of excited-state orbitals.

2.6 Fundamentals of XAS

X-ray absorption spectroscopy is an atomic probe. Importantly, a long-range order of crystalline material is not required for XAS. It makes this technique more advanced for investigating a few structural probes available for noncrystalline and highly disordered materials, including solutions. X-rays penetrate deep into almost all materials. Therefore, X-ray absorption spectroscopy is not inherently sensitive to the external surface region, and it requires some additional means for surface investigations. In many cases, measurements can be made on minority elements and even trace abundance, giving a unique and direct measurement of the chemical and physical state of dilute species in a variety of environments.

X-ray absorption experiments are relatively straightforward to yield a high precision information on the local environment because each atom has core-level electrons, provided that there is an intense and energy-tunable source of X-rays [35]. In practice, it usually means the use of a synchrotron, and its development is inextricably linked with that of synchrotron radiation. Various technical, experimental and sample conditions are applicable to XAS, including high spatial resolution, extreme conditions of temperature and pressure, and very fast measurements of *in situ* chemical processes.

2.6.1 Synchrotron radiation

Synchrotron radiation is electromagnetic radiation, similar to cyclotron[4] radiation, but generated by the acceleration of ultra-relativistic, i.e. moving near the speed of light, charged particles (usually electrons, e^-) through magnetic fields. This may be achieved artificially by storage rings of a synchrotron, or naturally by fast moving electrons moving through magnetic fields in space. The radiation typically includes **radio waves**, **infrared light**, **visible light**, **ultraviolet light**, and **X-rays**. The radiation was discovered in a General Electric synchrotron accelerator built in 1946 and announced in May 1947 [102].

Generally, electrons are accelerated to high speeds in several stages to achieve a final energy in the range of GeV. The electrons are stored in an ultrahigh vacuum ring and forced by strong magnetic fields to accelerate, traveling in a closed loop. This process is basically continuous. The magnet is also needed to repeatedly re-compress the

[4] it accelerates p^+ (positron)

Coulomb-exploding space charge electron bunches. The change of direction is a form of acceleration so that the electrons emit radiation at GeV frequencies. This is similar to a radio antenna system, but differs in that the relativistic speed changes the observed frequency by the γ factor due to the *Doppler Effect*. Relativistic Lorentz contraction bumps the frequency by another fraction of γ, thus multiplying the GeV frequency of the resonant cavity that accelerates the electrons into the X-ray range. Another dramatic effect of relativity is that the radiation pattern is also distorted from the isotropic dipole pattern expected from non-relativistic theory into an extremely forward-pointing cone of radiation. This makes synchrotron radiation the brightest effective sources of X-rays.

Third-generation synchrotron radiation sources, e.g. ESRF, were conceived and optimized from the outset to produce the bright X-rays[5]. These have many advantages due to the wide ability in energy and wavelength tuning by monochromator (eV up to MeV), high level of polarization (e.g. linear or elliptical), high collimation (i.e. small angular divergence of the beam), and low emittance. As is aforementioned, the bending by electromagnets is usually used to generate the radiation. In order to generate a stronger radiation, however, an insertion device is employed nowadays. Current third-generation synchrotron radiation sources are typically heavily based upon the insertion devices. Straight sections in the storage ring are used for inserting periodic magnetic structures (composed of many magnets having a special repeating row of N and S poles) that force the electrons into a sinusoidal path or helical path. Thus, instead of a single bend, many tens or hundreds of "wiggles" at precisely calculated positions add up or multiply the total intensity that is seen at the end of the straight section. These devices are basically called **wigglers** or **undulators**. The main difference between an undulator and a wiggler is the intensity of their magnetic fields and the amplitude of the deviation from the straight line path of the electrons. There are openings in the storage ring to let the radiation beam exit into the experimenters' vacuum chamber in the **hutch**.

2.6.2 Absorption of X-rays

X-rays are light with energies ranging from 500 eV to 500 keV and wavelengths of 25 Å to 0.25 Å. In this energy range, light is absorbed by all matter through the photo-electric effect[6]. This effect is illustrated in Figure 2.5. In a particular process, an X-ray photon is absorbed by an electron in a tightly binding quantum core level, i.e. $1s$ or $2p$ level, of an atom and the ejected electron is called the photo-electron. The incident beam of X-ray has an energy equal to or greater than the binding energy of the core-level electron. There is a sharp rise in the absorption edge corresponding to the promotion of the photo-electron to the continuum. X-rays will be absorbed according to *Beer's law*:

$$I = I_0 e^{-\mu d} \tag{2.23}$$

where I_0 is the intensity of the incident beam on a sample with the thickness of d and I is the intensity of the transmitted beam through the sample. The linear absorption coefficient $\mu(E)$ is a smooth function of energy and proportional to the sample density ρ and the atomic number Z,

$$\mu \approx \frac{\rho Z^4}{AE^3} \tag{2.24}$$

[5] many orders of magnitude higher than that of X-rays produced in conventional X-ray tubes
[6] an explanation of the photoelectric effect introduced by Albert Einstein in 1905

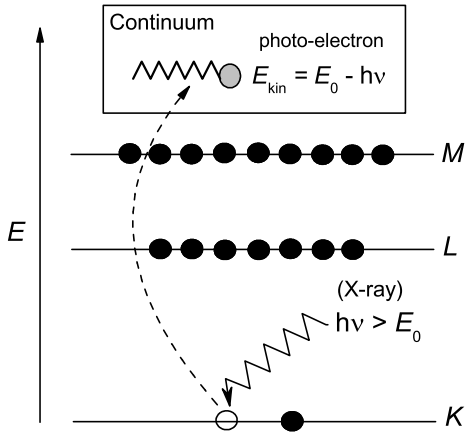

Figure 2.5: In the photoelectric effect, the X-ray is absorbed by atom, and the core-level system is promoted out of the atom. A photo-electron is created to possess kinetic energy, leaving a core-hole in a quantum level of the absorbing atom.

whereas it is inversely proportional to the atomic mass A and the energy E of the X-ray. The edge energy is well known for each atom and varies with the atomic number as approximately as Z^2. Thus, EXAFS can be considered *element specific*. In addition, the absorption edge increases as the cluster size decreases. The absorption edge is similar to the phenomenon of a **band gap**.

2.6.3 EXAFS equation

X-ray absorption induces the *transition* between two quantum states, thereby taking into account the initial state and the final state of the absorbing-scattering pair. The initial state is a spatial condition considering X-ray absorption and the core electron, but has no yield of the photo-electron [103]. In contrast, the final state has a yield of the photo-electron, thus considering backscattering, but no concern for X-ray absorption and the core electron. The linear absorption $\mu(E)$ is described by Fermi's Golden Rule

$$\mu(E) \propto |\langle i|\mathcal{H}|f\rangle|^2 \tag{2.25}$$

where the $\langle i|$ and $|f\rangle$ represent the initial state and the final state, respectively. Note that the final state in Equation (2.25) will be affected by the presence of the neighboring or backscattering atom, and the photo-electron is able to experience it. The backscattered photo-electron can return to the absorbing atom, modulating the amplitude of the photo-electron wavefunction at the absorbing atom. This in turn modulates the absorption coefficient $\mu(E)$, causing an additional term for the oscillatory fine structure $\chi(k)$ function of the EXAFS. The oscillation is well above the absorption edge, and the

oscillatory fine structure function is defined in the formula

$$\mu(E) = \mu_0(k)[1 + \chi(k)] \tag{2.26}$$

where μ_0 is the atomic background representing the "free or bare atom" absorption. This is only dependent on the absorbing atom, but is not dependent on the neighboring atom.

In EXAFS measurements, the oscillatory $\chi(k)$ function is a summation over all coordination shells around an absorbing atom and described via

$$\chi(k) = \sum_j \frac{S_0^2 N_j}{kR_j^2} f_j(k, R_j) \exp(-2\sigma_j^2 k^2) \exp\left(\frac{-2R_j}{\lambda(k)}\right) \sin[2kR_j + \varphi_j(k)] \tag{2.27}$$

where R_j, N and σ are inter-atomic distance, coordination number and root mean square displacement (Debye-Waller factor), respectively, for each atomic pair. In addition, λ is the mean-free-path of the photo-electron which is typically 5 Å up to 30 Å and has a fairly universal dependence on the photo-electron wave vector k. By including the terms of R_j^2 and $\lambda(k)$ in Equation (2.27) EXAFS is an inherent **local probe**, but is not able to detect the scattering much further than 5 Å from the absorbing atom. The back-scattering amplitude $f_j(k)$ and the phase factor $\varphi_j(k)$ of the sine function are both functions of the photo-electron wave vector k. Thus, Equation (2.27) is called the **EXAFS function** which provides information on the local structure of the central absorbing atom [103]. Finally, the oscillatory $\chi(k)$ function is proportional to the amplitude of the backscattered photo-electron at the absorbing atom in EXAFS.

3 Experimental and theoretical methods

This chapter deals with experimental and theoretical methods: i.e. chemical methods of preparation for small Ag clusters in the support pores, the operation details, and the selections of the optimum parameters for obtaining the well-resolved hyperfine spectra by continuous wave and pulse EPR spectroscopy measurements are adequately summarized. The experimental details for the manifestations of static magnetism of the reduced silver clusters using a SQUID magnetometer are summarized briefly. For determining the mean size and the surface effects, the local structure of the supported silver clusters, the optimum conditions and technical safety regulations are required for the Ag *K*-edge XAS experiments which are briefly introduced. In addition, the analysis of the absorption fine structure spectra will be introduced. Furthermore, the computational details of theoretical calculations for EPR parameters and principal methods of high-resolution TEM imaging are briefly described.

3.1 Ag cluster synthesis

Depending upon what properties are examined for clusters, different preparation methods and experimental techniques must be employed. A wide variety of methods can be used to prepare small metal clusters. The unsupported or free-standing clusters are prepared in molecular beams by laser jet expansion that are usually to be mass-selected. This type of clusters is not relevant to the purposes of the present research, thereby being deferred. A chemical method of ion-exchange [104, 105] and chemical reduction are suitable to deposit small metal clusters on the supports. This type of clusters can be basically size and shape selected. Metal ions in solutions are impregnated into the cages of the supports in order to get a relatively uniform distribution of ions. A chemical reduction leads to a stabilization of size-selected clusters within the cages [106] that prevent them from further aggregations. The size-selectivity of clusters is a likely requirement for diverse technical applications. In practice, the active phase is dispersed as very small clusters in dimensions less than 2 nm on porous oxide supports.

3.1.1 Preparations of Ag/NaA and Ag/NaY

The NaA (Si/Al = 1) zeolite was supplied by CU Chemie Uetikon AG in Switzerland. Zeolite samples were heated up in air at a rate of 0.5 K min^{-1} to 773 K where they were kept for 14 hours in order to burn off any organic impurities. Subsequently, 7 g of the heated sample was washed by stirring in 150 ml bi-distilled water containing 40 ml NaCl (10%) solution and 2.76 g of $Na_2S_2O_3{\cdot}5H_2O$ salt. The washing processes were repeated at least nine times. The washed sample was dried in air at 353 K for 24 hours.

Ag/NaA samples were prepared in a flask containing 2.25 g of pre-treated zeolite by aqueous ion-exchange with 50 ml 50 mM $AgNO_3$ solution (ChemPur GmbH in Germany, 99.998%) by stirring at 343 K in the dark for 24 hours. The ion-exchanged sample was filtered and rinsed with deionized water several times, and dried in air at 353 K

overnight. Chemical analysis by atomic absorption spectroscopy (AAS) demonstrated that the ion-exchange reaction leads to a silver loading of ca. 12% (wt.). A silver loading of 9% and 6% was also prepared separately.

Oxidation was performed under a gas stream of O_2 (Westfalen AG in Germany, 99.999%) with a flow rate of 17 ml min^{-1} g^{-1} from room temperature up to 673 K using a heating rate of 1.25 K min^{-1} where it was kept for an additional hour. While the sample was held at the final temperature, the residual O_2 gas in the reactor was purged by N_2 (Westfalen AG, 99.999%) gas for 1 hour. Subsequently, the sample was sealed and kept at 673 K overnight.

After cooling the sample, reduction was performed in a flow of H_2 gas (Westfalen AG, 99.999%, 16 ml min^{-1} g^{-1}) at room temperature or below for 20 minutes, which leads to the stabilization of the paramagnetic Ag_6^+ cluster. Alternatively, D_2 (Westfalen AG, 99.0%) reduction was carried out under a static gas pressure of 500 mbar.

The reduced sample was transferred into EPR quartz tubes (outer diameter about 4 mm) under nitrogen or argon gas in a glove box. The tubes were sealed with stopcocks for vacuum treatment and gas admission. The sample containing tube was evacuated for 30 minutes prior to each EPR measurement. The prepared sample can be handled in daylight because this is not photo/light sensitive.

Preparations were also performed with NaY zeolite (CU Chemie Uetikon AG, Si/Al = 2.7), and all treatments were performed in the same way as for Ag/NaA prepared for the purpose of paramagnetic Ag clusters.

3.1.2 H_2 isotope exchange and D_2 desorption

For hydrogen isotope exchange, the deuterium gas was filled into an evacuated EPR quartz tube containing about 120 mg of hydrogen reduced 12% (wt.) Ag/NaA sample. The gas was kept for 20 minutes at a D_2 partial pressure of 500 mbar at room temperature. After H/D exchange, the residual D_2 gas was pumped off and the sample tube was sealed for measurements.

D_2 desorption experiments were preformed using a turbo-molecular pump apparatus at temperatures of 383, 408 and 423 K. An EPR quartz tube containing 120 mg deuterium reduced 12% (wt.) Ag/NaA powder sample was connected by a glass adapter valve to the turbo-molecular pump apparatus. The vacuum system can achieve pressures as low as $10^{-5} - 10^{-6}$ mbar. The sample was heated to different temperatures for different time intervals during the evacuation, and then the spectra were collected by continuous wave X-band EPR at 20 K.

3.1.3 Adsorptions of NO, $^{16}O_2$, $^{17}O_2$, and C_2H_4

For adsorption, nitrogen monoxide (Westfalen AG, 99.9%) was filled into the EPR quartz tube containing about 200 mg H_2 reduced Ag/NaA zeolite sample. The sample was kept for 1 hour under a partial pressure of 100 mbar (10 kPa) NO at room temperature. Residual gas was evacuated before EPR measurements. The whole procedure of adsorptions was repeated three times. An impurity of O_2 gas with a trace amount leads slowly to the conversion of NO into NO_2 on the surface of the silver cluster. Comparative investigations were carried out on the temperature dependent properties of formed NO_2 onto the empty NaA (unloaded) and 12% (wt.) Ag/NaA zeolite samples.

The Ag_6^+ cluster containing hydrogen reduced 12% (wt.) Ag/NaA zeolite sample was exposed to 200 mbar of $^{16}O_2$ (Westfalen AG, 99.995%) at room temperature. The sample

was kept under $^{16}O_2$ for 1 hour, and the whole procedure of adsorptions was repeated six times. However, the spectrum was taken separately after evacuating gas residues by each of adsorptions on the sample.

250 mbar of $^{17}O_2$ (Westfalen AG, 99.7%) was adsorbed separately on the Ag_6^+ cluster in the H_2 reduced Ag/NaA sample in the quartz tube, and the sample was kept under a partial pressure of gas at room temperature for 1 hour and then evacuated for 30 minutes.

Adsorptions of C_2H_4 (Westfalen AG, 100%) were performed using a gas pressure of 500 mbar that was exposed to the reduced Ag_6^+ cluster in the 12% (wt.) Ag/NaA zeolite sample in the quartz tube. The sample was kept for half an hour under a partial pressure of 500 mbar (50 kPa) C_2H_4 at room temperature. The adsorptions were repeated three times on the same sample.

A mixture of C_2H_4 and $^{16}O_2$ ($P \approx 500$ mbar) was exposed to the reduced Ag_6^+ cluster containing sample in the tube, and the residues of gases were evacuated.

3.2 EPR measurements

Continuous wave EPR records derivatives of absorption spectra by using magnetic field modulation of 100 kHz, and this particular method enjoys the advantages of narrow-band detection at the modulation frequency and of better resolution of the derivative as compared to the absorption lineshape. Therefore, cw EPR spectra can be measured at ambient temperature for a number of transition metal ions, while liquid helium cooling is required for pulse EPR measurements. Calculating the derivative from the absorption lineshape obtained by pulse methods results in a decrease in signal-to-noise ratio. Pulse methods rely on relaxation times of the transverse magnetization which are longer than the spectrometer deadtime. Such a condition is much more restrictive than the condition on relaxation times for the observation of cw EPR. Nevertheless, there is an advantage of applying pulse EPR in which the measurement of electron spin transition frequencies is possible, even if the whole spectrum is not excited at once. To measure broad spectral features, cw EPR is rather a poor method, since field modulation amplitudes larger than 40 G (4 mT) cannot be easily obtained and the derivative is then very small. Such features are either invisible in cw EPR or perturbed even by small baseline drifts, while they can be well distinguished in the absorption spectra obtained with pulse EPR methods [107].

As is the case for all ESEEM methods, i.e. HYSCORE allows a high precision detection of smaller magnitude nuclear frequencies, particularly ENDOR methods are insufficiently performing the detection at frequencies of $f < 5$ MHz. Thus, ESEEM is a suitable tool to determine smaller hyperfine couplings of the nuclei, whereas ENDOR is a powerful method to chase the most strongly coupled nuclei in the environment of the unpaired electrons [34]. However, the application regions of ESEEM and ENDOR techniques strongly overlap.

3.2.1 Continuous wave EPR measurements

Continuous wave EPR spectra were recorded on a Bruker EMX spectrometer operating at X-band with a microwave frequency of 9.5 GHz. In order to avoid a saturation of signals, an optimized microwave power of 1 mW (23 dB) was used for all experiments, the signal is not saturated at this power at lower temperature. Figure 3.1 illustrates the

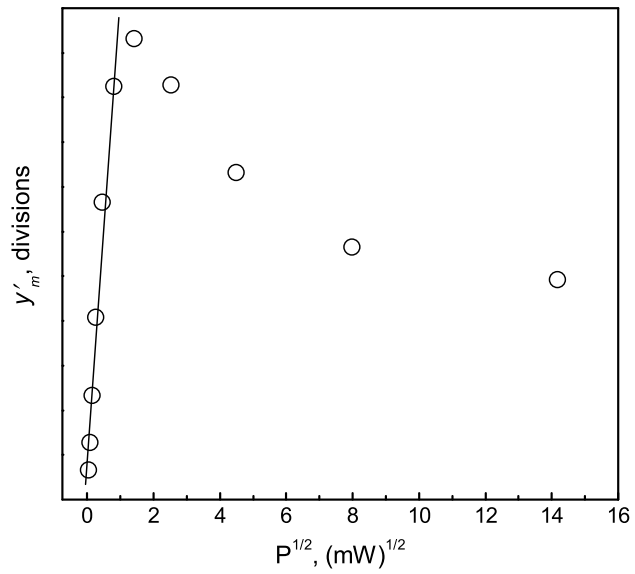

Figure 3.1: Microwave power saturation curve for the reduced Ag_6^+ cluster in 12% (wt.) Ag/NaA sample recorded at 20 K.

change of the EPR signal intensity as a function of the square root of microwave power at 20 K. The unsaturated maximum power is about 1.5 mW for hydrogen reduced Ag_6^+ in 12% (wt.) Ag/NaA sample at 20 K. Further, all measurements were carried out over the temperature range of 3.0 K to 298 K using an Oxford temperature controller. A modulation amplitude of 2 - 10 G is combined with a fixed modulation frequency of 100 KHz applying a receiver gain of 1×10^4 - 1×10^5 depending upon the signal-to-noise ratio. The spin concentration of cluster containing samples was calibrated with a standard sample (ultramarine blue diluted by KCl) using the double integral of the EPR derivative lines.

3.2.2 Numerical spectrum simulations

In the numerical spectrum simulations of the reduced Ag_6^+ cluster, high-field conditions, i.e. $\beta_e \mathbf{B_0} \cdot \mathbf{g} \cdot \mathbf{S} >> h\mathbf{S} \cdot \mathbf{A} \cdot \mathbf{I}$, were assumed so that the effects of the nuclear field on the alignment of the electron spin are negligible, thus the electron problem can be treated independently. The fine structure interaction is treated as a perturbation of the electron Zeeman level. The corresponding energy levels are well-separated and m_S becomes a main quantum number. The coaxial orientation of g and A is assumed for the simulation. It does not use perturbation theory, and each nucleus is treated independently allowing arbitrary magnitudes and orientations of the hyperfine tensors of the near-equivalent nuclei.

The EasySpin computational simulation package was used, especially for refining of spectroscopic g factor and hyperfine interaction A tensor of the atomic Ag^0, triatomic Ag_3^{n+} cluster, the adsorbed NO_2 and the adsorbed NO on the silver cluster surface. EasySpin is based on MATLAB numerical functions [108]. The simulation package is supplied with options including the perturbations of several nuclei.

An approach to the slow-motion least-square fitting requires the precise determination of the magnetic tensors from the static or rigid limit spectra and then to fix these parameters. It is allowed to vary only the dynamic and ordering parameters in the fitting script file. Based on this, the EasySpin MATLAB simulation package was used to evaluate a kind of Brownian rotational slow motion of the adsorbed NO_2 on the silver cluster surface. The software sets automatically the basis size of the eigenvalues of $E_{L,K,M}$ [109] of the diffusion operator (actually it specifies the number of orientational basis functions) for anisotropic rotational diffusion, and specifies the basis size by giving the maximum values for, in that order, an even L, odd L, M and K. The M and K must be less than or equal to the maximum value of the L. Each principal value of the axial rotational diffusion tensor is specified in Hz (Hertz, s^{-1}) by giving a 2-element vector for the dynamic parameter of the simulation. Presentation of data on a logarithmic scale (**log**10) reduces the data to a more manageable range. The logarithmic scaling allows an adjustment of the principal value of the rotational diffusion tensor to have the same order of magnitudes.

3.2.3 Pulse X-band EPR measurements

The pulse Q-band EPR measurements were carried out on a home-built spectrometer at 7 K. In detail, field-sweep ESE experiments were performed using the pulse sequence of $\frac{\pi}{2} - \tau - \pi$ with the parameters $t_{\pi/2} = 20$ ns, $t_\pi = 40$ ns and $\tau = 200$ ns.

The pulse X-band EPR measurements were performed on a Bruker ElexSys E580 spectrometer at 10 K. The hyperfine sublevel correlation [84] (HYSCORE) spectra were recorded employing the sequence $\frac{\pi}{2} - \tau - \frac{\pi}{2} - t_1 - \pi - t_2 - \frac{\pi}{2} - \tau -$echo with mw pulses of length $t_{\pi/2}$ = 16 ns and t_π = 24 ns, τ = 240 ns, starting times $t_{1,2}$ = 100 ns and time increments $\Delta t_{1,2}$ = 16 ns. Unwanted echoes were removed by means of a four-step phase cycle [110]. To avoid suppression effects, τ-values were varied from 100 to 300 ns. The sensitivity of the HYSCORE experiment can be significantly improved by replacing the second and the third $\frac{\pi}{2}$-pulses with matched pulses of length 48 ns. In both dimensions 512 data points were sampled. The echo decay was eliminated by a third-order polynomial baseline correction in both time domains, applying a Hamming window and zero-filling to 1024 data points in both dimensions. After 2D Fourier transformation absolute-value spectra were calculated. All data were collected at 10 K.

The X-band ^{1}H-ENDOR spectra were obtained using the Mims ENDOR sequence $\frac{\pi}{2} - \tau - \frac{\pi}{2} - T - \frac{\pi}{2} - \tau -$echo with mw pulses of length $t_{\pi/2} = 16$ ns and $t_\pi = 32$ ns, and delay times of $\tau = 150$ ns. In order to avoid blind spots in the Mims ENDOR experiment, 11 spectra with τ values between 100 and 200 ns, in steps of 10 ns, were recorded. During time T a radio frequency (rf) pulse of length t_{rf} = 15 ms and variable frequency that was supplied by a 500 W amplifier (AR 100500A) was applied. All data were collected at 10 K.

3.3 Construction of pulse Q-band EPR resonator

A microwave resonator[1] is a complex component and integral part of electron paramagnetic resonance spectroscopy [33] whose performance particularly influences the function of spectroscopy. Therefore, this section is devoted to describe the construction and design of the cylindrical TE_{011} resonator for Q-band ESE and pulse ENDOR

[1] also termed as resonant cavity

spectroscopy operating at 35 GHz. The resonator serves to strengthening and consolidating the spatial orientation of microwave fields inside the cavity. This resonator fits into a liquid He cryostat or probe head of CF935O (Oxford Instruments), thus allowing to conduct low temperature experiments. In the development of the Q-band cylindrical resonator, however, particular difficulties exist on the construction due to the requirement of the relatively small volume or the limited dimension of the resonator according to a microwave frequency selection, thereby leading to a complication to the tunning mechanism and the coupling of the cylinder with the microwave guide. At resonance, however, the designed resonator for pulse Q-band spectroscopy is capable of sustaining microwave oscillations in a TE_{011} mode of standing wave configurations (interference patterns) from superposed microwaves multiply reflected from the cavity walls.

3.3.1 Theoretical background

At Q-band frequency, a cylindrical resonator in TE_{011} mode is most frequently used. The basic advantage of the cylindrical TE_{011} resonator is its small and compact volume that results in high energy density and the high magnetic field strength B_1 (or H_1) in the center of the resonator to support the maximum of the standing-wave. For the TE_{mnp}, TE stands for *transverse electric wave* mode $B_1 \neq 0$ and $E_1 = 0$ for the electromagnetic field configuration (out of phase) inside the resonator, while the subscripts of m, n, and p describe the number of half-cycle/half-wavelength variations in the standing-wave pattern in the angular (ϕ), radial (r), and the longitudinal (z) directions. There is no flow of an electric current in either radial (r) or longitudinal (z) direction, only in angular (ϕ) direction. The resonance frequency of the cylindrical resonator for a particular mode is related to its dimensions via:

$$f_0 = \frac{\sqrt{\left(\frac{c(k_c a)_{mn}}{\pi}\right)^2 + \left(\frac{cp}{2}\right)^2 \left(\frac{2a}{d}\right)^2}}{2a} \tag{3.1}$$

where $(k_c a)_{mn}$ is the n-th root of the m-th-order Bessel function (the first derivative of $J_m(k_c a) = 0$ vanishes at the surface for TE_{mnp}), c is the light speed in vacuum, a is the radius and d is the length of the resonator [33]. This root is equal to 3.832 for the TE_{011} mode.

It is relatively easy to reach an optimal quality factor Q. For the cylindrical TE_{011} mode, the smallest ratio of the double radius ($2a$) to the length (d) of the resonator provides the largest quality factor Q. However, reaching the maximum quality factor is not really necessary for pulse EPR experiments, even undesirable. The complete formula for calculating the optimal Q factor for the TE_{mnp} cylindrical mode is found elsewhere [33]. A rough estimation is close to $Q = f_0/\Delta f$ during the experiments [32, 33]. In general, the quality factor must be optimal, i.e. high enough to allow the partial saturation of the EPR transitions and not too high in order to avoid the ringing of the resonator.

The TE_{011} cylindrical mode is particularly useful for a sample cavity since B_z is very strong along the cavity axis. At this stage, the B_1 field is always at the absolute maximum in the middle of the cylindrical resonator. The EPR signal at resonance is proportional to the amount of power absorbed by the sample, and this in turn is proportional to the

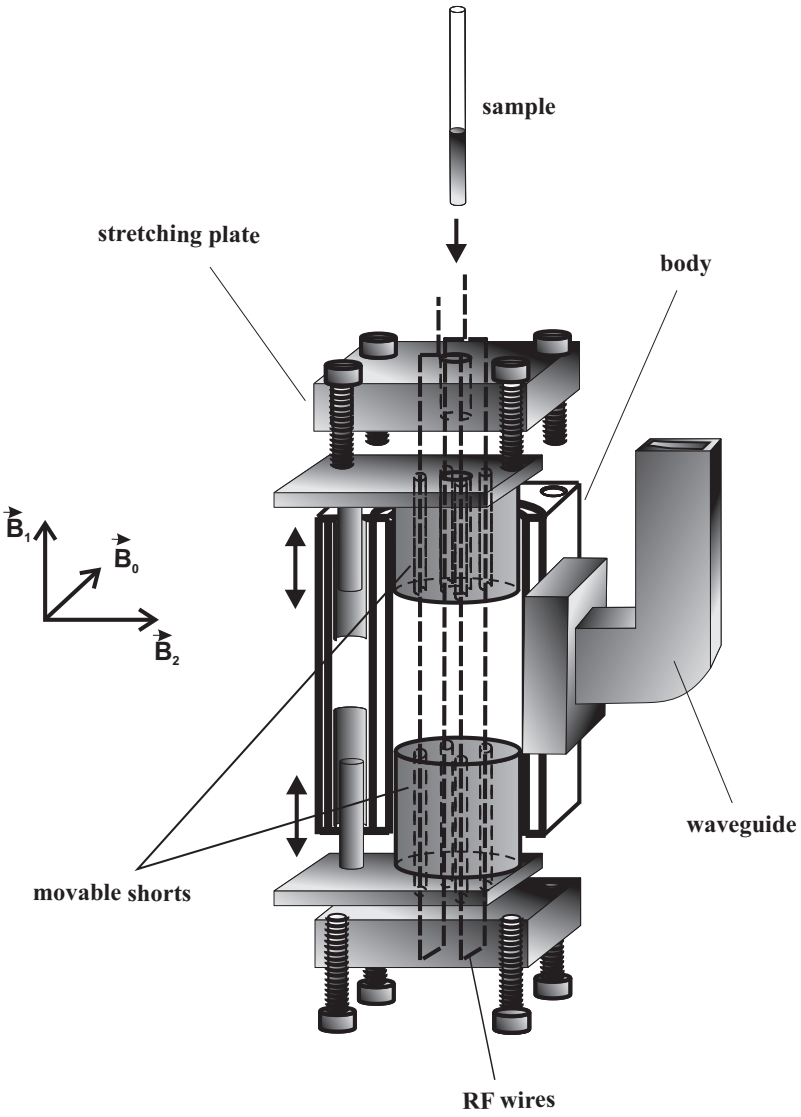

Figure 3.2: Pulse ESE/ESE-ENDOR cylindrical TE_{011} mode resonator.

average value of the microwave magnetic field $\langle B_1^2 \rangle_s$ at the sample where, in general,

$$\langle B_1^2 \rangle = \frac{\int B_1^2 dV}{\int dV} = \frac{1}{V} \int B_1^2 dV \tag{3.2}$$

B_1 is the component of the rf magnetic field perpendicular to the static magnetic field B_0. Thus, the filling factor η is defined by

$$\eta = \frac{\int_{sample} B_1^2 dV}{\int_{resonator} B_1^2 dV} \tag{3.3}$$

when the sample has an rf susceptibility (χ'') and a certain volume [33]. When the diameter of the sample is 2.5 mm for the optimum, the B_1 field is about 0.2 mT (2 G) in the middle of the present resonator according to its dimensions.

In addition to a strong mw field a sufficient rf field must be produced. The cavity coupling must be precisely adjusted, and rf interference effects as well as eddy currents must be avoided. B_2 is the rf field which is optimally produced by four straight rf bars parallel to the resonator axis representing a pair of Helmholtz coils. The available microwave sources for Q-band frequencies (Gunn and IMPATT diodes) usually have a narrow range frequency generation ($\approx$ 400 MHz). This disables one to obtain a capability of varying the resonance frequency in a broad range as is required. Another problem encountered is the usual need for low temperature measurements at minimized microphonic noise. The low temperatures must be kept while high rf currents, which flow through the ENDOR loops, add to the thermal load of the helium bath. In spite of these constraints several successful design approaches to the microwave resonators working at Q-band frequencies were reported [111, 112, 113].

3.3.2 Technical descriptions

Our design of the cylindrical TE_{011}-mode resonator is shown in Figure 3.2. It was constructed for low temperature operation, ca. $T < 1.5$ K, for both ESE and ESE detected ENDOR. All the parts of the resonator are made of brass.

The symmetry axis of the cavity is selected to be vertically perpendicular to the axis of the external or static magnetic field B_0. The basic architecture of the resonator is common and simple: the interior diameter of the cavity is 11 mm (thus the radius is 5.5 mm), and the length is also 11 mm. A pair of shorts (pistons) which face each other can be moved symmetrically along the axis of the resonator. The shorts form the top and bottom of the cavity whose distance can be adjusted from 5 mm to 12 mm by a fine thread to tune the resonator frequency to the output frequency of the source, ca. 35 GHz. The sample can be guided from the top of the cryostat and inserted into the cavity through an entrance hole (3.5 mm) in the top short.

Coupling with the WR28 rectangular waveguide (QuinStar Technology, Inc.) is performed via a small coupling iris on the back side of the cylinder. The coupling is made in such a way that the magnetic field orientation of the dominant TE_{10}-mode in the waveguide is parallel to the axis of the resonator. The diameter of the coupling iris equals to 2.9 mm. It was determined by trial and error. The thickness of the wall around the iris does not exceed 0.2 mm to avoid undesirable losses of the microwave power P. The integration of different coupling mechanisms was not successful. It was complicated by the small size of the cavity and the lack of space in the cryostat. Therefore, in the last version, no tuning mechanism for the coupling was applied. To avoid boiling of the liquid helium and air condensation inside the wave guide, the probe-head part of the waveguide is sealed with a mica film.

To construct the ENDOR coils of the resonator, four hair-pin copper wires, which form a pair of Helmholtz coils with one loop per coil surrounding the sample, were used. The rf magnetic field (B_2) is oriented horizontally and perpendicular to the magnetic field B_0. The wires are stretched along the cavity axis, i.e. they are firmly anchored in the upper plate, passed freely through the cavity close to the sample and then attached to the fixed plate below the cavity that served to stretch the wires. Stretching the wires prevents them from vibrating in the external magnetic field B_0. Teflon isolation prevents unwanted shorting of the wires within the upper and lower plates and shorts. The rf power is transmitted from the source to the cryostat part of the probe head by means of a semi-rigid coaxial cable. The characteristic impedance of the cable and the wires (loops)

must be close to 50 Ω at measurement frequencies, matching the output impedance of the rf high-power amplifier (50 Ω). The rf frequencies of up to 150 MHz could be applied without noticeable fluctuations of the hf-currents in the wires.

The quality factor Q of the unload cavity was calculated to be about 1000. The insertion hole in the top piston/short causes no appreciable loss of the quality factor.

3.4 SQUID measurements

Prior to SQUID measurements, X-band EPR experiments were performed on the electronic susceptibility of the reduced Ag_6^+ cluster. The zero field-cooled measurement was performed by cooling the sample to the lowest temperature for the measurements with zero applied magnetic field (H = 0). As the temperature stabilized, the magnetic field was applied to measure the magnetic susceptibility as a function of temperature up to the highest possible temperature. The field-cooled measurement was also carried out by cooling the sample in the presence of the magnetic field, and while increasing the temperature by a certain interval the magnetic susceptibility was measured.

Magnetic property measurements were performed using a Superconducting Quantum Interference Device (SQUID is an acronym) magnetometer (Quantum Design MPMS XL7). The sample inside the superconducting array (coil etc.,) was cooled from room temperature to 1.8 K in the applied magnetic field.

3.4.1 Sample preparation

The reduced Ag cluster containing 12% (wt.) Ag/NaA samples were transferred into NMR quartz tubes with outer diameter of 5 mm under nitrogen or argon gas in the glove box, and the tubes were sealed with stopcocks for vacuum treatments. This isolates the samples from air oxygen completely. Alternatively, the cluster containing zeolite samples were wrapped up in Teflon tapes and pressed into tablet (or pellet) forms. The prepared samples were put in the middle of the plastic tube to attach to the sample transport moving slowly inside the SQUID arrays for recording the induced currents in the respective coils. For each case, the mass of sample was about 60 mg on average which is mandatory to obtain a sufficient signal-to-noise ratio.

3.4.2 dc magnetization

Magnetization measurements were performed over the applied magnetic field range of 0 - 70000 Oe (7 T) using a field increment step of 2500 Oe at the fixed temperature of 1.8, 10, 25, 100 and 300 K, respectively. The sensitivity of the magnetization measurements was in the range of 0.1 Hz to 1 KHz at the applied field strength of 70000 Oe applying a field stability of 1ppm/hour for maximum detection of 7×10^{-8} EMU moments. At 1.8 K, the measurement is basically an estimate of the saturation magnetization $M(H)$ of the reduced Ag cluster system, and EMU values of magnetic moments were collected as a function of the applied magnetic field, i.e. EMU vs. H(Oe), at the same intervals of temperatures (see the above).

3.4.3 Magnetic susceptibility

Experiments on the direct current (dc) susceptibility of the nominal Ag_6^+ clusters in the reduced 12% (wt.) Ag/NaA samples were carried out at the temperature range of 1.8

K to 300 K with the fixed magnetic field of 1000, 2000, 3000 and 10000 Oe (0.1, 0.2, 0.3, 1 T), and the voltage response curves were collected consecutively. The measurement mode of EMU as a function of temperature, i.e EMU vs. $T(\mathrm{K})$, was applied for collecting the response curves. All measurement data were corrected by subtraction of the magnetic susceptibility of an identical amount (about 50 - 70 mg) of silver-free NaA zeolite samples to obtain the susceptibility of the nominal Ag_6^+ clusters alone.

3.5 XAS measurements and data analysis

The XAS measurements at the Ag *K*-edge (25.514 keV) were carried out at the Swiss-Norwegian Beamline (SNBL) BM01B of the Storage Ring of the European Synchrotron Radiation Facility (ESRF in Grenoble, France). The synchrotron beam current was 200 mA at 6.0 GeV energy of the storage ring. At the SNBL, the incident X-rays were focused by a Si(111) single crystal, channel-cut monochromator and a chromium-coated mirror rejected higher harmonics. All measurements were performed in transmission mode using ionization chambers for detection. A spectrum of a silver foil was acquired simultaneously with each measurement for energy calibration. All XAS spectra were collected at room temperature.

3.5.1 Samples for XAS

The oxidized catalysts of 12% (wt.) Ag/NaA were pressed into the self-supported wafer forms under Ar in the glove box. The pressed samples were directly loaded into the *in-situ* XAS cell in the glove box. Prior to reduction, the XAS spectra were collected under dynamic vacuum (or simply evacuation) for oxidized samples at 298 K. The reduction was performed on the same oxidized samples using diluted hydrogen in helium (5% H_2 in He) for safety reasons, and the spectra were collected under 500 mbar partial pressure of hydrogen at 298 K. For adsorptions, the gases diluted in He (5% C_2H_4, 5% O_2, 5% CO and 1% NO in He) were exposed separately to the hydrogen reduced samples in the *in-situ* XAS cell. The spectra all of these samples were also collected at room temperature.

3.5.2 Isolation of $\chi(k)$ function

XAS data analysis was carried out using the commercially available XDAP software package [114]. A first step in the data analysis is the subtraction of the monotonically decreasing pre-edge. After the pre-edge subtraction the edge energy (E_0) was defined and its value was used to calculate k (Å^{-1}). The atomic background (μ_0) was determined, and the absorption fine structures were background-subtracted by means of standard procedures [103]. Prior to the theoretical fit, the spectra were normalized on a per atom basis by division of the absorption data by edge-step at 100 eV above the absorption edge. As all the steps have been performed, $\chi(k)$ is isolated.

3.5.3 Fourier transform of $\chi(k)$ function

Fourier transform of $\chi(k)$ leads to a determination of a radial distribution function defined in *R*-space [115]. The radial function is a distance from the absorber atom to the backscatter atom. Fourier transform of the $\chi(k)$ function was performed in the range of $3 < k < 14$ Å^{-1} using the different *k*-weightings (k^1, k^2, k^3) depending upon the

isolations of the absorbing and back-scattering shells. The multiple-shell fittings were performed in R space of ca. $1.0 < R < 4.0$ Å, and neither the phase correction nor the amplitude correction was performed. Fourier transform is a complex function, the real and imaginary parts are obtained in consequence.

3.6 High-resolution TEM

A book covers the basic theoretical and physical background needed to understand how electron microscopic techniques allow scientists to look at atoms and atomic arrangements that determine basically the properties of matter [116, 117].

3.6.1 Background

In transmission electron microscopy, transmitted and diffracted electrons are used. The instrument is principally similar to an optical microscope, but optical lenses are replaced with electromagnetic lenses. In TEM, a primary electron beam of high energy and high intensity passes through a condenser to produce parallel rays, which impinge on the sample. The attenuation of the beam basically depends on the density and the thickness, the transmitted electrons form a two-dimensional projection of the sample mass, which is subsequently magnified by the electron optics to produce a so-called bright-field image. The dark-field image is obtained from the diffracted electron beams, which are slightly off-angle from the transmitted beam. Typical operating conditions of a TEM instrument are 100 to 200 keV electrons, 10^{-6} mbar vacuum, 0.3 nm resolution, and a magnification of 3×10^5 to 10^6. Image contrast in the transmission mode is caused not only by the attenuation of electrons, but also by diffraction and interference of electrons. For example, particles in TEM images may show less contrast than other identical particles because it is favorably oriented for *Bragg diffraction* by its lattice planes, such that the diffracted beam does not contribute to the image (amplitude or diffraction contrast). When tilting the sample, the changes in the orientation of the particle provide the means to recognize amplitude contrast. Another possibility is that the diffracted beam does contribute to the image, where it interferes destructively with the undeflected beam (phase contrast). It is usually warned that both effects are possible sources for misinterpretation of TEM images [118].

3.6.2 Information from TEM

Depending on the sample thickness, a fraction of the electrons passes through the sample without suffering energy loss. As the attenuation of the beam depends on density and thickness, the transmitted electrons form a two-dimensional (2D) projection of the sample. High magnification imaging requires a high electron dose, hence the need of a relative insensitivity to high vacuum for samples under investigation. If all those requirements are fulfilled successfully, the high resolution micrographs will be followed from TEM experiments.

HRTEM basically provides information on the morphology of the particles and clusters, the crystal structure, and the lattice constant (or parameters) with acceptable accuracy. The diffractogram is the Fourier transform of the HRTEM micrograph, thereby stipulating the crystal structure and the lattice parameters. Depending upon which region is used for the diffractogram it is also possible to find the defects or twin boundaries

(sometimes twin faults) in the structures.

3.6.3 TEM imaging of Ag clusters

Reduced silver cluster containing samples were ground in a mortar until getting enough homogeneity of powder dispersion and dissolved in an ethanol solution before loading on carbon lacey films (Plano GmbH). To determine the size of the reduced Ag clusters in 12% (wt.) Ag/NaA, TEM measurements were performed by means of high resolution electron microscope of JEOL-4000EX (JEOL Tokyo, Japan) operated at the acceleration voltage of 400 keV with an interpretable resolution defined by the contrast transfer function of the objective lens to be 1.6 ångström (Å). The images were scanned using a Microtek scanner at an optical resolution of 1200 dpi.

4 EPR of Ag clusters

This chapter will consider all the experimental results obtained from continuous wave and pulse EPR experiments on the supported silver cluster system. It is often difficult to characterize small metal clusters in different environments. Fortunately, EPR spectroscopy can provide unambiguity for the existence of mono-disperse paramagnetic clusters and ions in the micro-porous supports based upon their electronic structure and symmetry of the spin Hamiltonian [119].

The extension of EPR to high frequencies, with corresponding high magnetic fields, has been one of the most important instrumental advances. The frequency range would lie in the millimeter-wave end of the far-infrared region [120] that increases the range of the use and application enormously, e.g. rotation and vibration of molecules. Furthermore, the modern pulse spectroscopies have the added advantage of being a powerful tool to investigate the hyperfine interaction patterns of the more strongly or weakly coupled nuclei with the unpaired electrons depending upon a choice of the electron spin-echo detection method.

4.1 EPR results of Ag clusters

Numerous unsuccessful attempts were made on Ag/NaY to stabilize single paramagnetic silver clusters, but nevertheless were several irradiation derived atomic Ag^0 and Ag^{2+} species observed in hydrated silver zeolite samples up to 77 K by conventional continuous wave and pulse EPR spectroscopy [121, 123, 124]. It was also noted that the dehydration process caused an extensive clustering of silver species at elevated temperatures (mostly at 773 K), but most of them were paramagnetic inactive species.

Various studies of Ag^+ exchanged Ag/NaA zeolites were extensively carried out at low temperatures (mostly at 77 K), and different paramagnetic clusters were, i.e. Ag_2^+, Ag^{2+}, Ag_3^{2+}, Ag_4^{3+}, Ag_6^{n+} and $Ag_6^+ \cdot 8Ag^+$, stabilized as the direct consequences of irradiation with γ-ray and X-ray at 77 K. It was reported that the cluster nuclearity was basically dependent on higher Ag loadings and dehydration conditions, which were fulfilled by low temperature evacuation at 373 - 393 K, however, the hyperfine structures of different clusters were usually complicated to interpret reliably due to coexistence of many different hyperfine interactions [9, 10, 11, 12]. In hydrogen reduced Ag/NaA samples only paramagnetic six-atomic silver clusters were observed for very short time, and only early stages of the reduction process could be followed by *in situ* EPR measurements which enabled the determination of the Ag_6^{n+} clusters as intermediates [15, 16, 17, 18, 19]. Well-resolved hyperfine splitting patterns of smaller Ag clusters, e.g. Ag^0, tri- and four-atomic clusters, were not observed experimentally.

I have recently succeeded to prepare a single, well-defined paramagnetic atomic Ag^0, Ag_3^{n+}, Ag_4^{n+} and Ag_6^+ clusters by chemical reduction method in the pores of Ag/NaA. The Ag atoms exhibit hyperfine anisotropy, while Ag_3^{n+}, Ag_4^{n+} and Ag_6^+ clusters are isotropic, thus demonstrating that all of the silver atoms of the clusters are close to equivalent. These clusters are completely stable in a broad range of temperatures, espe-

cially the reduced Ag_6^+ cluster is spectroscopically observable up to 298 K. This is the main progress of this thesis and a step toward a complete research and understanding of unexplored physical, electronic, magnetic and chemical properties of reduced paramagnetic silver clusters in the support pores.

4.1.1 Spectrum of Ag/NaY

At the beginning of this experimental work, the synthesis of reduced silver clusters in Ag/NaY (Si/Al = 2.7) was attempted, but we did not succeed in forming and stabilizing any paramagnetic Ag species. A specific hyperfine structure of paramagnetic clusters had not been observed, only the signal observed at g = 2.00 was a superposition of the two axial g species instead. The numerical spectrum simulation with corresponding g values is displayed in Figure 4.1. The present signal is broadened immediately on increasing temperatures of 20 - 70 K. It is apparent that the axial g signals are assigned neither to silver cluster species nor to silver atomic species. This is because the identical signal with g = 2.004 was observed in the silver-free NaA after exactly the same treatments.

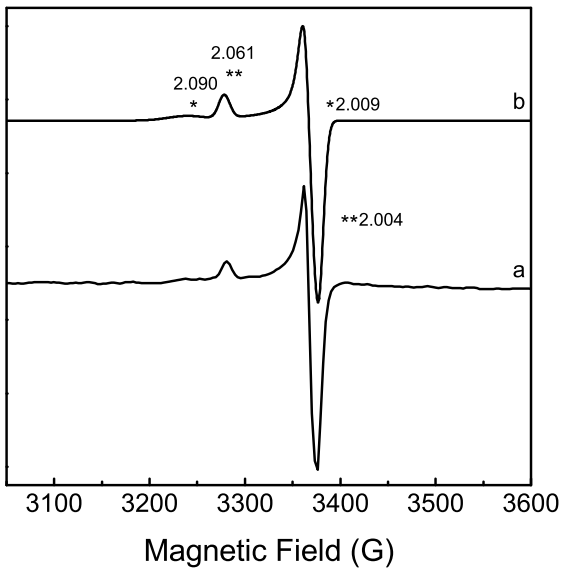

Figure 4.1: Experimental (a) and simulated (b) X-band EPR spectrum of the hydrogen reduced 12% Ag/NaY recorded at 20 K. In the superposition (1:1 weighting), the signal labeled * is from one species with $g_\perp$ = 2.009 and $g_\parallel$ = 2.090 and the signal labeled with ** is from another species with $g_\perp$ = 2.061 and $g_\parallel$ = 2.004, respectively.

In NaY supports, atomic Ag species normally exhibit well-resolved two doublets in the hyperfine splitting due to the silver isotopes ^{107}Ag and ^{109}Ag with the large isotropic hyperfine coupling constant of A_{iso} = 590 - 700 G [121, 122, 123, 124]. However, the hyperfine spectra of these atomic species were quite different than the present hyperfine signal. It is probable that the isotopic enrichment can be principally performed for the sake of isolating the hyperfine coupling contribution of the magnetic nuclei to the

linewidth effect according to the nuclear spin and the percentage in natural abundance, if they are indeed present. On the contrary, there is no use doing the isotopic enrichment for the present case. This is because Ag has naturally occurring two isotopes with same the nuclear spin number of $I = 1/2$ possessing almost the identical abundance, i.e. ^{107}Ag 51.839% and ^{109}Ag 48.161%. Furthermore, a conduction electron signal of metallic silver particles was observed in Ag/NaY exhibiting the EPR parameters of $g = 1.960$ and $\Delta H_{\mathrm{pp}} = 70$ G [125]. Generally, the conduction electron signal usually arises from the relatively larger particles with size of ≈ 5 nm that gives rise to only a single broad spectral line [15]. It is thus reasonable to assume that the present signal is due to defect centers within the framework of Ag/NaY zeolite. It was previously reported that a very similar signal with axial g species was observed in 6% (wt.) Pt/NaY zeolite by continuous wave EPR that was considered the signal arising from a zeolite center [55].

It is probably interesting to note that EPR active Ag cluster species have only been detected in dehydrated and reduced Ag/NaA. It is therefore probable that the spatial structure of the cages and channels of NaA zeolite can be a decisive factor in stabilizing the paramagnetic silver clusters, since it exhibits a different structure than NaY zeolite.

4.1.2 Spectra of Ag^0, Ag_3^{n+} and Ag_4^{n+} clusters in Ag/NaA

As an unpaired electron spin $S = 1/2$ interacts with nuclear spin $I = 1/2$, the spin Hamiltonian considering the hyperfine interaction of Ag nuclei and the unpaired electron is described via

$$\mathcal{H} = \beta_e \mathbf{B_0} \cdot \mathbf{g} \cdot \mathbf{S} + \sum_{i=1}^{N} \mathbf{S} \cdot \mathbf{A_i^{Ag}} \cdot \mathbf{I_i^{Ag}} - \beta_n \sum_{i=1}^{N} g_{n,i} \mathbf{B_0} \cdot \mathbf{I_i^{Ag}} \tag{4.1}$$

where the first and third terms are the electronic and nuclear Zeeman interaction in the external magnetic field B_0, respectively. The second term in Equation (4.1) corresponds to the hyperfine interactions due to nearby silver nuclei. The hyperfine tensors $\mathbf{A_i}$ and the external magnetic field $\mathbf{B_0}$ are given in the principal axes system of the $\mathbf{g}$ matrix.

The X-band EPR spectrum of hydrogen reduced 6% (wt.) Ag/NaA is illustrated in Figure 4.2, and the components of $g_{\parallel}$ and $g_{\perp}$ are labeled. On the ground that it appears on hydrogen reduction this well-defined doublet is assigned to neutral Ag atoms. Calibration of the signal reveals a spin concentration corresponding to 0.045% of the total Ag loading. Thus, most of the silver must be present in diamagnetic form. Numerical spectrum simulation provides the spin Hamiltonian parameters ($g_{\perp} = 1.998$ and $g_{\parallel} = 2.214$, coaxial with $A_{\perp} = 23$ G and $A_{\parallel} = 173$ G). Attempts to include the feature marked with an asterisk in the simulation did not lead to satisfactory agreement with experiment. $g_{\mathrm{iso}} = 2.070$ is significantly higher than g_{e} of the free electron, which normally indicates admixture of a transition metal d-orbital into the semi occupied orbital [80]. The axial symmetry of the g tensor means that the species is located at or near a typical cation site [126] and that the spherical symmetry of the free ion is lifted by the crystal field. $g_{\parallel} > g_{\perp} > g_{\mathrm{e}}$ corresponds to a $d^9_{x^2-y^2}$ elongated octahedral state due to spin-orbit coupling [80]. If we disregard that in the present case $g_{\perp}$ is slightly below g_{e} it means that the ground state of this species has the electron configuration [Kr]$4d^9 5s^2$, while the ground state of the *free* atom is [Kr]$4d^{10}5s^1$ with a g_{iso}-value very close to g_{e} [127]. In earlier work, the anisotropic spectrum of Ag^{2+} was observed in dehydrated Ag/NaA and its spin Hamiltonian parameters were $g_{\parallel} = 2.303$ and $g_{\perp} = 2.044$ coaxial with $A_{\parallel} = 25$ G and $A_{\perp} = 24$ G [128]. Interestingly, the general shape of this EPR spectrum

of this doubly charged ion was quite similar to the present signal, even though the g-components are significantly higher and the parallel hyperfine parameter is much lower. Moreover, it seems clear that Ag^{2+} cannot form when the starting material is reduced by hydrogen. Previously, it was also observed that paramagnetic silver atoms (Ag^0) are stabilized with near isotropic hyperfine components (528 G, 634 G, 706 G), much more than the present $A_{iso} \approx 73$ G, by γ-irradiation and only in hydrated but not in dehydrated Ag/NaA samples [122, 129, 130]. Those Ag^0 species were coordinated to four water molecules, two in the β-cage and two in the α-cage, and were thermally unstable. The water ligands obviously lead to a much softer and more isotropic crystal field than the zeolite.

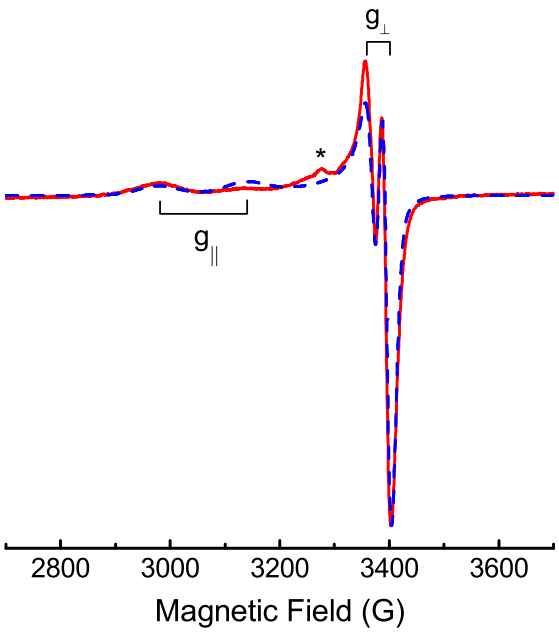

Figure 4.2: Experimental X-band EPR spectrum of 6% (wt.) Ag/NaA after H_2 reduction at 298 K recorded at 20 K with the corresponding numerical spectrum simulation (blue dashed line) based on the spin Hamiltonian parameters given in text. An asterisk indicates the presence of a second species.

Another anisotropic species which was observed previously in silver loaded zeolites on exposure to oxygen is the superoxide radical anion $O_2^{\bullet-}$ which exhibits g closer to g_e [131], and no hyperfine interaction was observed for $^{16}O_2$ due to $I = 0$ [132]. A single silver atom splits only $g_{zz} = 2.050$ of adsorbed $O_2^{\bullet-}$ by $A^{Ag} = 30$ G whereas $g_{yy} = 2.011$ and $g_{xx} = 2.002$ remained almost intact [128].

The isotropic hyperfine coupling constant, $A_{iso} \approx 73$ G, corresponds to an s-orbital contribution of 10.4% to the spin density in the semi-occupied orbital that is inferred from a comparison with the average atomic hyperfine coupling constant of 702 G of the ^{107}Ag and ^{109}Ag isotopes. The experimental dipolar component of anisotropic hyperfine matrix is $b_{\parallel} = -50$ G. The tabulated anisotropy value is 78.65 G, and the angular factor α is $-4/7$ for an atomic $d_{x^2-y^2}$ orbital [133] so that the corrected A_{aniso} value should be $4/7 \times 78.65$ G = 44.94 G for an electron in this orbital. This yields a spin population

of ca. 57% in $d_{x^2-y^2}$ and in total it accounts for ca. 67.5% of the unpaired electron. It is however noted that such an approximation provides a very rough estimate of spin density, as it disregards spin polarization and delocalization onto neighboring atoms without a nuclear spin.

On the other hand, the negative deviation of the experimental $g_\perp = 1.998$ component from the free electron g_e value is in the order of -0.43×10^{-2} that is noticeably less than the bulk shift of $\Delta g_{bulk} = -1.9 \times 10^{-2}$ for the silver metal and silver particles derived from the theoretical and experimental treatments [134, 135]. This probably supports the fact that the present Ag atomic species exhibit a molecular feature far beyond the metallic state which is only observable for more bigger metal particles through a conduction electron single signal.

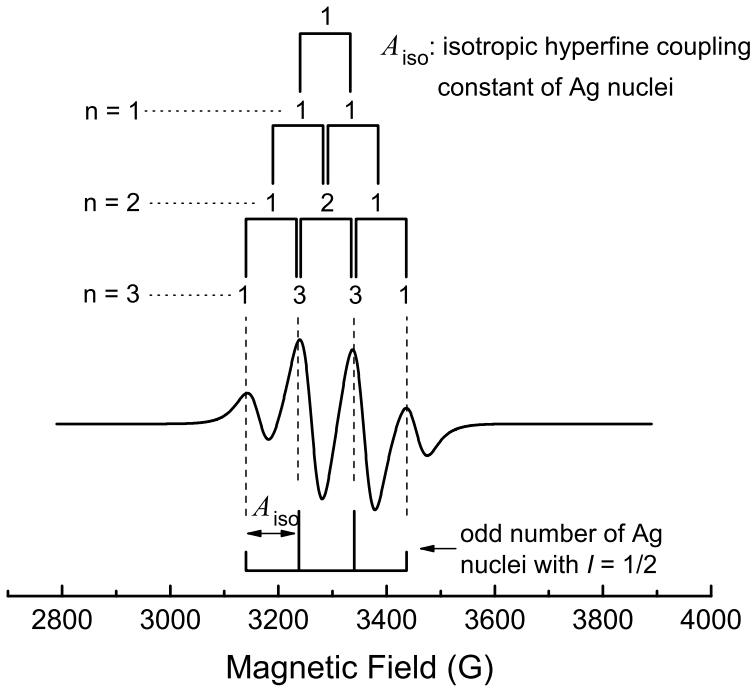

Figure 4.3: Upper part: A schematic drawing for the hyperfine splitting due to n equivalent Ag nuclei with $I = 1/2$. The hyperfine interactions with coupling constant of A_{iso}^{Ag} are taken as first-order perturbations. Lower part: The numerical spectrum simulation for the Ag_3^{n+} cluster in 9% (wt.) Ag/NaA after H_2 reduction at 298 K based on spin Hamiltonian parameters given in the text and the stick spectrum for the corresponding hyperfine splitting.

The X-band quartet EPR spectrum of hydrogen reduced 9% (wt.) Ag/NaA recorded at 70 K is illustrated in Figure 4.3 which is assigned to a triatomic Ag cluster. Some extra structure is likely due to a superposition with a second species and makes the spectrum somewhat difficult to analyze. However, the hyperfine spectrum of the reduced Ag_3^{n+} clusters remained essentially unchanged from 4.0 K to 160 K with very little g or hyperfine anisotropy. The cluster preserves the equivalence of the silver nuclei without distortions in the structure. This excludes the possibility that the spectrum is due to

alternative structures with three equivalent nuclei.

The main feature can be simulated with isotropic spin Hamiltonian parameters, g_{iso} = 2.044 and three equivalent silver nuclei with A_{iso} = 97.3 G. A similar signal with very similar EPR parameters had been observed previously and assigned to a Ag_3^0 cluster in γ-irradiated Ag/NaA [17], located inside the β-cage, but the signal intensity was relatively low at 77 K. The Hamiltonian parameters are isotropic within the uncertainty given by the linewidth and lead to the conclusion that all Ag nuclei of the hydrogen reduced triatomic silver cluster are close to equivalent. The g value is higher than g_e, which reveals that the spin density is mainly located on the silver nuclei and not on the light nuclei in the environment. The delocalized atomic 5*s*-orbitals of cluster Ag atoms partially contribute to the spin density populations. The silver hyperfine interaction of A_{iso} = 97.3 G corresponds to Ag 5*s* spin density populations of ca. 13.9% per nucleus or 41.7% in total. Any anisotropy of the hyperfine interaction is hidden in the line width and amounts to 25 G at maximum. Based on similar reasons as given above for Ag^0 a dipolar contribution of this order can account for the remaining 58.3% of the unpaired electron spin.

Principally, also the Ag_3^{2+} cluster is paramagnetic and can have a linear, bent, or triangular structure. The anisotropic signal of triangular $^{109}Ag_3^{2+}$ was observed in the isotope enriched ^{109}Ag/NaA after X-ray irradiation at 77 K, and the slight deviation from isotropic symmetry was characterized by the spin Hamiltonian parameters $g_{\parallel}$ = 1.958 and $g_{\perp}$ = 1.981 coaxial with $A_{\parallel}$ = 200 G and $A_{\perp}$ = 205 G at 250 K [136]. The relatively large hyperfine interaction led to second order hyperfine splitting. An isotropic signal of an equilateral triangular Ag_3^{2+} cluster exhibiting g_{iso} = 1.9803 was observed in Ag/NaA on γ-irradiation at 77 K [9]. The resolved Ag hyperfine interaction showed separate contributions from the two silver isotopes, i.e. $A_{iso}^{^{107}Ag}$ = 200 G and $A_{iso}^{^{109}Ag}$ = 230 G corresponding to almost the same probabilities in natural abundance, of the same I = 1/2 nuclear spin. A pair of the hyperfine quadruplet was separated by ca. 650 G in the low and high field regions, while the inner lines of unit intensity yielded parameters for $^{107}Ag_3^{2+}$, the outermost lines belonged to the $^{109}Ag_3^{2+}$ cluster [9]. Further, a triangular Ag_3^{2+} cluster exhibiting EPR parameters of g = 1.9722 and A = 208 G was also stabilized in Ag_1/NaA on hydrogen reduction at 295 K followed by γ-irradiation at 77 K [17]. This cluster must be located in the α-cage since it decayed immediately in the presence of O_2. Nevertheless, the cluster signal overlapped with several different hyperfine structures. It can therefore be concluded that the hyperfine splitting of Ag_3^{2+} clusters varies to some extent, but it is a factor of two larger than for the neutral species. The negative deviation of the experimental g tensor from g_e is a further peculiarity of the Ag_3^{2+} cluster [9, 17, 136] that contrasts the positive deviation of the hydrogen reduced neutral triatomic cluster with (g_{iso} = 2.044).

The silver atom which as a free species is of spherical symmetry shows strong axiality. This can plausibly be understood by the interaction with the host zeolite. Interestingly and in strong contrast, the triatomic cluster which for equivalent atoms can only assume the planar geometry of an equilateral triangle that is of clear axial symmetry shows a nearly isotropic spectrum. Fast isotropic rotation would average out anisotropies, but it is not likely that such motion persists down to 20 K.

Hydrogen reduced 12% (wt.) Ag/NaA zeolites were used to test the performance of the cylindrical TE_{011}-mode microwave resonator designed for the home-built pulse Q-band EPR spectroscopy and all experiments were performed at 7 K. Figure 4.4 shows the pulse Q-band field-sweep ESE absorption spectrum and the first derivative spec-

trum. The nearly symmetric quintet spectrum indicates a high symmetry of the observed species and arises from the reduced Ag cluster species formed in 12% (wt.) Ag/NaA, apparently at very low concentrations. The observed hyperfine multiplet is assigned to the interaction of the unpaired electron with four equivalent silver nuclei of $I = 1/2$ in the reduced Ag_4^{n+} cluster. The hyperfine splitting of the silver isotopes is not observed

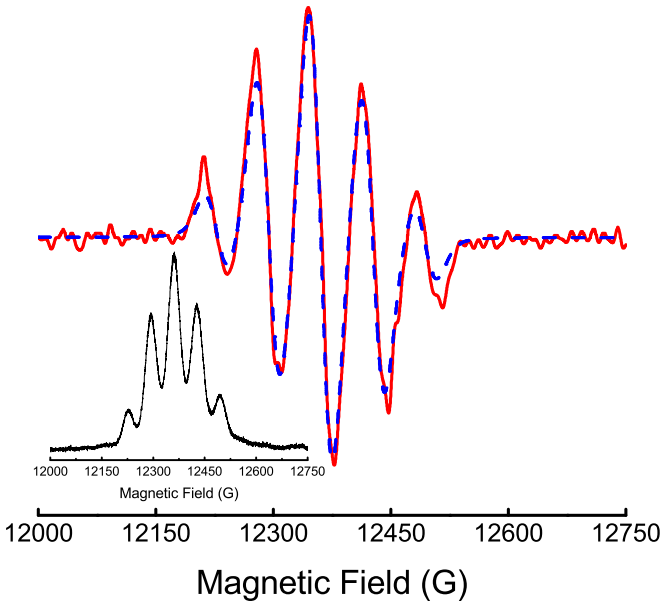

Figure 4.4: The first derivative of the experimental Q-band field-sweep ESE spectrum (solid line) of the reduced Ag_4^{n+} cluster in 12% (wt.) Ag/NaA zeolite is plotted after the 32-point FFT smoothing and the corresponding numerical simulation (dashed line) based upon the parameters given in the context. In the inset, the pulse Q-band field-sweep ESE absorption spectrum is recorded with the pulse sequence $\pi/2 - \tau - \pi$ with the parameters $t_{\pi/2} = 20$ ns, $t_\pi = 40$ ns and τ = 200 ns. The mw frequency was set to 35.009 GHz. The spectrum was recorded at 7 K with 100 averaged transients per point.

due to the small differences between their coupling constants relative to the linewidth. This cluster exhibits the isotropic hyperfine coupling of A_{iso}^{Ag} = 67.5 G which will be compared with an average atomic value of 702 G of the silver ^{107}Ag and ^{109}Ag isotopes. Thus, the 5*s* orbital contribution is of $\approx$ 10% per Ag nucleus or 40% for all Ag nuclei together on the basis of equal distribution of the electron spin density at each nucleus. The hyperfine spectrum is centered at $g_{iso} = 2.023$ which is slightly higher than the free electron g_e value. It implies that there is a significant *d* orbital contribution of the transition metal to the spin density distribution [80]. The numerical spectrum simulation was performed applying the experimental spin Hamiltonian parameters for four equivalent nuclei which is shown in Figure 4.4. The symmetry of the isotropic hyperfine A tensor and g_{iso} might depend on the symmetry of the cluster accommodating cage so that it provides an identical electronic surrounding. For instance, the β-cage possesses an inner symmetry of an octahedron, whereas the whole symmetry is cubic for the unit cell of

NaA [48].

Less well known is the fact that no reduced Ag_4^{n+} cluster was previously observed in Ag/NaA. It is worth noting that the most successful works were performed on stabilizations of paramagnetic Ag_4^{n+} clusters (usually Ag_4^{3+}) in Ag-rho and Ag-SAPO molecular sieves [137, 138, 139, 140]. It was found that the most successful support is the Ag-rho zeolite dehydrated at 773 K for the silver cluster formation. By hydrogen reduction a well-resolved five-line multiplet with $g_{iso} = 1.973$ exhibited an isotropic hyperfine coupling of $A_{iso} = 140$ G. With this multiplet extra structures were observed at 77 K, and these signals with $g = 2.004$ and $g = 1.950$ were assigned to the conduction electron signals of the larger metal Ag particles [137]. Interestingly, the cluster and all conduction electron signals disappeared completely on re-oxidation at 673 K and reappeared on hydrogen reduction. This supports the fact that this reduced Ag_4^{n+} cluster was located in the relatively bigger cages of Ag-rho than the β-cage (e.g. in Ag/NaA), since there was no hindrance for chemisorption or gas treatment with O_2 and H_2. In the case of Ag/NaA, for instance, the O_2 molecule cannot penetrate through the six-membered rings into the β-cages (sodalite cages), while the H_2 molecule can [141]. For these gases it basically depends on gas kinetic diameters which are dependent on temperatures [15]. Furthermore, the γ-irradiation induced Ag_4^{n+} clusters were bound to weak ligand molecules in the surroundings, e.g. D_2O, CH_3OH, and CD_3OH molecules, as observed in Ag-rho and Ag-SAPO in the broad range of temperatures of 110 K to 370 K [138, 139]. The cluster hyperfine splitting provided the EPR parameters of $g_{iso} = 1.973$ and $A_{iso} = 139$ G. The experimental g_{iso} was less than the free electron g_e value ($g_e > g_{iso}$), and this is rather peculiar. The negative deviation of the g tensor from the free electron g_e value is basically expected for the paramagnetic system in strong crystal-field surroundings [79]. Furthermore, in the presence of NH_3 molecules the formed Ag_4^{3+} cluster exhibited a smaller isotropic hyperfine coupling of $A_{iso} = 109$ G with nearly the same $g_{iso} = 1.967$ [138]. It is therefore assumed that our reduced Ag_4^{n+} cluster has a quite different surrounding than those silver clusters stabilized in Ag-rho and Ag-SAPO zeolites, specially no water ligands, since it was dehydrated at 673 K overnight.

Spin echoes can basically be produced in response to a suitable resonant microwave pulse sequence in the magnetic resonance experiments. The pulse sequences reorient the magnetic dipoles, which will be responsible for transverse magnetization of the electron spin system. The rephasing of the magnetic dipoles to reform macroscopic magnetic moments constitutes the spin echo [28]. The pulse sequence $\pi/2 - \tau - \pi$ is applied here, and the time τ between the two pulses is varied, thereby tracing out the echo amplitude, and a decay envelope may be modulated due to the weak electron-nuclear hyperfine interaction. In disordered system, an average structure of the system can be determined by a spherical analysis of the ESEM pattern which normally involves the nearest magnetic nuclei surrounding the paramagnetic species [142, 143]. If there is a small overlap of the unpaired wave function on the closest nuclei, the coupling will reveal the isotropic hyperfine coupling, A_{iso}. Currently, the reduced Ag_4^{n+} cluster exhibited the isotropic hyperfine coupling $A_{iso}^{Ag} = 67.5$ G and the weak echo signal could be observed only at low temperature of 7.0 K. By setting the magnetic field at the position of 12361 G, which nearly matches g_{iso} of the reduced Ag_4^{n+} cluster, weak electron spin echoes were observed, exhibiting a small modulation due to much weaker interaction with the lattice, i.e. ^{27}Al nuclei. It means that the more central location inside the β-cage is preferred for the reduced silver clusters on account of an identical charge distribution along the framework. The applied pulse sequence was $t_{\pi/2} = 20$, $t_\pi = 40$ ns

and the delay between pulses τ = 200 ns, however, no attenuation of the output power of the bridge was applied. The repetition rate of the sequences was set to 1 KHz, and 100 transients averaged per field point were necessary to record the spectrum with an acceptable signal-to-noise (S/N) ratio. Even at 7 K the longitudinal relaxation time (T_1) of the center line was measured to be about 540 ns which is apparently less than the transverse relaxation time (T_2 = 624 ns) and is a rather rare case (spectra not shown). T_2 is an estimate of the mutual spin (S_1) spin (S_2) flips. The decay time constant, i.e. $T_m \equiv T_2$, includes contributions from all processes that take spins off resonance - small amplitude vibrations, rotations, and nuclear spin flips. It implies that the nuclear spin flips are rather plausible, whereas the silver cluster to rotate freely is unlikely because all the measurements were performed at very low temperature, ca. 7.0 K.

4.1.3 EPR of the Ag_6^+ cluster in Ag/NaA

The X-band EPR spectrum of the hydrogen reduced 12% (wt.) Ag/NaA is illustrated in Figure 4.5. All the measurements were performed at 20 K. A typical iron signal is

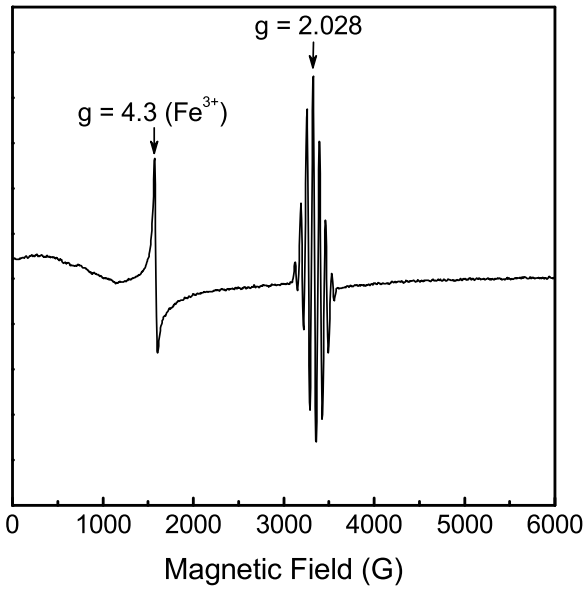

Figure 4.5: X-band EPR spectrum of the hydrogen reduced 12% (wt.) Ag/NaA recorded at 20 K, a signal at g = 2.028 representing the reduced Ag_6^+ cluster and a signal at g = 4.3 arising from the well-known iron Fe^{3+} center (or an impurity) in the zeolite lattice.

centered at g = 4.3, representing a framework Fe^{3+} site or impurity substituting either silicon or aluminium in the zeolite lattice [144, 145, 146] which also might have additional components around $g \approx 2.0$. In more detail, other signals of iron ions will appear at $g \approx 2.0$ and $g \approx 2.3$ [144], if the content of impurity is high enough, e.g. when introduced by the synthesis of the zeolite. These isolated iron ions basically occupy the exchangeable sites or are bound to weak ligands (e.g. water molecules) in the cages, respectively. Hyperfine information around g = 2.0 of all other iron signals is suppressed by the exchange with silver. The signal at g = 4.3 completely withstands the aqueous

ion-exchange.

A characteristic hyperfine structure is well resolved and assigned to a signal of the reduced Ag_6^+ cluster. The seven-line splitting with $g_{iso} = 2.028$ is due to the hyperfine coupling constant (A^{Ag}) of the silver nuclei. The isotropic g_{iso} is higher than the free electron g_e value, which normally indicates admixture of a transition metal *d*-orbital into spin density distribution [80]. In a simple picture, a hole in the 4*d*-shell implies a cluster charge that exceeds +6. More likely is a significant admixture of *d* atomic orbitals in the molecular cluster orbital containing the unpaired electron, or an angular momentum of the half-filled molecular orbital. For an even number of equivalent Ag (*I*

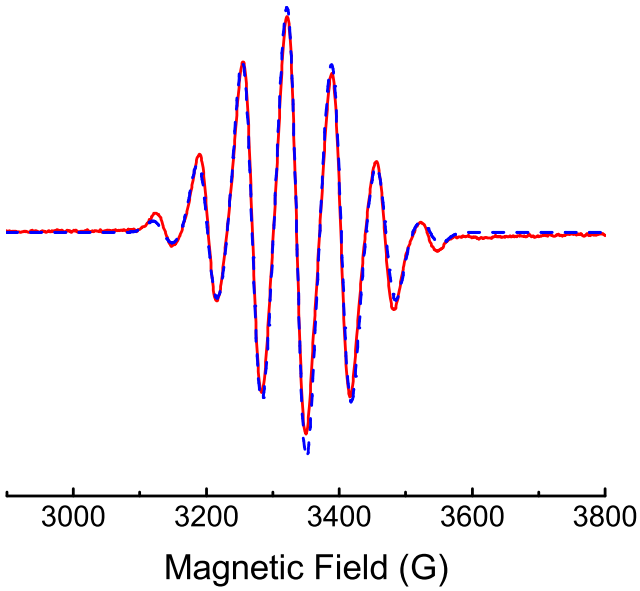

Figure 4.6: X-band EPR spectrum of the Ag_6^+ cluster after H_2 reduction at 278 K for 20 minutes (solid line) recorded at 20 K, and the corresponding numerical spectrum simulation (dashed line) based on the experimental hyperfine parameters of 6 equivalent Ag nuclei. The simulation is taking into account the statistical distribution of Ag isotopes.

= 1/2) nuclei, there is an odd number of lines with a most intense central peak, which are equally separated by isotropic hyperfine coupling constant A_{iso}^{Ag}. It is thus assumed that the unpaired spin density is delocalized equally over all Ag nuclei of the cluster, which leads to an identical and isotropic hyperfine coupling with all nuclei. It implies that there are allowed transitions $\Delta m_S = \pm 1$ between m_S = - 1/2 and m_S = + 1/2 states of the electron spin angular momentum. For noble metal clusters, the electronic structure is dominated by the number of valence electrons that are delocalized [7]. Since the bulk Ag has the electronic configuration of [Kr]$4d^{10}5s^1$, the paramagnetic property of small Ag clusters derives from the odd-number of 5*s* valence electrons in the open-shell configuration.

The observed multiplet must be explained as a superposition of spectra of clusters with statistical distribution of Ag isotopes. The statistical isotope distribution deter-

mines mainly the linewidth. The isotopes ^{107}Ag and ^{109}Ag have $I = 1/2$ spins and possess almost the identical abundance (51.839% and 48.161%). ^{109}Ag has a nuclear magnetic moment that is 15% larger than that of ^{107}Ag, and at the given spectral resolution the difference in magnetic moment is negligible. In the experiment the difference is not resolved but contributes to the linewidth. The experimental A_{iso} = 67.0 G is to be compared with an average atomic value of 702 G of the ^{107}Ag and ^{109}Ag isotopes. Thus, the 5*s* orbital contribution to the spin density is about 10% per Ag nucleus or 60% for all Ag nuclei together. It is well known from the free-electron approximation that if the size of clusters is small, there is a possibility of a partial fraction of the *s* orbital radial $|\psi_0(0)|^2$ wavefunction to remain outside of a quantum sphere or wall [4], leading to a significant missing fraction of the total spin density. The numerical spectrum simulation was performed applying the experimental spin Hamiltonian parameters for six equivalent nuclei which is shown in Figure 4.6. The simulation results were the same for the D_2 reduced cluster sample. This means that there is no significant spin density on hydrogen. Furthermore, the characteristic hyperfine structure of supported Ag_6^+ clusters remains well-resolved at 200 K and is still observable at room temperature. It should be noted that very little *g* or hyperfine anisotropy is present. This essentially excludes that the spectrum is due to alternative structures with six equivalent atoms, e.g. a planar hexagon. It is supposed to preserve the equivalence of the Ag nuclei without distortions in the cluster structure.

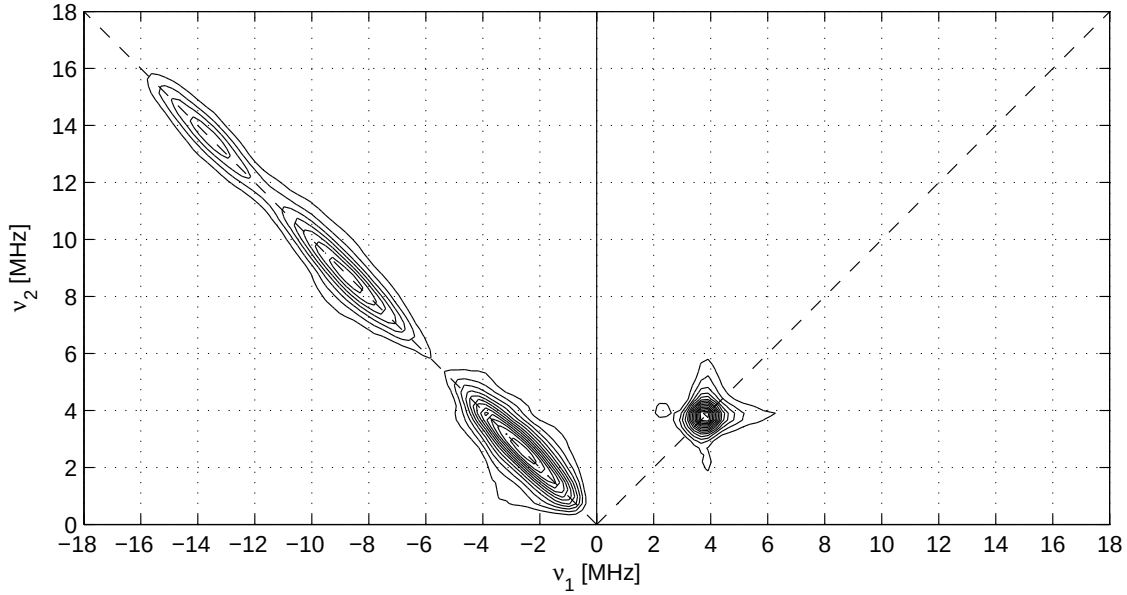

Figure 4.7: X-band HYSCORE spectrum of the reduced Ag_6^+ cluster in 12% (wt.) Ag/NaA was recorded at an observer position of 3480 G (348 mT) and at 10 K. The signal at frequency of 3.90 MHz represents distant ^{27}Al framework nuclei. (Spectra were provided by PD Dr. R.-A. Eichel at the Eduard-Zintl-Institute, Darmstadt University of Technology.)

The double integral of the EPR signal is directly proportional to the number of unpaired spins in a sample. Calibration with a standard sample (ultramarine blue was used in this case) and assuming $S = 1/2$ yields a value of 4.8×10^{16} spin g^{-1}, which accounts for only 0.0435% of all silver atoms in the sample. The loading of 12% (wt.)

corresponds to one Ag_6^+ cluster per 3 unit cells of Ag/NaA zeolite on average. The reduced Ag_6^+ cluster is assumed to reside inside the β-cage, since it was previously reported that even a much bigger Ag cluster, i.e. the reduced $Ag_6^+ \cdot 8Ag^+$ cluster, was observed by X-band EPR spectroscopy at 77 K in the β-cage of Ag_{12}/NaA zeolite [10]. This also means that most of the silver is EPR silent, i.e. diamagnetic or unobservable high spin states, and magnetism of the cluster will be discussed in the next chapter.

The HYSCORE spectrum of the reduced Ag_6^+ cluster was recorded at an observer position of 3480 G (348 mT) and at 10 K which is illustrated in Figure 4.7. The spectrum shows a single diagonal peak at 3.90 MHz which is consistent with the nuclear Larmor frequency of ν_{Al} = 3.89 MHz (see $(+,+)$ quadrant). It therefore basically represents distant ^{27}Al framework nuclei, and the presence of the aluminum "*matrix peak*" confirms the close proximity of the zeolite lattice to the silver cluster. It reveals a small isotropic hyperfine coupling of 1.3 MHz that is proportional to a partial spin density population of 3.32×10^{-4} on a ^{27}Al nucleus. Furthermore, there is no proton hyperfine coupling resolved experimentally, its nuclear Larmor frequency would normally be equal to ν_H = 14.2 MHz (see Figure 4.7) in the weak coupling $(+,+)$ quadrant.

On the other hand, it is impossible to consider that the hyperfine interaction arises from ^{23}Na nuclei, which is fundamentally excluded, because any well-resolved hyperfine splitting has not been observed in the silver-free NaA. The spectrum of the paramagnetic Ag_6^+ cluster appears only in the Ag^+ exchanged 12% (wt.) Ag/NaA sample after appropriate oxidation, dehydration treatments at 673 K and hydrogen reduction at room temperature. It is very sensitive to the duration of hydrogen reduction.

Furthermore, hydrogen isotope exchange on the reduced Ag_6^+ cluster was performed at room temperature by filling D_2 with 500 mbar into the cluster containing sample in the EPR quartz tube. The sample was kept under partial pressure of D_2 for 20 minutes. There were no observable changes, neither in the hyperfine splitting nor in the EPR parameters of the silver clusters by further isotope exchange reactions. Only a very slight difference was discernible that the baseline of the first-derivative signal drifted around $\approx$ 3600 G at a high magnetic field region that leads to observable but very small asymmetry of the hyperfine spectrum intensity (spectrum not shown). It means that the partially reduced Ag clusters contribute to the observability by EPR. By consecutive H/D exchange reactions, the other diamagnetic silver clusters located in the different environments are probably converted into the paramagnetic clusters, thus contributing to the EPR signals.

Moreover, continuous wave EPR experiments were performed on the deuterium desorption from the deuterium reduced Ag_6^+ clusters by evacuating the cluster containing samples at different elevated temperatures. All spectra were recorded at 20 K after evacuations for different time intervals at 383 K, 403 K and 423 K, respectively. The intensities decreased continuously with desorption times, and the highest desorption temperature led to the fastest decrease rate of the EPR signal intensity. This can be related to the deuterium coverage because the signal intensity is lost. The corresponding hyperfine spectra after desorption at 423 K are displayed in Figure 4.8. It is apparent that the silver cluster is mostly still intact and all the Ag atoms remain close to equivalent during the desorption. At room temperature the re-adsorption of D_2 gas with 500 mbar for 20 minutes restores the cluster hyperfine signal to almost the same intensity it had before the desorption. The numerical spectrum simulation was performed based upon coaxial g and A tensors, and the fit with 6 equivalent Ag provides rather a perfect match for the intensity distribution of the Ag_6^+ cluster multiplet after re-adsorption of D_2 in spite of a

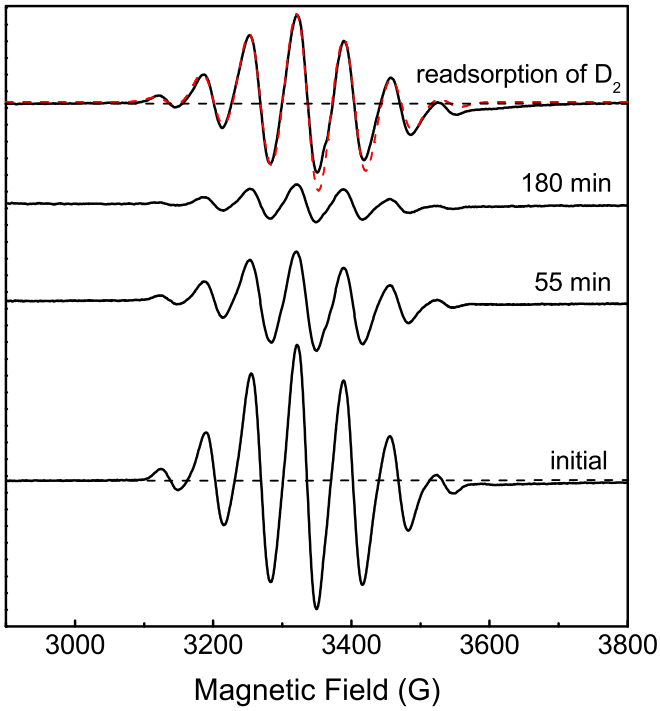

Figure 4.8: X-band EPR spectra of the deuterium reduced Ag_6^+ cluster after D_2 desorption at 423 K for different time intervals. All the spectra were recorded at 20 K, and there were no changes in the hyperfine splitting patterns, while the signal intensities continuously decreased. By re-adsorbing D_2 for 20 minutes at room temperature there is a discernible baseline drift at 3600 G. The spectrum of re-adsorption is with its corresponding simulation, and the parameters are found in context.

very slight mismatch around 3600 G due to a baseline drift which is shown in the upper part of Figure 4.8. The simulation necessitated accommodating a negligible or very slight anisotropy for both g and A tensors, i.e. $g_{\|} = 2.0271$; $g_{\perp} = 2.0281$ and $A_{\|} = 67.5$ G; $A_{\perp} = 68.0$ G, for reproducing of the hyperfine splitting spectrum, even though a deviation from isotropy is much too small. It might imply that the other silver clusters exist in the different surroundings with slightly different hyperfine parameters. In other words, when deuterium desorbs more easily from the first few clusters, they convert subsequently into the diamagnetic ones, while the other diamagnetic silver clusters in the different environments convert into the paramagnetic ones, since the EPR signal does not disappear by desorption of the deuterium molecules. Therefore, the numbers of the paramagnetic silver clusters are always calibrated somehow on average.

The signal intensity decay curves at different desorption temperatures are displayed as a function of different desorption time intervals in Figure 4.9(a), and the function of $I = \mathrm{A}_0 \cdot \exp(-\frac{t}{t_0})$ was applied to fit the experimental intensity decreases. I is the intensity which is a function of time t, and $1/t_0$ is the corresponding rate constant of the desorption dynamics, and the A_0 is a pre-exponential factor. All the fitting parameters

Table 4.1: The fit parameters for the signal intensity decay in Figure 4.9(a).

T^{-1} (K^{-1})	2.608×10^{-3}	2.478×10^{-3}	2.361×10^{-3}
$\ln(k/\mathrm{min}^{-1})$	6.8(0.1)	5.6(0.3)	4.5(0.3)

are tabulated in Table 4.1. The first-order rate constant can be expressed via

$$k = \mathrm{A}_0 \cdot \exp(-\frac{E_\mathrm{a}}{R_0 T}) \tag{4.2}$$

where A_0 is a constant, E_a is the activation energy or barrier, and R_0 is the gas constant that is equal to 8.31441 K^{-1} J mol^{-1}. The the corresponding first-order rate constant is considered to be proportional to the reciprocal time, i.e. $k \propto t_0^{-1}$, and by replacing it in Equation (4.2) and taking the natural logarithm it will lead to the following equation.

$$\ln\frac{1}{k} = \frac{E_\mathrm{a}}{R_0} \cdot \frac{1}{T} - \ln \mathrm{A}_0 \tag{4.3}$$

By applying Equation (4.3) the deuterium desorption energy $E_\mathrm{a} = 0.78$ eV at the Ag_6^+ clusters can be derived from the slope of the Arrhenius plot in Figure 4.9(b). Furthermore, the molecular deuterium desorption energy of 0.78 eV (75.26 kJ mol^{-1}) is obviously higher than the corresponding experimental value of 0.38 eV (36.4 kJ mol^{-1} or 8.70 kcal mol^{-1}) found for the desorption from the Ag(111) single crystal surface [147]. The reported lower experimental energy suggested the low Ag-H bonding energy which is a characteristic of noble metals compared to transition metals and has been interpreted to being due to the completely filled $4d^{10}$ band in noble metals [148]. In the case of the reduced Ag_6^+ cluster, the observed difference in the desorption energy may reveal the presence of size effects. Here the coordination number of the surface Ag atoms is ≈ 4.7 on average, if it has an octahedral symmetry, which is clearly less than that of the bulk Ag(111) crystal surface. This is compatible with that the atoms of smaller clusters possess a low coordination number which have a general tendency to saturate the coordination sphere and to form more stronger bonds. The coordination effect of the reduced Ag clusters will be discussed in the next chapter, because these clusters are considered well-isolated in the support pores.

It is quite interesting and also peculiar that hydrogen desorption from the hydrogen reduced Ag_6^+ clusters simply does not follow the continuous decrease of the hyperfine signal intensities at different elevated temperatures, especially at lower temperatures of 383 K and 403 K. Instead, it leads to oscillations of the signal intensity on heating, e.g. a decrease and increase in the signal amplitudes, for different time intervals. It strongly indicates that the diamagnetic clusters are converted into paramagnetic clusters on hydrogen desorption so that it contributes to the EPR signal, while leading to oscillations. However, on continuous desorption at different temperatures there are no other states for both hydrogen and deuterium reduced Ag_6^+ clusters, e.g. high spin states, since no other new hyperfine splitting develops as the cluster signal intensity has dimin-

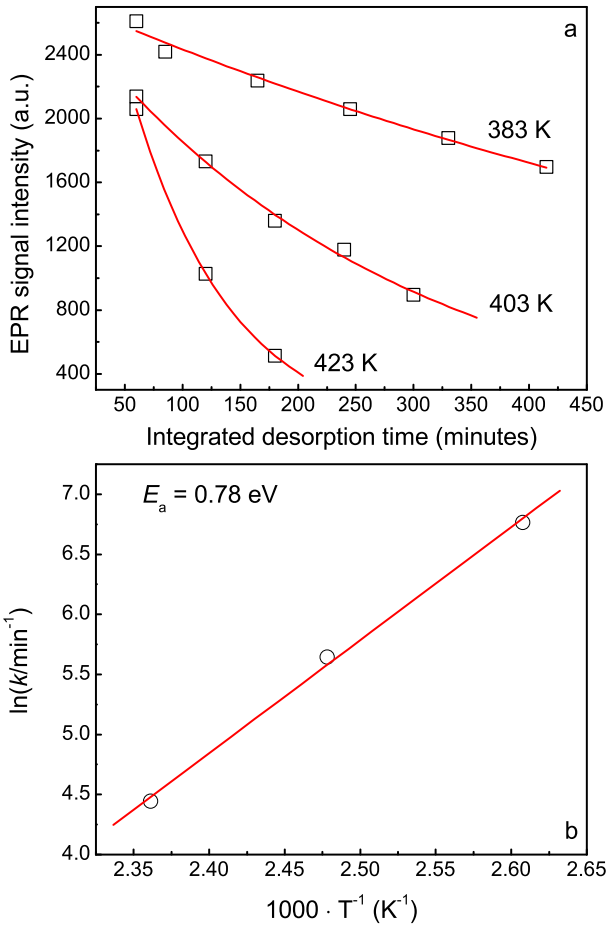

Figure 4.9: a) EPR signal intensity decrease as a function of desorption time at different temperatures. b) Arrhenius plot of the relative rate constants for D_2 desorption.

ished with time. Integer spin systems are commonly EPR silent at the conventional low frequency of X-band whereby they are being accompanied by half-field ($\Delta m_S = \pm 2$) transitions or transitions of higher order, if they are indeed present. Therefore, the paramagnetic Ag_6^+ cluster is likely to have $S = 1/2$ state with a positive odd charge. Since the ratio of Si/Al is equal 1, the silica-alumina framework contains a negative charge per Al atom due to electron deficiency in the aluminum-oxide site which can be compensated by a positive charge of the reduced silver cluster instead the extra-framework cation, Na^+.

4.2 Summary

No paramagnetic cluster species is found in Ag/NaY after appropriate treatments with hydrogen reduction. The oxidized silver clusters are completely EPR inactive, and only hydrogen or deuterium reduction unambiguously leads to the formation of paramagnetic silver clusters in Ag/NaA, even though only a small fraction of ion exchanged

silver is deposited on the support.

When applying continuous wave EPR, the formation of atomic Ag and a single, well-defined Ag_3^{n+} cluster was observed for the first time in hydrogen reduced 6% and 9% (wt.) Ag/NaA, respectively. The formed triatomic silver cluster is relatively stable in a broad range of temperatures, ca. 20 K - 160 K. Atomic clusters exhibit hyperfine anisotropy in contrast to triatomic Ag clusters which are isotropic.

By performing the field-sweep ESE measurements, the reduced Ag_4^{n+} cluster is observed in Ag/Na for the first time. Four atomic Ag clusters are also isotropic with $g_{iso} = 2.023$ and $A_{iso} = 67.5$ G. A significant transverse relaxation time ($T_2 = 624 > T_1 = 540$ ns) has been measured which is probably caused by flip-flop spin exchange relaxations.

Often hydrogen reduction provides a higher signal intensity by a factor of 2.5 than the deuterium reduction, which probably indicates the different uptakes between the hydrogen and deuterium by the Ag_6^+ clusters. It is assumed that there is no significant spin density on the protons in the vicinity of the silver clusters, and only the distant protons can be resolved by HYSCORE, if they are indeed present. However, reduction plays an important role in balancing spin density on the reduced clusters to maintain paramagnetic observability. A temperature activated desorption of D_2 overcomes an activation barrier of $E_a = 0.780$ eV. By comparing with Ag_4^{n+} clusters, the reduced Ag_6^+ clusters are also isotropic with EPR parameters of $g_{iso} = 2.028$ and $A_{iso} = 67$ G, but g_{iso} is higher than that of four atomic clusters. It implies that six atomic clusters have a more contribution from the *d* electron shell or a more strong spin-orbit coupling. Both clusters are observed in the reduced 12% (wt.) Ag/NaA, thus suggesting that different clusters with different nuclearities can be formed by the same treatments in Ag/NaA with the identical metal loading, some of them are paramagnetic, while the others are EPR-silent. Pulse Q-band field-sweep ESE spectroscopy can be more sensitive than continuous wave X-band spectroscopy because of the higher hyperfine and electron Zeeman splitting (*g*) selectivity.

Since not only the hydrogen reduction but also the heat treatments were performed under the same conditions for samples it is concluded that the silver loading affects the cluster nuclearity to some extent.

5 Magnetism of Ag clusters

The magnetic properties study is probably attractive in terms of diverse technical applications. Here the unpaired electron of the reduced Ag_6^+ cluster exhibits a contribution to spin paramagnetism, and static susceptibility due magnetic moment of this cluster will be examined in this chapter. At this stage, the interactions between magnetic moments on each silver atom of the cluster, or with magnetic moments of the surroundings, or non-static magnetism relative to the electron spin dynamics (i.e. ac susceptibility), are ignored. All that remains is therefore just the effective magnetic moments of the isolated silver clusters within the support pores/cages and their interactions with an applied magnetic field. Using such a simplification, a certain number of atoms merely leads to properties like the electronic magnetic susceptibility containing a factor of n on average, and then the number of effective unpaired spins is to be found per silver cluster.

5.1 HR-TEM results

Bright-field micrographs were taken for both of the deuterium and hydrogen reduced Ag clusters in order to determine the size. Although nearly spherical Ag clusters were formed on the nanometer scale, the sizes were inherently inhomogeneous. The D_2 reduced Ag clusters exhibited a size distribution around 8 nm, whereas the H_2 reduced ones were showing statistically much smaller size distributions. It is very interesting to notice that deuterium reduction leads to the core-shell structure (micrographs not shown), which is probably due to oxidation or oxygen atoms of the support. On the contrary, hydrogen reduction did not lead to such a core-shell structure after exactly the same preparations and treatments, and these phenomena remain rather mysterious. High-resolution micrographs indicate that the hydrogen reduced Ag clusters are relatively uniformly dispersed in 12% (wt.) Ag/NaA samples, and most fractions of the clusters are on the order of ≈ 2 nm in the size range which is displayed in Figure 5.1. The size of the reduced silver clusters was initially expected to be < 1 nm according to the pore/cage dimensions of the support, but was later proved to be slightly larger than expected.

It is generally known that HR-TEM is not sensitive enough for determining the cluster size of ≈ 1 nm or below depending upon the Bragg diffraction of the lattice planes relative to the phase of diffracted electron beam [116, 117]. It implies that the relative direction of the symmetry axis of the reduced silver clusters can be either parallel or perpendicular to the electron beam. The latter leads to anomalous contrast features by virtue of the extremely small size [118]. It is also possible that the electron diffractions of the silver clusters and zeolite structure interfere with each other.

It is currently considered that twin boundaries are intensively observed throughout the hydrogen reduced Ag cluster containing 12% (wt.) Ag/NaA samples. The two white arrows in Figure 5.1 represent the twin boundaries in the symmetrical position relative to each other. The formation of twin boundaries where the twin plane forms a boundary between the twinned subunits situated in mirror symmetry to each other

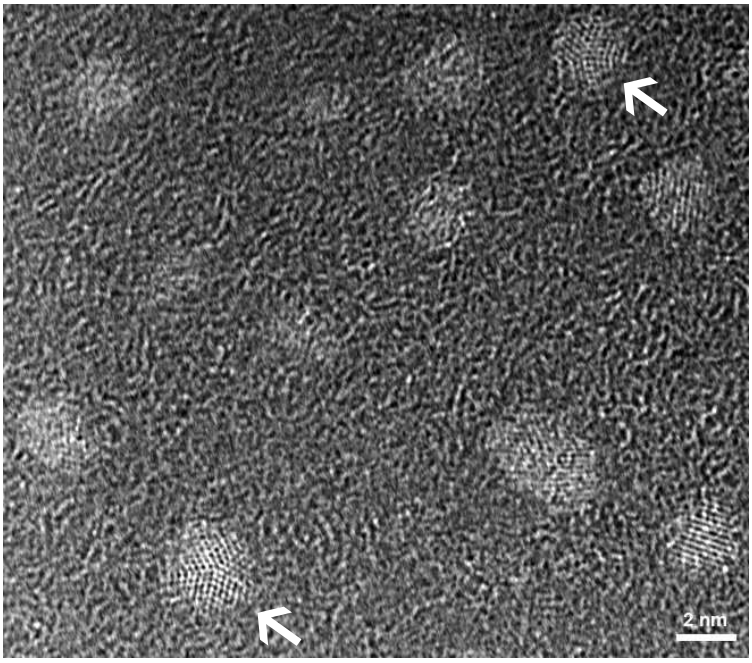

Figure 5.1: HR-TEM micrograph of the hydrogen reduced Ag clusters in 12% (wt.) Ag/NaA. The white arrows indicate the presence of so-called the twin boundaries for the reduced silver clusters on the support. (Measurements were performed by Dr. Lin Gu at the Stuttgart Center for Electron Microscopy in the Max-Planck Institute for Metals Research.)

is a characteristic of the face-centered-cubic (fcc) metal nano-clusters and particles even with smaller sizes of $\approx$ 1 - 5 nm [149]. Furthermore, there was no principal difference between the fabrication methods of silver ion exchange and ion implantation into the soda lime silicate glass supports to observe such a twin boundary configuration of the clusters which can also be dependent on high content of iron oxide in the support [150].

The diffractograms are basically used to confirm the presence of twin boundaries (or configurations) that are the Fourier transform of the corresponding diffraction pattern of the high resolution micrographs. In Figure 5.2, high-resolution electron micrograph embedded with the diffractogram patterns reveals the projection of the [110][1] direction for the individual planes of the hydrogen reduced silver clusters. The [110] direction is the cross product of the $\{200\} \times \{111\}$ equivalent planes which are displayed in Figure 5.2. If one carefully observes each image of the cluster marked by the white arrow in Figure 5.1, the specific structure with the five-fold junctions will probably be discernible. This is a quite interesting feature of the reduced Ag clusters, of course, it further requires more precise searching studies. This section is concerned only with magnetism of silver clusters, and so twin boundary configurations of the structure will not be further discussed. It is however known that the twin boundaries are one of the possible geometrical effects that can modify the magnetic properties of the surface atoms of the small metal clusters due to the induced symmetry changes generated in the vicinity of the twin boundaries [151].

It is ultimately emphasized that the resolution of HR-TEM does not permit determin-

[1] sometimes called zone axis direction

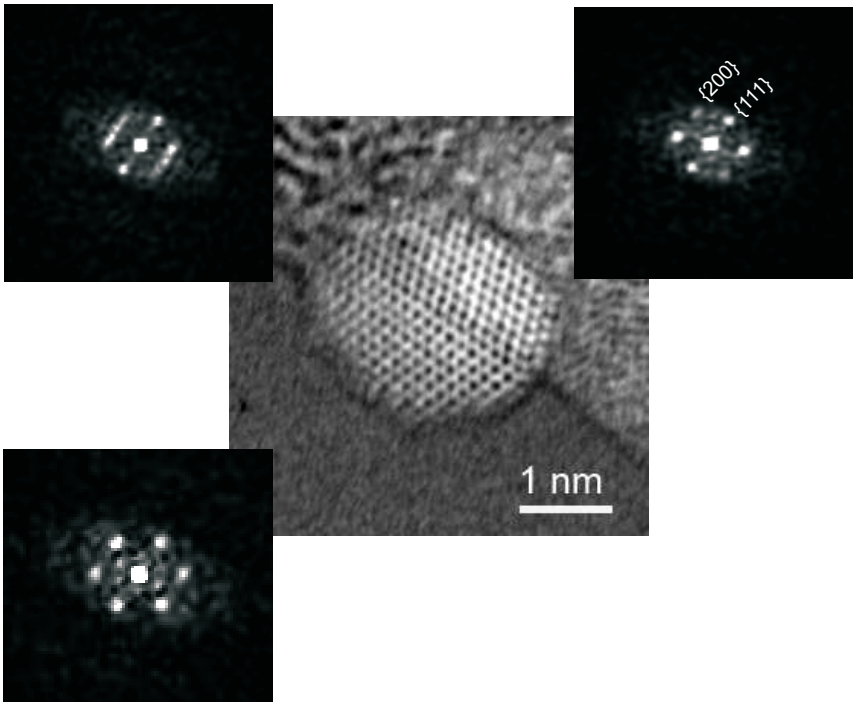

Figure 5.2: HR-TEM micrograph of the hydrogen reduced Ag clusters in 12% (wt.) Ag/NaA embedded with the corresponding diffractogram patterns. The diffractogram reveals the projection of the [110] direction of the planes. The [110] direction is the cross product of the equivalent $\{200\} \times \{111\}$ planes. (Measurements were performed by Dr. Lin Gu at the Stuttgart Center for Electron Microscopy in the Max-Planck Institute for Metals Research.)

ing a more precise and real smallness of reduced silver clusters, ca. < 1 nm, and the observed size distributions are actually reliable on the presence of silver nano-particles onto the support. It implies that the reduced silver clusters can be agglomerated to form the larger silver particles during the TEM measurements. It was previously reported that silver particles tend to accumulate in the surroundings of the **non-irradiated regions**, and the **formation rate** increases by increments of the **electron beam dose** [152]. The reason of an accumulation can be different mechanisms including surface thermodynamics and **electron beam induced ionization**. The latter is more plausible, and TEM measurements were extended by energy dispersive X-ray (EDX) microanalysis. It is thus considered that much bigger silver nano-particles are observable by TEM.

Thus, EXAFS spectroscopy allows determining a more accurate size of reduced clusters by analyzing changes in the absorption fine structure of X-ray photon absorbing silver atoms due to absorption intensity modulating or photon scattering silver atoms in the nearest neighboring shells.

5.2 EXAFS results

X-ray absorption spectroscopy (XAS) offers an excellent potential for estimating the mean size and local structure of the small metal clusters [153, 154]. The highest fraction of the surface atoms implies a low mean coordination number which is accompanied

by a direct consequence of the bond length contraction. This is taken as experimental evidence for the existence of the nano-size effects.

Absorption fine structure spectra for a doubly reduced supported silver sample are illustrated in Figures 5.3(a) and (b), respectively. The oscillatory $\chi(k)$ function is completely different from that of bulk Ag in that it is of much lower amplitude, has a longer wavelength and decreases more rapidly on increasing k values. The significant loss in intensity of $\chi(k)$ is due to the extremely small size of the Ag clusters.

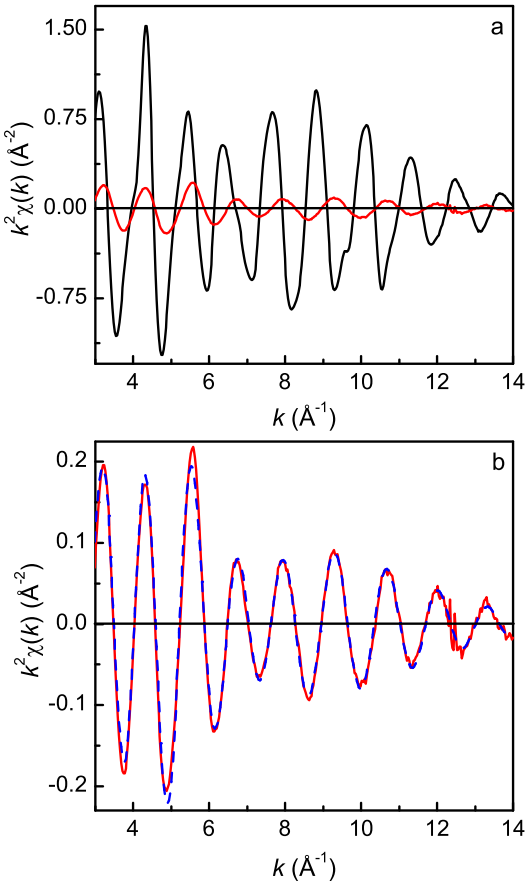

Figure 5.3: EXAFS spectra of the H_2 doubly reduced Ag/NaA sample at an Ag loading of 12% (wt.): a) Comparison of k^2-weighted $\chi(k)$ function (k^2, Δk = 3.0 - 14 Å^{-1}) of the experimental EXAFS data for the clusters (red line) with those of bulk Ag (black line). b) k^2-weighted $\chi(k)$ function (k^2, Δk = 3.0 - 14 Å^{-1}) of experimental EXAFS data (red line) and best fit (blue dashed-line) including the first and second Ag-Ag shell, and a single Ag-O shell. The spectrum (red line) in the entry (a) is enlarged.

Fourier transforms of the isolated $\chi(k)$ function were performed using the k^2-weighting in the k range from 3 to 14 Å^{-1}. The isolated shell contributions are represented as Ag-Ag and Ag-O peaks in the Fourier transform (R-space) at 2.5 and 2.1 Å in Figure 5.4(a) and (b), respectively. Note that no phase or amplitude corrections were performed during the Fourier transform. A heavy scatterer such as Ag experiences a phase-shift by photo-electron scattering that shifts the peak in Fourier space to a lower value of R. This

is clearly seen in Figure 5.4(a) and its Fourier transform.

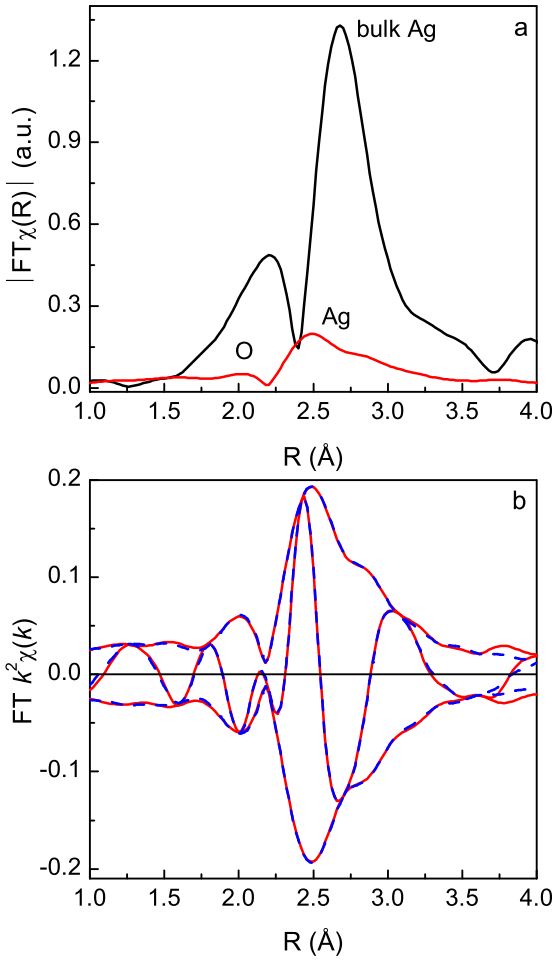

Figure 5.4: EXAFS spectra of the H_2 doubly reduced Ag/NaA sample at an Ag loading of 12% (wt.): a) Comparison of the Fourier transform of k^2-weighted $\chi(R)$ ($1.0 < R < 4$ Å) radial function of experimental EXAFS data for the clusters (red line) with that of bulk Ag (black line). b) Real and imaginary part of Fourier transform of the k^2-weighted $\chi(k)$ function (k^2, Δk = 3.0 - 14 Å^{-1}) of the experimental EXAFS data (red line), and best fit (blue dashed-line) including the first and second Ag-Ag shell, and a single Ag-O shell.

The absorbing Ag atom of the doubly-reduced cluster has an average coordination of $N \approx 3.35 \pm 0.05$ at an average distance of 2.76 Å in the second Ag-Ag shell, while the first Ag-Ag shell at 2.69 Å has $N \approx 0.55 \pm 0.05$ on average. When a second shell of atoms is introduced, the coordination number N of the first shell decreases [154, 155]. This represents a surface reconstruction due to energy minimization of the clusters. It is emphasized that the use of the two-shell model for Ag-Ag contribution improves the fit results significantly. The total Ag-Ag coordination number is 4.00 ± 0.07. All atoms belong to the cluster surface. This makes immediately clear that silver is present quantitatively as small clusters, as any contribution of nano-particles would increase N much closer to its bulk value of 12. A real size of very small silver clusters is therefore

defined extensively by EXAFS measurements, whereas we observe much larger silver nano-particles on the support by HR-TEM measurements as was stated elsewhere (see page 57). A regular 6-atom octahedron should give an overall N of 4.6, since the fifth backscattering atom sits across the body diagonal, ca. 4 Å from the absorbing atom and is thus not contributing to the scattering amplitude in the discussed range. Neutral 6-atomic silver clusters are predicted to be planar triangles of D_{3h} symmetry [56], which leads to an average N of 3. It should be noted that in the same work the most stable structure of neutral Ag_7 is predicted to be a pentagonal bipyramide, which has an average coordination number of 4.3, essentially identical with the above experimental value of 4.20.

The obtained experimental Ag-Ag distance of 2.77 Å on average reveals a contraction of the bond lengths in comparison to bulk Ag (2.889 Å), which is a typical nano-size effect. A separation between HOMO and LUMO increases with decreasing the bond length of small Ag clusters [6]. Furthermore, an oxygen shell is detected at 2.27 Å with a coordination of $N \approx 0.70 \pm 0.05$. These may be from the zeolite framework to which the cluster is loosely attached.

The Debye-Waller factor ($\Delta\sigma^2$) and the coordination number (N) are highly correlated in a fit. All structural parameters obtained from the three-shell model are summarized in Table 5.1.

In order to check a proper set of parameters, the fits to the real and imaginary parts of the k^1- and k^3-weighted Fourier transforms are compared, with the contributions consisting of the Ag-Ag and the Ag-O shells isolated in the range $1 < R < 4$ Å (see Figure 5.5(a) and (b)). The k^3-weighted data enhance the sensitivity for the heavy scatterers. The real part of the Fourier transform is dependent on N and disorder, while the imaginary part is extremely sensitive to the inter-atomic Ag-Ag distance and therefore used to judge the quality of a fit [103]. The k^3-weighted Fourier transform of the oscillatory $\chi(k)$ function of the reduced Ag cluster in Ag/NaA is almost symmetric, which is a strong indication of larger contributions by overlapping Ag-Ag shells. The appearance of multiple satellite peaks in the Fourier transform would describe a single absorbing backscattering pair. This is therefore excluded for the present Ag clusters.

For comparison with the doubly reduced sample Figure 5.5(b) shows the best fit of the Fourier transform of data after a single reduction process. The silver has an average Ag-Ag coordination of $N \approx 3.50 \pm 0.05$ at an average distance of 2.77 Å in the second shell, and $N \approx 0.40 \pm 0.05$ at a distance of 2.69 Å in the first shell. The coordination by oxygen is $N \approx 1.60 \pm 0.05$ at 2.22 Å, more than double of what it is after an additional reduction step. It thus seems that the cluster is indeed incompletely reduced. The agglomeration of the cluster is either incomplete, or less spherical, or the oxygen is partly interspersed between the silver atoms. The theoretical fit matches nicely the imaginary and real parts of the Fourier transform, though a small asymmetry of the spectrum is induced by the presence of a light back-scatterer below 1.6 Å in R-space in Figure 5.5(a), perhaps O atoms of the support. Furthermore, the root mean-square displacement ($\Delta\sigma^2 = 0.012$) is relatively large and may be taken as evidence of structural disorder or temperature activated fluctuations because all measurements were carried out at room temperature.

Upon evacuating the samples, there were no significant changes in the structural parameters of the silver clusters. All the bond lengths in the first- and second Ag-Ag shells are given with the experimental errors, which have a general tendency to decrease, while the edge energy increases slightly (see Table 5.1). This indicates the edge energy is slightly *blueshifted*.

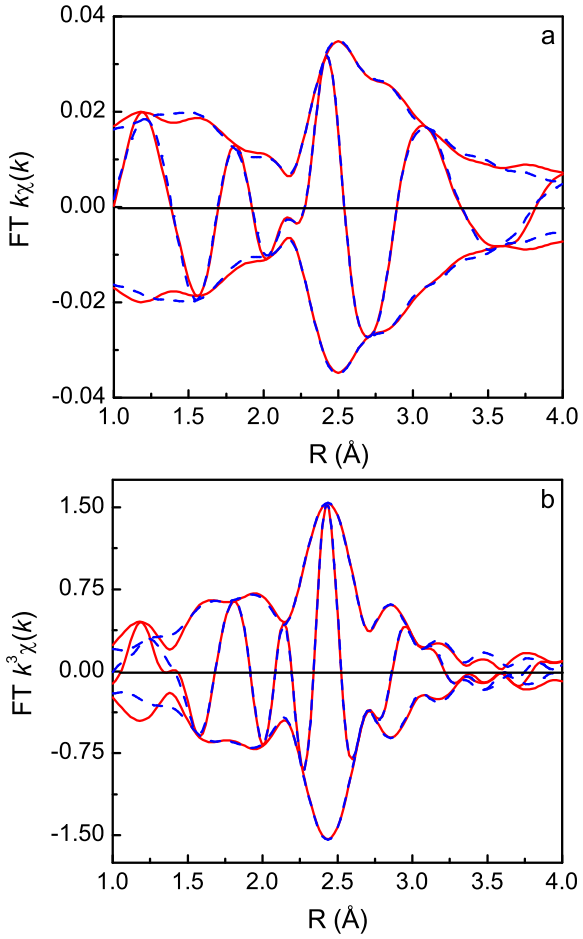

Figure 5.5: EXAFS spectra of the H_2 reduced silver sample: Fourier transform of a) k^1-weighted and b) k^3-weighted $\chi(k)$ function (k^1 and k^3, Δk = 3.0 - 14 $Å^{-1}$) of experimental EXAFS data (red line) with the corresponding fit (blue dashed-line) including the first and second Ag-Ag shell, and a single Ag-O shell.

5.3 EPR results

Paramagnetic observability of the reduced silver clusters implies that there is an odd number of electrons per cluster. In detail, if the number of even-electron clusters and the number of odd-electron clusters are about the same in a sample, the total measured electron magnetic susceptibility will be dominated by effects of odd-electron clusters, if they are indeed present [5]. This is the characteristic of the *quantum size effect*.

The double integrated intensity of the first derivative EPR signal is directly proportional to the number of unpaired electron spins in a sample, thereby reflecting the electron magnetic susceptibility and magnetization. The temperature dependence of the susceptibility had been studied carefully as a function of temperature, exhibiting convincing evidence for the odd-number of the electrons per silver cluster. Figure 5.6 is to represent the susceptibility of the reduced Ag_6^+ cluster in 12% (wt.) Ag/NaA as a function of temperatures. It is assumed that the integrated intensity is proportional to

the Pauli susceptibility, and the paramagnetism arises from the unpaired 5*s* electrons of the reduced silver clusters. Both the zero-field cooling and field cooling (not shown)

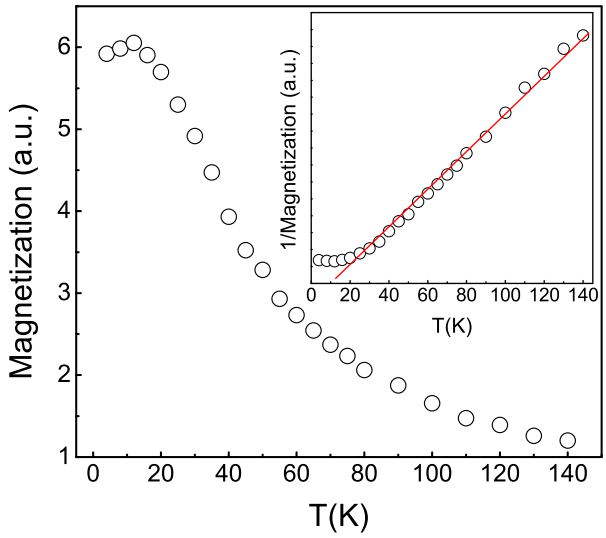

Figure 5.6: The integrated intensity of the EPR line of the hydrogen reduced Ag_6^+ cluster in 12% (wt.) Ag/NaA as a function of temperature. In the inset, an inverse signal amplitude is related to the Curie-type dependence of the electron magnetic susceptibility at low temperatures that is clear evidence of the size effect.

experiments on the susceptibility follow a similar behavior as a function of temperature in the range of 4 K to 140 K. Above 12 K the susceptibility apparently decreases as shown in Figure 5.6, and in the inset the inverse signal amplitude is also plotted in the same temperature range, exhibiting convincing evidence for the Curie behavior (see the inset in Figure 5.6), in agreement with nearly non-interacting unpaired electron spins exhibiting $|\theta| \approx 10$ K. It is probable that there is a small and negligible antiferromagnetic interactions arising from the local moments (e.g. Fe^{3+}) of the zeolite support which are coupled to the cluster spin at low temperatures leading to a small value of θ, since the reduced Ag cluster is a supported cluster system. This is however rather difficult to prove experimentally. Anyway, it is reasonable to consider that the paramagnetic silver clusters are well isolated from each other in the support pores. Neither the hyperfine splitting nor the linewidth and the g shift of EPR spectra actually changes in a relatively broad range of temperatures (see also Chapter 4). Furthermore, in practice there is no clear general trend for the behavior of the g shift as a function of the cluster size although there are specific theoretical predictions [134, 156].

EPR experiments on the electron magnetic susceptibility were performed with the microwave power of 0.64 mW in order to avoid a signal saturation during the both zero-field cooling and field cooling measurements. As is stated elsewhere (page 50 of Chapter 4), calibration with a standard sample (ultramarine blue was used in this case) and assuming $S = 1/2$ yields a value of $n = 4.8 \times 10^{16}$ spin g^{-1}, which accounts for only 0.044% of all silver atoms in the sample. Thus, most of the exchanged silver is to form a part of diamagnetic, EPR silent or unobservable clusters with high spin

states by conventional low-frequency EPR. A count of paramagnetic spins is consistent with the fact that only one of 24 β-cages in Ag/NaA is occupied by a nominal Ag_6^+ cluster. It was reported that a paramagnetic $Ag_6^+ \cdot 8Ag^+$ cluster was formed in the β-cage of Ag_{12}/NaA by γ-irradiation at 77 K [10]. Irradiation converts only ≈ 1 of 5000 EPR silent clusters into the paramagnetic $Ag_6^+ \cdot 8Ag^+$ cluster, even though the exchanged Ag^+ replace completely all 12 Na^+ in the unit cell of NaA (Ag_{12}/NaA prepared from 1 M $AgNO_3$ solutions). It therefore implies that there is no particular necessity of being the number of odd-electron clusters equal the number of even-electron clusters on average so that the total magnetic susceptibility is dominated by effects of odd-electron clusters. A very tiny fraction of atoms can still exhibit spin paramagnetism to contribute to the total magnetization, and the rest can be diamagnetic and EPR silent high spin fractions.

It was also pointed out that the detail of the energy level spectrum of an individual particle or cluster would be determined by its precise geometry [22]. It means that other particles with similar sizes but with different geometrical shapes or surface conditions would lead to different EPR spectra, even though they have the same average electronic level spacing. Moreover, for clusters of transition metals of Pd, Au or Ag possessing the sizes < 10 nm most routes of synthesis produce a great variety of cluster shapes accompanied by various internal structures [157]. It is thus apparent that the cluster size and geometry have not only equal but also enormous influence upon magnetism.

5.4 SQUID results

5.4.1 Magnetization

The experiments on the field dependence of magnetization $M(H)$ were performed up to 70 kOe in steps of 2500 Oe at different selected temperatures. Magnetization of an equivalent amount of the silver-free zeolite (or before ion exchange) but with the same treatment was subtracted.

At a low temperature regime of 1.8 K, $M(H)$ increases, but exhibits a nonlinear dependence on the magnetic field strength. Assuming an $S = 1/2$ state, the $M(H)$ curve was fitted using the modified and extended version of Equation (2.15), i.e. $M(H) = N\mu_0\mu_B \tanh(\mu_0\mu_B H/k_B T) + \chi_0 H$. The first term accounts for a nonlinearity of $M(H)$ due to alignment of the unpaired spin by a magnetic field at a low temperature. This term includes the effect of the magnetic moment on the Curie-Weiss dependence regarding the odd-electron susceptibility [5]. The second term describes a significant linear contribution of a temperature-independent susceptibility χ_0 to the $M(H)$ curve. In some other cases with a few exceptions, this also describes an appreciable linear contribution to $M(H)$ determined by a field-independent susceptibility χ_0 [158]. It is emphasized that the subtraction/correction of a constant and temperature independent component (e.g. χ_0) for magnetization excludes the determination of any *diamagnetic* or *Pauli paramagnetic contribution* [159].

Three magnetization curves recorded at 1.8 K are displayed in Figure 5.7, and the measurements contain a more reliable magnetic information of the cluster ground state. The curvature does not depend on the total magnetization, therefore, two independent pieces of information can be obtained, the magnetic moment (μ) per cluster and the fraction (f) of magnetic atoms per mole in the sample. Since the number of atoms is 6 in each nominal Ag_6^+ cluster, N can be taken as the number of clusters in a **mole** and the number of Ag atoms constituting the cluster can be also expressed in a **mole**

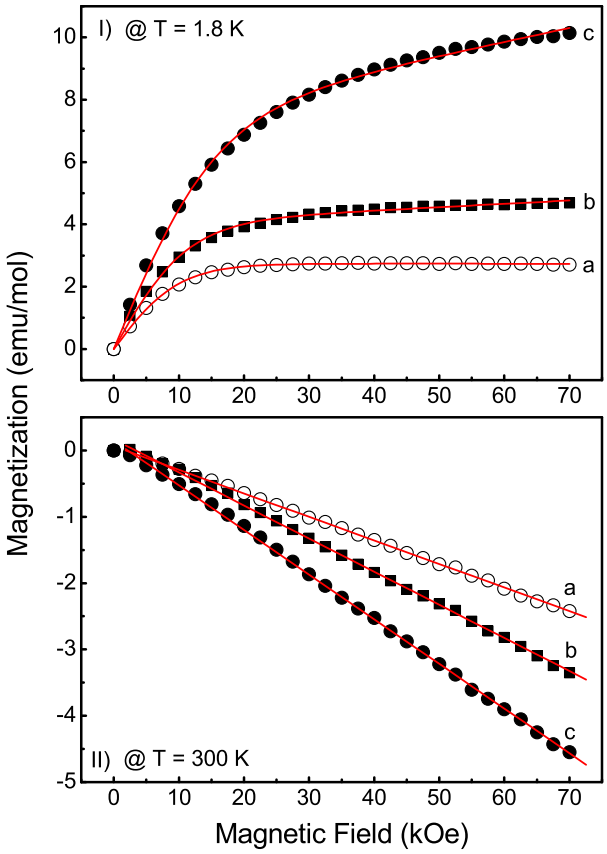

Figure 5.7: Magnetic field-dependence of magnetization (in emu/mol) for reduced clusters in 12% (wt.) Ag/NaA measured in a range of 0 to 70000 Oe: I) at at 1.8 K and II) at 300 K; (a) H_2 reduced (b) H_2 desorbed (c) D_2 reduced samples. The red lines are the theoretical fits to the field-dependence using the extended version of Equation (2.15) at 1.8 K (I) and of the linear behavior describing a temperature-independent χ_0 contribution at 300 K (II).

($f = \mathrm{N}_{\mathrm{Ag}}^{\mathrm{cl}}/N_{\mathrm{A}} = 6\mathrm{N}/N_{\mathrm{A}}$). All fit parameters and calculated magnetic moments are summarized in Table 5.2.

The magnetic moment per nominal Ag_6^+ cluster, is 3.0 μ_B, 4.0 μ_B, and 4.8 μ_B on average, respectively. Only 1.52%, 0.6%, and 0.4% of the exchanged silver atoms contribute forming a part of magnetically active Ag_6^+ clusters in the deuterium-reduced, hydrogen-desorbed and hydrogen-reduced samples. Furthermore, the values of the magnetic moment probably imply that there is an odd electron effect of the cluster because the difference is almost 1 μ_B per cluster [160]. At higher temperatures magnetization is not consistent with any Curie type behavior. This is probably not that surprising, because Curie's law is only valid in the high-temperature/low-field regime. Since the $M(H)$ curves are linear but negative at 300 K (see Figure 5.7(II)), the slope of the linear fit gives an access to the value of χ_0 at any magnetic field strength. It is however emphasized that this negative linear relation of χ_0 can include all the temperature independent contributions such as van Vleck and diamagnetism of the ion cores, as well as other spurious

contributions of the sample holder and errors in the substrate subtraction [161]. Thus, the fit derived χ_0 cannot represent a pure diamagnetic contribution to magnetism, and the sign of the values has no physical meaning.

The surface is highly important to metal nano-clusters, the surface potential has an effect on the electronic wavefunction. A high abundance of clusters with a certain size (so-called magic numbers) is often related to a particular stabilization in closed-shell geometric or electronic structures. The only magic cluster with six equivalent atoms is a regular octahedron. However, paramagnetic clusters do not have a closed shell, thus often adopting a lower symmetry. In fact, all Ag atoms belong to the surface of the nominal Ag_6^+ cluster, while no atoms are in the core.

By theoretical predictions all Ag atoms of bare free Ag_3 to Ag_{12} clusters are at the surface, and even-numbered clusters are diamagnetic because of the even number of electrons in the closed-shell electronic configuration [56]. Furthermore, theoretical calculations predicted a sextet high spin ground state for free icosahedral neutral Ag_{13}, a doublet ground state for all the smaller odd-atomic neutral clusters, and singlet ground states for even-atomic clusters with less than 14 atoms [56]. The larger clusters were predicted to be "magnetically fluxional", with low energy excited magnetic states. For positively charged clusters such calculations have not yet been performed, and in the real system the interaction with the zeolite lattice will play a role as well, which opens the possibility for a wide variety of clusters which differ in their detailed properties even though they have a narrow size distribution. A coordination of 4 atoms in the second shell and of one in the first shell is strongly reduced compared with the bulk metal, suggesting that a degeneracy is lifted by small irregularity in an octahedral symmetry of the reduced Ag_6^+ cluster.

5.4.2 Susceptibility

The temperature dependence of the dc susceptibility was measured at a magnetic field strength of 2000 Oe after a number of different reduction treatments of silver clusters in 12% (wt.) Ag/NaA.

The temperature dependence of $\chi(T)$ can be fitted using Equation (2.20), which contains a sum of a Curie-Weiss term and a temperature-independent term χ_0, and the values of the three-parameter fit are given in Table 5.3. By subtracting a temperature-independent χ_0 contribution, the static susceptibility $\chi(T)$ of the hydrogen-desorbed cluster demonstrates a nearly ideal paramagnetic Curie-Weiss dependence with $|\theta|$ = 0.5 K. The fit result is displayed in Figure 5.8. Furthermore, the inverse susceptibility $1/\chi$ is plotted in a temperature range of 1.8 K to 120 K in Figure 5.9. The Curie-Weiss temperature θ is very close to zero, ca. $|\theta| < 1$ K, as demonstrated by the straight line. This supports the implicit assumption that there is no interaction between the magnetic moments of neighboring paramagnetic silver clusters which can be isolated by diamagnetic or EPR-silent clusters. At a higher temperature range of 120 K to 300 K, there is a deviation from a linearity of the inverse susceptibility.

Using Equation (2.22) where N_A is Avogadro's number (6.02×10^{23}) and k_B is Boltzmann's constant (1.38×10^{-16} erg/K), the molar Curie constant C_m derived from the $\chi(T)$ fit was applied to calculate the effective magnetic moment μ_{eff} per Ag atom which will be in units of erg/Oe. The effective moment is usually reported in units of Bohr magnetons (denoted μ_B). Dividing by 0.927×10^{-20} (erg/Oe)/μ_B will give μ_{eff} in units[2]

[2]It will be found in *Fundamentals of Magnetism and Magnetic Measurements: Featuring Quantum Design's*

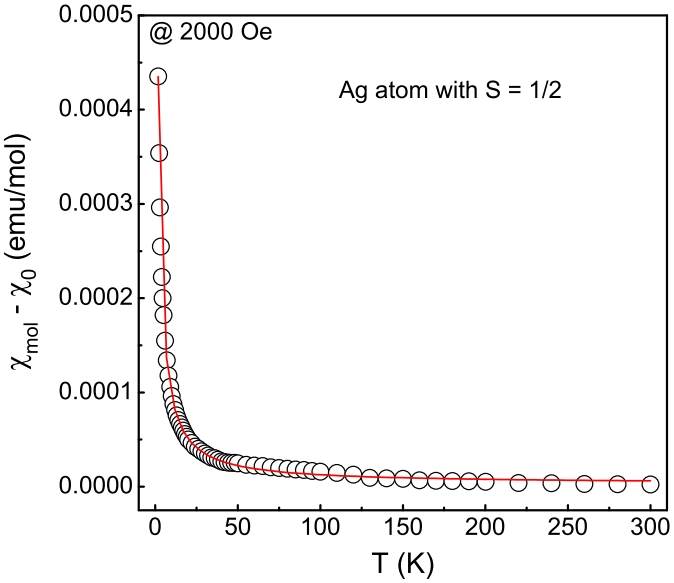

Figure 5.8: Magnetic susceptibility $\chi(T)$ as a function of temperature for hydrogen desorbed clusters in 12% (wt.) Ag/NaA at a magnetic field of 2000 Oe. The red line representing the fit to the temperature dependence is calculated using Equation (2.20), and the fit values of χ_0 are subtracted to obtain the contribution of $\chi(T)$ to the paramagnetic susceptibility.

of μ_B (see Table 5.3). However, the actual formula is only valid for an ideal system of *identical clusters*, each comprise 6 atoms with moment μ_B. All Ag clusters cannot be identical as for the atomic size and magnetic activity, only a fraction f of Ag atoms forms a part of magnetically active clusters which bear an effective or permanent magnetic moment. By utilizing $f\mu_{cl}^2/6 = \mu_{eff}^2$, the magnetic moment μ_{cl} per Ag cluster can be calculated applying the effective moment μ_{eff} derived from the $\chi(T)$ fit and f deduced from the $M(H)$fit. This yields 2.6 μ_B, 2.9 μ_B, and 3.1 μ_B per Ag cluster, respectively (see Table 5.3). It is therefore considered that the $\chi(T)$ fit provides nearly consistent data with the $M(H)$ fit given in Table 5.2. The strength of the applied magnetic field is very decisive to induce the susceptibility [162].

A pure spin magnetism results in a temperature-independent $\mu_{eff} = 1.73\ \mu_B$ [162], as it is found for example of $S = 1/2$ Cu^{2+} which has a $3d^9$ electron configuration. It is however the case that there is a quenching of orbital contribution to μ_{eff} with the reduced symmetry, e.g. C_{2v}, so that spin-orbit coupling has no effect. The effective magnetic moment is 0.81 μ_B per Ag atom of the hydrogen reduced cluster (see Table 5.2). If it is compared to the pure spin effective moment, only < 1 spin is shared among two Ag atoms or about ≈ 3 unpaired spins are per nominal Ag_6^+ cluster on average. Since it is merely assuming pure $S = 1/2$ state for paramagnetic Ag_6^+ clusters with one unpaired spin observable by EPR, there must also be a fraction of EPR silent high-spin states with $S > 1/2$, which in turn would mean that a significant fraction would have to be diamagnetic ($> 45\%$). As was previously stated elsewhere [22], other clusters

Magnetic Property Measurement System, Quantum Design 1994

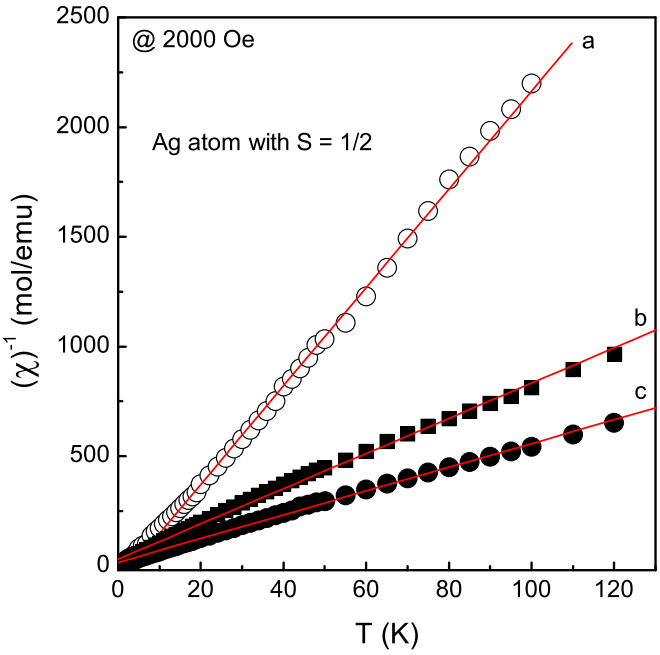

Figure 5.9: Inverse magnetic susceptibility (magnetization divided by the field in Oe) in mol/emu per Ag atoms in Ag/NaA as a function of temperature in the range of 1.8 K to 120 K) at a field of 2000 Oe: (a) H_2 reduced (b) H_2 desorbed (c) D_2 reduced. The slope of the curves is proportional to $1/C_m$, which is used for calculating the effective magnetic moment. The inverse susceptibility $(\chi)^{-1}$ is the inverse of $\chi(T)$ plotted in Figure 5.8.

with similar sizes but different shapes or surface conditions have different energy level spectra even though each has the same average level spacing. Therefore, there can be a large reservoir of EPR-silent clusters of the identical size probably with the different shape because a large spin polarization is in the electron spin reservoir. It is clearly seen from the $M(H)$ fit that each Ag atom of 3.30 clusters (given in **mol**) possesses 0.81 μ_B on average (see Table 5.2), thus suggesting that the corresponding 4.8 μ_B per nominal Ag_6^+ cluster must be a local maximum. Excess electron spins must be distributed over another EPR-silent clusters in environment of the nominal Ag_6^+ cluster. Thus, while the exact composition may vary from one sample to another it is clear that the results can only be explained with a mixture of different magnetic clusters such as diamagnetic, EPR active spin $S = 1/2$ and EPR silent high-spin species. The important thing is we have a fraction of paramagnetic Ag_6^+ clusters which are observable by EPR.

It is conceivable that a contribution of the orbital angular momentum is responsible for a remarkably high g factor ($g_{iso} \approx 2.028$) of the EPR active species. An enhanced diamagnetism has been predicted for small metal clusters and was ascribed to the larger radius of the ring currents in the overall cluster molecular orbitals compared with the atomic orbitals which are normally held responsible for diamagnetism [101]. It will depend also on the number of conduction electrons which are available in the cluster, and thus on the cluster charge. In terms of charge, a diffuse electron density renders a

deficiency of the electron inside the quantum sphere of the Ag clusters leading to a hole contribution to the positive shift of the g tensor.

It is assumed that 5s electrons are mainly responsible for spin paramagnetism of reduced Ag_6^+ clusters. Additional unpaired electrons are abstracted from hydrogen molecules to the cluster during the reduction. It implies that the more empty orbitals are needed for further occupation of s electrons with parallel spins. Therefore, the allowed electronic energy states spread out into the conduction band and the orbital degeneracy can be removed by spin-orbit coupling. Since the conduction band is a band of orbitals, which are high in energy, temperature increase basically leads to a continuous depletion of the number of spin-up electrons, thus reducing magnetization of the system.

A tight-binding molecular dynamics study demonstrated that the HOMO of the Ag clusters are located in the s-like electronic states [163]. TDDFT calculations revealed that the excitations of 5s electrons from the doubly degenerate HOMO to the LUMO are responsible for the absorption spectra of Ag_6 clusters with C_{5v} symmetry [6]. This is because the HOMO consists of 77.1% 5s, 20.6% 5p, and 4.8% 4d orbitals. However, an effect of the d orbital is not negligible, there is an contribution to the absorption spectra. It is obvious that the total susceptibility contains a diamagnetic contribution from the 4d electrons. Unfortunately, it is impossible to distinguish diamagnetism, since the subtraction/correction of a temperature-independent χ_0 term for the magnetization excludes the determination of any diamagnetic or temperature-independent paramagnetic state.

A temperature dependence of magnetic susceptibility $\chi(T)$ was also measured at the different magnetic fields of 1000, 3000 and 10000 Oe, respectively. All reduced samples were sealed in the NMR tubes prior to measurements. The fit of $\chi(T)$ was severely hampered by the presence of an antiferromagnetic transition which was observed in a lower temperature range of $T < 6$ - 13 K. The average of the Curie temperatures was close to $\theta \approx -9$ K. Above 13 K the antiferromagnetic state becomes paramagnetic, exhibiting Curie-Weiss behavior to contribute to magnetic susceptibility. By fitting the data, the highest moment was in the order of $\mu_{\text{eff}} \approx 0.11\ \mu_{\text{B}}$ per Ag atom in the deuterium-reduced cluster at 3000 Oe, whereas the lowest was $\mu_{\text{eff}} \approx 0.095\ \mu_{\text{B}}$ for the re-reduced cluster at 10000 Oe. The values of μ_{eff} are generally quite close to each other in spite of being measured at 3000 and 10000 Oe. Furthermore, the antiferromagnetic is a long range ordered state, hence not relevant (see page 64) to the silver clusters in the support pores. In contrast, with regard to interatomic spin-spin couplings in the range of cm^{-1}, one should consider that an external magnetic field of 10000 Oe corresponds to the energy equivalent wavenumber of 0.466864 cm^{-1}, so that spin-spin coupling and applied field have to be regarded as competing effects [162].

A temperature dependence of magnetic susceptibility $\chi(T)$ generally survived at 1000 Oe. However, experimental data points were severely scattered since the magnetic field strength was too weak to align the magnetic moments sufficiently, while temperature increased. The spin-system entropy is a function of the population distribution, hence the spin entropy is a function only of an external magnetic field - temperature ratio (H/T). The entropy is lowered by the field [96].

5.5 Summary

Hydrogen reduction leads to relatively uniform dispersions and the smallest size is on the order of 2 nm. Thus, the determined size is more reasonable to the distribution of the reduced Ag nano-particles. The diffractogram of the HRTEM micrographs reveals the

presence of twin boundaries of the hydrogen reduced particles. Deuterium reduction leads to the core-shell structure, which does not occur to the hydrogen reduced particles, and the size is on the order of 8 nm on average, suggesting that more EPR silent Ag species are non-uniformly distributed. It is considered that much larger silver nanoparticles are merely observed by HRTEM measurements and are probably accumulated on the zeolite external surfaces (see page 57).

EXAFS measurements allow determining a real and precise size of very small silver clusters in the support pores. By using the multiple scattering path to analyze the absorption fine structure, the reduced silver cluster exhibits a quite mono-disperse and size-selected structure, while all Ag atoms belong to the surface. The cluster consists of 6 ± 1 atoms with an average coordination of $N \approx 4.00 \pm 0.05$, since the size of the cluster is an average estimate of the direct coordination in the first and second Ag-Ag shells. The inter-atomic distance of each Ag-Ag shell is contracted by $< 10\%$ as compared to the bulk Ag distance (2.889 Å).

Applying the double integration of the first-derivative EPR signals, the temperature dependent susceptibility of the paramagnetic Ag_6^+ cluster exhibits the Curie type dependence. Measurements of field cooling and zero-field cooling are identical in the temperature dependence.

The magnetic behavior of the nominal Ag_6^+ cluster supported on NaA zeolite was investigated by SQUID magnetometry. To investigate a static susceptibility contribution to spin paramagnetism in detail, the equation that combines the Curie-Weiss term and a temperature-independent term was used to fit a temperature dependence of magnetic susceptibility. A paramagnetic susceptibility is induced by some probability that very fine clusters can be occupied by odd numbers of electrons in singly occupied molecular orbital configuration delocalized over all cluster atoms. A field dependence of magnetization revealed the highest magnetic moment which is on the order of 0.81 μ_B per Ag atom of clusters in the hydrogen-reduced sample. However, only 1.52%, 0.6%, and 0.4% of all exchanged silvers contribute forming a fraction of magnetically active nominal Ag_6^+ clusters in the deuterium-reduced, hydrogen-desorbed and hydrogen-reduced clusters. Ag atoms not participating in magnetically active clusters contribute to a temperature independent term.

Table 5.1: Structural parameters of the reduced Ag clusters in 12% (wt.) Ag/NaA obtained from the three-shell fitting of $\chi(k)$ function.

Remarks	Ag-Ag				Ag-O				Ag-Ag			
	R(Å)	N	$\Delta\sigma^2$(Å^2)	ΔE_0	R(Å)	N	$\Delta\sigma^2$(Å^2)	ΔE_0	R(Å)	N	$\Delta\sigma^2$(Å^2)	ΔE_0
Ag-foil	2.889	12.0	-	5.50 eV*								
Reductions @ 293 K												
H_2 reduced	2.77	3.50(5)	0.013	2.09 eV	2.22	1.60(5)	0.011	8.52 eV	2.69	0.35(5)	-0.007	1.57 eV
H_2 evacuated	2.76	3.50(5)	0.015	2.03 eV	2.21	1.39(1)	0.012	10.0 eV	2.69	0.40(5)	-0.005	1.52 eV
H_2 re-reduced	2.75	3.35(5)	0.013	2.60 eV	2.26	0.70(5)	0.009	8.14 eV	2.69	0.55(5)	-0.002	2.60 eV

R(Å) - bond length
N - coordinations
$\Delta\sigma^2$(Å^2) - DW factor
ΔE_0 - edge shift
E_F - Fermi energy*

Table 5.2: Magnetic moments and fit parameters derived from experimental $M(H)$ data for different reduction conditions. Measurements as a function of applied magnetic field were performed at a fixed temperature of 1.8 K.

Parameters	D_2-reduced	H_2-desorbed	H_2-reduced	Remarks
$\mu_{cl} = 6\mu_{at}$ (μ_B/Ag_6^+)	3.018	4.122	4.884	from $M(H)$ fit
μ_{at} (μ_B/Ag atom)	0.503	0.687	0.814	from $M(H)$ fit
N (number of clusters in a mol)	14.141	5.622	3.283	from $M(H)$ fit
$M_S = N\mu_{at}$ (emu/mol)	7.113	3.862	2.672	from $M(H)$ fit
$f = 6N/0.927 \times 10^{-20} N_A$	0.0152	0.0061	0.0036	from $M(H)$ fit
$f\mu_{at}$ (μ_B/Ag atom)	0.0077	0.0042	0.0029	from $M(H)$ fit
$\chi_0(\times 10^{-6})$ (emu/mol)	-40.0	-10.0	-0.064	from $M(H)$ fit
$\chi_0(\times 10^{-6})$ (emu/mol)	-67.31	-49.95	-35.4(5)	from the linear fit at 300 K

Table 5.3: Magnetic moments and fit parameters derived from experimental $\chi(T)$ data for different reduction conditions. Measurements as a function of temperature were performed at a fixed magnetic field of 2000 Oe. Note that the unit of the magnetic field is given as Oe in CGS, since the unit of μ_{eff} is not different in the SI and the CGS system.

Samples	μ_{eff} (μ_{B})	μ_{eff}^2 –	f –	μ_{cl} (μ_{B})	$\chi_0(\times 10^{-6})$ (emu/mol)	$C_{\text{m}}(\times 10^{-5})$ (emu·K/mol)	θ (K)
D_2 reduced	0.130(1)	0.0172	0.0152	2.603	-17(5)	16.1(1)	-0.6(1)
H_2 desorbed	0.092(1)	0.0086	0.0061	2.898	+23(1)	9.8(1)	-0.5(1)
H_2 reduced	0.074(1)	0.0057	0.0036	3.052	-12(1)	6.1(1)	-0.2(2)

6 Chemistry of Ag clusters

XRD measurements demonstrated that the Ag_6 cluster in Ag_{12}/NaA reacted with ammonia and ethylene, and the reaction with ammonia led to the formation of N_3H_5 and N_3H_3 [164, 165]. The diffraction method can be merely selective and sensitive to the macroscopic ensemble of supported silver clusters exhibiting a structure such as a single-crystal.

As is stated elsewhere (page 2 of the Chapter 1), that paramagnetic species possessing an unpaired electron are often expected to be "*chemically reactive*". The chemical interactions, i.e. the adsorption activities of the reduced silver clusters against some gas adsorbate molecules will be considered extensively in this chapter. In the following sections, the changes in the well-resolved hyperfine splitting of the paramagnetic Ag_6^+ clusters as NO and C_2H_4 gas molecules are adsorbed onto the cluster containing 12% (wt.) Ag/NaA samples at room temperature are fundamentally highlighted. The EPR parameters of the new as well as adsorption products will be discussed, and some kinetic information can be derived from the motional dynamic parameters of the conversion products at the surface. At this stage, the determinations of the exact structure of adsorption or chemical interaction derived centers and their interactions with the immediate surroundings are not completely proposed. However, the EPR observations are extended by the XAS spectroscopy measurements to provide additional information on the silver cluster local structure and its changes by chemical or adsorption reactions.

6.1 EPR results of NO adsorption

Transition metal clusters supported on zeolites are important for heterogeneous catalytic processes, and a specific selectivity basically depends on the size of the clusters [166]. However, bulk silver would be considered unlikely an active catalyst due to a completely filled $4d^{10}$ electronic state, thereby small Ag clusters being considered to be intermediate from viewpoints of effective catalysts. Paramagnetic silver clusters probably appear to exhibit a catalytic activity on account of the unpaired 5*s* electrons.

Adsorption behavior of NO in various zeolites was extensively studied by means of the continuous wave and the pulse EPR spectroscopy [167, 168, 169, 170, 171, 172]. The orientation of the unpaired electron with respect to the orbital angular momentum in the external magnetic field leads to rotational ground states, viz. $^2\Pi_{1/2}$ and $^2\Pi_{3/2}$, in the free NO molecule. In the $^2\Pi_{1/2}$ state, the spin and orbital angular momentum are anti-parallel, thus the spin magnetism is compensated. An unpaired electron resides in the anti-bonding $2\pi_y^*$ molecular orbital [167]. If NO is adsorbed onto the zeolite, an electrostatic field quenches this orbital degeneracy and reveals the EPR signals. Extra-framework cations, e.g. Na^+ and K^+, are responsible for electrostatic fields in zeolites. This is the experimental specification how to monitor NO adsorptions.

Copper ion-exchanged zeolites are active to adsorb NO gas molecules, and the hyperfine splittings of ^{14}N and Cu^+ were resolved simultaneously [173, 174].

However, Ag^+ ion-exchanged zeolites and supported Ag catalysts demonstrated quite

diverse activities to interact with nitrogen monoxide, e.g. a photo-catalytic reactivity for the photodecomposition of NO [175] and a selective catalytic reduction which leads to a direct decomposition of NO into N_2 and O_2 [176]. These Ag containing catalysts were investigated by spectroscopic techniques different from EPR.

It is therefore fascinating to know whether the paramagnetic Ag_6^+ cluster has an enhanced/diverse catalytic activity or not against molecular NO, if it is compared to that of bulk silver.

6.1.1 Adsorbed NO

Theoretical description

An appropriate theoretical description of the obtained EPR and HYSCORE spectra for an unpaired electron with spin $S = 1/2$ interacting with N nuclei of arbitrary spin I is based on the following spin-Hamiltonian:

$$\mathcal{H} = \beta_e \mathbf{B_0} \cdot \mathbf{g} \cdot \mathbf{S} + \sum_{i=1}^{N} \mathbf{S} \cdot \mathbf{A_i} \cdot \mathbf{I_i} - \beta_n \sum_{i=1}^{N} g_{n,i} \mathbf{B_0} \cdot \mathbf{I_i} + \sum_{I \geq 1} \mathbf{I_i} \cdot \mathbf{Q_i} \cdot \mathbf{I_i} \tag{6.1}$$

where $g_{n,i}$ are the corresponding nuclear g factors while β_e, β_n are the Bohr and nuclear magnetons, respectively. The first and second term are the electronic and nuclear Zeeman interaction, respectively, where $\mathbf{B_0}$ denotes the external field. The last terms correspond to the hyperfine interactions due to nearby magnetic nuclei and the nuclear quadrupole interaction for nuclei with $I \geq 1$. Hyperfine ($\mathbf{A_i}$) and quadrupole tensors ($\mathbf{Q_i}$) as well as the external field ($\mathbf{B_0}$) are given in the principal axes system of the **g**-matrix, and the index i refers to a particular nucleus.

Hyperfine and nuclear quadrupole interaction with the 99.636% natural abundance ^{14}N manifests in the recorded HYSCORE spectra, where correlation peaks (ν_α, ν_β) and (ν_β, ν_α) are further split into multiplets as a function of the quadrupole coupling constant $\kappa = e^2qQ/4h$ and the corresponding asymmetry parameter $\eta = (Q_{xx} - Q_{yy})/Q_{zz}$. These are defined by the diagonal elements of the traceless nuclear quadrupole tensor using standard notation. At X-band frequencies, often the so-termed "*cancellation condition*" is met [177, 178], according to which $2\nu_I \approx |A|$. As a consequence, the effective field experienced by one of the two m_S manifolds vanishes because nuclear Zeeman and hyperfine interaction cancel each other. This reduces the orientation dependence and narrow zero-field quadrupole transitions may be observed even in disordered samples. Corresponding nuclear spin transitions are predicted to occur at frequencies close to

$$\nu_0 = \frac{e^2qQ}{2h}\eta = 2k\eta \tag{6.2}$$

$$\nu_\pm = \frac{3e^2qQ}{4h}\left(1 \pm \frac{\eta}{3}\right) = \kappa(3 \pm \eta) \tag{6.3}$$

The nuclear transition frequencies of the m_S manifold, in which the hyperfine and the Zeeman fields add rather than cancel each other, are denoted as single-quantum $\nu_{1,2}^{\mathrm{sq}}$ ($\Delta m_I = \pm 1$) and double-quantum ν^{dq} ($\Delta m_I = \pm 2$) transitions, the latter found at

$$\nu^{\mathrm{dq}} \approx 2\left[\left(|\nu_I| + \left|\frac{a_{\mathrm{iso}}}{2}\right|\right)^2 + \kappa^2(3+\eta^2)\right]^{\frac{1}{2}} \tag{6.4}$$

The expression for the double-quantum transition frequency ν^{dq} is only approximately valid even under the assumption that the anisotropic part of the hyperfine interaction can be neglected. Equation (6.4) can nevertheless be used in order to obtain an estimate of the dipolar hyperfine coupling, even though only "*nuclear-quadrupole frequencies*" are observed.

$$E_{M_I} = \pm(g_{zz}\beta|B_0|)/2 + M_I(|a_\pm|/2)$$

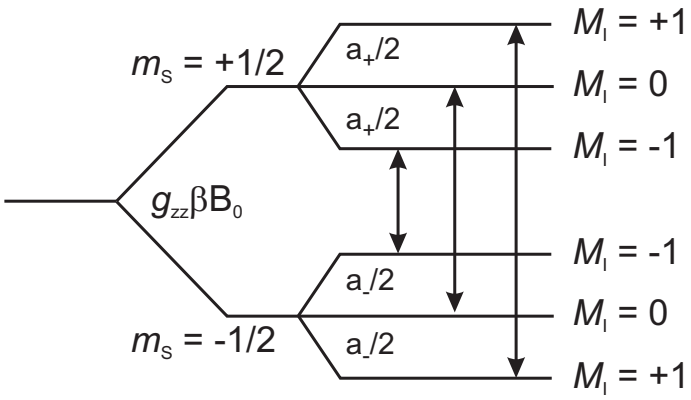

Figure 6.1: Energy levels of ^{14}N split by an external magnetic field. The arrows indicate allowed EPR transitions observable by continuous wave spectroscopy measurements.

The energy levels of the Hamiltonian can be obtained from first-order perturbation theory taking the secular part of the electronic Zeeman splitting as zero-order approximation of the Hamiltonian, and the nuclear Zeeman and the hyperfine interactions as the first-order perturbations (see Figure 6.1).

cw EPR

As NO gas ($P \approx 100$ mbar) was adsorbed at room temperature, the yellowish-brown color of the hydrogen reduced Ag/NaA zeolite sample turned immediately into a weak pink color.

The hyperfine structure of the reduced Ag_6^+ cluster completely disappeared, and a new hyperfine structure was observed. It mainly consists of a central prominent hyperfine splitting at 3390 G. In terms of effective g values, the spectrum is described with g_{xx} = 1.982, g_{yy} = 1.978 and g_{zz} = 1.841 and these values are significantly less than the free electron g_e value ($g_e > g_{xx} > g_{yy} > g_{zz}$). The symmetry of the system is orthorhombic, though the deviation from axial symmetry is very small ($g_{xx} \approx g_{yy}$). The orientation of the g and A tensors is assumed coaxial, however, only A_{yy}^N and A_{zz}^{Ag} components are resolved experimentally. The experimental spin Hamiltonian parameters are summarized in Table 6.1, and the numerical spectrum simulation was based on these parameters.

The best fit between the experimental and simulated spectra is displayed in Figure 6.2. In the signal of adsorbed NO, only the hyperfine component A_{yy}^N = 33 G of the ^{14}N atom is resolved. There is also a larger splitting at the g_{zz} component by the hyperfine component A_{zz}^{Ag} = 200 G of a single Ag atom to which NO is bound. The other five Ag atoms are diamagnetic.

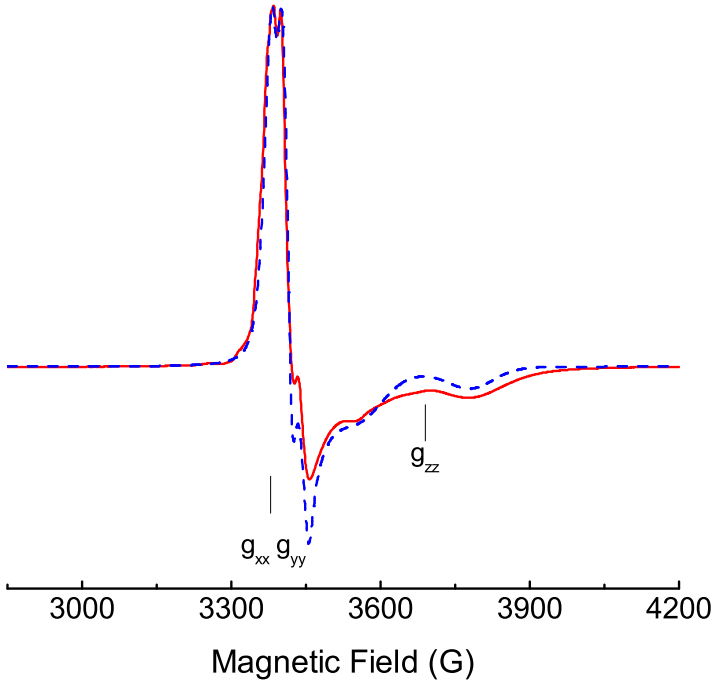

Figure 6.2: X-band EPR spectrum (solid line) of NO adsorbed on the reduced Ag_6^+ cluster recorded at 20 K, and a corresponding simulation (dashed line) based on the spin Hamiltonian parameters listed in Table 6.1. The numerical spectrum simulation assuming only one unpaired electron spin interacting with ^{14}N (I = 1) and Ag (I = 1/2) nuclei. The species being assumed $Ag_6(NO)$, however, the unpaired spin density is mostly on the ^{14}N.

There was no half-field signal detected at 1680 G after the first adsorption (see Figure 6.3). A half-field signal would indicate the existence of a triplet state [168]. The absence of a triplet state means that we are observing either the NO adduct to a previously diamagnetic and therefore EPR silent Ag cluster, or that a red-ox reaction precedes NO adsorption. By integrating the EPR signal, the spin count (2.73×10^9 spins) followed by adsorption of NO on the EPR silent clusters is higher than that of the adduct-free Ag_6^+ clusters (5.07×10^8 spins calculated before NO adsorption).

After adsorbing a second dose of NO ($P \approx 170$ mbar), the spectrum became much more complex, however no destruction of the original signal was observed as illustrated by *ii* in Figure 6.4. The g_{zz} component survived with no shifts and amplified its intensity. A new paramagnetic center appeared on the flanks of the central line, and the extra peaks at the left and right flanks are indicated by vertical dashed-lines. These peaks developed further on the third adsorption of NO with $P \approx 130$ mbar that is depicted by the entry *iii* in Figure 6.4. A determination of the spin Hamiltonian parameters of the new center is fairly complicated, especially in central line positions. The local symmetry of the new center is also rhombic with g_{xx} = 2.008, g_{yy} = 1.997 and g_{zz} = 2.001. The new structure is considered as an intermediate state of adsorbed NO_2 and will be discussed in more detail in the next part.

Table 6.1: EPR Spin Hamiltonian Parameters of the Adsorbed NO in Different Matrices.

Matrix	T(K)	g tensor	A^{14}N[G]	B^{14}N[G]	Energy (eV)	Ref.
Ag/NaA	20	$g_{xx} = 1.982$	$A^N_{xx} = 0$	$B^N_{xx} = -11$	δ = 0.144	this work
		$g_{yy} = 1.978$	$A^N_{yy} = 33$	$B^N_{xx} = 22$	Δ = 1.260	
		$g_{zz} = 1.841$	$A^N_{zz} = 0$	$B^N_{xx} = -11$		
		$g_{iso} = 1.934$	$a^N_{iso} = 11$			
			$A^{Ag}_{xx} = 0$			
			$A^{Ag}_{yy} = 0$			
			$A^{Ag}_{zz} = 200$			
			$a^{Ag}_{iso} = 67.0$			
NaA	77	$g_{xx} = 1.980$	$A^N_{xx} = 11.9$		0.210	[168]
		$g_{yy} = 1.987$	$A^N_{yy} = 30.6$			
		$g_{zz} = 1.905$	$A^N_{zz} = 0$			
NaA	4.7	$g_{xx} = 1.999$	$A^N_{xx} = 6.8$		0.260	[169]
		$g_{yy} = 1.993$	$A^N_{yy} = 32.3$			
		$g_{zz} = 1.884$	$A^N_{zz} = 0$			
NaA	4.5	$g_{xx} = 1.999$	$A^N_{xx} = 9.1$		–	[170]
		$g_{yy} = 1.993$	$A^N_{yy} = 32.5$			
		$g_{zz} = 1.884$	$A^N_{zz} = 9.5$			
NaA	10	$g_{xx} = 1.999$	$A^N_{xx} = 5.8$		0.272	[171]
		$g_{yy} = 1.994$	$A^N_{yy} = 32.7$			
		$g_{zz} = 1.884$	$A^N_{zz} = 0$			
NaA	5.0	$g_{xx} = 2.002$	$A^N_{xx} = 0$		–	[172]
		$g_{yy} = 1.996$	$A^N_{yy} = 33$			
		$g_{zz} = 1.886$	$A^N_{zz} = 0$			
NaA	110	$g_{xx} = 1.979$	$A^N_{xx} = 0$		–	[172]
		$g_{yy} = 1.989$	$A^N_{yy} = 30$			
		$g_{zz} = 1.909$	$A^N_{zz} = 0$			

To explore a possible half-field signal at $\approx$ 1680 G, a broad field scan was also taken. Though it was expected that the triplet state might be a function of gas pressure, only the typical Fe^{3+} signal was detected after the third adsorption. There was no effect on the resolution of the hyperfine splitting pattern on evacuation at room temperature.

HYSCORE

To confirm the conclusion about adsorption of NO onto the silver clusters, HYSCORE was also performed after addition of NO gas, probing for coupled nitrogen spins. The corresponding orientation-selective spectrum (g_{yy}) is depicted in Figure 6.5; the observed pattern being characteristic for "remote" ^{14}N in a "*cancellation regime*" [177, 178]. The obtained ^{14}N-HYSCORE spectrum reveals well-defined diagonal peaks being characteristic for the "pure" nuclear-quadrupole transitions **(1-3)** occurring only in one of the $m_S = \pm\frac{1}{2}$ electron-spin sublevels. The frequencies of these transitions are quasi field-independent, indicating near cancellation of the external field at the nuclear site in the corresponding sublevel. The additional strong peak **(4)** is attributed to a double-

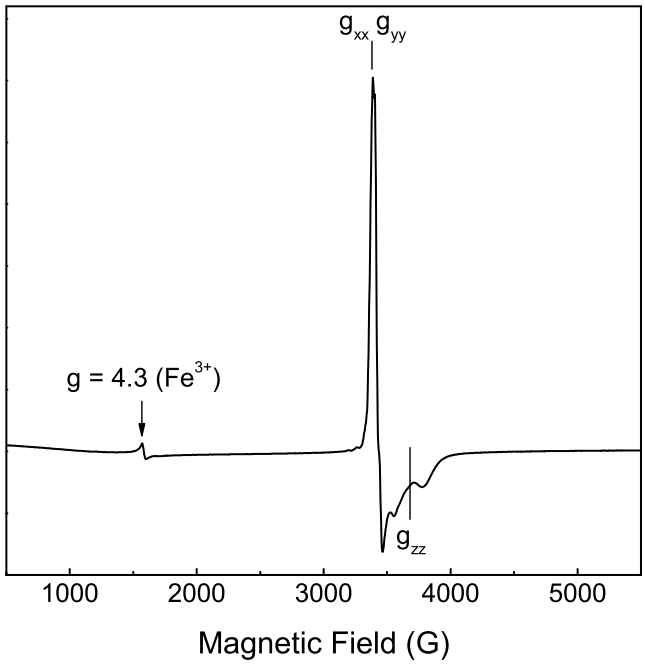

Figure 6.3: A broad field scan demonstrates the absence of a half-field signal at 1680 G, which would indicate the triplet state. The spectrum was recorded at 20 K. The typical iron signal of Fe^{3+} is centered at $g = 4.3$.

quantum transition ν^{dq} between $m_I = \pm 1$ nuclear levels in the other electron-spin sublevel, being superimposed to the ^{27}Al matrix peak. As cross-correlation peaks occur simultaneously in both quadrants of the HYSCORE spectrum, the existence of near cancellation is further supported.

From the cancellation pattern **(1-4)**, $\kappa = e^2qQ/4h = 670$ kHz and $\eta = 0.3$ is obtained, corresponding to $A^{\mathrm{N}}_{\mathrm{iso}} \approx 1.5$ MHz. This value is considerably smaller than the ^{14}N-hyperfine coupling resolved in the EPR spectrum, which is too large for being observed in the HYSCORE spectrum. We thus assign the small ^{14}N-hyperfine interaction to a second nitrogen spin in the vicinity of the silver cluster. As an explanation, N_2O molecules may also be adsorbed to the silver clusters, exhibiting a strongly anisotropic distribution of spin densities over the two nitrogens.

6.1.2 Adsorbed NO_2

The Ag_6^+ cluster slowly catalyzes a reaction between NO and O_2 (a trace amount impurity) gas molecules. This is seen from the fact that the spectrum of adsorbed NO changed to quite a different spectrum over several days. The new hyperfine structure clearly has to be attributed to NO_2, based on literature data [179, 180, 181, 182].

The NO_2 molecule has already been known as a classical probe molecule to study reorientation dynamics occurring at the gas-solid interface in channels of aluminium-silicate supports. As the molecule tumbles in the channels, there is an indication of a weak interaction of the NO_2 molecule with zeolitic atoms. The computer simulation

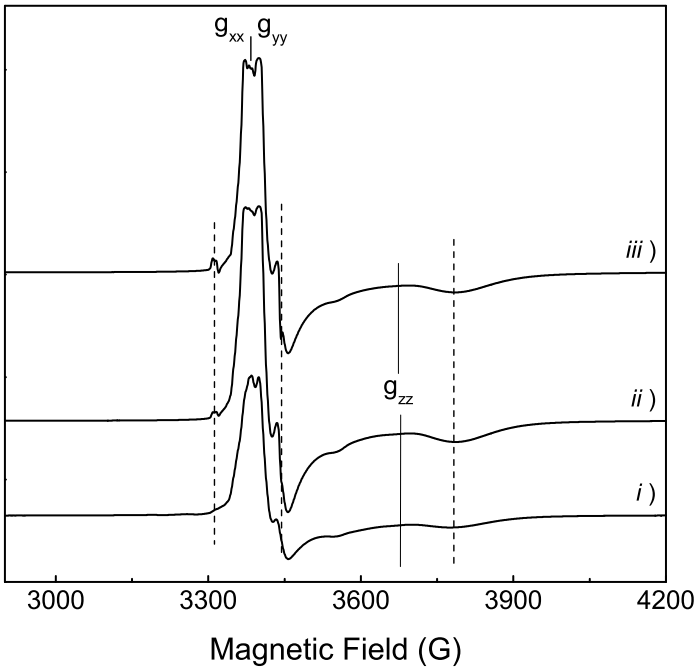

Figure 6.4: The experimental spectrum after a first dose of NO is renormalized, and taken as *i* in order to compare with signals by further adsorptions. The spectra with *ii* and *iii* were recorded after a second and third dose of NO, respectively. The extra peaks represented by vertical dashed-lines in *ii* and *iii* that are attributed to a new hyperfine structure. This is considered the first trace of the adsorbed NO_2. All the measurement were performed at 20 K.

method seems a more effective way to interpret the spectra based on molecular reorientation dynamics. The theoretical spectra were reproduced by adjusting a correlation time τ_c to fit the lineshape of the experimental EPR spectra.

Low temperature spectrum

The spectrum of the adsorbed NO_2 was recorded at 20 K. In Figure 6.6, the transitions ($M_I = \pm 1$; $M_I = 0$) are separated in the first order by the hyperfine coupling constant of the ^{14}N nucleus. The three lines are not equidistant on account of the orthorhombic g tensor. The central line is affected solely by the g anisotropy, which is therefore determined first. On top of this, the two outer lines reflect the hyperfine anisotropy.

Experimental spin Hamiltonian parameters, derived from numerical spectrum simulation, are summarized in Table 6.2. The calculated spectrum is superimposed on the experimental spectrum and exhibits an excellent agreement. The symmetry is non-axial C_{2v}. The best fit indicates that only one ^{14}N ($I = 1$) nucleus interacts with the unpaired electron spin in the adsorbed NO_2 molecule. This interaction leads to nearly the same principle values as those of the g and A tensors in the gas phase of the free NO_2, a single crystal of $AgNO_3$ and $NaNO_2$ [183, 184, 185]. The only slight differences in the numerical values of the g and A tensors arise from silver nuclei in the cluster. The somewhat

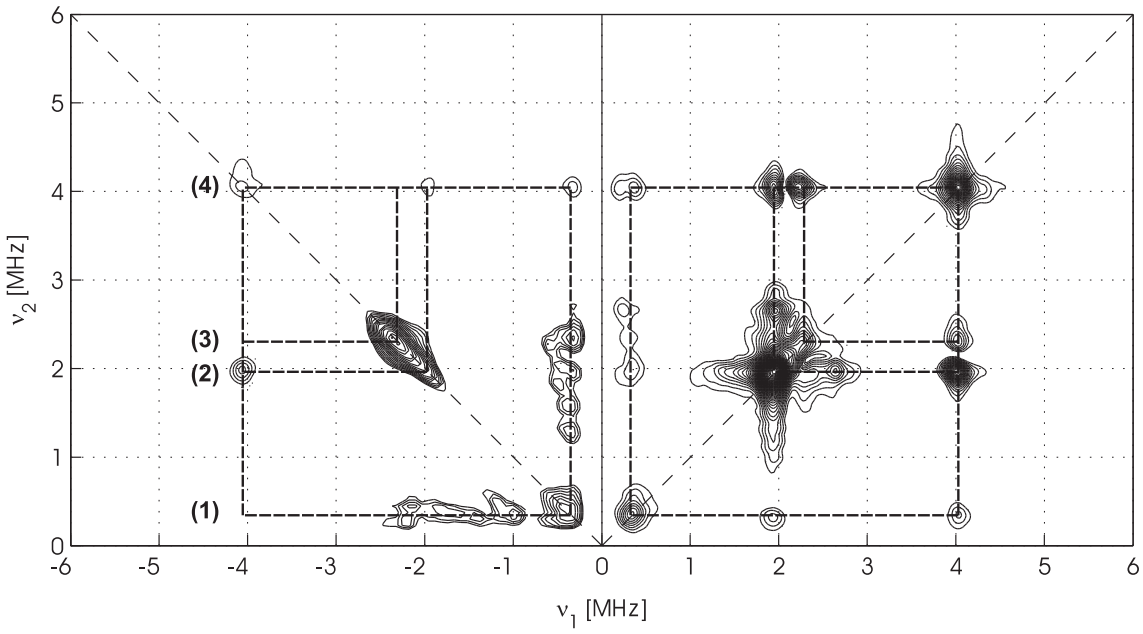

Figure 6.5: "matched" X-band ^{14}N-HYSCORE spectrum of NO-adsorbed reduced Ag_6^+ cluster, recorded at an observer position of 3480 G (348 mT) and at 10 K. Under near cancellation condition, three nuclear-quadrupole transitions in one m_S sublevel labeled **(1-3)** can be identified. A double-quantum transition in the other m_S sublevel is indicated by **(4)**. (Spectra were provided by PD Dr. R.-A. Eichel at the Eduard-Zintl-Institute, Darmstadt University of Technology.)

higher values of g_{xx} and g_{zz} components are also taken as evidence of some admixture of the transition metal (e.g. Ag) orbital.

Furthermore, the molecular motion information is of particular importance, a critical modulation amplitude (2 G) is used to limit any lineshape distortion. A higher modulation amplitude (4 G and 8 G) strongly affects the resolution of the spectral lineshape even at 20 K.

Temperature dependence of spectra

Variations in spectral linewidths may generally be due to the reorientation of the molecule. The spectra recorded at temperatures of 30 K to 110 K are shown in Figure 6.7(a), illustrating that the lineshapes are strongly changed. By increasing the temperature to 30 K, the triplet spectrum reflects less pronounced resolution, the x and z components at each of the $M_I = \pm 1$; $M_I = 0$ transition bands move rapidly towards their centers. This behavior reflects a molecular motion. The relative peak-to-peak amplitude of the y components at all transitions get significantly weaker. Subsequently, each hyperfine line converts to one broad line at 40 K that is quite distinct from the static spectrum that is depicted in Figure 6.6. From 30 K to 70 K, the y components at $M_I = +1$ and $M_I = 0$ are also slowly shifted from the initial position towards the common center. The reorientation of the NO_2 molecule is close to axially symmetric about its molecular y axis, and averages the hyperfine dipolar B_{xx} and B_{zz} components. It is however emphasized that large amplitude tilting with this axis is more realistic. Finally at 70 K, all

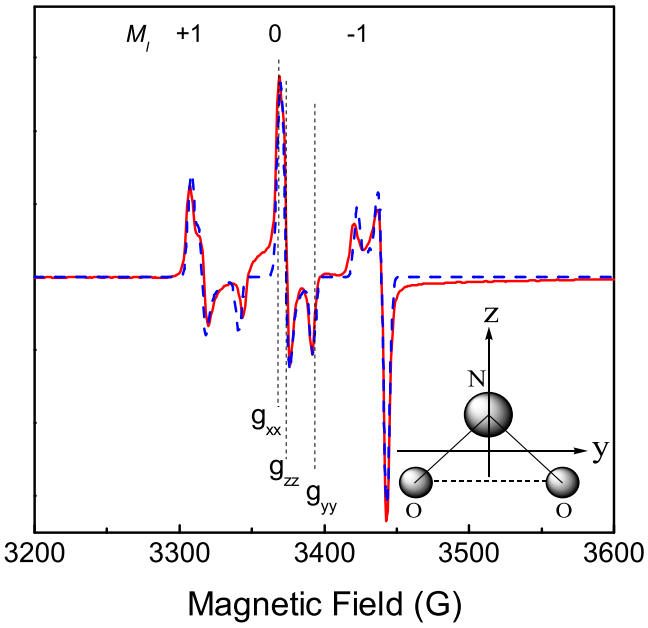

Figure 6.6: EPR spectrum of the adsorbed NO_2 (solid line) recorded at 20 K, and the corresponding simulation (dashed line) based on the parameters listed in Table 6.2 for $^{14}NO_2$. The spectrum of adsorbed NO converted to the present signal of NO_2 over several days. The inset shows a schematic representation of the molecular y axis of the rotational diffusion of the adsorbed NO_2 on the Ag_6^+ cluster. The rotational diffusion takes place primarily about this axis.

lines have merged by motional narrowing into single central lines with nearly averaged components of the g and A tensors. At 90 K, individual components of the hyperfine lines no longer persist, and eventually the spectrum becomes close to isotropic. The tumbling rate is rapid enough in order that the line positions correspond to those of the completely averaged spectra at 110 K and 125 K (see also the entry i in Figure 6.9).

Double integration of the spectra allows a quantitative estimation of the number of NO_2 molecules. Comparison with the double integral of the EPR spectrum of the standard (ultramarine blue) results in of the order of 10^{16} spin g^{-1} (8.5×10^{-9} mol g^{-1}), a relatively low concentration. This signal intensity is much less than the amount of NO exposed initially to the reduced Ag/NaA. After each cycle of gas adsorptions (totally three cycles) the remaining NO was evacuated.

According to the Curie law, the signal should be inversely proportional to temperature, which is verified in Figure 6.8(a).

Spectral simulation of the slow-motion

Simulations were performed by using the EasySpin simulation package [108]. Initially, the slow motion spectra were simulated using an isotropic Brownian rotational diffusion model, but the fits between the experimental and reproduced spectra were not perfect. Simulation using an anisotropic Brownian rotational diffusion model gave a rather good

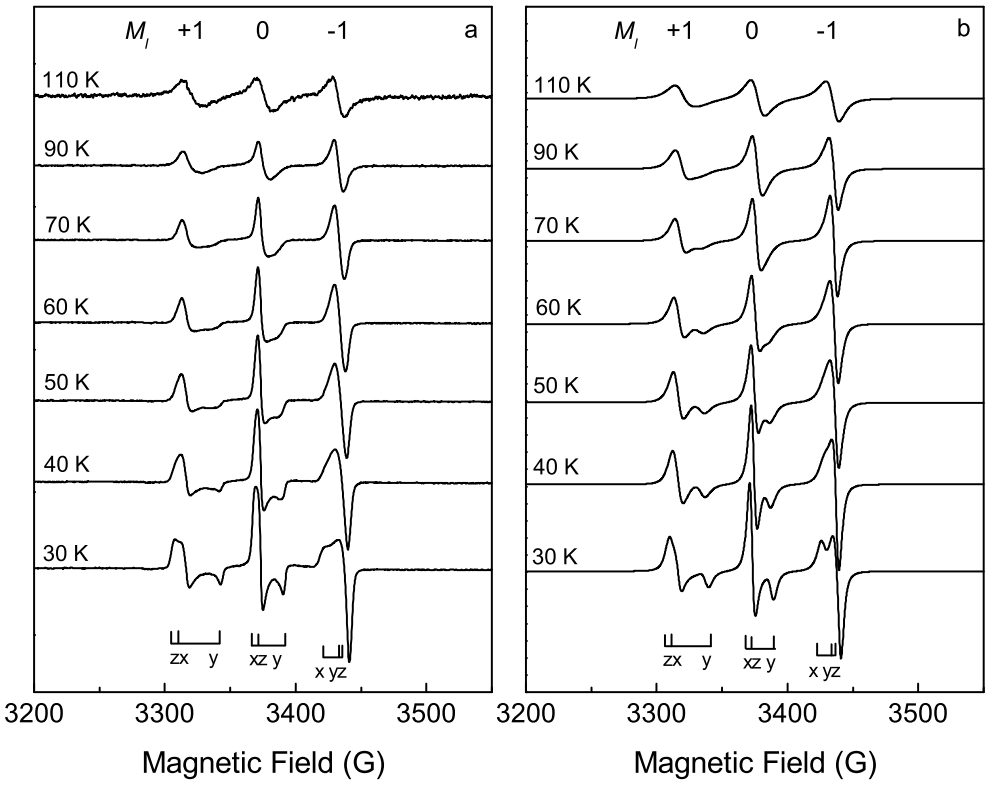

Figure 6.7: a) Temperature dependence of X-band EPR spectra of the adsorbed NO_2 onto the reduced Ag_6^+ clusters. b) Theoretical fittings using an anisotropic Brownian rotational diffusion model.

agreement. The orientation of the g and A tensors are still assumed coaxial, but are *static parameters* in the slow-motion simulation. Each principal value of the axial rotational diffusion tensor was specified in Hz (Hertz, s^{-1}) by giving a 2-element vector for the dynamic parameter of the simulation. Presentation of data on a logarithmic scale (**log**10) reduces the data to a more manageable range. Furthermore, to reduce the number of variables and because this gave the best agreement with experiment, $R_{\|}$ is fixed here at $10^7\ s^{-1}$. Finally, the principal values of the correlation times were calculated applying the formulae $R_{\|} = \frac{1}{4\tau_{\|}}$ and $R_{\perp} = \frac{1}{6\tau_{\perp}}$, respectively [186]. A residual linewidth ($1/T_2^0$) is required and the general aspect is a decrease with temperature. The fitting parameters are summarized in Table 6.3 and displayed in Figure 6.7(b). The simulations reproduce the characteristics of the experimental spectra quite well. The remaining differences are probably due to relatively close components, $R_{\|}$ and $R_{\perp}$, of the rotational diffusion tensor. $R_{\|}$ is along the molecular y axis of NO_2. It may mean that the motion is a **large amplitude tilting and flipping** of the NO_2, which is bound via N to the silver cluster, rather than a full rotation. $R_{\perp}$ is along the x and z axes and increased from $2\times10^6\ s^{-1}$ (at 30 K) to $1\times10^7\ s^{-1}$ (at 110 K) as a function of temperature. The rotation of NO_2 is rather anisotropic at 30 K, with $N \equiv R_{\|}/R_{\perp} \approx 5$, and this ratio decreases with temperature and eventually approaches unity for isotropic motion at 90 K. In spite of the different

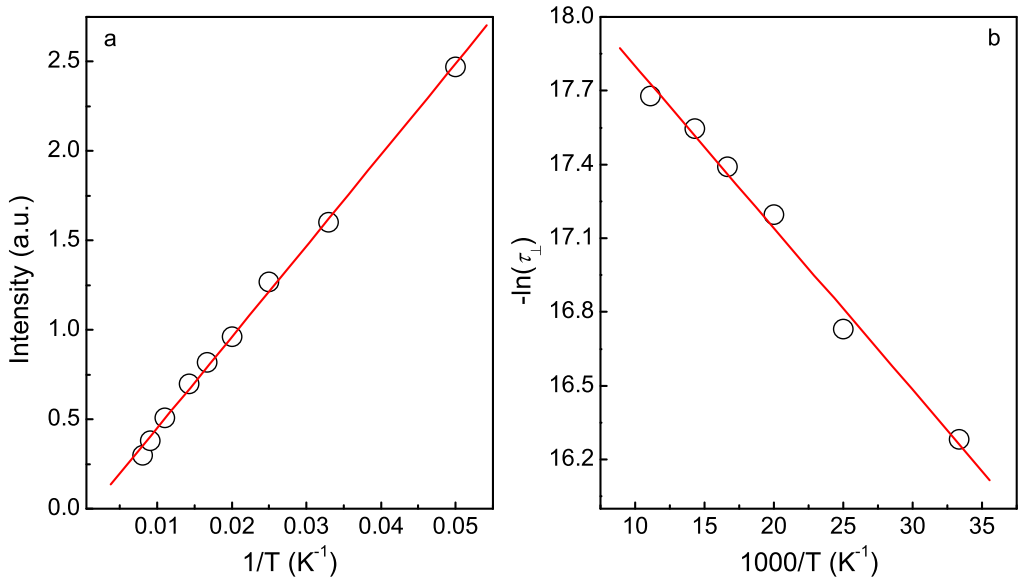

Figure 6.8: a) Intensity of double integral of NO_2 spectra verifying the accordance with the Curie law. b) Arrhenius plot of the $\tau_\perp$ correlation time derived from the simulation with an anisotropic Brownian diffusion model.

relative peak amplitudes (intensities), the rotational diffusion is fairly isotropic at 110 K and 125 K that have the same rotational diffusion rates, $R_\parallel \approx R_\perp = 1\times10^7\ s^{-1}$, but the signal-to-noise ratio is much worse at 125 K (see the entry *i* in Figure 6.9). $\ln\tau_\perp$ of the motional correlation time of NO_2 is plotted against the inverse temperature in Figure 6.8(b), and it follows Arrhenius behavior with an activation energy of about 550 J mol^{-1} and a pre-exponential factor of $1.04\times10^8\ s^{-1}$.

The rates of the rotational diffusion tensor components correspond to a moderate slow motion. This is because the time window of EPR resides between NMR and IR spectroscopy. A few small flaws in peak-to-peak amplitudes and line positions could not be improved by any different dynamic models. Similar problems had been encountered in earlier work on Na-Zeolon in which the simulation spectra were not very sensitive to the rates of $R_\parallel$ and $R_\perp$ components of the rotational diffusion tensor so their precision was about $\pm50\%$ [186]. In addition, slow-motion simulations were performed separately, which took into account the reorientation of the adsorbed NO_2 being close to axially symmetric about its molecular x and z axis, respectively. However, all simulated spectra provided quite different lineshapes than those of the experimental spectra. These results are clearly consistent with the theoretical simulations that a rotational diffusion only takes place about molecular y axis ($R_\parallel \parallel y$) of the adsorbed NO_2 [186].

It is generally known that continuous wave EPR spectra, especially at conventional frequencies, have only a limited resolution to the molecular motions. In the first instance, at the same motional rate, at conventional frequencies (e.g. at 9 GHz) the motionally narrowed spectra may be observed, whereas at higher frequencies (e.g. at 250 GHz) the spectra may display very slow motion, almost at the rigid limit. This behavior is a direct consequence of the increased importance of the g tensor as the magnetic field is

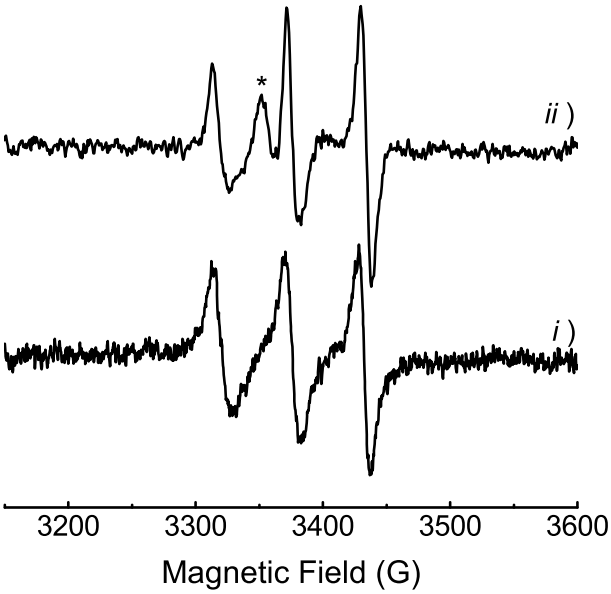

Figure 6.9: Comparison between X-band EPR spectra of the adsorbed NO_2 on the silver-free NaA zeolite recorded at 70 K (entry *ii*) and on the reduced Ag_6^+ cluster in 12% (wt.) Ag/NaA recorded at 125 K (entry *i*). The hyperfine splitting of these spectra are the same, only their intensities are slightly different. Both spectra are very close to isotropic. The tumbling rate of the adsorbed NO_2 on the NaA is quite rapid in comparison with that on Ag/NaA. A different paramagnetic center is marked by an asterisk.

increased. This snapshot feature has led to the recommendation of a multi-frequency EPR approach for studying the dynamics, because at higher frequencies EPR can "*freeze-out*" the slow tumbling motions of the molecule [187, 188].

In order to compare with previous results from Ag/NaA zeolite, NO (with oxygen impurity) was also adsorbed on the silver-free NaA zeolite at room temperature. The triplet spectrum developed over some days as NO_2 was formed. In Figure 6.9, the X-band EPR spectrum recorded at 70 K is compared with the spectrum recorded at 125 K arising from NO_2 on the silver cluster in 12% (wt.) Ag/NaA. At 70 K, there is a small peak of a different center which is marked by an asterisk. The two spectra are quite similar, thus leading to the conclusion that there is no significant spin density on the Ag_6^+ cluster, we are seeing the adsorbed NO_2 on a diamagnetic cluster. These hyperfine spectra are close to isotropic, though recorded at different temperatures. The higher tumbling rate of NO_2 on the silver-free zeolite shows that adsorption on the silver clusters is slightly stronger than on sodium ions.

6.1.3 General discussions

Interpretation of g and A tensors of adsorbed NO

The g tensor gives information on the symmetry, the spin-orbit coupling, and the excited electronic states. A large degree of orbital quenching is normally expected for solid state

species.

The spin density on the silver atom, to which NO is bound, amounts to ca. 10% based on the $A_{\mathrm{iso}}^{\mathrm{Ag}} = 67.0$ G (see Table 6.1). It contributes to the g anisotropy, especially to a significant deviation of g_{zz} from g_{e}. This is the crystal-field effect, and a weaker crystal-field correlates with a lower value of g_{zz}. Here $g_{\mathrm{zz}} = 1.841$ is significantly separated from the g_{xx} and g_{yy}. The g tensor is not quite axial, but the rhombic distortion from axial symmetry, $g_{\mathrm{xx}} - g_{\mathrm{yy}} = 0.004$, is quite small.

The spin-orbit interaction causes an orbital contribution to the angular momentum, while the crystal field has the tendency to quench the orbital angular momentum. Therefore, the Δg shift depends on the ratio of λ/Δ, i.e., the spin orbit coupling is compared to the crystal-field energy. The negative Δg shift obtained is typical for *'electron'* centers of a system, where $\lambda > 0$, while the positive Δg shift is characteristic of *"hole"* centers, for which $\lambda < 0$ [79].

The observation of the negative Δg shift indicates a partial quenching of the orbital angular momentum contributions to the g tensor occurring under the influence of the electrical crystal-field of the surrounding, here the interaction with the cluster. If the angular momentum of the $2p$ electron of a system is only due to spin angular momentum (spin-only electron Zeeman), wherein the orbital contribution is totally quenched, the g tensor will be isotropic or near g_{e}. It is adequate for systems with $S = 1/2$. The experimental spectrum of adsorbed NO reveals that the g tensor is not isotropic. The largely quenched or residual spin-orbit coupling mixes the excited $2\pi_{\mathrm{x}}^*$ and $2\pi_{\mathrm{y}}^*$ state into the $2\pi_{\mathrm{x}}$ and $2\pi_{\mathrm{y}}$ states. When the crystal-field dominates the spin-orbit coupling ($\lambda < \delta < \Delta$), the system may be treated by first order perturbation theory. The principle z axis of the g and A tensors is along the direction of the N-O bond, and the y axis defines the symmetry axis of the $2\pi_y^*$ orbital of the adsorbed NO in which the unpaired electron resides [167]. For the orientation of the applied magnetic field B_0 along the z axis ($B_0 \parallel z$, or $B_0 \perp xy$ plane), the orbital splitting by the crystal-field can be calculated using the experimental principle g_{zz} component. The spin-orbit coupling constant of NO is well known, ca. $\lambda = 123.16$ cm^{-1} [189], and the following equations are applied [79]:

$$\begin{aligned} g_{\mathrm{yy}} &= 2.0023 - (2\lambda/\Delta) \\ g_{\mathrm{zz}} &= 2.0023 - (2\lambda/\delta) \end{aligned} \tag{6.5}$$

Here δ measures the splitting energy of the $2\pi_x^*$ and $2\pi_y^*$ orbital and the Δ measures the splitting energy of the $2\pi_y^*$ and 2Σ orbital in the adsorbed NO molecule. If we use these equations and plug in $g_{\mathrm{zz}} = 1.841$, the energy splitting of the $2\pi_x^*$ and $2\pi_y^*$ orbital will be $\delta \approx 0.144$ eV. The splitting energy of the $2\pi_y^*$ and 2Σ orbital is about $\Delta \approx 1.260$ eV. These values represent the orbital splitting energy by the crystal field on the silver cluster.

Since the adsorbed NO has an unpaired electron, the multiplicity or degeneracy of such a state is $2S^* + 1$. When $S^* = 1/2 \approx J$, the degeneracy is only lifted by the external field, e.g. electric or magnetic field, and then an EPR signal is observable. As NO is adsorbed at an angle on the surface, the symmetry of the linear molecule is broken and the orbital contribution of the effective g factor deviates from unity, $g < 1$.

The only resolved hyperfine component of the ^{14}N nucleus is $A_{\mathrm{yy}}^{\mathrm{N}} = 33$ G (see Table 6.1). Thus, the isotropic coupling is $A_{\mathrm{iso}}^{\mathrm{N}} = 11$ G which is to be compared to 646 G of the full $2s$ orbital contribution to the hyperfine coupling of an ^{14}N atom [32, 133]. The $2s$ orbital contribution is ≈ 0.017, thus indicating that the unpaired electron is mostly in

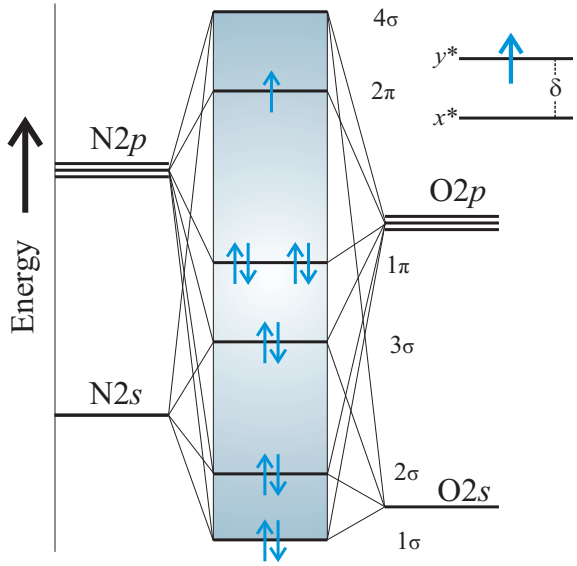

Figure 6.10: A schematic representation of molecular orbitals for the free NO molecule. The splitting energy δ between the $2\pi_x^*$ and $2\pi_y^*$ orbitals of the NO molecule in the crystal field after adsorption on the silver cluster.

the $2p$ orbital of NO. The principle values of the anisotropic hyperfine coupling for one unpaired electron in the p orbital are calculated from the following equations,

$$\begin{aligned} A_{\parallel}^{\mathrm{N}} &= A_{\mathrm{iso}}^{\mathrm{N}} + B_{\parallel}^{\mathrm{N}} = A_{\mathrm{iso}}^{\mathrm{N}} + 2b \\ A_{\perp}^{\mathrm{N}} &= A_{\mathrm{iso}} + B_{\perp}^{\mathrm{N}} = A_{\mathrm{iso}}^{\mathrm{N}} - b \end{aligned} \tag{6.6}$$

and the extracted values are tabulated in Table 6.1. Using the Equation (6.6), the value of $b = 11$ G will be compared to $\frac{2}{5}(49.5)$ or 19.81 G of an ^{14}N atom [133]. Thus a spin density contribution of 0.555 in the $2p$ ^{14}N orbital describes the anisotropy, while a contribution of 0.445 is left for the $2p$ ^{16}O orbital in a first approximation. However, the unnormalized wave function of the unpaired electron in the adsorbed NO can be expressed as a combination of atomic orbitals: $\psi \approx \sqrt{(0.1)}\psi_{5\mathrm{s}}^{\mathrm{Ag}} + \sqrt{(0.017)}\psi_{2\mathrm{s}}^{\mathrm{N}} + \sqrt{(0.555)}\psi_{2\mathrm{p}}^{\mathrm{N}} + \sqrt{(0.445)}\psi_{2\mathrm{p}}^{\mathrm{O}}$. The contribution of one Ag to the spin density distribution is included since the isotropic hyperfine coupling, $A_{\mathrm{iso}}^{\mathrm{Ag}} = 67.0$ resolved experimentally, accounts for a spin population of about 0.1 in the $5s$ orbital, and the total spin population is therefore 1.117. Besides the contribution of Ag and N this also accounts for a small fraction of spin polarization.

The anisotropic part of hyperfine interaction can give information on a distance of the electron to the coupled nucleus and the following formula will be applied for finding the value of r

$$b = \frac{2}{5}\frac{\mu_0}{4\pi} g_n \beta_n \left\langle \frac{1}{r^3} \right\rangle_p \text{ [in G]} \tag{6.7}$$

where the angular brackets imply an integration over the p orbital [32]. Currently, the integration goes over the unpaired electron distribution on the $2p_y$ orbital, the angular brackets are replaced by $\int_0^{\pi} \frac{3\cos^2\theta - 1}{r^3} d\theta$ because the integration is to be with respect to the angle θ. By using the experimental b (11 G) we finally calculated the distance from the unpaired electron to a coupled ^{14}N nucleus, ca. $r \approx 70 \times 10^{-12}$ m (70 pm). This

is a slightly less than that for free NO (115 pm). As was stated elsewhere [190], the ionic radius is not always a fixed parameter for a given ion, but varies with coordination number, spin state and other parameters. For the same element, an ion in a high-spin state will be larger than the same ion in a low-spin state, while the ionic size can also increase by increasing coordination numbers.

One should keep in mind that such calculations should only be applied for systems containing a localized electron spin, and therefore these results provide only very rough estimations for our system. An approximation leads to an underestimate of the distance to the unpaired electron that can therefore be regarded as a lower limit.

Interpretation of g and A tensors of adsorbed NO_2

All principle values of the g tensor are assumed coaxial with components of the A tensor. g_{yy} is always the intermediate component that is less than the g_e value. The system is asymmetric, but the g_{xx} = 2.0078 and g_{zz} = 2.0054 components are very close so the symmetry is near-axial. The s orbital contribution of one Ag nucleus probably exists in the spin density distribution to some extent. The somewhat higher values of two g components are also taken as evidence of some admixture of the transition metal orbital. In the presence of both g and A anisotropies the left and right sides of the spectrum exhibit different linewidths.

The NO_2 carries the unpaired electron ($S = 1/2$) in the $^2A_1$ ground state. The experimental A_{iso} = 56.4 G is compared to 550 G of the full 2s orbital of the $^{14}NO_2$ radical in $NaNO_2$ [185], thus the spin population is about 0.10 (ca. 10%). A very small anisotropy is observed, i.e. B_{xx} = -3.6 G, B_{yy} = -6.4 G and B_{zz} = 10 G, that is summarized in Table 6.2. The smallness of these values indicates that NO_2 is not rigidly fixed at the surface. By assuming $A_{xx} \approx A_{yy} = A_\perp$ and $A_{zz} = A_\parallel$, the value of b = 5 G is obtained from Equation (6.6). As it is compared to $\frac{2}{5}$(49.5) or 19.81 G of the ^{14}N atom, the spin population is $\approx$ 0.252 in the 2p orbital of NO_2. The spin population in the 2p orbital of each oxygen atom is about 0.373 as estimated from $\rho_O \approx \frac{1}{2}(1 - \rho_N)$. The 2$p$ and 2s orbital ratio reflects the orbital hybridization, $2p/2s \approx 2.5$ for the ^{14}N nucleus, which is somewhat larger than expected for the 134^0 bond angle of NO_2.

For the rigid limit simulation, the effect of the ^{14}N nuclear quadrupole **Q** tensor could be omitted since the principal values (0.32 G, 0.58 G, -0.90 G) were much smaller than components of the A tensor [183].

Slow motion at different temperatures

NO_2 is usually rotating about its twofold axis z (see the inset in Figure 6.6), even in a solid, then a small anisotropy arises from the rotation [191]. In a molecular dynamic simulation, a molecule is set in motion by heating it to a specified temperature. The spectrum of the rotating species exhibits typical features in which the two separated components of the static species are merged by averaging to one line that appears in the center of gravity of the components (depicted in Figure 6.7).

The rotational diffusion is anisotropic with $N \equiv R_\parallel / R_\perp \approx 5.0$ at 30 K. The magnetic interactions are however anisotropic, e.g. the g tensor and the A tensor deviate from axiality. At 40 K, the lineshape of the spectrum reflects an intermediate rotational diffusion with $N \equiv R_\parallel / R_\perp \approx 3.3$. Finally, it becomes very rapidly nearly isotropic with $N \equiv R_\parallel / R_\perp \approx 2.0$ - 1.3 from 50 K to 90 K. The simulation suggests that the rotation takes place about the molecular y axis at lower temperature and occurs isotropically at higher

temperature. The spectrum is almost isotropic at 125 K which is plotted in Figure 6.9. The rotational diffusion of adsorbed NO_2 on different supports were still anisotropic in the relatively high temperature range of 110 - 180 K, suggesting that NO_2 binds more strongly [179, 181, 182, 186]. Interestingly, the resolutions of the x and z components of the high field hyperfine line (M_I = - 1) were not always identical for NO_2 on these different supports.

Spin-exchange narrowing was not detected by the EPR measurements. Exchange narrowing would cause the hyperfine lines to coalesce into a single line that becomes narrower at even higher concentrations, if they are indeed present. However, all three lines are still disctinct at 125 K in Figure 6.9. The encounter frequency of NO_2 is considerably less than in the gas phase because it is hindered in the zeolite pores. In contrast, the Brownian rotational model and the Heisenberg spin exchange model were used simultaneously to simulate and explain the motional dynamics of NO_2 on different supports [179, 181, 182, 186].

Dipolar effect

It is adequate to discuss a dipolar effect on adsorbed NO_2 spectra as a function of temperature. The low-field line (M_I = +1) is broader than the high-field line (M_I = -1) at 70 K to 110 K (see Figure 6.7). In a theoretical approach, if the nucleus has a p orbital that is part of the π-electron system and contains the unpaired electron, then for such nuclei the high-field components of the spectra are broader due to positive isotropic hyperfine coupling constant [32]. Perhaps the opposite is true here, since most of the spin density is on the oxygen atoms of NO_2. The linewidth of each hyperfine component has the following form: $\Gamma = \alpha + \beta M_I + \gamma M_I^2$. The coefficients depend on the anisotropy of the g tensor and of the A tensor as well as the mean tumbling rate. The spectral parameters, β and γ, were obtained from the experimental spectra of nitric oxide in frozen solution [192]. From these parameters the correlation time (τ_c) of the anisotropic tumbling was calculated iteratively. The formula, to give access to τ_c through these spectral parameters, primarily applied the anisotropy of the g and the A tensor, and the deviations from axiality were also supplemented elsewhere [192]. However, the access to the correlation time is not proposed for the present, we consider here only a general form of the formula ([192]) to derive spectral parameters of adsorbed NO_2.

$$\beta = \tfrac{1}{2}\Delta B_{pp}\left[(h_0/h_{+1})^{\frac{1}{2}} - (h_0/h_{-1})^{\frac{1}{2}}\right]$$
$$\gamma = \tfrac{1}{2}\Delta B_{pp}\left[(h_0/h_{+1})^{\frac{1}{2}} + (h_0/h_{-1})^{\frac{1}{2}} - 2\right] \quad (6.8)$$

In Equation (6.8), ΔB_{pp} is the peak-to-peak linewidth in Gauss of the M_I = 0 line. The $h_{\pm 1}$ and h_0 are the first derivative amplitudes of $M_I = \pm 1$ and M_I = 0 lines, respectively. Both parameters are positive and decrease as $R_\perp$ increases, in agreement with theory. The coefficients β depend on the anisotropy of the magnetic tensors and cause the spectrum to appear asymmetric. At 30 K to 40 K, the coefficient γ is relatively close to β, but it decreases rapidly at higher temperatures. γ is a function only of the hyperfine anisotropy. α is a constant term including all line broadening effects that are the same for all hyperfine components, but it is difficult to evaluate α from the experimental spectra. Anyway, β and γ decrease as a function of temperature, which correlates with the anisotropic rotation becoming rapidly isotropic. The parameters are summarized in

Table 6.3.

A few words are summarized for conclusions relating to the adsorption of NO. The paramagnetic Ag_6^+ cluster was stabilized in NaA by hydrogen reduction. The reduction leads to unpaired electron density on the molecular orbitals delocalized over the Ag_6^+ cluster which is quite stable in the broad range of temperatures of 4.0 - 200 K. The cluster is observable even at room temperature.

The cluster hyperfine structure immediately disappeared when NO gas was adsorbed. The reaction monitored by EPR demonstrated that there is no significant spin density on the silver cluster, the adduct is adsorbed on a diamagnetic cluster because a red-ox reaction precedes the adsorption of NO. The $g_{zz} = 1.841$ component of the adsorbed NO spectrum is split by the hyperfine coupling of $A_{zz}^{Ag} = 200$ G which renders the crystal field and lifts the orbital degeneracy of NO. Only the hyperfine component $A_{yy}^{N} = 33$ G was experimentally resolved, and the unpaired electron was mostly centered in the $2p$ orbital of the ^{14}N. Allowing no doubt, the reduced Ag_6^+ cluster containing Ag/NaA zeolites have demonstrated quite diverse activities to interact with nitrogen monoxide, e.g. different than a photo-catalytic reactivity for the photodecomposition of NO and a selective catalytic reduction which leads to a direct decomposition of NO into N_2 and O_2. From the cancellation pattern of HYSCORE, the corresponding $A_{iso}^{N} \approx 1.5$ MHz is considerably smaller than the ^{14}N-hyperfine coupling resolved in the continuous wave EPR spectrum, which is too large for being observed in the HYSCORE spectrum. The small ^{14}N-hyperfine interaction is thus assigned to a second nitrogen spin in the vicinity of the silver cluster. As an explanation, N_2O molecules may also be adsorbed on the silver clusters, exhibiting a strongly anisotropic distribution of spin densities over the two nitrogens.

In the rigid limit, the principle values of magnetic tensors the adsorbed NO_2 were fairly comparable with earlier results. The NO_2 rotational motion dynamics was studied by EPR spectroscopy, suggesting that the axial rotation takes place about the molecular y axis at lower temperatures. It is however considered that the motion is a large amplitude tilting and flipping of the NO_2 which is bound via N to the silver cluster, rather than a full rotation. The motion approaches very rapidly isotropic conditions from 50 K to 90 K. Analysis of $\tau_\perp$ derived from the EPR lineshapes was performed to provide the kinetic parameters, and the Arrhenius plot gave access to $E_a = 550$ J mol^{-1} for the overall rotational motion. It indicates that NO_2 is only very weakly adsorbed on the silver cluster, more weakly than on other supports, but more strongly than on the silver-free zeolite.

It is ultimately concluded that a simple stoichiometric pathway for adsorption of NO onto the silver cluster is a red-ox reaction corresponding to $3NO \rightarrow N_2O + NO_2$.

6.2 EPR results of O_2 adsorptions

Various forms of the adsorbed oxygen species have been proposed on the basis of kinetic adsorption data and electric conductivity measurements, however, the role of oxygen in surface reactions still remains uncertain. Very little direct spectroscopic evidence is available apart from that provided by EPR spectroscopy, and different oxygen ion species were, i.e. O^-, O_2^- and O_3^-, firmly established [193]. Nevertheless, the hyperfine splitting spectra of these oxygen ion species were quite different from each other depending upon the unpaired electron trapping metal surfaces, thus making the assignments for distinct ion species from one another very doubtful.

There was no effect on the hyperfine coupling of the Ag_6^+ cluster as $^{16}O_2$ was exposed to it at room temperature. The interaction of $^{17}O_2$ with the reduced Ag_6^+ cluster was monitored by means of cw EPR that revealed a kind of molecular motions causing the anisotropy of the hyperfine spectrum of the silver cluster at 3.0 K. The disappearance of motional effects with the presence of $^{17}O_2$ was very instantaneous at 7.0 K to 10.5 K.

6.2.1 Adsorption of $^{16}O_2$

Examination on the interaction of the reduced Ag_6^+ cluster with $^{16}O_2$ revealed no distortion of the cluster hyperfine structure. After adsorptions at room temperature, the signal intensity (or peak-to-peak amplitude) of the silver clusters decreased with increasing of gas pressure. As is depicted in Figure 6.11, the hyperfine splitting spectra remain well defined. All the measurements were performed at 4.0 K to 20 K. $^{16}O_2$, which has no nu-

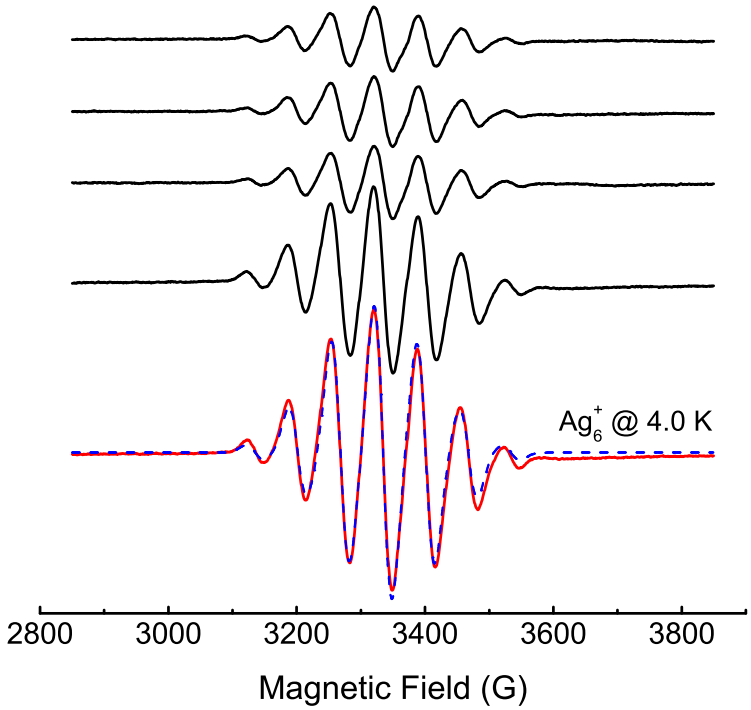

Figure 6.11: X-band EPR spectra recorded at 20 K after each consecutive adsorption of 200 mbar $^{16}O_2$ exposed to the reduced Ag_6^+ cluster at room temperature (from bottom to top). The hyperfine splitting pattern of the cluster is unchanged, even though the intensities are getting weaker. The spectrum of the cluster before adsorption is marked as Ag_6^+ @ 4.0 K, and the dashed line represents the corresponding numerical spectrum simulation.

clear spin, dominates in the natural abundance ($> 99.8\%$) so that no hyperfine coupling is observed experimentally. As the orbital degeneracy of $^{16}O_2$ is lifted, its symmetry is broken on adsorption, and EPR signals of oxygen ion species may become observable. However, the only effect of oxygen adsorption is a decrease of the signal amplitude,

which means that apparently the oxygen renders the silver clusters somehow EPR inactive by oxidizing them.

High abundance of silver anion clusters with a certain size (so-called magic numbers) is often related to particular stabilization in closed shell geometric or electronic structures [194, 195]. These silver cluster were very active for O_2 adsorptions. The only magic cluster with six equivalent atoms is a regular octahedron. Assuming that each silver atom of the Ag_6^+ cluster contributes its 5*s* unpaired electron to the delocalized cluster orbital we conclude that paramagnetic silver clusters have no electronic closed shells. It is a common experience that the closed shell system would need 8 electrons at least and be diamagnetic at all.

6.2.2 Adsorption of $^{17}O_2$

Below 10 K the interaction of $^{17}O_2$ (I = 5/2 nucleus) with the reduced Ag_6^+ cluster leads to a distinct and remarkable behavior which was not observed with $^{16}O_2$. This is demonstrated by the EPR spectra shown in Figure 6.12, where the spectrum is clearly anisotropic at 3.0 K. As temperature rises, the spectrum shifts gradually to isotropic and the hyperfine lines become symmetric at temperatures of 10.5 K to 20 K. These features are fully reversible, thus leading to a tentative conclusion that the adsorbed $^{17}O_2$ causes an observable alteration in the total wavefunctions of the Ag_6^+ cluster. However, neither HYSCORE nor EPR reveals the hyperfine coupling of $^{17}O_2$.

Furthermore, changes in the hyperfine splitting spectra are very instantaneous, thereby considering that the adsorbed $^{17}O_2$ molecules are not adsorbed rigidly at the surface of the Ag_6^+ cluster. If there is a kind of molecular motion affecting the real lineshape of the Ag_6^+ cluster, it will not be similar to a well-known theoretical model underlying *slow*, *jump*, and *fast rotational* motions of the molecule. It is therefore reasonable that there is the quantum mechanical contribution (simply *residual motions*) to the molecular motions of the exposed $^{17}O_2$ molecule. Assuming that there is, however, a rotation to take place about the z axis (rotating in the xy plane, the O_2 bond axis is along x and y axes) of the $^{17}O_2$ molecule that is perpendicular to the bonding of oxygen atoms. This is an approach to calculate the moment of inertia of the molecule using the average distance (r = 1.21 $\times 10^{-10}$ m) between the two ^{17}O atoms at room temperature and the mass (m = 2.82 $\times 10^{-26}$ kg) of each ^{17}O atom. Thus, a straightforward application to define the moment of inertia I is

$$I = \sum_i m_i r_i^2 = m\left(\frac{r}{2}\right)^2 + m\left(\frac{r}{2}\right)^2 = \frac{mr^2}{2} \tag{6.9}$$

where the rotation axis is considered to pass through the center of $^{17}O_2$ molecule and perpendicular to the bond. Finally, it is found that the moment of inertia is equal 2.10×10^{-46} kg·m^2 for $^{17}O_2$ and higher than that of $^{16}O_2$ (1.95×10^{-46} kg·m^2). In an approach according to quantum mechanical motion, the particle on a sphere is a reasonable model for the description of the rotation of a diatomic molecule, because the molecule is currently considered not rigid and free to move. In general, the energy of the rotating particle is related to its angular momentum J by $E = J_z^2/2I$. According to the solution of the Schrödinger equation, the energy E of the rotating molecule can be restricted to the values

$$E = l(l+1)\frac{\hbar^2}{2I} \tag{6.10}$$

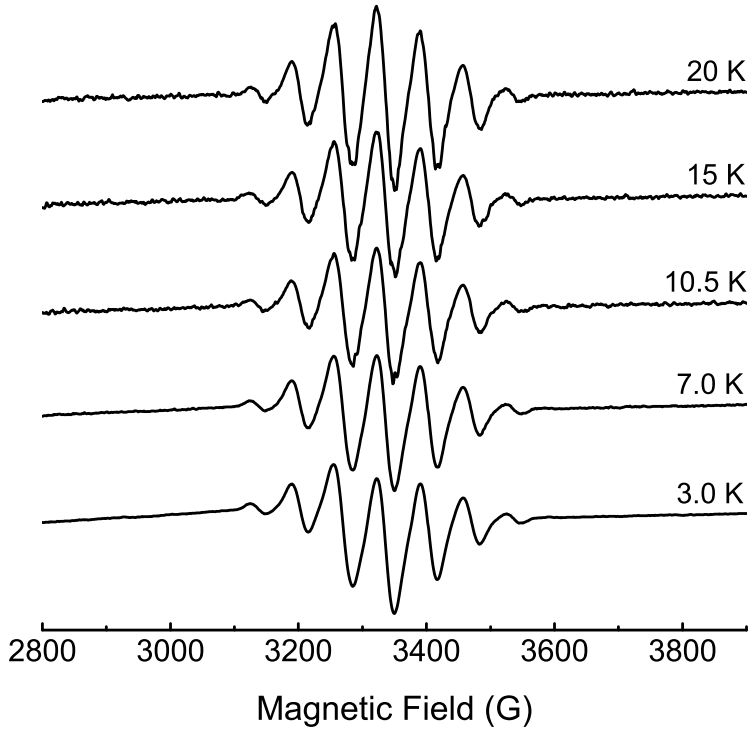

Figure 6.12: X-band EPR spectra recorded at different temperatures after adsorbing 250 mbar of $^{17}O_2$ on the reduced Ag_6^+ cluster at room temperature. At 3.0 K, the hyperfine spectrum appears quite anisotropic, and as measurement temperature increases the spectra become gradually isotropic. It is assumed that $^{17}O_2$ is not adsorbed rigidly at the surface but exhibits dynamic behavior that causes the anisotropy of the Ag_6^+ cluster.

where l is the orbital angular momentum quantum number ($l = 0, 1, 2, \dots$) and I is the moment of inertia. From Equation (6.10), the energies of the rotational levels are therefore 0 ($l = 0$), 0.053 zJ[1] ($l = 1$), 0.159 zJ ($l = 2$), and 0.318 zJ ($l = 3$) according with the magnitudes of the orbital angular momentum. The degeneracies of these levels are 1, 3, 5, and 7, respectively (corresponding to $2l + 1$). A separation between the rotational $l = 0$ and $l = 1$ levels is in the order of $\Delta E = 0.053$ zJ, and this energy corresponds to $\approx$ 32 J mol^{-1}. Furthermore, the rotational energy level separation ΔE of $^{17}O_2$ amounts to $\approx$ 96 J mol^{-1} between $l = 0$ and $l = 2$. This corresponds to RT at ca. 12 K, so rotation can get excited at that temperature. A transition between the first two rotational levels of the $^{17}O_2$ molecule can be excited by photon absorption with a frequency of

$$\nu = \frac{\Delta E}{h} = \frac{0.53 \times 10^{-22}\ \text{J}}{6.626 \times 10^{-34}\ \text{J} \cdot \text{s}} = 0.7993 \times 10^{11}\ \text{Hz} = 79.93\ \text{GHz} \tag{6.11}$$

where h is Planck's constant. Although radiation of this frequency still belongs to the

[1] zepto-joules - 10^{-21} J

microwave region of the electromagnetic spectrum, X-band EPR spectroscopy is even not sufficient to excite the transition between the first rotational energy levels or states of the $^{17}O_2$ molecule. Unfortunately, HYSCORE experiments did not reveal any transitions and nuclear coherences due to the interaction of $^{17}O_2$ with the reduced Ag_6^+ cluster.

6.3 EPR results of C_2H_4 adsorption

The Ag catalysts are almost unique, *inter alia*, for a selective oxidation of ethylene to ethylene-oxide. Relatively large ($\approx$ 5 nm) Ag particles supported on a non-porous α-Al_2O_3 surfaces tailored to catalyze a specific reaction, viz. a selective oxidation of ethylene to ethylene-oxide at an elevated temperature of 523.5 K [27].

X-band EPR investigations previously proved that mono and bi-ligand silver-ethylene complexes were stabilized by co-condensation of Ag atoms with C_2H_4 in rare-gas matrices at low temperatures of 4.0 K to 77 K [196, 197, 198]. However, information on the hyperfine coupling of Ag-molecule adsorption complexes was rather equivocal. Further, the studies of interactions between the supported paramagnetic $Ag_6^+ \cdot 8Ag^+$ cluster and C_2D_4 demonstrated that the reactions caused a rapid disintegration of the silver cluster into smaller clusters, e.g. Ag_3 or Ag_4, below room temperature [199]. The original cluster was produced by γ-irradiation in fully loaded Ag_{12}/NaA zeolite. It is thus interesting to note the activity of the paramagnetic Ag_6^+ cluster against C_2H_4.

6.3.1 ENDOR

The Mims ^{1}H-ENDOR spectrum recorded at a magnetic field of 3443 G and a microwave frequency of ν_{mw} = 9.732 GHz exhibits a strong signal with center frequency ν_H = 14.7 MHz corresponding to the proton Larmor frequency which is illustrated in Figure 6.13(a). The signal reveals the extremely weak hyperfine coupling of the protons, ca. $A \approx 1.7$ MHz, while the central sharp powder pattern with the small splitting (< 1 MHz) is due to very remote ^{1}H nuclei. Within the experimental resolution it seems to be isotropic, indicating that the observed protons of C_2H_4 are presumably equivalent. On the other hand, no resolution for hyperfine anisotropies makes the spectrum impossible to provide information on the orientation dependence of the ^{1}H nuclei by ENDOR. Virtually all orientations contribute to the ENDOR spectrum. The hyperfine interactions of the weakly coupled protons were not observed by the Davies ^{1}H-ENDOR measurements because of hyperfine selectivity.

Also by Mims ENDOR experiments the nuclear frequencies of ^{27}Al and ^{29}Si ($I = 1/2$) were nicely resolved at the positions of 3.93 MHz and 2.93 MHz, respectively (see Figure 6.13(b)). The absence of an isotropic coupling indicates that the unpaired electron does not delocalize onto the zeolite framework, and the signals arise from dipolar coupling to nuclei in the immediate environment. The weakness of the Si signal is due to the low natural abundance of the ^{29}Si isotope (4.7%), while the more abundant isotope ^{28}Si has no nuclear spin.

6.3.2 HYSCORE

In the case of the weakly coupled nucleus, when the hyperfine coupling is smaller than twice the nuclear Larmor frequency ($A < 2\nu_L$), the dominant cross peaks will be

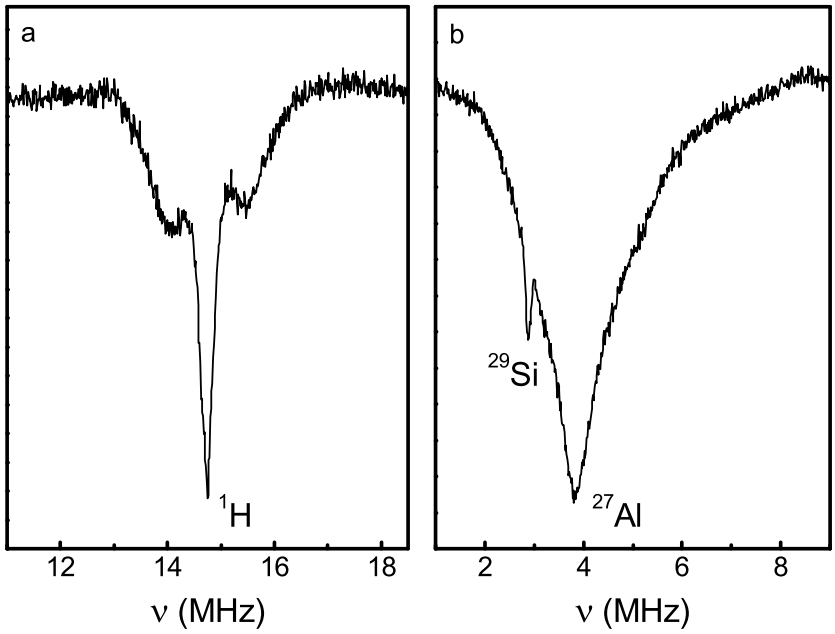

Figure 6.13: a) X-band Mims ^{1}H-ENDOR displayed around the center frequency of the proton at the corresponding field of 3443 G. b) Mims ^{29}Si- and ^{27}Al-ENDOR displayed around the center frequency of the nuclei at the corresponding field of 3443 G. The ENDOR data were taken at field positions corresponding to $g = 1.965$ of the X-band EPR spectrum. The spectra were recorded at 10 K after adsorbing C_2H_4 on the reduced Ag_6^+ cluster at room temperature.

observed in the $(+,+)$ quadrant, whereas a strongly coupled nucleus gives rise to the cross peaks in the $(-,+)$ quadrant of the HYSCORE spectrum.

HYSCORE measurements were carried out at 10 K at a magnetic field of 3340 G. Two-dimensional plots of the spectra are depicted in Figure 6.14. The strong peak at 3.90 MHz corresponds to the nuclear Larmor frequency of ^{27}Al (ν_{Al} = 3.89 MHz) representing framework nuclei of the lattice as discussed in Figure 6.13. This peak demonstrates that the isotropic hyperfine interactions and quadrupole interactions are small. Furthermore, the presence of the matrix peak proves the close proximity of the lattice to the Ag cluster. ^{27}Al is naturally most prominent to contribute to quadrupole hyperfine coupling due to its I = 5/2 nucleus. However, ^{27}Al peaks arising from combination frequencies of the type (ν_α,$2\nu_\beta$) and ($2\nu_\alpha$,ν_β) transitions were not observed, while the cross-peaks in the $(-,+)$ quadrant corresponded to the signal due to the $2\nu_L$ or $A/2 \approx 3.5$ MHz condition.

The nuclear Larmor frequency of ^{1}H is naturally observed at the frequency position of ν_{H} = 14.7 MHz in the $(+,+)$ quadrant of the spectrum (see Figure 6.14). A pair of ^{1}H cross-peaks perpendicular to the diagonal, which corresponds to $(\nu_\beta,\nu_\alpha)_{\mathrm{H}}$ centered at 14.0 MHz and 15.7 MHz, represents a very weak hyperfine coupling of protons with $A \approx 1.6$ MHz which is deduced from $A \approx \nu_\alpha - \nu_\beta$. This is in good agreement with the result obtained by ENDOR experiments on the hyperfine coupling of ^{1}H in the environment. Both ridges only exhibit a small maximum shift $\nu^{\mathrm{S}}_{\mathrm{max}} \approx 0.05$ MHz from the $\nu_1 = -\nu_2$ frequency axis, corresponding to a dipolar hyperfine coupling of $T \approx 1.6$

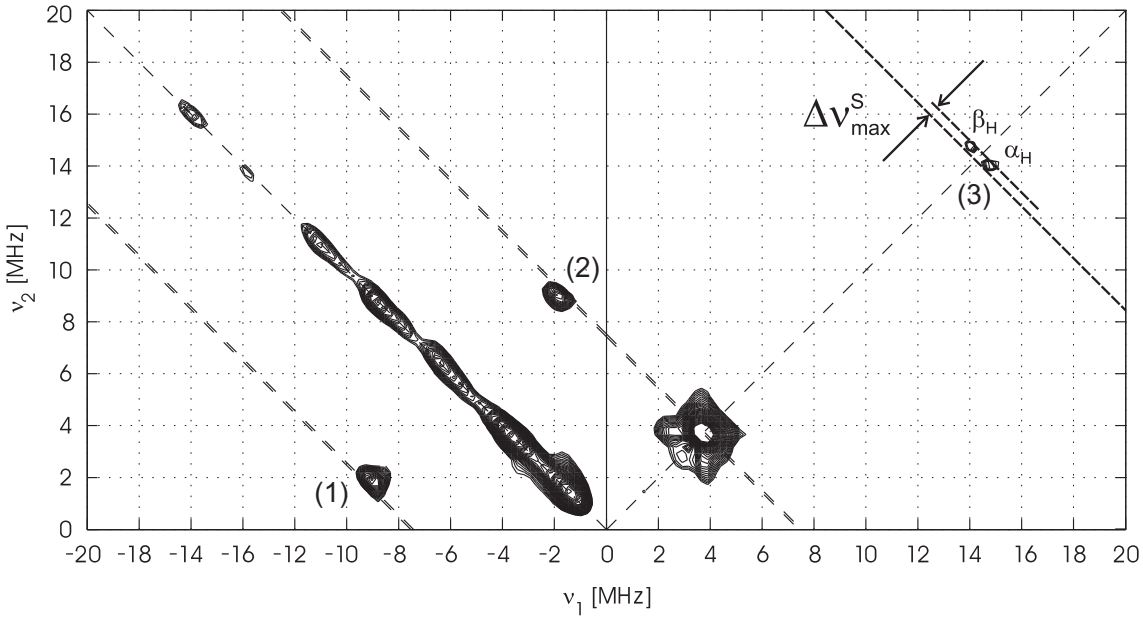

Figure 6.14: X-band HYSCORE spectrum of C_2H_4 adsorbed on the reduced Ag_6^+ cluster sample recorded at 3340 G and 10 K. The ^1H nuclear Larmor frequency at the corresponding magnetic field is 14.9 MHz. The maximum frequency shift ν^S_{max} of the cross-peaks from the $\nu_1 = -\nu_2$ frequency axis is illustrated by a dashed line. (Spectra were obtained from PD Dr. R.-A. Eichel at the Eduard-Zintl-Institute, Darmstadt University of Technology.)

MHz which is calculated applying $T = 4/3(2\nu_L\Delta\nu^S_{max})^{1/2}$ in the limit of the point-dipole approximation. Thus, the isotropic hyperfine coupling is only on the order of $A_{iso} < 0.1$ MHz. By using $T \approx 1.6$ MHz from the HYSCORE experiment, a distance of ≈ 3.7 Å between the electron spin and the proton is estimated based upon the point-dipole approximation $T = \mu_0/4\pi(gg_n\beta_e\beta_n/r^3h)$. It is only adequate for localized spin wavefunctions, the calculated distance is therefore regarded as a lower limit since the unpaired electron is strongly delocalized through Ag clusters.

6.4 XAS results of gas interactions

6.4.1 Red-ox properties

Understanding the **oxidation** and **reduction** process of small metal clusters in the pores of supports is of great importance in particular. However, no evaluation of kinetic data has been attempted since a simple kinetic model cannot be proposed for the complex mechanisms during the oxidation and reduction towards the formation of Ag clusters in Ag/NaA.

By heating Ag/NaA *in vacuo*, intensive color changes, from white to yellow or dark yellow depending on a silver loading, were observed and assigned to the formation of partly reduced silver clusters coexisting with Ag^0 due to *autoreduction* of the exchanged Ag^+ in the zeolite pores by the presence of **zeolitic water** and **lattice oxygen** [43, 44, 200]. This process was considered accompanying a dehydration process at elevated temperatures of 573 K to 748 K [141, 165, 201, 202, 203]. At this stage it was assumed that the

dehydration process leads to a redistribution of Ag^+ (silver ions), thereby intensifying the cluster formation, and is accompanied by the loss of lattice oxygen on heating. It means that the exchanged Ag^+ were reduced by *oxide ions* to Ag^0 (silver atoms). Oxide ions were released from the lattice, and the whole process proceeded by two separate reaction mechanisms. Initially, it was oxide ions of residual water molecules which were reduced to oxygen gas, while leaving H^+ or protons on the lattice [165, 204]. Approximately 1/3 of the water molecules remained per unit cell after an initial vacuum-dehydration process at 623 K, which reacted with Ag^+, whereas the residual 2/3 were removed from the lattice without any reactions by further dehydrations. This process was expressed by the following simple equation:

$$Ag_2(H_2O)^{2+} \rightarrow 2H^+ + 2Ag^0 + 1/2O_2. \tag{6.12}$$

The reaction apparently led to a decrease of the number of Ag^+ in the unit cell. As the silver loaded sample was continuously dehydrated at 723 K, the availability of the water molecules was depleted, additional Ag^+ could only be reduced by oxide ions of the zeolite lattice. This was the second mechanism and described by the unit cell reaction:

$$Ag_2^0Ag_{10}^+H_2^+Si_{12}Al_{12}O_{48} \rightarrow Ag_4^0Ag_8^+H_2^+Si_{12}Al_{12}O_{47} + 1/2O_2. \tag{6.13}$$

It was finally considered that the produced Ag^0 migrate and interact with other Ag^0 and Ag^+ to form the cationic Ag_m^{n+} clusters which are immobilized at specific sites of the lattice [200]. It is reasonable that the mobility of Ag^0 is enhanced due to electrical neutrality. We expect that the interaction of the reduced Ag^0 with other atoms and ions is driven by the attraction force such as van der Waals interaction to form the autoreduced clusters. The bonding between atoms of such clusters can be at least partially covalent, thereby rendering the closed-shell electronic structure. Very often the autoreduced Ag clusters are not EPR active [44].

Our ultimate aim is to synthesize and stabilize paramagnetic Ag clusters in the pores of Ag/NaA. It is currently believed that **oxidation** prevents Ag^+ and the silver clusters from being **autoreduced** in the lattice. In the narrower sense, oxygen treatment renders the migration of silver ions (Ag^+) from other lattice framework sites to specific sites, which immobilize/entrap ions for forming silver clusters, if an ion-exchange is at a lower rate [43]. It is however noted that autoreduction is an inevitable consequence of dehydration, since oxidation is performed at a temperature range of 298 K to 673 K. Anyway, oxidation depletes significantly the level of autoreduction. In general, autoreduction causes distortions in the lattice by losing/releasing oxygen at higher temperatures of 400 K to 700 K to preserve charge balance, and the coordination sphere of the silicon and aluminum in the framework remains incomplete [141]. Oxygen deficient sites and reduced silver ions leaving these damaged sites are irreversibly formed [141, 203]. However, additional oxygen treatments can cause re-adsorption of missed silver on the lattice framework, only while suitable lattice sites will be available for newly oxidized silver ions [203].

Subsequently, hydrogen reduction is performed to stabilize the nano-size paramagnetic Ag_6^+ clusters. The whole process is the principle difference of our preparation strategy for forming paramagnetic silver clusters, whereas hydrogen reduction of Ag/NaA were previously followed by oxidation at elevated temperatures [203]. The point is the red-ox properties of Ag^+ and Ag clusters are reviewed in this section. The changes in the local structure of silver clusters are compared at each step of oxidation and reduction.

The experimental results of *in-situ* EXAFS spectroscopy measurements are currently introduced.

Oxidized clusters

The silver loaded catalysts of 12% (wt.) Ag/NaA were previously heated in the temperature range of 298 K to 673 K under oxygen flow for 6 hours and followed by vacuum-dehydration overnight. By treatments at 673 K, the formation of oxidized silver clusters is favored and the size is expected to be larger, but it is still in the nano-size range.

By collecting the absorption fine structure spectra at the Ag *K*-edge, the oxidized and dehydrated Ag/NaA sample was evacuated using the *in-situ* cell (or simply dynamic vacuum) at room temperature. The data were isolated in the range of k from 3 to 14 Å^{-1} using different k-weightings, and the oscillatory $\chi(k)$ function of oxidized silver clusters was completely different from that of bulk Ag. The corresponding spectrum of the k^2-weighted $\chi(k)$ function and its Fourier transform are illustrated in Figure 6.15. The significant loss in intensity of $\chi(k)$ is due to the very small size of silver clusters as illustrated in Figure 6.15(a). The real and imaginary parts of the FT spectrum nicely fit with the simulated spectrum, which is shown in Figure 6.15(b). The structural parameters of oxidized Ag clusters deduced from the multiple-shell fitting are summarized in Table 6.4. It is emphasized that the use of the two-shell model for the Ag-Ag contribution improves the fit results significantly. The coordination number of the first and second Ag-Ag shell provides an estimate of the mean size of oxidized silver clusters.

The absorbing atoms of oxidized Ag clusters have an average coordination of $N \approx 0.40 \pm 0.05$ at an average distance of 2.92 Å in the second Ag-Ag shell, whereas the first Ag-Ag shell at 2.71 Å has $N \approx 5.60 \pm 0.05$ on average. The coordination of the second Ag-Ag shell indicates that this shell is merely begun to develop. The total coordination is 6.0 ± 0.1 which corresponds to the cluster size with 13 ± 0.5 atoms. It is probably better to discuss about the size of oxidized silver clusters based upon cation occupation sites in NaA zeolite. There are three sets of equivalent occupied cation sites. One set contains eight sodium ions per pseudo unit cell (six-ring positions, S6), one set three ions (eight-ring positions, S8 in the center of the α-cage), and one set only a single ion (four-ring position, S4L in the site of the α-cage), which adds up to 12 sodium ions per pseudo unit cell. In NaA, first the **four-ring Na^+** is exchanged for Ag^+, followed by the **three eight-ring ions**, while the **eight six-ring ions** are exchanged only at the end [205]. In the present case, only two Na^+ are exchanged by Ag^+ per unit cell according to a simple stoichiometric calculation, suggesting that a first Ag^+ is in the four-ring site while a second one is in the center of the α-cage due to an incomplete exchange. As was previously stated elsewhere (in page 96 and reference [43]), oxygen treatment presumably induces some other eight-ring Ag^+ of different unit cells to migrate to the cluster trapping α-cage in which oxidized silver clusters can be formed and accumulated as silver ions and atoms interact with each other. It is to remember that oxidation is performed at 673 K. In addition, only one type Ag^+ was observed in the center of eight-ring of dehydrated Ag/NaA and had rather long distances to framework oxygens with very weak coordinations [206], suggesting that these ions can be easily removed from the occupation sites. On the other hand, oxygen molecules cannot enter the six-ring of the β-cage [141]. It implies that oxygen molecules cannot carry silver ions and clusters into the β-cage, thereby allowing oxidized clusters entrapped within the α-cage. By vacuum dehydration autoreduced Ag_m^{n+} clusters with high nuclearity ($m \approx 6-13$ coexisting with Ag_2^+) formed in the α-cage of fully exchanged zeolites, and subsequent

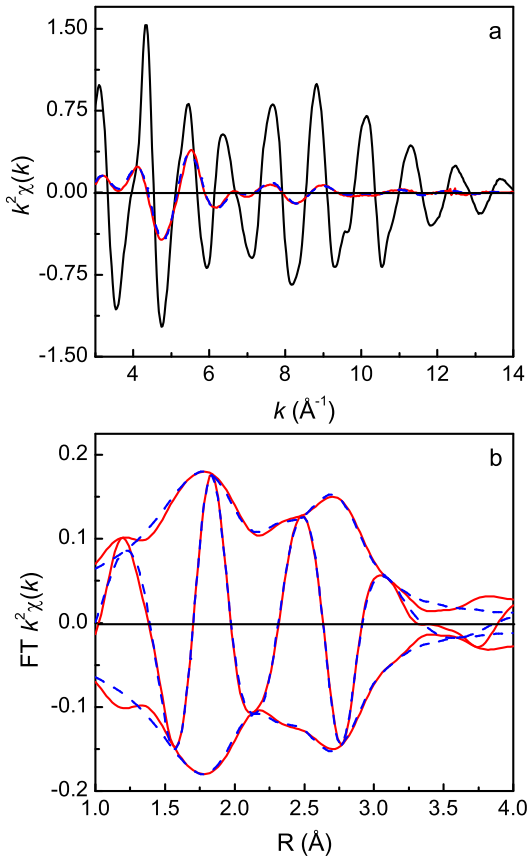

Figure 6.15: EXAFS spectra of the oxidized silver clusters in 12% (wt.) Ag/NaA: a) k^2-weighted $\chi(k)$ function (k^2, Δk = 3.0 - 14 Å^{-1}) (red line) with the corresponding fit (blue dashed line) compared to the spectrum of Ag foil (black line) and b) Fourier transform of the k^2-weighted $\chi(k)$ function (k^2, Δk = 3.0 - 14 Å^{-1}) of experimental EXAFS data (red line) with the corresponding fit (blue dashed line) including the first and second Ag-Ag shells, and a single Ag-O shell.

oxygen treatment partially oxidized these α-cage accessible clusters to Ag^+ at 773 K, which become sufficiently mobile to enter the sodalite cage [43, 71]. Even though it appears rather harsh condition for clustering, four weakly interacting Ag_3^{n+} clusters are entrapped in the β-cage. Anyway, there is plenty of space for clusters in this cage but the charge state must be different for different clusters.

The distance of the first Ag-Ag shell is contracted by $< 10\%$ as compared to the bulk Ag distance. Further, the obtained experimental Ag-Ag distance of 2.92 Å for the second Ag-Ag shell is comparable to the bulk bond length of 2.889 Å. The distinctly higher Debye-Waller factor (see Table 6.4) indicates a large static disorder due to a high fraction of silver atoms at the cluster surface. It is natural for small metal clusters that all the atoms are expected at the surface and the contraction of the inter-atomic distance is an essential concomitant of a low mean coordination number. This surface reconstruction is driven by the energy minimization which is a typical nano-size effect of fine metal

clusters.

Furthermore, an oxygen shell is detected at 2.24 Å with a coordination of $N \approx 2.50 \pm 0.05$. An asymmetric peak of the spectrum is observed by the presence of a light back-scatterer (e.g. O atoms) around 1.75 Å in *R*-space of the Fourier transform (see Figure 6.15(b)). The theoretical fit matches pretty nicely the imaginary and real parts, especially perfect for the k^1-weighted FT of $\chi(k)$ (the spectrum not shown). The appearance of multiple satellite peaks in the Fourier transform spectrum would describe a single absorbing backscattering pair of higher shells and could be excluded for oxidized silver clusters here. Furthermore, the distance of the Ag-O shell is always in the order of 2.22 Å - 2.27 Å which is quite comparable with the distance of 2.26 Å for Ag-O deduced from XRD experiments on the silver clusters in Ag_{12}/NaA [203]. In addition, the distance of 2.27 Å for the Ag-O shell indicates that Ag^+ is triply coordinated to zeolite oxygen [207].

All the local structural parameters are very comparable to previously reported results [208, 209]. The formation of Ag clusters was suggested on full evacuation at room temperature and dehydration at a higher temperature. Furthermore, *in situ* experiments at the Ag *K*-edge proved that a small silver cluster consisting of 6 Ag^0 and 8 Ag^+ was stabilized inside the β-cage of Ag_{12}/NaA after dehydration (without oxygen) at 773 K [209]. It can be considered the formation of fully *autoreduced silver clusters* thus. The arrangement was supposed to represent silver atoms which were surrounded by cubically close-packed Ag^+, while the whole cluster was confined by the lattice oxygens. It is however very interesting to note that the structural parameters, i.e. $N = 5.1 \pm 0.2$, the inter-atomic Ag-Ag distance $R = 2.81$ Å, and Debye-Waller factor $\sigma = 0.13$ Å, were nearly consistent with our results (see Table 6.4). The only difference is that the curve-fitting analysis was considering the model consisting of a single Ag-Ag shell, a second (long) and a first (short) Ag-O shell. The second Ag-O shell was detected at the distance of 2.92 Å with the oxygen coordination of $N = 2.9$ on average. It makes sense to accept our assumption that the second Ag-Ag shell of the oxidized silver cluster is starting to form at the distance of 2.92 Å exhibiting $N \approx 0.40 \pm 0.05$ on average.

Oxidation is preferentially proposed to prevent silver ions from being autoreduced. However, autoreduction of Ag^+ appears a natural consequence of dehydration, to some extent at least. Hopefully, it takes place merely in the early stage of dehydration from 293 K to 523 K with the presence of zeolitic water [141]. Of course, autoreduced Ag^0 are formed by oxide ions of water molecules, but will be immediately re-oxidized to Ag^+ by oxygen. On the other hand, oxygen molecules can combine with produced H^+ to form water molecules which are possibly recycled to reduce Ag^+ to Ag^0 and excess water molecules are easily removed by evacuation. In general, autoreduction with the presence of zeolitic water leaves H^+ on the lattice, and about 1/3 of water molecules remained per unit cell after an initial vacuum dehydration at 623 K [203]. If these two processes occur in parallel, which is reasonable for the reduction and oxidation of Ag^+ and Ag^0 at the same time, the number of silver ions and atoms are equilibrated to form partially oxidized silver clusters. It seems that the whole mechanism is reversible so that there is an equilibrium, which can be expressed via the general equation of $O_2 + 2H^+ + 2e^- \Leftrightarrow 1/2O_2 + H_2O$, but nevertheless the total electron transfer could not be estimated completely due to non-negligible interactions between oxidized silver ions or clusters and the support. Turning attention to a main important clue, the color change is due to formation of silver clusters via autoreduction. The dark yellow color, which gives rise to a strong absorption band at 19000 cm^{-1} of UV/vis, is observed when the

four-ring Ag^+ has a second Ag^+ as a neighbor [207]. The fully reversible color change which depends on the hydration state of Ag/NaA was attributed to electronic charge transfer from oxygen lone pairs of the lattice framework to the empty 5*s* orbital of Ag^+ [207].

A main point considers that oxygen treatment compensates a loss of the lattice oxygen by dehydration at the temperature range of 400 K to 653 K [141] as described in a stoichiometric Equation of 6.13. Since Ag/NaA samples were kept under oxygen flow for additional one hour at the final temperature, formed silver clusters are prevented sufficiently from being autoreduced. It is also to remind that autoreduction causes distortions in the lattice by releasing oxygen at higher temperatures of 400 K to 700 K to preserve charge balance [141], and oxygen treatment restores damaged lattice sites [203]. There is no evidence for the charge, but it must be positive because of the framework negative charge. By contrast, oxygen treatments are cause increases in the positive charge state of autoreduced and reduced silver clusters [200].

Utilizing the coordination number derived from the multiple-shell fitting, it is ultimately concluded that Ag^+ of the oxidized clusters prefers the occupation sites in the α-cage of 12% (wt.) Ag/NaA.

The evacuation was also performed for relatively longer time (about 4 hours) during the measurements and exhibited no effects on the structure of the oxidized silver clusters. It is thus considered that very stable clusters have been formed by oxidation and dehydration at 673 K.

Clustering upon reduction

The oxidized Ag clusters are completely EPR silent [122, 129, 123]. The paramagnetic Ag_6^+ clusters can only be produced in 12% (wt.) Ag/NaA by hydrogen reduction at room temperature or below. EPR spectroscopy is probably well suited to detect very fine clusters with a size of < 1 nm containing a few silver atoms. Since EXAFS collects the back-scattering of the excited photo-electrons on all atoms in neighboring shells, it enables a more sensitive detection of the broad size distributions of the small metal clusters with a diameter up to 5 lattice parameters [25]. Here the coordination number is an average estimate of the mean size of the reduced Ag clusters. The size which is derived from the absorption fine structure analyses is in the same order of that which is directly deduced from the EPR hyperfine spectrum, and discussions follow.

By measuring the absorption fine structure spectra under partial pressure of hydrogen gas, a remarkable change in the structure of oxidized silver clusters was demonstrated. The reduction leads to the formation of positively charged silver clusters which are proposed to be EPR active. However, there is no Coulomb repulsion between the clusters because the Coulomb energy of the positive charges is basically compensated by the negatively charged tetrahedral framework, where Al^{3+} is surrounded by 4 oxygen atoms, to which reduced silver clusters are loosely attached. Thus, the reduced Ag clusters are assumed to be well isolated in the pores of Ag/NaA.

The best spectral fit demonstrated the formation of mono-disperse Ag clusters. Fourier transform of the oscillatory $\chi(k)$ function was performed in the range of k from 3 to 14 $Å^{-1}$. Corresponding k-weighted spectra of reduced Ag clusters in 12% (wt.) Ag/NaA sample are illustrated in Figure 5.5(a),(b) and Figure 6.16, respectively. The fit parameters are found in Table 5.1, and the mean size of the reduced Ag clusters is much smaller than that of the oxidized Ag clusters (see Table 6.4). It was previously reported that autoreduced high nuclearity silver clusters in the α-cage are disintegrated into smaller

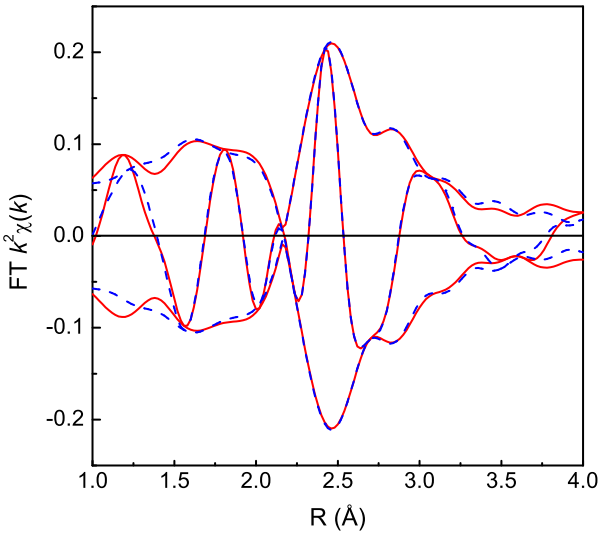

Figure 6.16: EXAFS spectra of the hydrogen reduced silver clusters in 12% (wt.) Ag/NaA sample: Fourier transform of k^2-weighted $\chi(k)$ function (k^2, Δk = 3.0 - 14 Å^{-1}) (red line) with the corresponding fitting (blue dashed line) including the first and second Ag-Ag shell and a single Ag-O shell.

clusters under mild condition hydrogen reduction at 273 K to 343 K [43]. These disintegrated clusters were transferred into the β-cage and stabilized as smaller Ag_3^{n+} clusters. Further reduction at 343 K led to the formation of Ag_6^{n+} clusters due to agglomerations of Ag_3^{n+} clusters in the same cage, and residual reduced silver atoms and ions were left in the α-cage. There is no barrier to the silver atom and ion migration into the sodalite unit because the hydrogen molecule can enter the six-ring of the β-cage [141].

The absorbing silver has an average coordination of $N \approx 3.50 \pm 0.05$ at an average distance of 2.77 Å in a second Ag-Ag shell, and $N \approx 0.40 \pm 0.05$ at a distance of 2.69 Å in the first shell. It is obvious that the second Ag-Ag shell is developed unambiguously, while its inter-atomic distance is contracted. This leads to an implicit assumption that silver atoms in the first Ag-Ag shell migrated/re-dispersed into the second shell after hydrogen reduction. This surface reconstruction occurs due to the smallness of the silver cluster. It is known that when a second shell of atoms is introduced, the coordination number N of the first shell decreases continuously [154, 155]. The total Ag-Ag coordination number is $\approx 3.90 \pm 0.07$ and corresponds to the size of a six-atomic cluster (see Table 5.1 in Chapter 5) that is quite compatible with EPR observations. It is thus reasonable that the oxidized silver clusters are disintegrated into smaller clusters by hydrogen reduction at 298 K, because we are seeing only a half (1/2) of silver atoms in the reduced cluster compared with the state before reduction. Fourier transform of the k^3-weighted of $\chi(k)$ function is extremely sensitive to the heavy scatterer, because there is an overlapping of Ag-Ag shells, and the real and imaginary part is nicely fitted to the experimental spectrum (see Figure 5.5(b)). The imaginary part is very sensitive to the inter-atomic Ag-Ag distance and therefore used to judge the fit quality [103].

The coordination of oxygen is $N \approx 1.60 \pm 0.05$ at 2.22 Å, hence the number of oxygen atoms is depleted by factor of 1/3 after reduction (see Table 5.1 and 6.4). This is seen in

the Fourier transform of the k^2-weighted $\chi(k)$ spectrum in Figure 6.16, if it is compared to the spectrum in Figure 6.15(b). The peak at 2.5 Å in R-space of the Fourier transform represents the overlapped Ag-Ag shells of the reduced silver clusters which amplified its intensity, while the intensity of the Ag-O shell decreased. However, hydrogen reduction just leads to a partial reduction of the oxidized silver clusters. It means that the agglomeration of the cluster is either incomplete, or their shape is less spherical, or the oxygen is partly interspersed between the silver atoms.

The reduction effect was also investigated by "*quick*" XAFS (acronym is QXAFS) on oxidized Ag_{83}/MFI zeolite samples [210]. The results demonstrated that significant structural changes occurred to small silver clusters by hydrogen (0.5% H_2 in He) reduction at 573 K under static condition (not flow). Only a single Ag-Ag shell developed for Ag clusters with the coordination of $N \approx 3.20$ at the distance of 2.74 Å, while the coordination of the Ag-O shell decreased through $N \approx 2.60$ to $N \approx 1.10$ at the distance of 2.53 Å on average. In contrast, no Ag-Ag shell was detected in all these oxidized Ag_{83}/MFI samples before hydrogen reduction. Furthermore, the nano-sized (2 - 11 nm) spherical silver particles were formed in the Ag^+ exchanged sodium silicate glasses by treatments under hydrogen atmosphere at 773 K and characterized by EXAFS [211]. These results indicated that the partially reduced silver clusters were trapped in different supports, even though the reduction was performed at a higher temperature.

Since X-ray photons have an energy much greater than the band gap energy of the clusters, it easily excites the electron from the filled band to the unfilled band leading to an *electron-hole pair*. If there is *Coulomb attraction* between the positive hole and the negative electron, a bound pair (so-called *exciton*) is formed which can move through the cluster. When the cluster size is critically smaller than the radius (or root mean square displacement) of the exciton, this will no longer exist, and the hole and electron will move independently. Thus, the formation of the reduced Ag clusters is developed by trapping the hole (h^+) and the electron (e^-). It means that the reduction and oxidation process (or simply red-ox reaction) of Ag^+ or silver clusters take place simultaneously during the cluster stabilization in the specific site. The mechanism can be simply described by Equation (6.14).

$$\begin{aligned} Ag^+ + h^+(\equiv Si - O - Al \equiv^-) &\rightarrow Ag^{2+}(\equiv Si - O - Al^- \equiv) \\ Ag^+ + e^- &\rightarrow Ag^0 \end{aligned} \tag{6.14}$$

It is seen that a direct consequence of the mechanism is the release of one electron, while the hole is trapped in the lattice. A similar red-ox reaction of Ag^+ occurred in silver ion exchanged soda-lime silicate glasses and eventually led to paramagnetic Ag doped centers observable by X-band EPR spectroscopy [67]. It was previously reported that γ-irradiation led to a disproportionation reaction of $2Ag^+ \rightarrow Ag^0 + Ag^{2+}$ *in vacuo* dehydrated Ag^+ exchanged zeolites [19]. This red-ox reaction provided precursors of paramagnetic Ag clusters.

Anyway, reduction is performed on oxidized Ag clusters in 12% (wt.) Ag/NaA at 298 K which leads to the release of the electron from the hydrogen molecule, and Ag^+ is simply reduced to Ag^0. This makes silver atoms pretty easy to migrate into the β-cage, and the range of motion of the reduced Ag^0 within the cage is rather unrestricted due to electrical neutrality. In addition, the reduced Ag^0 agglomerated into neutral Ag^0_m clusters after hydrogen reduction [43]. Of course, reduction is incomplete, but the residual Ag^+ can combine with Ag^0 and neutral Ag^0_m clusters to form positively

charged clusters. The whole process seems crucially important for the observability of the cluster spin paramagnetism by EPR spectroscopy so that the unpaired electron is trapped/confined in the reduced Ag cluster.

By evacuating the hydrogen reduced Ag/NaA at 398 K, no further structural changes occurred to reduced silver clusters. Moreover, the reduction at room temperature is basically considered very mild conditions, thus rendering no destruction of the lattice. XRD measurements proved that the crystalline structure of the silver ion exchanged NaA zeolite was intact after consecutive treatments of oxidation and dehydration at 673 K as well as reduction at room temperature (diffraction pattern not shown).

In doubly reduced samples, the isolated shell contributions are represented as Ag-Ag and Ag-O peaks in the Fourier transform (R-space) at 2.5 and 2.1 Å, respectively (see Figure 5.4(a) and (b) in Chapter 5). A heavy scatterer such as Ag leads to a phase-shift by photo-electron scattering that shifts the peak in Fourier space to a lower value of R which was performed using k^2-weighting of the $\chi(k)$ function in the range of k from 3 to 14 $Å^{-1}$.

The absorbing Ag atom of the doubly-reduced cluster has an average coordination of $N \approx 3.40 \pm 0.05$ at an average distance of 2.75 Å in the second Ag-Ag shell, while the first Ag-Ag shell at 2.69 Å has $N \approx 0.55 \pm 0.05$ on average. The total Ag-Ag coordination number is 4.0 ± 0.05 which is slightly higher than that of the reduced silver clusters. On average the obtained experimental Ag-Ag distance of 2.75 Å reveals a contraction of the bond length as compared to bulk Ag (2.889 Å) due to nano-size effect. Furthermore, an oxygen shell is detected at 2.26 Å with a coordination of $N \approx 0.70 \pm 0.05$ on average. Here the coordination is depleted more than twice as detected after reduction, whereas the distance exhibits no changes. This can be seen if one compares Figure 5.4(b) with Figure 6.16.

Ultimately, the total number of oxygen is depleted by factor of $\approx 3/4$ by different reduction conditions, e.g. reduction, evacuation on reduction and re-reduction (see Table 5.1 and 6.4). This probably proves that oxygen atoms previously surrounded much larger oxidized silver clusters in the α-cage, and as hydrogen reduction leads to the formation of much smaller silver clusters by carrying reduced Ag^+ and Ag^0 into the β-cage, the newly formed clusters have rather long distances to framework oxygens with very weak coordinations.

In order to identify the presence of small Ag clusters, the Ag K-edge X-ray absorption near edge spectra (XANES) were collected on the silver clusters in oxidized and hydrogen reduced 12% (wt.) Ag/NaA and compared with the spectrum of a Ag foil. All measurements were performed at room temperature and the corresponding spectra are displayed in Figure 6.17. By comparison with the bulk Ag, the background subtracted absorption spectra of the oxidized and hydrogen reduced silver clusters demonstrate a significant reduction in their intensities above the absorption edge, while the absorptions were shifted by 4.75 eV above the edge. It is rendered due to the very small size of silver clusters. It is generally known that the band gap (similar to the absorption edge) increases as the cluster size decreases. It is however emphasized that the edge position of Ag in the clusters does not change too much at the K-edge experiments (see Table 6.4). On the other hand, a likely cause for the small discrepancy observed in shape could be the displacement of the bound/valence electrons, leading to Debye-Waller smearing of the fine structure, especially for further oscillations above the edge. However, the thermal effects in XANES and near-edge XAFS have previously been reported to be negligible [212, 213]. The white lines of the spectra exhibit higher intensities than that of

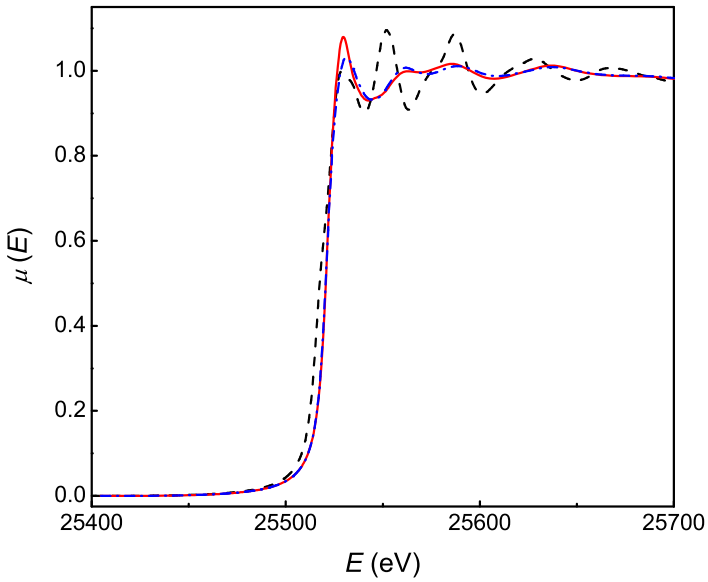

Figure 6.17: XANES spectra of the silver foil (dashed black line), the oxidized (solid red line) and hydrogen reduced Ag clusters (dash-dot blue line) in 12% (wt.) Ag/NaA sample.

the bulk Ag. It is however well known that XAS experiments on the Ag *K*-edge are presumably not enough to detect *L*-edge transitions which normally indicate the presence of the hole in the core *d* electronic states to contribute to the white lines. By theoretical investigations on the Ag *K*-edge, the silver clusters with a size of 7 Å (79 Ag atoms) exhibiting an electronic configuration of [Kr]$4d^9 5s^2$ revealed similar intensity in their XANES spectra with bulk Ag spectra showing electronic configuration of [Kr]$4d^{10} 5s^1$ and the results were proven by comparison with experimental spectra. The general tendency was that the smaller cluster (19 Ag atoms with 5 Å) exhibited higher intensities in the white lines than those of the bulk Ag [214].

At higher temperatures, an aggregation of silver clusters takes place and results in the formation of larger clusters. All structural parameters are tabulated in Table 6.4, but the absorption fine structure spectra are not shown. Similar results were observed by the "*quick*" XAFS technique (QXAFS): Ag_4^{n+} clusters aggregated into large clusters of Ag_m^{n+} ($m > 8$), and Ag metal particles appeared on the external surface of the MFI zeolite [210].

6.4.2 Gas adsorptions

Fourier transform of the $\chi(k)$ function provides the highest resolution over 3.5 Å for heavy-scatterer atoms. However, there is no sensitivity to light-scatterer atoms beyond 4 Å. It is assumed that the backscattering amplitude and phase shift of C, N and O atoms are very similar, because these atoms are consecutively located in the periodic table. Perhaps it is difficult to distinguish these light atoms simultaneously, thus the backscattering atoms are represented here as O in all fitting results.

Even though the number of XAS experiments have been performed on small Ag clus-

ters on different supports [215, 216, 217, 218, 219, 220], there are scarce investigations (one can say almost nothing) devoted to the interactions between the supported Ag clusters and adsorbate molecules. The bond length is contracted for the Ag-Ag in the reduced clusters which is on the order of 5 - 7% shorter than the bulk value. This bond length contraction can probably render enormous consequences for adsorption interactions, since there is a concomitant increase in the orbital overlap.

The spin paramagnetism of the Ag_6^+ cluster completely disappears when NO gas is adsorbed. As is stated elsewhere, we are observing either the NO adduct to a previously diamagnetic and therefore EPR silent Ag cluster, or that a **red-ox reaction** precedes NO adsorption.

Red-ox reaction by NO adsorption

The reduced silver cluster undergoes a very slight structural change by adsorption of NO. The FT of the k^2-weighted $\chi(k)$ function reflects an intensity depletion of the oxygen shell, and the fitting for the absorption fine structure spectrum is fairly good as illustrated in Figure 6.18. The coordination of the second Ag-Ag shell is in the order of $N \approx 3.20 \pm 0.05$, whereas only < 0.2 atom is missed in the first Ag-Ag shell. The

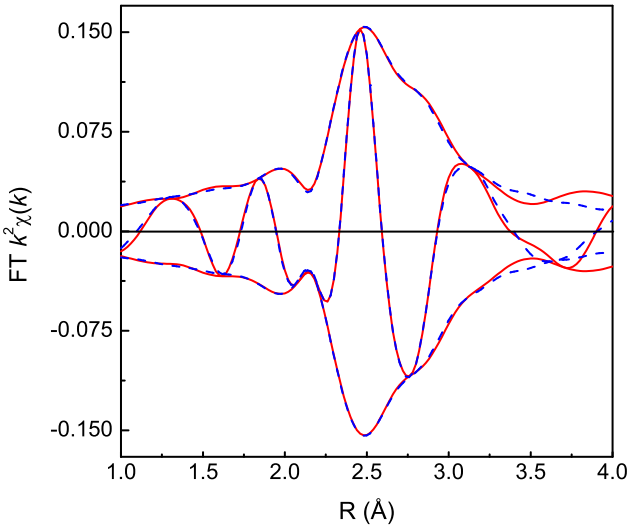

Figure 6.18: Fourier transform of the k^2-weighted $\chi(k)$ function (k^2, Δk = 3.0 - 14 Å^{-1}) (red line) and the best fit (blue dashed-line) including the first and second Ag-Ag shells coupling with a single Ag-O shell isolated after adsorption of NO on the hydrogen reduced silver cluster.

coordination of the Ag-O shell is $N \approx 0.90$ at the distance of 2.29 Å on average. On adsorption, all the inter-atomic distances virtually survive for each shell, i.e. 2.77 Å, 2.29 Å and 2.69 Å. Note that the structural parameters are always compared with the parameters derived from the multiple-shell fitting for the hydrogen reduced silver clusters (see Table 5.1). Furthermore, in the FT in R-space, a small deviation of the fitting from the experimental spectrum above 3.5 Å is due to a contribution of a lighter atom. This is because EXFAS is not sensitive enough to light scatterers above 4.0 Å.

A key point is that EXAFS is an averaging technique, therefore, it really does not matter whether NO is adsorbed on diamagnetic or on paramagnetic Ag clusters. It was proposed that a red-ox reaction precedes NO adsorption so that nitrogen monoxide is adsorbed on previously diamagnetic and therefore EPR silent Ag clusters. This is because paramagnetic Ag clusters are calibrated and there are significant fractions of diamagnetic Ag clusters.

By evacuating adsorbed NO at room temperature, there are further significant changes to silver clusters. It is assumed that a reduction in symmetry occurs, thus flattening the cluster structure. In the first Ag-Ag shell, the coordination increases drastically from 0.35 ± 0.05 to 3.50 ± 0.05 at the almost identical distance of 2.74 Å, and approximately 3.20 silver atoms rejoin the cluster on average. In contrast, the inter-atomic distance is appreciably elongated up to 2.94 Å in the second Ag-Ag shell with a very small coordination of $N \approx 0.25 \pm 0.05$ on average. A gradual dissolution of this shell on evacuation indicates that NO is not tightly bound to the silver cluster. The coordination by oxygen and nitrogen is $N \approx 1.50 \pm 0.05$ at a distance of 2.26 Å on average.

The multiple-shell fitting demonstrates that the dissolved second Ag-Ag shell has been reformed by adding O_2 into the NO adsorbed silver clusters at 298 K. In this shell, the coordination increases from 0.25 ± 0.05 up to 4.50 ± 0.05 with a distance contraction from 2.94 Å to 2.76 Å. The coordination of the first Ag-Ag shell decreases from 3.50 ± 0.05 to 0.20 ± 0.05 at a distance of 2.70 Å. This indicates that the cluster structure becomes more prolate, because the first Ag-Ag shell falls apart by reducing its average coordination. The oxygen coordination increases up to 2.10 ± 0.05 at the distance of 2.27 Å. The intensity of the Ag-O shell increases in the FT of the k^2-weighted fine structure spectrum (spectrum not shown), and suggests that the silver clusters were oxidized.

C_2H_4 adsorption

Adsorption of C_2H_4 on the reduced silver cluster leads to virtually no changes in the local structure of the cluster. Only the silver coordination increases slightly, e.g. $\Delta N \approx 0.40 - 0.70$, in the first Ag-Ag shell at the slightly elongated distance of 2.72 Å, whereas the coordination number of the second Ag-Ag shell completely survives. There is however a sharp rise in the coordination of the Ag-O shell, viz. $N \approx 1.60 - 2.15$, at a distance of 2.22 Å. Perhaps this is due to carbon atoms which are not easily distinguished from oxygen atoms. Interestingly, all the contact distance remain relatively unperturbed, and the fitting for the spectrum of ethylene adsorption was fairly good (spectrum not shown).

Adsorbing C_2H_4 and O_2 simultaneously onto reduced silver clusters leads to significant changes in the local structures, which were also previously monitored by continuous wave EPR spectroscopy, and a reaction pathway is probably driven by mechanisms different than ethylene adsorptions. This simultaneous adsorption (co-adsorption) also gives rise to observable increases in the intensity of the Ag-O shell of the fine structure spectrum which is depicted in Figure 6.19. All the spectra were collected at 298 K. Surprisingly, it was relatively straightforward to do a proper fitting for the experimental spectra, even though an addition of the molecular oxygen could perturb the Ag-O shell to some extent. There were some negligible difficulties in fitting the Ag-Ag shells after the simultaneous adsorption. The fit nicely matches to the imaginary and the real part of the Fourier transform, respectively. Illustrated in Figure 6.19(b) is the spectrum of the k^2-weighted Fourier transform of the oscillatory $\chi(k)$ function, the contribution to the Ag-O shell is significantly increased, if it is compared with that of the hydrogen reduced

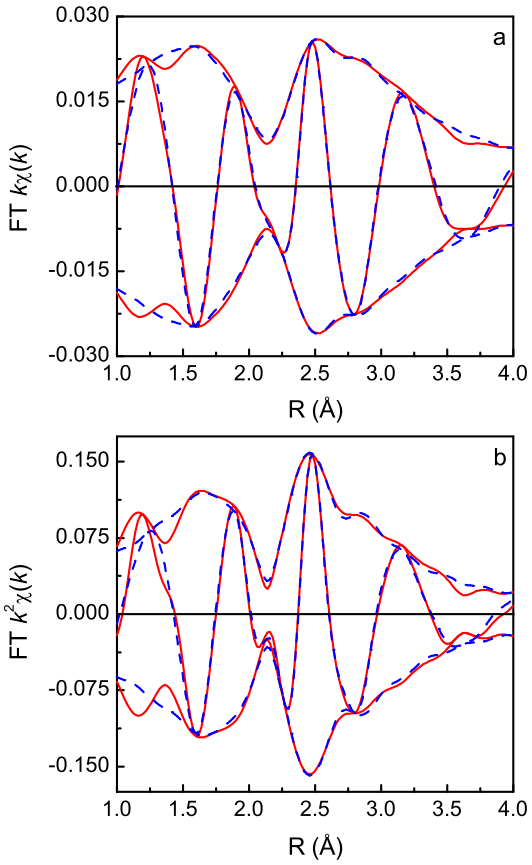

Figure 6.19: Comparison of Fourier transform of oscillatory $\chi(k)$ functions isolated after the simultaneous adsorption of C_2H_4 and O_2 on the hydrogen reduced silver cluster: a) k^1-weighted $\chi(k)$ function (k^1, Δk = 3.0 - 14 Å^{-1}) (red line) and the best fit (blue dashed-line) including the first and second Ag-Ag shells coupling with a single Ag-O shell. b) k^2-weighted $\chi(k)$ function (k^2, Δk = 3.0 - 14 Å^{-1}) (red line) and the best fit (blue dashed-line).

cluster spectrum. The situation is more apparent in the spectrum of the k^1-weighted Fourier transform, since both of the real and imaginary part are almost symmetric for the Ag-O and Ag-Ag shells in the oscillatory $\chi(k)$ fine structure spectrum, respectively (see Figure 6.19(a)). This is because the use of the k^1-weighted Fourier transform of the $\chi(k)$ function provides a sufficient sensitivity to the contributions of the light scatterer atomic shell, e.g. O atoms. The coordination of oxygen is $N \approx 2.50 \pm 0.05$ at 2.27 Å. By the best fit the silver has an average coordination of $N \approx 3.70 \pm 0.05$ at an average distance of 2.86 Å in the second Ag-Ag shell, while the coordination of $N \approx 0.60 \pm 0.05$ is detected at the distance of 2.72 Å in the first Ag-Ag shell. The inter-atomic distance in the second Ag-Ag shell is slightly elongated from 2.78 Å to 2.86 Å that indicates some further rearrangements of the surface atoms to take place for the cluster. It probably means as though some silver atoms in the framework change their positions and then the silver cluster shifts to a less compact structure.

Moreover, the FT of the $\chi(k)$ function is presumably sensitive to a hydrogen atom

contribution < 1.0 Å in R-space of the radial function. The contribution of hydrogen atoms to lower R(Å) can be merely distinguished by another isolation technique of the oscillatory $\chi(k)$ function, so-called "*atomic*" XAFS (AXAFS) [221], if it is indeed present. However, it is currently not proposed.

CO adsorption

The interaction with CO leads to distortions of the reduced silver cluster structures, especially in the first and second Ag-Ag shells, respectively. The total number of silver atoms is reduced, thus detecting lower coordination to the absorbing silver atom in the cluster. It is rather peculiar that the coordination number decreases to $N \approx 0.50 \pm 0.05$, while the contact distance is elongated to 2.92 Å in the second Ag-Ag shell. The reduction in the coordination number of the second Ag-Ag shell generally proves that the cluster elongates or falls apart in this shell. The inner electron distribution probably takes places over silver atoms of the whole cluster, and the number of the surface atoms has been depleted with the contact distance elongation in the second Ag-Ag shell, thereby resulting in the coordination number increasing in the first Ag-Ag shell. A less compact structure of the cluster has to be judged based on the coordination of the first Ag-Ag shell, and each absorbing silver atom has $N \approx 3.00$ direct neighbors at the distance of 2.74 Å on average. There has been a sharp rise in the coordination number in this shell after CO adsorption by comparison with that of the hydrogen reduced Ag cluster. Moreover, each silver atom has $N \approx 1.30$ of oxygen neighbors at a distance of 2.26 Å on average which is slightly less than the coordination of the reduced silver cluster.

The evacuation of CO adsorbed cluster containing samples leads to an increase of the coordination number in the first Ag-Ag shell. The Ag-Ag coordination is $N \approx 4.30$ at a distance of 2.76 Å in the first Ag-Ag shell. By evacuation the absorbing atom loses only < 0.1 neighboring atoms, and $N \approx 0.40$ silver atoms are detected at a distance of 2.92 Å in the second shell. At this stage, the Ag-O shell virtually survived and there were almost no changes except for the coordination number of Ag-O shell which increased slightly to $N \approx 1.30 - 1.50$ at the same distance of 2.27 Å. All structural parameters will be found in Table 6.4.

6.5 Summary

Upon adding NO gas at room temperature, the hyperfine spectrum of the reduced Ag_6^+ cluster disappears immediately, and there is no significant spin density on the cluster. The $g_{zz} = 1.841$ component of the adsorbed NO spectrum is split by the hyperfine coupling of $A_{zz}^{Ag} = 200$ G which renders the crystal field and lifts the orbital degeneracy of NO. Only the hyperfine component $A_{yy}^{N} = 33$ G was experimentally resolved, and the unpaired electron was mostly centered in the $2p$ orbital of the ^{14}N.

The hyperfine spectrum of the adsorbed NO shifted to the spectrum of the adsorbed NO_2 over some days. At 30 K, the rotational motion is axially symmetric about the molecular y axis of the adsorbed NO_2. Above 50 K, the rotational motion becomes very rapidly nearly isotropic. The motion is a large amplitude tilting and flipping of the adsorbed NO_2 which is bound via N to the silver cluster, rather than a full rotation. By analyzing the EPR lineshapes, the $\tau_\perp$ components of the correlation time are derived

to provide the kinetic parameters, and an Arrhenius representation gives access to the activation energy $E_a = 550$ J mol^{-1} for the overall rotational motion.

There was no effect on the hyperfine interaction of the reduced Ag_6^+ cluster when it was exposed to $^{16}O_2$ at room temperature. The interaction of $^{17}O_2$ with the cluster surface revealed some anisotropy of the hyperfine structure at 3.0 K. The sudden disappearance the anisotropy in the range of 7 K to 10.5 K is ascribed to the motional effects by $^{17}O_2$. The energy separation $\Delta E = 96$ J mol^{-1} between the first two rotational levels of $^{17}O_2$ molecule can be simply calculated from a relation between the total angular momentum J and the moment of inertia I.

Pulse X-band EPR measurements, i.e. ^{1}H-ENDOR and HYSCORE, revealed the very weak couplings of the remote protons after the adsorption of C_2H_4 on the reduced Ag_6^+ clusters.

A red-ox effect of Ag^+ on the structural change of silver clusters is discussed for the first time for utilizing *in-situ* EXAFS spectroscopy measurements. Oxidation of Ag^+ in the support pores prevents the exchanged ions from being autoreduced. An average coordination of the Ag-O shell decreases continuously by different reduction treatments. It proves that the newly formed silver clusters are become weakly coordinated to framework oxygens as the oxidized silver clusters are reduced by hydrogen.

A reduced silver cluster undergoes a slight structural change, and a red-ox reaction precedes adsorption of NO. The adsorbed NO is on diamagnetic and EPR silent Ag clusters but the cluster still exhibits the same structure as determined by EXAFS. Since EXAFS is an averaging technique, it detects an ensemble of different clusters on average, i.e. no matter whether they are diamagnetic or paramagnetic silver clusters.

Table 6.2: EPR Spin Hamiltonian Parameters from Simulations of Adsorbed NO_2 in Different Matrices to Experimental Spectra.

Matrix	T(K)	g tensor	A^{14}N[G]	B^{14}N[G]	Reference
Ag/NaA	20	$g_{xx} = 2.0078$	$A^N_{xx} = 52.8$	$B^N_{xx} = -3.6$	this work
		$g_{yy} = 1.9941$	$A^N_{yy} = 50.0$	$B^N_{yy} = -6.4$	
		$g_{zz} = 2.0054$	$A^N_{zz} = 66.4$	$B^N_{zz} = 10.0$	
		$g_{iso} = 2.0024$	$a^N_{iso} = 56.4$		
Na-Mor	77	$g_{xx} = 2.0051$	$A^N_{xx} = 51.0$	–	[179]
		$g_{yy} = 1.9910$	$A^N_{yy} = 48.0$		
		$g_{zz} = 2.0017$	$A^N_{zz} = 66.0$		
NaX	77	$g_{xx} = 2.0055$	$A^N_{xx} = 50.8$	–	[180]
		$g_{yy} = 1.9915$	$A^N_{yy} = 48.5$		
		$g_{zz} = 2.0015$	$A^N_{zz} = 69.7$		
Na-ZSM-5	3.0	$g_{xx} = 2.0050$	$A^N_{xx} = 51.0$	–	[181]
		$g_{yy} = 1.9911$	$A^N_{yy} = 47.7$		
		$g_{zz} = 2.0017$	$A^N_{zz} = 67.7$		
KL	30	$g_{xx} = 2.0051$	$A^N_{xx} = 51.3$	–	[182]
		$g_{yy} = 1.9910$	$A^N_{yy} = 47.4$		
		$g_{zz} = 2.0017$	$A^N_{zz} = 67.8$		
NaK-Fer	20	$g_{xx} = 2.0050$	$A^N_{xx} = 53.6$	–	[182]
		$g_{yy} = 1.9912$	$A^N_{yy} = 48.7$		
		$g_{zz} = 2.0017$	$A^N_{zz} = 68.3$		
NO_2	293	$g_{xx} = 2.0026$	$A^N_{xx} = 45.6$	$B^N_{xx} = -6.7$	[183]
(gas)		$g_{yy} = 1.9910$	$A^N_{yy} = 45.1$	$B^N_{yy} = -7.1$	
		$g_{zz} = 2.0020$	$A^N_{zz} = 66.1$	$B^N_{zz} = 13.8$	
			$a^N_{iso} = 52.3$		
$AgNO_3$	77	$g_{xx} = 2.0090$	$A^N_{xx} = 51.2$	$B^N_{xx} = -5.1$	[184]
		$g_{yy} = 1.9978$	$A^N_{yy} = 48.5$	$B^N_{yy} = -7.8$	
		$g_{zz} = 2.0039$	$A^N_{zz} = 69.6$	$B^N_{zz} = 13.3$	
		$g_{iso} = 2.0035$	$a^N_{iso} = 56.3$		
$NaNO_2$	77	$g_{xx} = 2.0057$	$A^N_{xx} = 49.3$	$B^N_{xx} = -5.4$	[185]
		$g_{yy} = 1.9910$	$A^N_{yy} = 46.7$	$B^N_{yy} = -8.0$	
		$g_{zz} = 2.0015$	$A^N_{zz} = 67.7$	$B^N_{zz} = 13.0$	
		$g_{iso} = 1.9994$	$A^N_{iso} = 54.7$		

Table 6.3: Fitting Parameters for Slow Motion Spectra of Adsorbed NO_2.

T(K)	Model	Diffusion tensor (s^{-1})	Ratio N	Correlation time (τ_c, s)	$1/T_2^0$ (MHz)	Parameters
30	BD	$R_{\parallel} = 1 \times 10^7$ $R_{\perp} = 2 \times 10^6$	5.0	$\tau_{\parallel} = 2.50 \times 10^{-8}$ $\tau_{\perp} = 0.85 \times 10^{-7}$	4.0	β = 5.30 γ = 5.72 ΔB_{pp}= 21 G
40	BD	$R_{\parallel} = 1 \times 10^7$ $R_{\perp} = 3 \times 10^6$	3.3	$\tau_{\parallel} = 2.50 \times 10^{-8}$ $\tau_{\perp} = 0.57 \times 10^{-7}$	3.5	β = 4.82 γ = 4.93 ΔB_{pp} = 18 G
50	BD	$R_{\parallel} = 1 \times 10^7$ $R_{\perp} = 5 \times 10^6$	2.0	$\tau_{\parallel} = 2.50 \times 10^{-8}$ $\tau_{\perp} = 0.34 \times 10^{-7}$	3.5	β = 3.92 γ = 3.47 ΔB_{pp} = 15 G
60	BD	$R_{\parallel} = 1 \times 10^7$ $R_{\perp} = 6 \times 10^6$	1.7	$\tau_{\parallel} = 2.50 \times 10^{-8}$ $\tau_{\perp} = 0.28 \times 10^{-7}$	3.5	β = 3.59 γ = 2.57 ΔB_{pp} = 14 G
70	BD	$R_{\parallel} = 1 \times 10^7$ $R_{\perp} = 7 \times 10^6$	1.4	$\tau_{\parallel} = 2.50 \times 10^{-8}$ $\tau_{\perp} = 0.24 \times 10^{-7}$	3.0	β = 3.36 γ = 1.97 ΔB_{pp} = 13 G
90	BD	$R_{\parallel} = 1 \times 10^7$ $R_{\perp} = 8 \times 10^6$	1.3	$\tau_{\parallel} = 2.50 \times 10^{-8}$ $\tau_{\perp} = 0.21 \times 10^{-7}$	1.0	β = 2.70 γ = 0.30 ΔB_{pp} = 12 G
110	BD	$R_{\parallel} = 1 \times 10^7$ $R_{\perp} = 1 \times 10^7$	1.0	$\tau_{\parallel} = 2.50 \times 10^{-8}$ $\tau_{\perp} = 1.67 \times 10^{-7}$	1.0	
125	BD	$R_{\parallel} = 1 \times 10^7$ $R_{\perp} = 1 \times 10^7$	1.0	$\tau_{\parallel} = 2.50 \times 10^{-8}$ $\tau_{\perp} = 1.67 \times 10^{-7}$	1.0	

Table 6.4: Structural parameters of the adsorption complexes on the reduced clusters obtained from the three-shell fittings for $\chi(k)$ function and of the supported Ag clusters in 12% (wt.) Ag/NaA.

Remarks	Ag-Ag				Ag-O(C, N)				Ag-Ag			
	R(Å)	N	$\Delta\sigma^2$(Å^2)	ΔE_0	R(Å)	N	$\Delta\sigma^2$(Å^2)	ΔE_0	R(Å)	N	$\Delta\sigma^2$(Å^2)	ΔE_0
Adsorptions @ 293 K												
Oxidized	2.92	0.40(5)	-0.0016	-9.7 eV	2.24	2.50(5)	0.0012	8.48 eV	2.71	5.60(5)	0.0174	8.02 eV
NO adsorbed	2.77	3.20(5)	0.0120	4.68 eV	2.29	0.90(5)	0.0090	7.45 eV	2.69	0.35(5)	-0.0030	4.68 eV
NO evacuated	2.94	0.25(5)	-0.0070	5.62 eV	2.26	1.50(5)	0.0090	10.0 eV	2.74	3.50(5)	0.0060	5.62 eV
NO + O_2 ads.	2.76	4.50(5)	0.0110	4.92 eV	2.26	2.10(5)	0.0130	8.96 eV	2.70	0.20(5)	-0.0070	4.92 eV
C_2H_4 adsorbed	2.79	3.40(5)	0.0167	3.53 eV	2.25	2.15(5)	0.0190	10.8 eV	2.72	0.75(5)	-0.0040	3.53 eV
C_2H_4 + O_2 ads.	2.85	3.70(5)	0.0160	2.13 eV	2.29	2.50(5)	0.0175	7.38 eV	2.72	0.55(5)	-0.0038	5.53 eV
CO adsorbed	2.92	0.50(5)	-0.0030	2.84 eV	2.26	1.30(5)	0.0110	6.67 eV	2.74	3.00(5)	0.0050	2.84 eV
CO evacuated	2.93	0.40(5)	-0.0050	9.67 eV	2.27	1.50(5)	0.0110	8.44 eV	2.76	4.30(5)	0.0060	4.78 eV
Reductions @ 473 K												
Oxidized	2.79	5.00(5)	0.0080	5.44 eV	2.25	2.70(5)	0.0100	6.32 eV	2.66	1.15(5)	-0.0006	-1.19 eV
Reduced	2.81	5.30(5)	0.0120	2.92 eV	2.27	0.80(5)	0.0150	10.0 eV	2.71	2.50(5)	-0.0012	2.92 eV
Evacuated	2.93	1.40(5)	-0.0010	0.91 eV	2.26	0.30(5)	0.0020	10.0 eV	2.74	4.70(5)	0.0006	3.13 eV
Re-reduced	2.86	3.70(5)	0.0080	4.40 eV	2.29	0.70(5)	0.0200	10.0 eV	2.72	3.70(5)	0.0008	4.40 eV

R(Å) - bond length
N - coordinations
$\Delta\sigma^2$(Å^2) - DW factor
ΔE_0 - edge shift

7 Conclusions

This thesis is composed of three basic experimental parts which deal with the characteristics underlying the paramagnetic, structure-dependent magnetic, and chemical properties of the reduced Ag clusters supported on Ag/NaA. In contrast, paramagnetic silver species have not been formed in Ag/NaY by the same consecutive treatments.

Often autoreduced Ag clusters are not paramagnetic. Calcination with oxygen was performed on Ag/NaA at 673 K to prevent Ag^+ from undergoing *autoreduction*. This leads to the intensive color change from white to dark yellow color which is caused by the occupation of exchanged Ag^+ in the site of the four-membered ring (S4L) coupled to a second Ag^+ in the center of the eight-membered ring (S8). By oxidizing Ag/NaA, some other eight-ring Ag^+ of different unit cells migrate to the cluster trapping cage. It is however impossible to stabilize any paramagnetic silver clusters and species within the pores where the bonding between atoms is assumed to be at least partially covalent. Therefore, oxidized Ag clusters are presumably EPR inactive due to the lack of unpaired electrons and are assumed to be located in the α-cage of Ag/NaA because of their larger sizes than that of reduced clusters. Subsequently, the oxidized samples were reduced in the flow of H_2 gas at 298 K or below in order to form the paramagnetic Ag clusters. Hydrogen molecules reduce oxidized Ag clusters in the α-cage and carry reduced Ag^+ into the β-cage because of their gas kinetic diameters. Reduction subsequently renders the formation of the paramagnetic Ag clusters from reduced silver ions and atoms in this cage. Paramagnetic Ag clusters are positively charged to balance a negative charge of the Si-O-Al framework of the lattice. Since a ratio of Si/Al = 1 is uniformly distributed throughout the lattice, a formation of negatively charged Ag clusters is excluded due to electrostatic repulsion by Coulomb interactions. Furthermore, the formation of the low nuclearity paramagnetic Ag clusters is dependent on the metal loading in Ag/NaA which follows a simple form of Ag_m^{n+} to keep maintaining the geometric and electronic open-shell configuration with $n+(\text{odd}) < m(\text{even})$ or $n+(\text{even}) < m(\text{odd})$. The sequence of treatments leading to a paramagnetic cluster formation is the principal difference in a preparation method, because reduction typically followed by oxidation in previous syntheses lead to magnetically silent Ag clusters.

A main advantage of a particular preparation strategy is that the size of zeolite-supported clusters is constrained in one or more dimensions. Such constraints basically render substantial changes in the physical, electronic, structural, and magnetic properties of small Ag clusters which differ fundamentally from those of the bulk silver, despite the fact that a system is composed of the same element.

The well-resolved multiplet spectra arise from reduced silver clusters, i.e. Ag_3^{n+} and Ag_4^{n+}, and practically exhibit isotropic hyperfine interactions due to nearly equivalent silver nuclei. These paramagnetic clusters are likely to have a simple $S = 1/2$ state so that the electronic ground state is a doublet. The formed triatomic cluster is relatively stable in a broad range of temperatures, from ca. 20 K to 160 K, and keeps the equivalence of silver nuclei. Hence the effects of thermal motion on g tensors and hyperfine coupling constants could be ignored. There is no inhomogeneous spectral line broadening and line splitting effect due, in part, to the couplings of the electron spins

to many surrounding nuclear spins. In addition, the energy of triatomic clusters has overcome the interaction energy with the lattice, and clusters appear isotropic and isolated. In contrast, the atomic Ag^0 species which is located at the lattice aluminum site exhibits anisotropy due to lattice environment. Linewidth and g-shift are considered to be caused by spin-orbit coupling. Therefore, the EPR parameters of these cluster species are heavily dependent not only on intra-structural characters but also the cluster environment.

The reduced Ag_6^+ cluster is the most stable and prominent species among paramagnetic clusters. The numerical simulation of the hyperfine spectrum simply indicates that the electronic *Zeeman* splitting is isotropic for symmetry reasons for the unpaired 5*s* electrons, while the magnetic dipole moments of six-equivalent Ag nuclei coupled to the unpaired electron's magnetic dipole moment lead to the isotropic hyperfine interaction. A single set of parameters strongly supports that a single, well-defined paramagnetic cluster structure dominates the distribution of non-uniform cluster species. The effective $g_{iso} = 2.028$ is significantly higher than the free electron g_e value. $g > g_e$ also indicates a positive charge on the cluster. There is an admixture of orbital momentum through the spin-orbit coupling which is a *relativistic effect*. However, the orbital angular momentum of the unpaired electron is normally quenched for Ag atoms in the cluster, circular components of the electronic wavefunctions (an orbiting electron) around the silver cluster circumference or the delocalizing spin of the electron gives rise to a magnetic moment. It means that electrons in the clusters acquire the angular momentum from cluster orbitals so that the effect is to be distinct from that of a *mono-atomic center*. The isotropic coupling constant (A_{iso}) of the Ag_6^+ cluster is over 10 times smaller than the isotropic hyperfine coupling of the isolated Ag atom in the gas phase. No hyperfine anisotropy due to p or d-orbital contributions is observed. As there is no anisotropic hyperfine coupling, the unpaired spin is uniformly distributed among the silver nuclei rather than localized on a single Ag atom. The structural ordering of the Ag_6^+ cluster is a close-packing (even atoms) with the electronic open shell for a doublet ground state. This cluster is still observable at 298 K without any magnetic tensor distortions, indicating that there is no inhomogeneous spectral line broadening. For silver SOC is sufficiently large that observation of the resonance from the bulk[1] is only possible at very lower temperatures.

An application of pulse EPR methods, i.e. ESE, HYSCORE and ENDOR, is favorable to perform the investigations of spin dynamics and a behavior of the nuclear spin coupled to the electron spin in the surroundings. By comparing with Ag_6^+ clusters, the reduced Ag_4^{n+} clusters are also isotropic with EPR parameters of $g_{iso} = 2.023$ and $A_{iso} = 67.5$ G, but g_{iso} is lower than that of six atomic silver clusters. It implies that six atomic clusters have a larger contribution from the d electron shell or a stronger spin-orbit coupling. Both clusters are observed in the reduced 12% (wt.) Ag/NaA, thus suggesting that different clusters with different nuclearities can be formed by the same treatments in Ag/NaA with the identical metal loading, some of them are paramagnetic, while the others are EPR-silent. Pulse Q-band field-sweep ESE spectroscopy can be more sensitive than continuous wave X-band spectroscopy because of the higher hyperfine and electron Zeeman splitting (g) selectivity. Hyperfine coupling constants of cationic Ag clusters have a general tendency to a cluster size dependence, for instance, $A_\perp$ = 23 G and $A_\parallel$ = 173 G for Ag^0; A_{iso} = 97.3 G for Ag_3^{n+}; A_{iso} = 67.5 G for Ag_4^{n+}

[1]It was claimed that the bulk g shift was measured for bulk Ag metal by Châtelain *et al.* in 1976. *J. Appl. Phys.* **47**, 3670.

and A_{iso} = 66.7 G for Ag_6^+, and the latter exhibits the smallest hyperfine coupling constant. A perfectly resolved hyperfine structure allows paramagnetic Ag clusters to have a *molecular character* rather than *metallic character*. This is a direct consequence of *size effects*. In contrast, a single Lorentzian line is expected for metallic clusters because of the scattering effect of conduction electrons, and linewidth is assumed to increase with decreasing size. In addition, isotropic silver clusters (except triatomic) may exhibit lower symmetry, i.e. *tetrahedral* and *octahedral*, rather than a planar geometry. The determination of the exact structure of paramagnetic Ag clusters challenges up-to-date quantum chemical calculations.

Furthermore, pulse measurements, e.g. HYSCORE and Mims ^{1}H-ENDOR, reveal no spin density on the protons in the vicinity of the reduced silver clusters. The presence of protons (H^+) to balance a spin density distribution is proven by an indirect experimental method. A temperature activated reversible desorption of D_2 overcomes an activation barrier of $E_a = 0.78$ eV which is appreciably higher than the binding energy to the bulk Ag surface. Weak interactions between the electron spin and ^{27}Al nuclei have been resolved by HYSCORE, thus indicating that there is either fractional spin density on ^{27}Al nuclei or negligible dipolar coupling between the unpaired electron and aluminum nuclei. It can be an explanation for the *missing spin density* of paramagnetic clusters.

EXAFS analysis yields high precision values for the local environment of *atoms* in silver nano-clusters but not a complete structure and symmetry. Atomic arrangements in clusters are well ordered locally, but are not long-range ordered as was expected. Precisely, Ångström resolution distance data are experimentally available from the atomic pair (Ag-Ag) in clusters under different reduction conditions. The inter-atomic Ag-Ag distance is contracted on the order of $\approx 1/10$ (9.5%) of an Ångström as compared to the bulk 2.889 Å distance, and this change is sufficient to render a size effect on cluster properties. The number of neighbors in the first and second coordination shell cannot provide information on the cluster geometry, but is used to estimate the mean size. Since silver clusters are supported systems, the interaction with the matrix can generally influence symmetry and geometry of the nano-clusters in terms of energy and again the analysis of the first two shells is not sufficient to determine the cluster shape.

The bulk Ag is typically diamagnetic, but exhibits paramagnetism when atoms are dispersed into smaller clusters in the support pores. Odd numbers of electrons are distributed in singly occupied molecular orbitals (usually HOMO) which strongly delocalizes over all atoms of the nominal Ag_6^+ cluster. And the conduction electron band becomes indeed discrete, and energy level separation is to be comparable to $\mu_B H$. An odd-electron susceptibility leads to a Curie-Weiss dependence on temperature fluctuations, and magnetization is dominated by paramagnetic alignment of the spins at the lowest temperature of 1.8 K. Only 0.04% of the exchanged atoms contribute, forming a fraction of magnetically active clusters, suggesting that a mixture of diamagnetic, EPR active spin $S = 1/2$ and EPR silent high-spin species is present.

The state of the reduced Ag_6^+ clusters in 12% (wt.) Ag/NaA catalysts was observed by continuous wave and pulse EPR methods after numerous reactions with gas adsorbate molecules, and the alterations in the hyperfine splittings were taken as direct evidence for the catalytic effectiveness. As noted before, there is a mixture of paramagnetic and diamagnetic silver clusters, e.g. Ag_6 (EPR silent) and Ag_6^+ (EPR active). When adding NO, the EPR silent clusters become EPR active and the EPR active ones become silent, thus suggesting that either the adduct is on a previously diamagnetic and therefore on EPR silent cluster, or that a red-ox reaction precedes adsorption of NO. If adsorption

is only on Ag_6^+ clusters which will become EPR silent when NO is added, these EPR active clusters will bind an excess of NO. Hence NO can easily become NO^+ or NO^-. On the other hand N_2O molecules can also be formed by disproportionation reactions of NO on the silver clusters. By HYSCORE, there is a small ^{14}N hyperfine interaction to a second nitrogen spin in the vicinity of the silver cluster so that a significant transfer (or an anisotropic distribution) of spin densities is over the two nitrogens. In the case of covalent bonding, the transferred spin density would give rise to a non-vanishing isotropic ^{14}N hyperfine interaction which is on the order of $A_{iso}^N \approx 1.5$ MHz in the HYSCORE spectrum. This small nitrogen isotropic hyperfine coupling is notoriously difficult to detect by ENDOR, because expected transitions are just in the range of a few MHz. One Ag atom of the cluster forms a partial covalent bond with nitrogen, resulting in a contact nuclear spin and electron spin interaction ($\mathbf{I} \cdot \mathbf{S}$ type) which split the resonance line at the $g_{zz} = 1.841$ component of the adsorbed NO to a sufficient extent to be visible in conventional EPR (Ag hyperfine interaction with $A_{zz}^{Ag} = 200$ G). Pulse Q-band ENDOR is required to detect the small nuclear Larmor frequency of Ag, i.e. 0.61 MHz of ^{107}Ag and 0.70 MHz of ^{109}Ag.

The lineshape of the EPR spectrum is basically determined by the field-dependent electron Zeeman splitting and the field-independent hyperfine interaction of the nuclear spin with the unpaired electron spin. The relaxation of the electron magnetization can be principally coupled to the orientational motion of the NO_2 spin probe via motion-induced fluctuations of the effective A and g values. These fluctuations can be induced by reorientations of the magnetic interaction tensors or modulation of the elements of the motional tensors. Thus, molecular motion leads to stochastic Larmor frequency fluctuations, which can be characterized by a motional correlation time τ_c and an amplitude $\Delta\omega$ that depend on the orientation of the spin probe relative to the external magnetic field B_0. It can be very useful and therefore required to apply electron spin-echo detected EPR for studying the influence of molecular motion on T_2. In the slow-motion regime ($\Delta\omega\tau_c < 1$), the time constant of the echo decay can depend monotonously on τ_c of the stochastic process and then the transverse relaxation rate $1/T_2$ is a function of both τ_c and $\Delta\omega$. The extent of the Larmor frequency fluctuations ($\Delta\omega$) may require different microwave high frequency approaches, because the spectral width is dominated by the anisotropic Zeeman interaction and the components of the g tensor become more resolved which leads to an enhanced orientation selectivity. Currently, magnetic tensors of the NO_2 molecule are fixed in the simulation, only rotational diffusion of molecular slow-motion is simulated according to the least-square fitting. At cw X-band, the motional rate at the hyperfine component corresponding to $M_I = +1$ is larger than at the $M_I = -1$ component. This finding is probably due to the fact that the g tensor anisotropy influences the relaxation or motion, and A and g anisotropies partially compensate each other at the $M_I = +1$, whereas A anisotropies average out rapidly at the $M_I = -1$.

In order to determine the efficiency and selectivity of heterogeneous catalytic systems at a molecular scale, it is useful to investigate supported cluster catalysts under working condition or *in-operando* which permits a simultaneous evaluation of structure and catalytic performance in a single experiment. Often a single spectroscopy method is insufficient for this purpose due to the limited content of information and different timescales. EXAFS spectroscopy has been proven to be as a suitable tool for particular purposes, for instance, a reduced silver cluster undergoes a slight structural change and a red-ox reaction precedes adsorption of NO.

Bibliography

[1] B. Zhou, S. Han, R. Raja, G.A. Somorjai (Eds.), Nanotechnology in Catalysis. Vol 3. Springer Science+Business Media, LLC: New York, 2007

[2] B. Corain, G. Schmid, N. Toshima (Eds.), Metal Nanoclusters in Catalysis and Materials Science: The Issue of Size Control. Elsevier: Amsterdam, 2008

[3] J. Bourdon, Growth and Properties of Metal Clusters: Application to the Catalysis and the Photographic Process. Proceeding of the 32nd International Meeting of Society de Chemical. Elsevier: New York, 1980

[4] R.F. Marzke, Catal. Rev.-Sci. Eng. **19** (1979) 43-65

[5] W.P. Halperin, Rev. Mod. Phys. **58** (1986) 533-607

[6] G.F. Zhao, Y. Lei, Z. Zeng. Chemical Physics. **327** (2006) 261-268

[7] W.A. de Heer, Rev. Mod. Phys. **65** (1993) 611-676

[8] A. Alkauskas, A. Baratoff, C. Bruder, J. Phys. Chem. A. **108** (2004) 6863-6868

[9] J.R. Morton, K.F. Preston, J. Magn. Res. **68** (1986) 121-128

[10] J.R. Morton, K.F. Preston, Zeolites. **7** (1987) 2-4

[11] T. Wasowicz, J. Michalik, Radiat. Phys. Chem. **37** (1991) 427-432

[12] J. Michalik, T. Wasowicz, A. van der Pol, E.J. Reijerse, E. de Boer, J. Chem. Soc., Chem. Commun. (1992) 29-30

[13] J. Michalik, M. Zamadics, J. Sadlo, L.Kevan, J. Phys. Chem. **97** (1993) 10440-10444

[14] J. Michalik, N. Azuma, J. Sadlo, L.Kevan, J. Phys. Chem. **99** (1995) 4679-4686

[15] D. Hermerschmidt, R. Haul, Ber. Bunsenges. Phys. Chem. **84** (1980) 902-907

[16] P.J. Grobet, R.A. Schoonheydt, Surf. Sci. **156** (1985) 893-898

[17] J. Michalik, L. Kevan, J. Am. Chem. Soc. **108** (1986) 4247-4253

[18] R.A. Schoonheydt, H. Leeman, J. Phys. Chem. **93** (1989) 2048-2053

[19] R. A. Schoonheydt, J. Phys. Chem. Solids, **50** (1989) 523-539

[20] A. Kawabata, R. Kubo, J. Phys. Soc. Jpn. **21** (1966) 1765-1772

[21] L.P. Gor'kov, G.M. Eliashberg, Sov. Phys. JETP. **21** (1965) 940-947

[22] R. Kubo, J. Phys. Soc. Jpn. **17** (1962) 975-986

[23] F. Aguilera-Granja, J.M. Montejano-Carrizales, A. Vega, Solid State Commun. **133** (2005) 573-578

[24] N. Watari, S. Ohnishi, Phys. Rev. B. **58** (1998) 1665-1676

[25] A. Jentys, Phys. Chem. Chem. Phys. **1** (1999) 4059-4063

[26] R.E. Benfield, J. Chem. Soc., Faraday Trans. **88** (1992) 1107-1110

[27] P.A. Kilty, W.M.H. Sachtler, Catal. Rev.-Sci. Eng. **10** (1974) 1-16

[28] L. Kevan, R.N. Schwartz (Eds.), Time Domain Electron Spin Resonance. Wiley: New York, 1979

[29] I. Gromov, V. Krymov, P. Manikandan, D. Arieli, D. Goldfarb, J. Magn. Reson. **139** (1999) 8-17

[30] H. Blok, J.A.J.M. Disselhorst, S.B. Orlinskii, J. Schmidt, J. Magn. Reson. **166** (2004) 92-99

[31] K. Möbius, A. Savitsky, A. Schnegg, M. Plato, M. Fuchs, Phys. Chem. Chem. Phys. **7** (2005) 19-42

[32] John A. Weil, James R. Bolton, John E. Wertz, Electron Paramagnetic Resonance: Elementary Theory and Practical Applications. Wiley: New York, 1994

[33] Charles P. Poole, Jr., Electron Spin Resonance: A Comprehensive Treatise on Experimental Techniques. Wiley: New York, 1983

[34] A. Schweiger, G. Jeschke, Principles of Pulse Electron Paramagnetic Resonance. Oxford University Press: New York, 2001

[35] D.C. Koningsberger, R. Prins (Eds.), X-ray Absorption: Principles, Applications and Techniques of EXAFS, SEXAFS and XANES. Wiley: New York, 1988

[36] J. Clarke, A.I. Braginski (Eds.), The SQUID Handbook. Wiley: Weinheim, 2004

[37] H. van Bekkum, E.M. Flanigen, P.A. Jacobs, J.C. Jansen (Eds.), Introduction to Zeolite Science and Practice. Elsevier Science: Amsterdam, 2001

[38] J.B. Nagy, P. Bodart, I. Hannus, I. Kiricsi, Synthesis, Characterization and Use of Zeolitic Microporous Materials. DecaGen Ltd: Szeged, 1998

[39] W. Loewenstein, American Mineralogist. **39** (1954) 92-96

[40] J. Weitkamp, L. Puppe, Catalysis and Zeolites. Springer-Verlag: New York, 1998

[41] J. Jiao, W. Wang, B. Sulikowski, J. Weitkamp, M. Hunger, Microporous Mesoporous Mater. **90** (2006) 246-250

[42] J. Huang, Y. Jiang, V.R. Reddy Marthala, B. Thomas, E. Romanova, M. Hunger, J. Phys. Chem. C. **112** (2008) 3811-3818

[43] M.D. Baker, G.A. Ozin, J. Godber, J. Phys. Chem. **89** (1985) 305-311

[44] J. Texter, R. Kellerman, T. Gonsiorowski, J. Phys. Chem. **90** (1986) 2118-2124

[45] B. Mihailova, V. Valtchev, S. Mintova, A.-C. Faust, N. Petkov, T. Bein, Phys. Chem. Chem. Phys. **7** (2005) 2756-2763

[46] M. Petrera, A. Gennaro, P. Gherardi, G. Gubitosa, N. Pernicone, J. Chem. Soc., Faraday Trans. 1, **80** (1984) 709-720

[47] Y. Kim, K. Seff, J. Phys. Chem. **82** (1978) 921-924

[48] Ch. Baerlocher, W.M. Meier, D.H. Olson, Atlas of Zeolite Framework Types. Elsevier: Amsterdam, 2001

[49] M. Brack, Rev. Mod. Phys. **65** (1993) 677-732

[50] F. Baletto, R. Ferrando, Rev. Mod. Phys. **77** (2005) 371-423

[51] J.A.A. Perenboom, P. Wyder, F. Meier, Phys. Rep. **78** (1981) 173-292

[52] E. Roduner, Nanoscopic materials: Size-Dependent Phenomena. The Royal Society of Chemistry: Cambridge, 2006

[53] M. Aslam, I.S. Mulla, K. Vijayamohanan, Appl. Phys. Lett. **79** (2001) 689-691

[54] H.W. Kroto, Nature. **329** (1987) 529-531

[55] X. Liu, H. Dilger, R.A. Eichel, J. Kunstmann, E. Roduner, J. Phys. Chem. B. **110** (2006) 2013-2023

[56] M. Pereiro, D. Baldomir, J.E. Arias, Phys. Rev. A. **75** (2007) 063204

[57] A.J. Millis, Nature. **392** (1998) 147-150

[58] M.O. Nutt, J.B. Hughes, M.S. Wong, Environ. Sci. Technol. **39** (2005) 1346-1353

[59] L. Josephson, C.-H. Tung, A. Moore, R. Weissleder, Bioconjugate Chem. **10** (1999) 186-191

[60] J.W.M. Bulte, T. Douglas, B. Witwer, S.-C. Zhang, E. Strable, B.K. Lewis, H. Zywicke, B. Miller, P. van Gelderen, B.M. Moskowitz, I.D. Duncan, J.A. Frank, Nat. Biotechnol. **19** (2001) 1141-1147

[61] Y. Yang, M. Nogami, Sci. Technol. Adv. Mater. **6** (2005) 71-75

[62] V.P. Drachev, S.V. Perminov, S.G. Rautian, V.P. Safonov, JETP Letters. **68** (1998) 651-656

[63] V.P. Drachev, W.D. Bragg, V.A Podolskiy, V.P. Safonov, W. Kim, Z.C. Ying, R.L. Armstrong, V.M. Shalaev, J. Opt. Soc. Am. B. **18** (2001) 1896-1903

[64] V.P. Drachev, E.N. Khaliullin, W. Kim, F. Alzoubi, S.G. Rautian, V.P. Safonov, R.L. Armstrong, V.M. Shalaev, Phys. Rev. B. **69** (2004) 035318

[65] V.N. Pustovit, T.V. Shahbazyan, Chem. Phys. Lett. **420** (2006) 469-473

[66] L.A. Peyser, A.E. Vinson, A.P. Bartko, R.M. Dickson, Science. **291** (2001) 103-106

[67] M. Eichelbaum, K. Rademann, A. Hoell, D.M. Tatchev, W. Weigel, R. Stösser, G. Pacchioni, Nanotechnology. **19** (2008) 135701

[68] A. Cho, Science. **299** (2003) 1684-1685

[69] R.L. Thomas, A.K. Sarkar, K. Kohata, S.A. Abbas, K.L. Matta. Tetrahedron Lett. **31** (1990) 2825-2828

[70] E.L. Force, A.T. Bell, J. Catal. **40** (1975) 356-371

[71] G.A. Ozin, F. Hugues, S.M. Mattar, D.F. McIntosh, J. Phys. Chem. **87** (1983) 3445-3450

[72] P.P. Borbat, A.J. Costa-Filho, K.A. Earle, J.K. Moscicki, J.H. Freed, Science. **291** (2001) 266-269

[73] J.H. Freed, Ann. Rev. of Phys. Chem. **51** (2000) 655-689

[74] K.A. Earle, J.H. Freed, Appl. Magn. Reson. **16** (1999) 247-272

[75] R. Grinter, The Quantum in Chemistry: An Experimentalist's View. Wiley: Chichester, 2005

[76] A. Abragam, B. Bleaney, Electron Paramagnetic Resonance of Transition Ions. Oxford University Press: London, 1970

[77] E. Beaurepaire, H. Bulou, F. Scheurer, J.-P. Kappler (Eds.), Magnetism: A Synchrotron Radiation Approach. Springer-Verlag: Berlin, 2006

[78] J.R. Pilbrow, Transition Ion Electron Paramagnetic Resonance. Oxford University Press: New York, 1990

[79] J.-M. Spaeth, H. Overhof, Point Defects in Semiconductors and Insulators: Determination of Atomic and Electronic Structure from Paramagnetic Hyperfine Interactions. Springer-Verlag: Berlin, 2003

[80] K. Dyrek, M. Che, Chem. Rev. **97** (1997) 305-331

[81] M. Kaupp, R. Reviakine, O.L. Malkina, A. Arbuznikov, B. Schimmelpfennig, V.G. Malkin, J. Comput. Chem. **23** (2002) 794-803

[82] C.P. Slichter, Principles of Magnetic Resonance. Springer-Verlag: Heidelberg, 1996

[83] G.R. Eaton, S.S. Eaton, L.J. Berliner (Eds.), Biological Magnetic Resonance, Vol. 19. Kluwer Publishing: Amsterdam, 2000

[84] P. Höfer, A. Grupp, H. Nebenführ, M. Mehring, Chem. Phys. Lett. **132** (1986) 279-282

[85] A. Pöppl, L. Kevan, J. Phys. Chem. **100** (1996) 3387-3394

[86] G. Jeschke, R. Rakhmatullin, A. Schweiger, J. Magn. Reson. **131** (1998) 261-271

[87] E.R. Davies, Phys. Lett. A. **47** (1974) 1-2

[88] W.B. Mims, Proc. Roy. Soc. London, Series A: Mathematical and Physical Sciences. **283** (1965) 452-457

[89] B.S. Deaver, W.M. Fairbank, Phys. Rev. Lett. **7** (1961) 43-46

[90] R. Doll, M. Näbauer, Phys. Rev. Lett. **7** (1961) 51-52

[91] B.D. Josephson, Phys. Lett. **1** (1962) 251-253

[92] B.D. Josephson, Adv. Phys. **14** (1965) 419-451

[93] B.D. Cullity, Introduction to Magnetic Materials, Addison-Wesley: 1972

[94] R.L. Carlin, Magneto-chemistry, Springer-Verlag: Berlin, 1986

[95] S. Blundel, Magnetism in Condensed Matter. Oxford University Press Inc: New York, 2001

[96] Ch. Kittel, Introduction to Solid State Physics. Wiley: New Jersey, 2005

[97] J. Sólyom, Fundamentals of the Physics of Solids: Structure and Dynamics. Vol I. Springer-Verlag: Berlin, 2007

[98] J.D. Patterson, B.C. Bailey, Solid-State Physics: Introduction to the Theory. Springer-Verlag: Berlin, 2007

[99] P. Carra, B.T. Thole, M. Altarelli, X. Wang, Phys. Rev. Lett. **70** (1993) 694-697

[100] J. Stör, H.C. Siegmann, Magnetism: From Fundamentals to Nanoscale Dynamics. Springer-Verlag: Berlin, 2006

[101] V. Kresin, Phys. Rev. B. **38** (1988) 3741-3746

[102] F.R. Elder, A.M. Gurewitsch, R.V. Langmuir, H.C. Pollock, Phys. Rev. **71** (1947) 829-830

[103] D.C. Koningsberger, B.L. Mojet, G.E. van Dorssen, D.E. Ramaker, Top. Catal. **10** (2000) 143-155

[104] S.T. Homeyer, W.H.M. Sachtler, Appl. Catal. **54** (1989) 189-202

[105] Z. Zhang, W. H. M. Sachtler, J. Chem. Soc., Faraday Trans. **86** (1990) 2313-2319

[106] P.A. Jacobs, N.I. Jaeger, P. Jiru, G. Schulz-Ekloff (Eds.), Metal Microstructures in Zeolites. Elsevier: Amsterdam, 1982

[107] E. Hoffmann, A. Schweiger, Appl. Magn. Reson. **9** (1995) 1

[108] S. Stoll, A. Schweiger, J. Magn. Reson. **178** (2006) 42-55

[109] D.E. Budil, S. Lee, S. Saxena, J.H. Freed, J. Magn. Reson, Series A. **120** (1996) 155-189

[110] C. Gemperle, G. Aebli, A. Schweiger, R.R. Ernst, J. Magn. Reson. **88** (1990) 241-256

[111] B. Simovic, P. Studerus, S. Gustavsson, R. Leturcq, K. Ensslin, R. Schuhmann, J. Forrer, A. Schweiger, Rev. Sci. Instrum. **77** (2006) 064702

[112] I. Gromov, J. Forrer, A. Schweiger, Rev. Sci. Instrum. **77** (2006) 064704

[113] J. Hoentsch, Yu. Rosentweig, D. Heinhold, K. Köhler, M. Gutjahr, A. Pöppl, G. Völkel, R. Böttcher, Appl. Magn. Reson. **25** (2003) 249-259

[114] M. Vaarkamp, J.C. Linders, D.C. Koningsberger, Physica B. **208-209** (1995) 159-160

[115] D.E. Sayers, E.A. Stern, F.W. Lytle, Phys. Rev. Lett. **27** (1971) 1204-1207

[116] N. Yao, Z.L. Wang, Handbook of Microscopy for Nanotechnology. Kluwer Academic Publishers: New York, 2005

[117] J.W. Niemantsverdriet, Spectroscopy in Catalysis: An Introduction. Wiley: Weinheim, 2007

[118] M.M.J. Treacy, A. Howie, J. Catal. **63** (1980) 265-269

[119] L. Kevan, *Electron Spin Resonance of Transition Metal Ions in Zeolites*, in *Electron Spin Resonance*. Vol. 12B, ed. M.C.R. Symons, The Royal Society of Chemistry: Cambridge, 1991

[120] M. Bennati, T.F. Prsiner, Rep. Prog. Phys. **68** (2005) 411-448

[121] A. Abou-Kais, J.C. Vedrine, C. Naccache, J. Chem. Soc., Faraday Trans. 2, **74** (1978) 959-967

[122] N. Narayana, L. Kevan, J. Chem. Phys. **76** (1982) 3999-4005

[123] N. Narayana, L. Kevan, J. Chem. Phys. **83** (1985) 2556-2559

[124] D.R. Brown, L. Kevan, J. Phys. Chem. **90** (1986) 1129-1133

[125] F. Blatter, K.W. Blazey. Z. Phys. D. **18** (1991) 427-429

[126] H. Klein, H. Kirschhock, H. Fuess, J. Phys. Chem. **98** (1994) 12345-12360

[127] Landoldt-Börnstein Tables - Group II, Molecules and Radicals, Volume 9a, Atoms, Inorganic Radicals and Radicals in Metal Complexes, Eds. H. Fischer, K.H. Hellwege, Springer: Berlin, 1977

[128] D. Hermerschmidt, R. Haul, Ber. Bunsenges. Phys. Chem. **85** (1981) 739-745

[129] N. Narayana, L. Kevan, J. Am. Chem. Soc. **107** (1985) 4643-4647

[130] M. Narayana, A.S.W. Li, L. Kevan, J. Phys. Chem. **85** (1981) 132-133

[131] R.B. Clarkson, S. McClellan, J. Phys. Chem. **82** (1978) 294-297

[132] P.H. Kasai, J. Chem. Phys. **43** (1965) 3322-3327

[133] J.R. Morton, K.F. Preston, J. Magn. Res. **30** (1978) 577-582

[134] S. Schultz, M.R. Shanabarger, P.M. Platzman, Phys. Rev. Lett. **19** (1967) 749-754

[135] F. Beuneu, P. Monod, Phys. Rev. B. **18** (1978) 2422-2425

[136] A. van der Pol, E.J. Reijerse, E. de Boer, T. Wasowicz, J. Michalik, Molecular Physics. **75** (1992) 37-42

[137] B. Xu, L. Kevan, J. Phys. Chem. **95** (1991) 1147-1151

[138] J. Michalik, J. Sadlo, J.S. Yu, L.Kevan, Colloids Surfaces A: Physicochem. Eng. Aspects. **115** (1996) 239-247

[139] J. Michalik, T. Wasowicz, J. Sadlo, E.J. Reijerse, L.Kevan, Radiat. Phys. Chem. **47** (1996) 75-81

[140] J. Michalik, J. Sadlo, T. Kodaira, S.Shimomura, H.Yamada, J. Radioanalyt. Nuclear Chem. **232** (1998) 135-137

[141] P.A. Jacobs, J.B. Uytterhoeven, H.K. Beyer, J. Chem. Soc., Faraday Trans. 1, **75** (1979) 56-64

[142] L. Kevan, M.K. Bowman, N. Narayana, R.K. Boeckman, V.F. Yudanov, Y.D. Tsvetkov, J. Chem. Phys. **63** (1975) 409-416

[143] T. Ichikawa, L. Kevan, M.K. Bowman, S.A. Dikanov, Y.D. Tsvetkov, J. Chem. Phys. **71** (1979) 1167-1174

[144] E.G. Derouane, M. Mestdagh, L. Vielvoye, J. Catal. **33** (1974) 169-175

[145] D. Goldfarb, M. Bernardo, K.G. Strohmaier, D.E.W. Vaughan, H. Thomann, J. Am. Chem. Soc. **116** (1994) 6344-6353

[146] D. Goldfarb, K.G. Strohmaier, D.E.W. Vaughan, H. Thomann, O.G. Poluektov, J. Schmidt, J. Am. Chem. Soc. **118** (1996) 4665-4671

[147] G. Lee, P.T. Sprunger, D.B. Poker, D.M. Zehner, E.W. Plummer, J. Vac. Sci. Technol. A. **12** (1994) 2119-2123

[148] P. Nordlander, S. Holloway, J.K. Nørskov, Surf. Sci. **136** (1984) 59-81

[149] S. Iijima, T. Ichihashi, Mater. Trans., The Japan Institute of Metals. **31** (1990) 582-587

[150] H. Hofmeister, M. Dubiel, G.L. Tan, K.-D. Schike, Phys. Stat. Sol. (a). **202** (2005) 2321-2329

[151] B. Sampedro, P. Crespo, A. Hernando, R. Litrán, J.C. Sánchez-López, C. López-Cartes, A. Fernandez, J. Ramírez, J. González-Calbet, M. Vállet, Phys. Rev. Lett. **91** (2003) 237203

[152] J.S. Romero, A.G. Fitzgerald, M.J. Rose, Appl. Surf. Sci. **234** (2004) 369-373

[153] D.C. Koningsberger, M.K. Oudenhuijzen, J.H. Bitter, D.E. Ramaker, Top. Catal. **10** (2000) 167-177

[154] M. Vaarkamp, J.T. Miller, F.S. Modica, D.C. Koningsberger, J. Catal. **163** (1996) 294-305

[155] S.K. Nayak, S.N. Khanna, B.K. Rao, P. Jena, J. Phys. Chem. A. **101** (1997) 1072-1080

[156] A. Kawabata, J. Phys. Soc. Jpn. **29** (1970) 902-911

[157] L.D. Marks, Rep. Prog. Phys. **57** (1994) 603-649

[158] E. Vavilova, I. Hellmann, V. Kataev, C. Täschner, B. Büchner, R. Klingeler, Phys. Rev. B. **73** (2006) 144417

[159] B. Corzilius, K.-P. Dinse, J. van Slageren, K. Hata, Phys. Rev. B. **75** (2007) 235416

[160] Y. Yamamoto, T. Miura, Y. Nakae, T. Teranishi, M. Miyake, H. Hori. Physica B. **329-333** (2003) 1183-1184

[161] M.E. Saleta, J. Curiale, H.E. Troiani, S. Ribeiro Guevara, R.D. Sánchez, M. Malta, R.M. Torresi, Appl. Surf. Sci. **254** (2007) 371-374

[162] S. Hatscher, H. Schilder, H. Lueken, W. Urland, Pure Appl. Chem. **77** (2005) 497-511

[163] J. Zhao, Y. Luo, G. Wang, Eur. Phys. J. D. **14** (2001) 309-316

[164] Y. Kim, J.W. Gifje, K. Seff, J. Am. Chem. Soc. **99** (1977) 7057-7059

[165] Y. Kim, K. Seff, J. Am. Chem. Soc. **100** (1978) 175-180

[166] D. Astruc (Ed.), Nanoparticles and Catalysis, Vol 1. Wiley: Weinheim, 2008

[167] P.H. Kasai, R.J. Bishop, Jr., J. Am. Chem. Soc. **94** (1972) 5560-5566

[168] P.H. Kasai, R.M. Gaura, J. Phys. Chem. **86** (1982) 4257-4260

[169] T. Rudolf, A. Pöppl, W. Brunner, D. Michel, Magn. Reson. Chem. **37** (1999) S93-S99

[170] A. Pöppl, T. Rudolf, P. Manikandan, D. Goldfarb, J. Am. Chem. Soc. **122** (2000) 10194-10200

[171] T. Rudolf, A. Pöppl, W. Hofbauer, D. Michel, Phys. Chem. Chem. Phys. **3** (2001) 2167-2173

[172] H. Yahiro, A. Lund, R. Aasa, N.P. Benetis, M. Shiotani, J. Phys. Chem. A. **104** (2000) 7950-7956

[173] V. Umamaheswari, M. Hartmann, A. Pöppl, J. Phys. Chem. B. **109** (2005) 10842-10848

[174] V. Umamaheswari, M. Hartmann, A. Pöppl, J. Phys. Chem. B. **109** (2005) 1537-1546

[175] S.M. Kanan, M.A. Omary, H.H. Paterson, M. Matsuoka, M. Anpo, J. Phys. Chem. B. **104** (2000) 3507-3517

[176] K. Shimizu, A. Satsuma, Phys. Chem. Chem. Phys. **8** (2006) 2677-2695

[177] A. Gembus, B. Corzilius, R.-A. Eichel, K.P. Dinse, S. Immel, D. Stumm, M. Flauaus, H. Plenio, J. Phys. Chem. B. **110** (2006) 15012-15020

[178] E. Ramic, R.-A. Eichel, K.P. Dinse, A. Titz, B. Schmidt, J. Phys. Chem. B. **110** (2006) 20655-20663

[179] M. Nagata, H. Yahiro, M. Shiotani, M. Lindgren, A. Lund, Chem. Phys. Lett. **256** (1996) 27-32

[180] H. Yahiro, M. Shiotani, J.H. Freed, M. Lindgren, A. Lund, Stud. Surf. Sci. Catal. **94** (1995) 673

[181] H. Li, A. Lund, M. Lindgren, E. Sagstuen, H. Yahiro, Chem. Phys. Lett. **271** (1997) 84-89

[182] H. Li, H. Yahiro, K. Komaguchi, M. Shiotani, E. Sagstuen, A. Lund, Microporous Mesoporous Mater. **30** (1999) 275-281

[183] G.R. Bird, J.C. Baird, A.W. Jache, J.A. Hodgeson, R.F. Curl, Jr., A.C. Kunkle, J.W. Bransford, J. Rastrup-Andersen, J. Rosenthal, J. Chem. Phys. **40** (1964) 3378-3390

[184] W.C. Mosley, W.G. Moulton, J. Chem. Phys. **43** (1965) 1207-1214

[185] H. Zeldes, R. Livingston, J. Chem. Phys. **35** (1961) 563-567

[186] M. Shiotani, J.H. Freed, J. Phys. Chem. **85** (1981) 3873-3883

[187] J.P. Barnes, J.H. Freed, Biophys. J. **75** (1998) 2532-2546

[188] K.A. Earle, W. Hofbauer, B. Dzikowski, J.K. Moscicki, J.H. Freed, Magn. Reson. Chem. **43** (2005) S256-S266

[189] T.C. James, R.J. Thibault, J. Chem. Phys. **41** (1964) 2806-2813

[190] R. D. Shannon, Acta Cryst. **A32** (1976) 751-767

[191] P.W. Atkins, M. C. R. Symons, J. Chem. Soc. (1962) 4794 - 4797

[192] J.H. Spielberg, E. Gelerinter, J. Chem. Phys. **77** (1982) 2159-2165

[193] J.H. Lunsford, Catal. Rev.-Sci. Eng **8** (1973) 135-157

[194] Y.D. Kim, G. Ganteför, Chem. Phys. Lett. **383** (2004) 80-83

[195] M. Schmidt, Ph. Cahuzac, C. Brechignac, H.-P. Cheng, J. Chem. Phys. **118** (2003) 10956-10962

[196] P.H. Kasai, D. McLeod, Jr., T. Watanabe, J. Am. Chem. Soc. **102** (1980) 179-190

[197] P.H. Kasai, J. Phys. Chem. **86** (1982) 3684-3686

[198] J.A. Howard, H.A. Joly, B. Mile, J. Phys. Chem. **94** (1990) 6627-6631

[199] J.R. Morton, K.F. Preston, A. Sayari, J.S. Tse, J. Phys. Chem. **91** (1987) 2117-2120

[200] G.A. Ozin, M.D. Baker, J. Godber, J. Phys. Chem. **88** (1984) 4902-4904

[201] T. Sun, K. Seff, Chem. Rev. **94** (1994) 857-870

[202] Y. Kim, K. Seff, J. Am. Chem. Soc. **99** (1977) 7055-7057

[203] Y. Kim, K. Seff, J. Am. Chem. Soc. **100** (1978) 6989-6997

[204] Y. Kim, K. Seff, J. Phys. Chem. **82** (1978) 925-929

[205] M. Meyer, C. Leiggener, G. Calzaferri, Chem. Phys. Chem. **6** (2005) 1071-1080

[206] L.R. Gellens, W.J. Mortier, R.A. Schoonheydt, J.B. Uytterhoeven, J. Phys. Chem. **85** (1981) 2783-2788

[207] R. Seifert, R. Rytz, G. Calzaferri, J. Phys. Chem. A. **104** (2000) 7473-7483

[208] Y. Suzuki, T. Miyanaga, H. Hoshino, N. Matsumoto, T. Ainai, Phys. Scr. **T115** (2005) 765-768

[209] T. Miyanaga, H. Hoshino, H. Endo, J. Synchrotron Rad. **8** (2001) 557-559

[210] Ken-ichi Shimizu, K. Sugino, K. Kato, S. Yokota, K. Okumura, A. Satsuma, J. Phys. Chem. C. **111** (2007) 1683-1688

[211] M. Dubiel, X.C. Yang, S. Brunsch, Phys. Scr. **T115** (2005) 729-732

[212] N. Dimakis, G. Bunker, Phys. Rev. B. **58** (1998) 2467-2475

[213] J.J. Rehr, R.C. Albers, Rev. Mod. Phys. **72** (2000) 621-654

[214] E.C. Cosgriff, C.T. Chantler, C. Witte, L.F. Smale, C.Q. Tran, Phys. Lett. A. **343** (2005) 174-180

[215] P.A. Montano, W. Schulze, B. Tesche, G.K. Shenoy, T.I. Morrison, Phys. Rev. B. **30** (1984) 672-677

[216] T. Miyanaga, H. Hoshino, H. Endo, H. Sakane, J. Synchrotron Rad. **6** (1999) 442-444

[217] J.S. Ogden, N.E. Bogdanchikova, J.M. Corker, V.P. Petranovskii, Eur. Phys. J. D. **9** (1999) 605-608

[218] Y. Suzuki, N. Matsumoto, T. Ainai, T. Miyanaga, H. Hoshino, Polyhedron. **24** (2005) 685-691

[219] M. Dubiel, R. Schneider, H. Hofmeister, K.-D. Schike, J.C. Pivin, Eur. Phys. J. D. **43** (2007) 291-294

[220] K. Shimizu, M. Tsuzuki, K. Kato, S. Yokota, K. Okumura, A. Satsuma, J. Phys. Chem. C. **111** (2007) 950-959

[221] D.E. Ramaker, G.E. van Dorssen, B.L. Mojet, D.C. Koningsberger, Top. Catal. **10** (2000) 157-165

Symbols

Grecian symbols

α	angular factor of orbital contribution to A_{dip}
α	electron-spin state with $m_S = -1/2$
β	electron-spin state with $m_S = +1/2$
β_e	electron Bohr magneton
β_n	nuclear magneton
γ_e	electron magnetogyric ratio
γ_n	nuclear magnetogyric ratio
δ	the mean energy spacing of adjacent electronic levels
δ	difference between the phases φ_1 and φ_2
ΔE	difference of energies or edge shift
Δg	shift of electronic g tensor relative to the g_e value
$\Delta H_{\frac{1}{2}}$	the full width at half-height
ΔH_{pp}	peak-to-peak linewidth
$\Delta \nu^S_{max}$	the maximum vertical frequency shift
η	resonator filling factor
θ	angle
$\theta(K)$	Curie-Weiss temperature
λ	the mean-free-path of the photo-electron
λ	spin-orbit coupling constant
μ_0	the atomic background of the free atom
μ_0	vacuum permeability
μ	magnetic permeability
$\mu(E)$	linear absorption coefficient
μ_{eff}	effective magnetic moment
$\mu(k)$	oscillatory absorption coefficient
μ_l	orbital quantum number
μ_N	nuclear magnetic moment
ν_L	nuclear Larmor frequency
π	180^0 mw pulse
$\pi/2$	90^0 mw pulse
$\rho_{\alpha,\beta}$	the electron spin density of α or β states
ρ	the sample density
σ^2	Debye-Waller factor
$\tau_{1,2}$	a delay time
τ_c	Correlation time
Φ_0	Magnetic flux quantization
$\varphi_j(k)$	the phase factor
$\varphi_{1,2}$	the phases of Josephson junction (SQUID)
χ	scalar dimensionless magnetic susceptibility

χ_0	temperature-indpendent magnetic susceptibility
χ_{band}	diamagnetic susceptibility
χ_{ion}	ionic core magnetic susceptibility
χ_{m}	molar magnetic susceptibility
χ_{Pauli}	Pauli paramagnetic susceptibility
$\chi(k)$	oscillatory fine structure function (XAS)
$\lvert\psi_0(0)\rvert^2$	finding probability for electron per unit volume
Ω	electric impedance

Roman symbols

1D, 2D, 3D	one-, two- and three-dimensional
ac	alternating current
a_{iso}	isotropic hyperfine coupling constant
$\mathbf{A}$	hyperfine coupling matrix
A_{aniso}	anisotropic hyperfine coupling matrix
$\mathbf{A}_{\mathrm{dip}}$	dipole-dipole hyperfine coupling matrix
AAS	atomic absorption spectroscopy
$\mathbf{B}$	magnetic flux density
B_0	external static magnetic field
B_1	effective part of the external microwave field
B_2	effective part of the external radio frequency field
B_{r}	resonant magnetic field
c	speed of light
cgs	centimeter-gram-second (system of units)
C	Coulomb
C_{m}	molar Curie constant
cw	continuous wave
d	diameter
dc	direct current
DFT	density functional theory
DRS	diffuse reflectance spectroscopy
DTA	differential thermal analysis
e	charge of electron
E	the total energy
E_{a}	activation energy
E_F	Fermi energy
EMU	electron magnetic unit
ENDOR	electron nuclear double resonance
EPR/ESR	electron paramagnetic/spin resonance
ESE	electron spin echo
ESEEM	electron spin echo envelope modulation
EXAFS	extended X-ray absorption fine structure
f	frequency
fcc	face-centered-cubic
$f_j(k)$	the back-scattering amplitude
F	atomic dispersion of surface
F_{ENDOR}	Mims-ENDOR efficiency

FAU	faujasite zeolite
FID	free induction decay
FT	Fourier transform
FTIR	Fourier transform infrared
g	g factor
g_e	the free electron g factor
g_n	nuclear g factor
G	Gauss
GeV	gigaelectron volt (10^9 eV)
GHz	gigahertz (10^3 MHz = 1 GHz)
h	Planck's constant (6.626176×10^{-34}) J s
$\hbar$	$h/2\pi$
H	magnetic field strength
H_m	modulation amplitude
$\hat{H}$	Hamiltonian operator
$\mathbf{H}_0$	magnetic field vector
HOMO	highest occupied molecular orbital
HRTEM	high-resolution transmission electron microscopy
HYSCORE	hyperfine sublevel correlation spectroscopy
I	spin quantum number of the nuclear spin
I_0	intensity of the incident beam or critical electric current
ICP	inductively coupled plasma
IP	ionization potential
J	total angular momentum
J_m	m th-order Bessel function
k	the photo-electron wave vector
k	the first order rate constant
k_B	Boltzmann constant (1.380662×10^{-23}) J K^{-1}
keV	kiloelectron volt
KHz	kilohertz
$\mathbf{L}$	orbital angular momentum tensor
$\hat{L}$	orbital angular momentum operator
LTA	Linde type A zeolite
LUMO	lowest unoccupied molecular orbital
m_e	electron mass
m_I	magnetic quantum number of the nuclear spin
m_S	magnetic quantum number of the electron spin
mw	microwave
$M(H)$	magnetization
MRI	magnetic resonance imaging
M_s	saturation magnetization
MHz	megahertz
N	number of atoms or coordination number
N	ratio of $R_\parallel$ to $R_\perp$ component of the diffusion tensor
NaA	sodium A zeolite
nm	nanometer (10^{-9} meter)
NMR	nuclear magnetic resonance
ppm	parts per million

pm	picometer (10^{-12} meter)
P	microwave power
q	electric charge
Q	quadrupole moment
Q	resonator quality factor
r	distance
r	unit vector in r direction
R_0	the gas constant (8.31441 K^{-1} J mol^{-1})
R	resistance
rf	radio frequency
$R_{\parallel}$	parallel component of the diffusion tensor
$R_{\perp}$	perpendicular component of the diffusion tensor
S	spin quantum number of the electron spin
$\hat{S}$	spin angular momentum operator
S_0^2	the amplitude reduction factor (XAS)
SOC	spin-orbit coupling
SOMO	singly occupied molecular orbital
S/N	signal-to-noise ratio
SQUID	superconducting quantum interference device
T	Tesla
$T(K)$	temperature in Kelvin
T_1	spin-lattice (longitudinal) relaxation time
T_2	spin-spin (transverse) relaxation time
TE	transverse electric
TGA	thermogravimetric analysis
UV	ultraviolet
V	volume of the particle
Wb	Weber
wt.	weight
y'_m	EPR signal amplitude
XANES	X-ray absorption near edge spectroscopy
XAS	X-ray absorption spectroscopy
XMCD	X-ray magnetic circular dichroism
XRD	X-ray diffraction
Z	the atomic number
zJ	zepto-joules (10^{-21} J)
ZFS	zero-field splitting

List of Figures

List of Tables

List of Publications

Peer-Reviewed Articles

1. I. Tkach, **A. Baldansuren**, E. Kalabukhova, S. Lukin, A. Sitnikov, A. Tsvir, M. Ischenko, Yu. Rosentzweig and E. Roduner: *A Homebuilt ESE Spectrometer on the Basis of a High-Power Q-Band Microwave Bridge*. Appl. Magn. Reson. **35** (2008) 95-112.

Conference Posters

1. **A. Baldansuren**, E. Roduner: *Reaction properties of size-selected clusters supported on an LTA zeolite*. 72nd Annual Meeting 2008 and DPG-Spring Meeting of the Condensed Matter Section., Proceeding: Verhandlungen der Deutschen Physikalischen Gesellschaft 1/2008 p.575, Berlin, Deutschland (2008)

2. **A. Baldansuren**, E. Roduner: *Studies of zeolite supported silver clusters*. AMPERE Group Conference and AMPERE NMR Summer School 2007., Proceeding: AMPERE NMR Book of Abstracts p.73, Bukowina Tatrzanska, Poland (2007)

3. I. Tkach, **A. Baldansuren**, E. Kalabukhova, S. Lukin, E. Roduner: *A home-built Q-band Electron Spin Echo spectrometer*. AMPERE Group Conference and AMPERE NMR Summer School 2007., Proceeding: AMPERE NMR Book of Abstracts p.93, Bukowina Tatrzanska, Poland (2007)

4. **A. Baldansuren**, E. Roduner: *Studies on the activity of silver clusters in NaA zeolite*. 105th Bunsentagung, Deutschen Bunsen-Gesellschaft für Physikalische Chemie e.V., DBG Proceeding: *Heterogene Katalyse: Brüke zwischen Ideal- und Realsystemen* p.P31, Erlangen, Deutschland (2006)